THE UNIVERSITY
of EDINBURGH

THE UNIVERSITY of EDINBURGH

Development and fluid dynamic evaluation of novel circulating fluidised bed elements for low-temperature adsorption based carbon capture processes

Francisco Javier Zaragoza Martín

Thesis submitted for the degree of Doctor of Philosophy

School of Engineering
The University of Edinburgh

2016

Declaration

I hereby declare that:

- This thesis has been composed by me.
- The work presented in this thesis is my own.
- The work presented in this thesis has not been submitted for any other degree or professional qualification except as specified on the title page.

Francisco Javier Zaragoza Martín

Lay Summary

Overwhelming scientific evidence points to the anthropogenic emissions of carbon dioxide as the cause of global warming and climate change. In December 2015 a new worldwide agreement to take further action against climate change was reached at COP21, denominated the *Paris Agreement*, which pursues to limit the increase in the global average temperature to "well below" 2°C above pre-industrial levels and "pursue efforts" to limit the temperature increase to 1.5°C. Carbon capture and storage (CCS) is recognised to play a fundamental role in achieving this.

Among the technologies used in the first link of the CCS chain, *carbon capture*, solid sorbates that bond chemically with CO_2 from power station flue gas at atmospheric pressure can be used in circulating fluidised beds (CFBs) to meet the stringent specifications of 90% capture and 95% purity of CO_2. However, conventional CFB configurations operate in co-current contact mode that limits their performance and incur high operational costs.

In this work, a novel CFB configuration featuring a counter-current adsorber is evaluated from a thermodynamic-kinetic perspective against a conventional co-current adsorber. The methodology developed in the CFB evaluation shows that adsorption equilibrium alone is sufficient to demonstrate quantitatively the superior performance of counter-current systems with respect co-current systems. Experimental determination of the fluid dynamic characteristics in parallel to theoretical assessment is justified as it provides information about phenomena that can impact the process performance, like operational instabilities originated from incorrectly designed system geometry. Residence time distribution (RTD) data for the gas and solid phases in cold model CFB rigs were obtained to gain insight in the CFB system fluid dynamics and quantify axial dispersion of both phases. RTD data could be validated using computational fluid dynamic (CFD) models to estimate the performance of the CFB configurations as real carbon capture processes.

Abstract

A methodology for the thermodynamic-kinetic evaluation of circulating systems as TSA carbon capture processes is developed and used in the assessment of a novel CFB configuration against a benchmark (co-current riser). The novel CFB features a counter-current adsorber, a counter-current regenerator and a riser, the latter element playing a double role of solids conveyer and co-current adsorber. The advantages sought by using a counter-current adsorber are not only the more efficient gas-solid contact mode with respect co-current, but also a low pressure drop derived from operation at lower gas velocities and hydrostatic head partially supported on the contactor internals. Knowledge of the adsorption equilibrium alone is sufficient to realise the much higher sorbent circulation rates required by co-current configurations –compared to counter-current– to meet the stringent carbon capture specifications of 90% recovery and 95% purity. Higher solids circulation rates imply higher energy requirements for regeneration, and therefore research and development of co-current gas-solid contactors cannot be justified in terms of searching for energy-efficient post-combustion carbon capture processes.

Parallel experimental investigation in the operation and fluid dynamics of cold model CFB rigs is carried out with the purposes of: 1) providing information that may impact the process performance and can be fed into the mathematical model used in the theoretical assessment for more realistic evaluation, and 2) determine gas and solids residence time distributions (RTDs), which are used for the estimation of axial dispersion and comparison with published results in similar systems. Gas RTD data is generated using a tracer pulse injection-detection technique, whereas RTD for the solid phase is studied using positron emission particle tracking (PEPT).

The PEPT technique proved to be adequate for the identification of flow regimes in the novel design of the counter-current adsorber, featuring inclined orifice trays. At low gas velocities the particles flow straight down through the tray holes, whereas at higher velocities the particles flow down in zig-zag, increasing the residence time of the particles and reducing the particle axial dispersion, both beneficial in terms of separation efficiency.

Acknowledgments

I gratefully acknowledge the Engineering and Physical Sciences Research Council (EPSRC) of the UK for their financial support under the grant EP/I010939/1.

My deepest gratitude goes to my supervisors, Professor Stefano Brandani and Dr. Xianfeng Fan, for their guidance and expertise throughout this work. Special thanks to Dr. Donald Glass for his help, first in the design of the experimental equipment, and later in a more "hands-on" fashion during our visit to the University of Birmingham.

Equally, I would like to say thank you very much to my fellow members of the Adsorption & Membrane group within the University of Edinburgh's carbon capture group. They were the first source of knowledge, encouragement and inspiration during all these years of hard work.

I am profoundly indebted to the Technical Services of the School of Engineering, not only for the enormous effort they made to bring things from paper to reality, but also for their honest friendship. My thoughts are with Dave and Susan, who sadly passed away during my years at the School.

During my PhD I had the unique opportunity to join SSE's Engineering Centre for eighteen months during the basic design phase of a demonstration carbon capture project, the Peterhead CCS. Although the project did not come into existence due to political circumstances, I could never thank Steve's and Paul's teams enough for the experience. Special thanks to Tom, who was my interviewer, mentor, and now friend.

Thank you to all the people I made friends with during my years in Scotland, whether in Edinburgh, Glasgow or Perth. You were a true support and made me feel at home. I would like to thank my friend Roland for his genuine interest in CCS in general and my work in particular, and for introducing me to the Scottish culture through five-in-a-row Burns Nights.

Last, but not least, I wish to thank my friends and family in Spain for all the encouragement, love and support I received from them. Thank you, Kiko, for the

copy of your PhD thesis, which I kept on my desk to believe that mine would also, in the end, become a reality.

Table of Contents

List of Tables

List of Figures

List of Symbols

NOTES:

All gas volumetric flow rates are assumed to be measured at standard ambient conditions (25°C, 1 bara) unless otherwise stated.

Symbol	Definition	Units
A	Cross-sectional area of adsorber model (Chapter 3 only)	m^2
a	Surface area per unit volume of particle available for adsorption (Chapter 3 only)	m^{-1}
ak_m	Lumped mass transfer coefficient (Chapter 3 only)	s^{-1}
b_0	Langmuir pre-exponential factor	bar^{-1}
D_g	Gas axial dispersion coefficient	m^2/s
d_p	Mean particle size	m
D_s	Solids axial dispersion coefficient	m^2/s
$E(t)$	Exit age distribution function	s^{-1}
$E(\theta)$	Reduced-time exit age distribution function, eq. (6.7)	-
F_g	CO_2-free gas mass flow rate, eq. (3.1) (Chapter 3 only)	kg/s
F_s	Solids flow rate	kg/s
$F_{s,min}$	Minumum solids circulation rate (Chapter 3 only)	kg/s
$F_{s,min,cc}$	Minumum solids circulation rate in pure counter-current system (Chapter 3 only)	kg/s
$F_{s,min,co}$	Minumum solids circulation rate in pure co-current system (Chapter 3 only)	kg/s
g	Aceleration of gravity	m/s^2
G_s	Solids flux	$kg/m^2/s$
h_{reg}	Height of bed of solids in the regenerator	m
k_m	Overall mass transfer coefficient (Chapter 3 only)	m/s
m_{inj}	Mass of tracer injected	mg
N	number of mass transfer units between plug flow and stagnant regions (DPFS flow model)	-

Pe	Péclet number (defined in eq. (3.16))	-
Pe_g	Péclet number of the gas phase (defined in eq. (3.18))	-
Pe_s	Péclet number of the solid phase (defined in eq. (3.17))	-
P_{inj}	CO_2 pulse injection pressure	barg
$P_{reg,bot}$	Pressure at the regenerator bottom	mbarg
$P_{reg,bot,max}$	Maximum pressure achievable at the regenerator bottom	barg
$P_{ris,bot}$	Pressure at riser solids inlet	mbarg
q	Sorbent loading (Chapter 3 only)	kg CO_2/kg solids
Q_{ads}	Air flow rate through counter-current adsorber	l/min
$Q_{ads,in}$	Counter-current adsorber inlet air flow rate	l/min
Q_{dc}	Air flow rate in top downcomer	l/min
q_{eq}	Sorbent loading at equilibrium (Chapter 3 only)	kg CO_2/kg solids
Q_{fg}	Flue gas flow rate (Chapter 3 only)	l/min
q_{in}	Lean sorbent loading (Chapter 3 only)	kg CO_2/kg solids
Q_{lube}	Lube air flow rate	l/min
Q_{Lv}	Air flow from regenerator bottom to riser	l/min
q_{max}	Sorbent maximum loading (Chapter 3 only)	kg CO_2/kg solids
q_{out}	Rich sorbent loading (Chapter 3 only)	kg CO_2/kg solids
Q_{reg}	Air flow rate through solids bed in regenerator	l/min
$Q_{reg,in}$	Regenerator inlet air (primary air) flow rate	l/min
Q_{ris}	Air flow rate through riser	l/min
$Q_{ris,in}$	Riser inlet air flow rate	l/min
U_{Cch}	C-type choking superficial gas velocity	m/s
u_g	Interstitial gas velocity	m/s
U_g	Superficial gas velocity	m/s

$U_{g,ads}$	Superficial gas velocity in novel CFB adsorber	m/s
$U_{g,mf}$	Solids minimum fluidising velocity	m/s
$U_{g,ris}$	Superficial gas velocity in riser	m/s
$U_{g,tray}$	Superficial gas velocity through novel CFB adsorber tray holes	m/s
u_s	Solids vertical velocity	m/s
u_{slip}	Slip velocity	m/s
$u_{slip,av}$	Axially-averaged slip velocity	m/s
u_t	Solids terminal velocity	m/s
y	Gas CO_2 concentration (% vol.) (Chapter 3 only)	-
Y	Molar fraction of CO_2 in CO_2-free gas (Chapter 3 only)	-
y_{in}	Flue gas initial CO_2 concentration (Chapter 3 only)	-
z	Axial coordinate of adsorber model (Chapter 3 only)	m

Greek symbols

Symbol	**Definition**	**Units**
ΔH_{ads}	Heat of adsorption	kJ/mol
ΔP	Pressure drop	mbar
ε_{mf}	Volumetric solids fraction at minimum fluidising conditions	-
ε_s	Volumetric solids fraction	-
$\varepsilon_{s,c}$	Volumetric solids fraction in compact solids bed	-
$\varepsilon_{s,l}$	Volumetric solids fraction in loose solids bed	-
ϕ	Fraction of fluid in plug flow, DPFS flow model	-
ϕ_s	Particle sphericity	-
γ	Skewness of residence time distribution function, eq. (6.6)	s^3
γ_θ	Skewness of reduced-time RTD function	-

μ	Gas viscosity	kg/s/m
μ_n	RTD n-th moment around the origin, eq. (6.2)	s^n
θ	Reduced time, eq. (6.7)	-
ρ_g	Gas density	kg/m^3
ρ_s	Particle density	kg/m^3
σ^2	Variance of residence time distribution function, eq. (6.5)	s^2
σ^2_θ	Variance of reduced-time RTD function	-
τ	Mean residence time, eq. (6.4)	s

List of Abbreviations

ASU	Air separation unit
CCC	Committee on Climate Change
CCS	Carbon capture and storage
CFD	Computational fluid dynamics
CFB	Circulating fluidised bed
DOE	Department of Energy
DPF	Dispersed plug flow
DPFS	Dispersed plug flow with stagnant zone
EOR	Enhanced oil recovery
FCC	Fluid catalytic cracking
HX	Heat exchanger
ID	Inner diameter
IPCC	Intergovernmental Panel on Climate Change
LoR	Line of response
NETL	National Energy Technology Laboratory
OD	Outer diameter
PEPT	Positron emission particle tracking

PF	Plug flow
RTD	Residence time distribution
TSA	Temperature swing adsorption
UNFCCC	United Nations Framework Convention on Climate Change

1 General introduction

1.1 Background

Scientific evidence points to the rising concentration of carbon dioxide (among other greenhouse gases) in the Earth's atmosphere as the cause of global warming and climate change. The signs of such climate change "are unequivocal, and since the 1950s many of them are unprecedented over decades to millennia" (IPCC, 2013). Among the forecasted consequences are: sea level rise due to melting of polar ice, flooding, harsher weather, loss of plant and animal species diversity, loss of tropical forest, and adverse effects on food and water supply (IPCC, 2013).

Reducing anthropogenic emissions of CO_2 to overcome this situation was agreed worldwide through the United Nations Framework Convention on Climate Change (UNFCCC) in 1992. In the UNFCCC's principal update, the *Kyoto Protocol* (1997), developed countries agreed to reduce their collective greenhouse gas emissions by 5.2% below 1990 levels by the year 2012 (IEAGHG, 2001). This goal was a starting point to be updated at formal meetings held yearly between the Parties to the UNFCCC denominated *Conferences of the Parties* (COP). In December 2015, a new agreement to take further action against climate change was reached at COP21, denominated the *Paris Agreement*. The agreement entered into force in November 2016, after ratification of "at least 55 Parties accounting in total for at least 55 per cent of the total greenhouse gas emissions". Among the countries that have ratified the Agreement are the two world's largest CO_2 emitters, the US and China (EDGAR, 2013). The Parties agreed to "hold the increase in the global average temperature to well below 2°C above pre-industrial levels and pursue efforts to limit the temperature increase to 1.5°C, recognizing that this would significantly reduce the risks and impacts of climate change" (UNFCCC, 2015). In achieving such goal, "Parties aim to reach global peaking of greenhouse gas emissions as soon as possible and to undertake rapid reductions thereafter in accordance to the best available science, so as to achieve a balance between anthropogenic emissions by sources and removals by sinks of greenhouse gases in the second half of this century" (UNFCCC, 2015).

1.2 Carbon capture and storage

Among the main actions that can be used to reduce CO_2 emissions are (IEA, 2016): a) reducing the energy demand by avoiding energy losses and improving the efficiency of energy conversion or utilisation; b) switch to fuels with less carbon content per unit of energy produced, e.g. natural gas instead of coal; c) using energy sources with very low or zero net CO_2 emissions, like renewable or nuclear energy; and d) carbon capture and storage (CCS). CCS can be defined as a process where CO_2 is 1) separated from other gases in the utilisation of fossil fuels or biomass, 2) transported to a storage place, and 3) stored for long-term isolation from the atmosphere (IPCC, 2005). The natural candidates for application of CCS are those industrial sectors with large CO_2 emission facilities, namely fossil fuel-fired power generation and energy-intensive industries like iron and steel, cement, chemicals and oil and gas, which accounted for 42% and 19% of CO_2 global emissions in 2013 respectively (IEA, 2015b). Suitable CO_2 storage locations are geological formations like depleted oil and gas reservoirs, deep saline aquifers and unmineable coal seams. Captured CO_2 is also used in enhanced oil recovery (EOR), where CO_2 is used to facilitate the extraction of crude oil by displacement (IPCC, 2005).

The *Intended Nationally Determined Contributions* (INDCs) put forward by different countries towards achieving the goals of the Paris Agreement contain the CO_2 emissions-reducing measures above in higher or lower degrees. Despite that, the International Energy Agency believes that such pledges will, even if fully implemented, lead to an increase in global temperature of 2.7°C by 2100, rather than "well below" 2°C (IEA, 2015a). Increasing the contribution of CCS in the mix of mitigation measures against global warming is therefore essential to raise the ambition of the INDCs to meet targets. This is especially true given the stronghold of fossil fuels in the energy sector in the short-term and "little scope for substitution of fossil flue energy use in the industrial sector" (Global CCS Institute, 2016a).

In the context of the UK, the Paris Agreement sets a higher level of ambition that the currently set by means of the legally-binding *Climate Change Act 2008*, the target of which is that "the net UK carbon account for the year 2050 is at least 80% lower than the 1990 baseline" (UK Government, 2008). This limit was intended to limit global

temperature rise around 2°C in 2100 (CCC, 2016b). The current scenarios devised by the Committee on Climate Change consider CCS "very important given its potential to reduce emissions across heavy industry and the power sector" (CCC, 2016b). It has been estimated that failure to deploy CCS in the UK could double the cost of meeting the Climate Change Act 2008 (ETI, 2015).

An effort towards implementation of commercial-scale CCS in the UK was made through the *CCS Commercialisation Competition*, which started running in April 2012. Two preferred bidders, namely the *Peterhead CCS* and the *White Rose CCS* projects were awarded funding to undertake full-chain Front End Engineering Design studies of their respective CCS technologies. The Peterhead CCS project involved post-combustion liquid amine capture of 1 $MtCO_2/y$ from a CCGT power station in Scotland with storage in a depleted Goldeneye gas reservoir 2.5 km beneath the North Sea. In the White Rose project, oxy-fuel combustion technology was proposed for capture of 2 $MtCO_2/y$ from a coal-fired power station in England, with CO_2 storage in a deep saline aquifer in the North Sea. The winning project (either one or both) would have been awarded with £1 billion capital funding plus operational support in form of a Contract for Difference deal (UK Government, 2013). Unfortunately the competition was cancelled in November 2015 due to political circumstances on the ground of being an expensive technology against climate change mitigation. Action was taken by CCS research groups and parliamentary advisory bodies to stress the essential role of CCS in meeting climate change mitigation targets and suggest implementation strategies (UKCCSRC, 2016; CCC, 2016a).

A number of challenges have to be overcome if CCS is to be deployed worldwide, including public acceptance and the increase in the cost of electricity that it would inevitably involve, a direct consequence of the energy-intensive nature of CCS. Because the most expensive component of the CCS chain is carbon capture, current research efforts are focused on developing new carbon capture technologies with lower capital and operational expenditure or improving already existing ones (IPCC, 2005).

1.3 Carbon capture technologies

The first step of the CCS chain is denominated *carbon capture* (or *CO_2 capture*). In carbon capture, CO_2 is obtained as a concentrate stream (>95% to avoid corrosion in transport pipelines, see for example Wilcox, 2012) using a range of technologies that can be classified into three categories: post-combustion, pre-combustion and oxy-fuel combustion (IPCC, 2005). In post-combustion carbon capture processes CO_2 is separated from the exhaust gas, thus after the fuel is burned. In pre-combustion carbon capture, a mixture of CO_2 and H_2 is first produced by steam reforming or gasification of the carbon-containing fuel and a subsequent water gas shift reaction, from which the CO_2 is separated. Oxy-fuel combustion capture, on the other hand, implies burning the fuel with pure oxygen and therefore the exhaust gases would contain virtually pure CO_2 and water vapour, the latter being eliminated by condensation (water knock-out)[1]; O_2 separation from air is then the costly part of the process, which is typically achieved by cryogenic distillation, although new oxygen separation technologies like membranes are under development (IPCC, 2005).

Abanades et al. (2015) presented a review of emerging technologies that were recognized in the IPCC Special Report (SR) on CCS (IPCC, 2005) as potential competitors of more mature technologies in terms of lower capital and operational costs. In the same work, the authors presented a carbon capture technology toolbox (Table 1.1) based on that of the IPCC SR, showing the progress made in the field in the previous 10 years in form of technology readiness level (TRL) values.

[1] In practice, part of the produced CO_2 or CO_2/water mixture is recycled and mixed with oxygen to lower the excessively high flame temperature (IPCC, 2005).

Table 1.1. CO_2 capture technologies (adapted from Abanades et al., 2015, with permission)

Separation Process	Application	TRL*		Comments
		2005	2015	
Absorption				
Physical	Industry	9	9	Separation of CO_2 from syngas
	Pre-combustion	8	8	Most components TRL 9, but H_2-based power production less mature
Chemical	Industry	9	9	Natural gas sweetening
	Post-combustion	7	8	Demonstrated up to 1 Mt CO_2/y
Cryogenics				
Air separation	Industry	9	9	O_2 production
	Oxy-combustion	5	7	Combustion island demonstrated up to 30 MW
CO_2 anti-sublimation	Post-combustion	3	3	
High temperature solid looping				
Chemical looping	Oxy-combustion	3	6	Demonstrated up to 1 MW
	Pre-combustion	2	3	
Calcium looping	Post-combustion	2	6	Demonstrated up to >1 MW
	Pre-combustion	2	2	Challenging at high P and T
Solid sorbents				
Adsorption	Industry	9	9	Natural gas sweetening and H_2 production
	Pre-combustion	8	8	Most components TRL 9, but H_2-based power production less mature
	Post-combustion	2	5	VPSA: <2 tCO_2/d
	Oxy-combustion	6	6	VPSA commercial for low-capacity O_2 production
Low temp. gas-solid reactions	Post-combustion	4	6	CFB with K solids: 10 MW
	Pre-combustion	3	5	Sorption enhanced water gas shift (SEWGS)
Membranes				
Polymeric	Industry	9	9	Natural gas processing
	Post-combustion	3	5	Demonstrated up to 1 tCO_2/d
Other	Pre-combustion	3	3	
	Oxy-combustion	4	5	O_2 production: 5 tO_2/d

*Technology readiness level (see definition in Abanades et al., 2015)

- *Absorption processes:*

Absorption processes imply contacting the CO_2-containing gas with a liquid solvent that selectively bonds with the CO_2 physically or chemically. Chemical sorbents are preferred in post-combustion carbon capture as they show higher absorption capacity at low CO_2 partial pressures than physical sorbents. The latter, on the other hand, show higher absorption capacity than the former at high CO_2 partial pressures and therefore are more used in pre-combustion carbon capture. The different absorption mechanisms also dictate how the solvents are regenerated: CO_2 is released from chemical sorbents by application of heat, whereas physical sorbents are regenerated by pressure reduction (Jansen et al., 2015).

Absorption processes have been used at commercial scale for many decades in natural gas sweetening and removal of CO_2 in chemical processes like ammonia and hydrogen production (IPCC, 2005; Abanades et al., 2015; Jansen et al., 2015). This has made absorption processes benchmark technologies against which to assess new carbon capture processes. In particular, absorption in 30% wt. aqueous solution of monoethanolamine (MEA) has been used as the benchmark post-combustion carbon capture in coal-fired power plants in the US Department of Energy's Carbon Capture Programme (DOE NETL, 2015). A schematic diagram of the conventional system configuration is presented in Figure 1.1. Boot-Handford et al. (2014) state however that DOE NETL's MEA process "can no longer be used as a representative baseline for post-combustion capture since a number of vendors have developed processes substantially better". Ahn et al. (2013), for example, propose "a new concept of amine process design having multiple strategies applied" where regeneration energy demand and plant overall energy penalty are reduced from 3.52 MJ/kg CO_2 to 2.22 MJ/kg CO_2 and from 9.0% to 8.1%, respectively, with respect the DOE NETL's MEA process.

Post-combustion carbon capture by retrofitting an amine scrubbing process to a coal-fired power station has been demonstrated for the first time at the commercial-scale in the Boundary Dam CCS Project in Saskatchewan, Canada. The system was designed for capturing 1 $MtCO_2/y$ from a retrofitted 110 MW power unit. The captured CO_2 is sold for EOR. In July 2016, the owning company "announced that

the CO_2 unit had surpassed the capture of one million tonnes of CO_2 since operations began in October 2014" (Global CCS Institute, 2016b).

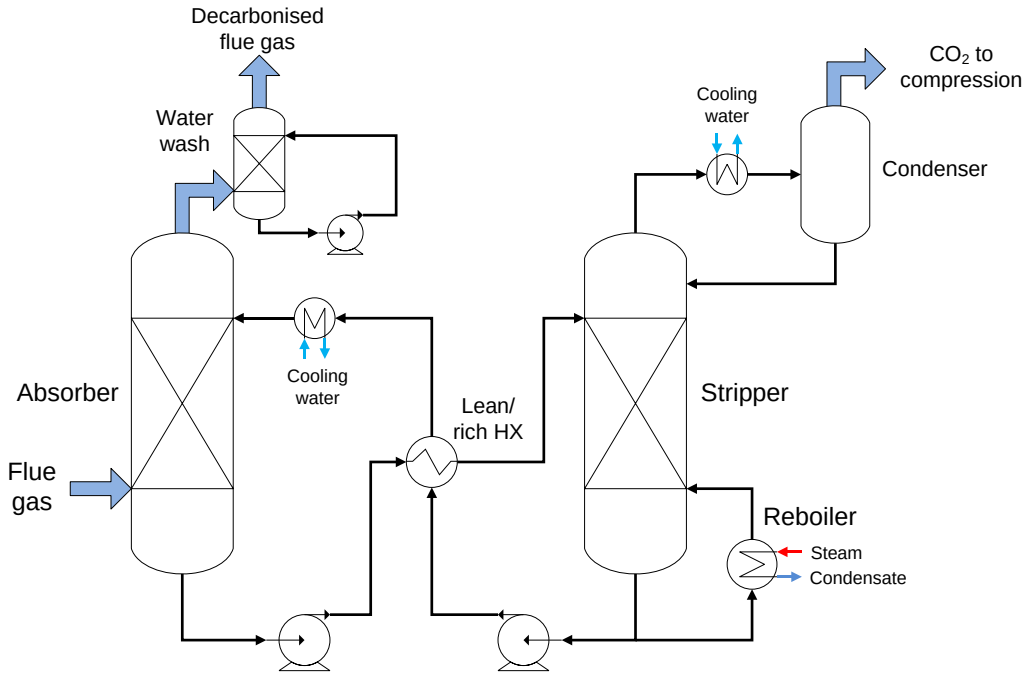

Figure 1.1. Post-combustion capture amine absorption process (adapted from Ahn et al., 2013, with permission)

- *Chemical looping (Abanades et al., 2015):*

Chemical looping is a combustion technology in which transfer of oxygen from air to fuel occurs indirectly by means of a metal oxide acting as an "oxygen carrier". The process is shown schematically in Figure 1.2. The oxygen carrier is circulated between the "air reactor" and "fuel reactor". The net reaction is the same as the ordinary combustion of fuel (and so is the amount of heat produced), but with the benefit of inherent CO_2 separation and flameless combustion (reduced thermal NO_x emissions). Best performances (100% CO_2 capture and 100% fuel conversion) are obtained with gas fuels, which also facilitate CFB operation as the fuel act as the fluidising medium. However, gas-fuelled chemical looping combustion is not as competitive as burning the fuel in gas turbine combined cycles despite having no direct energy penalties. Pressurised systems are more competitive but require further development. The shift in recent years regarding pilot-scale testing is to use solid fuels at atmospheric pressure. Chemical looping using solid fuels presents the

challenges of fuel reactor design and high cost of oxygen carriers for high conversions.

Chemical looping is also being developed for other processes different from full combustion, like reforming and gasification.

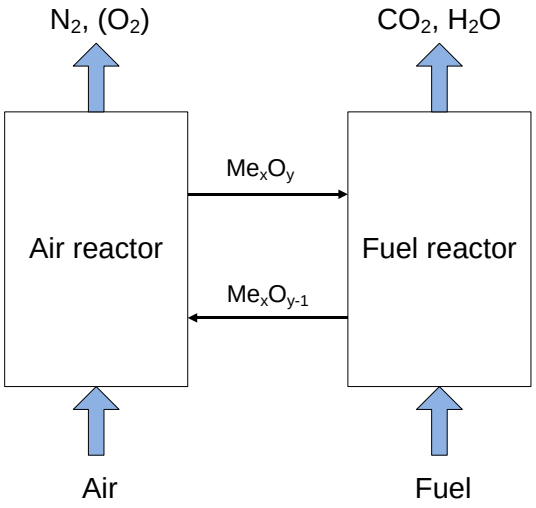

Figure 1.2. Chemical looping combustion (adapted from Abanades et al., 2015, with permission)

- *Calcium looping (Abanades et al., 2015):*

Calcium looping is a family of high-temperature carbon capture processes that share the use of calcium oxide as the separation agent. CO_2 reacts exothermically with CaO in the "carbonator" to produce $CaCO_3$, which is circulated to the "calciner" to reverse the reaction and release the CO_2. CaO is then recirculated to the carbonator, closing the loop. The process requires the supply of heat at high temperature in the calciner. In its simplest configuration (Figure 1.3), this is accomplished by oxy-fuel combustion. The addition of extra fuel is compensated by the recovery of high-temperature reaction heat in the carbonator and waste heat in outlet gases in both reactors using conventional steam cycles. This calcium looping configuration utilises components that are commercially available, namely (interconnected) CFB combustion technology and cryogenic air separation, and therefore the level of maturity of such carbon capture process has evolved from TRL2 to TRL6 (see Table 1.1). Demonstration of the technology exists at scales above 1 MW. Full

system studies show that calcium looping is competitive with benchmark post-combustion carbon capture (amine scrubbing), although there is room for improvement, e.g. reduction of the energy consumption in the calciner. A characteristic of all calcium looping systems is the poor stability of the sorbent, which incurs a relatively large purge/make-up flow rate. However, the usefulness of CaO as raw material for cement production offers potential for synergy in the decarbonisation of power generation and the cement industry (Ozcan, 2014).

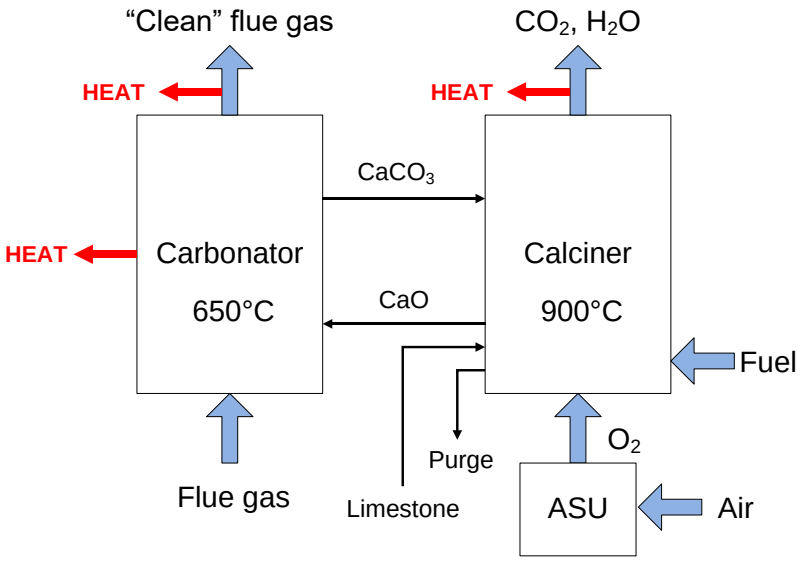

Figure 1.3. Calcium looping for post-combustion carbon capture (adapted from Abanades et al., 2015, with permission)

- *Membranes (Abanades et al., 2015):*

Separation of gases using membranes relies on the different permeabilities of the different gas species, which lead to different permeation rates (or no flow at all) when a partial pressure difference is imposed between both sides of the membrane. Membranes can be arranged in a variety of configurations (e.g. spiral wound, hollow fibers, flat sheets) within a module, and a number of such modules can be combined in series/parallel stages to cater to the process specifications.

Membranes are a mature technology in the separation of CO_2 from natural gas. Progress in their application for carbon capture has been made in the last 10 years, in particular polymeric membranes for post-combustion (TRL3 to TRL5, see

Table 1.1), with some applications reaching the pilot scale. The attractiveness of polymeric membranes stems from their relative low cost and versatility of fabrication and composition. For example, mixed matrix membranes are formed by an inorganic filler embedded in a polymer matrix, combining the properties of both materials.

Advantages of the use of membranes are the absence of moving parts or phase changes, small footprint, ease to scale-up and high flexibility. Aspects to focus on in their development are, for instance, the tolerance to contaminants or water, long-term thermal and chemical stability, and capacity – especially in post-combustion carbon capture, due to the large volumes of flue gas to treat and low CO_2 partial pressure.

- *Solid sorbents:*

Adsorption processes can be classified according to the type of interaction between sorbate and sorbent (physical or chemical) and the regeneration method (pressure/vacuum and/or temperature swing). In physisorption sorbates bond weakly to the sorbent surface due to dispersion/electrostatic forces, whereas in chemisorption covalent chemical bonds are formed. The former group of materials (e.g. activated carbon, zeolites, aluminas, silicas, MOFs) are adequate for pre-combustion carbon capture since they have high carrying capacities at high CO_2 partial pressures. Chemisorbents, on the other hand, saturate at low CO_2 partial pressures and are the choice in post-combustion carbon capture (Abanades et al., 2015).

A promising group of materials in post-combustion carbon capture are *solid amines*, i.e. mesoporous materials functionalized with amine groups (Sjostrom and Krutka, 2010; Samanta et al., 2012; Zhao et al., 2013). Solid amines present similar characteristics to liquid solutions of amine in terms of affinity for CO_2 at low partial pressures and heat of reaction, but with the advantages of 1) lower heat capacities and higher CO_2 loadings per unit mass of sorbent/solvent, and 2) evaporation of water is avoided (Tarka et al., 2006; Yang and Hoffman, 2009; Sjostrom and Krutka, 2010; Pirngruber et al., 2013; Abanades et al., 2015). These two characteristics of solids sorbents compared to liquid amine solutions translate directly into potential reductions in regeneration energy demand (1.4 MJ/kg CO_2 compared to 3.5 MJ/kg

CO_2) and sorbent/solvent inventory (5 l/kg CO_2 versus 50 l/kg CO_2) (Tarka et al., 2006).

Of paramount importance is the selection of the technology for gas-solid contact that allows exploiting such advantages with respect gas-liquid systems at the (very) large volumetric gas flow rates and low pressures of post-combustion carbon capture. Cyclic operation in fixed beds is advantageous in terms of driving force for separation as the sorbent is saturated at the feed conditions of the flue gas, but presents the problems of high pressure drop and mass and heat transfer limitations at the fast cycle times required (Yang and Hoffman, 2009; Sjostrom and Krutka, 2010; Pirngruber et al., 2013; Webley, 2014; Abanades et al., 2015).

CFBs can be used to overcome some of these issues by "mimicking liquid absorption systems" (Webley, 2014). The work presented in this thesis is in the context of use of CFB technology for TSA post-combustion carbon capture in coal-fired power plants.

1.4 FOCUS – Fundamentals of Optimised Capture Using Solids

The work presented in this thesis was carried out in the context of a collaborative project between the University of Edinburgh (UoE) and North China Electric Power University (NCEPU) denominated FOCUS – Fundamentals of Optimised Capture Using Solids. The UK part of the project was funded by the Engineering and Physical Sciences Research Council (EPSRC) under the grant EP/I010939/1.

The objective of the FOCUS project was to reduce the energy requirement for post-combustion CO_2 capture by 25-50% compared to amine scrubbing technology (Fan, 2011). The methods included the development of a novel process based on CFB technology and amine-functionalised sorbents that would capture CO_2 from coal-fired power plants and its assessment against a benchmark CFB configuration (Figure 1.4). The novel CFB features a counter-current adsorber, a counter-current regenerator and a riser, the latter element playing a double role of solids conveyer and co-current adsorber. The advantages sought by using a counter-current adsorber are not only the more efficient gas-solid contact mode with respect co-current, but also a low pressure drop derived from operation at lower gas velocities and hydrostatic head partially supported on the contactor internals. Compression requirements in the riser are expected to be low as only a small fraction (10-15%) of the total flue gas stream is used to convey the solids.

The project tasks were divided into five work packages (WP) (Fan, 2011):

WP1: Development and evaluation of amine-functionalised adsorbents.

WP2: Investigation of CFB configurations.

WP3: Computational fluid dynamic (CFD) description of fluidised beds.

WP4: Modelling of adsorption processes.

WP5: Process integration in power plants and overall optimisation.

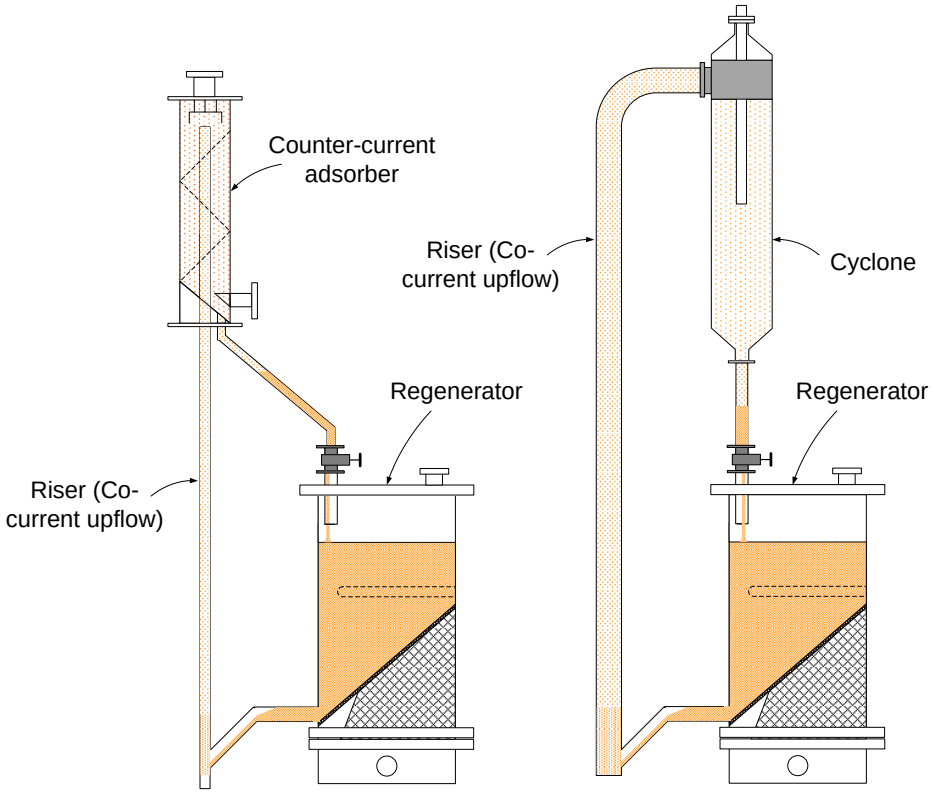

Figure 1.4. Novel (left) and benchmark (right) CFB configurations evaluated in the FOCUS project

In WP1 new CO_2 sorbent materials were developed at NCEPU by immobilising different amine groups onto the surface of different types of silicas. Characterisation of sorbents was carried out at the UoE: stability was determined by thermogravimetric analysis (TGA), whereas a rapid screening technique based on the zero length column (ZLC) developed at the UoE was used to rank the materials in terms of CO_2 capacity (Mangano et al., 2013; Hu et al., 2015). Potential for regeneration was investigated from the generation of breakthrough curves using N_2/CO_2 mixtures with and without water, SO_x and NO_x, and adsorption/desorption kinetic data using the Dual Piston Pressure Swing Adsorption (DP-PSA) technique (Dang et al., 2013; Friedrich et al., 2013). As part of the collaboration between project partners, a researcher from NCEPU was hosted at the UoE to learn the ZLC and DP-VSA characterisation techniques.

The work presented in this thesis was included in WP2. Data regarding CFB operation, gas/solids residence time distribution and fluid dynamic characteristics in

the different CFB elements were to be generated using sand, resins and sorbent pellets. The experimental results obtained were to be used to validate CFD models developed at NCEPU. Such models were meant to predict the impact of changes in particle density during the adsorption and regeneration stages. The FOCUS project was closed in June 2014 (after 3.5 years of duration), when experimental data was still being generated and sand was the only solid material tested. Tasks in work packages WP3 to WP5 were not carried out. Nevertheless, they are described next for completeness.

In WP4, combined heat and mass transfer at the particle level was to be modelled at the UoE using the adsorption cycle simulator CySim (Friedrich et al., 2013; Beck et al., 2015). The CySim adsorption model was to be used to validate the kinetic data obtained by the ZLC technique in WP1, and then combined with the CFD models developed in WP3 to predict process performance in terms of separation efficiency and energy requirements.

Process integration in a coal-fired power plant was to be carried out in WP5 at the UoE. Integration tasks included: evaluation of modifications to the conventional steam cycle to cater to the carbon capture process in terms of energy demand; co-optimisation of CO_2 compression, capture process heat supply and heat recovery; and assessment of water consumption, cooling requirements and emissions of pollutants.

1.5 Objectives of this thesis

The goals pursued in this work are:

- To develop a methodology for the thermodynamic-kinetic evaluation of circulating systems as TSA carbon capture processes and use it in the assessment of a novel CFB configuration against a benchmark (co-current riser).

- To assess the fluid dynamic characteristics of cold model CFB elements to advance in the understanding of gas-solid flow, in particular in those elements that bring potential advantages with respect conventional ones (counter-current adsorber). The systems' fluid dynamics are assessed by determination of residence time distributions (RTDs) of both phases.

- To show the characteristics and potential of the positron emission particle tracking (PEPT) technique in the study of solids flow, in particular in those elements that bring potential advantages with respect conventional ones (counter-current adsorber).

- To describe the methodology to combine experimental and modelling approaches to obtain reliable models to predict performance of the carbon capture processes.

1.6 Structure of this thesis

This thesis is organised in nine chapters:

- Chapter 1 introduces the problematic of climate change and how carbon capture and storage can contribute significantly in the reduction of CO_2 emissions. Several carbon capture technologies are presented, included TSA post-combustion using solid amines in circulating fluidised beds, which is the topic of this work.

- Chapter 2 presents a literature review focusing on the aforementioned technology and in counter-current gas-solid contactors, stressing their operational and fluid dynamic characteristics.

- In Chapter 3 a methodology for the thermodynamic-kinetic evaluation of circulating systems as TSA carbon capture processes is developed, and used in the assessment of a novel CFB configuration against a benchmark (co-current riser).

- Chapter 4 describes the cold model CFB rigs used in this work, including design and geometric characteristics, instrumentation, data logging system and measures implemented against the generation and accumulation of static electricity.

- In Chapter 5 the cold model CFB rigs are described from an operational point of view, showing the ranges of gas and solids flow rate achievable (operating windows) and other characteristics that have an influence in their performance as carbon capture systems, like pressure drop.

- Chapter 6 concerns the determination of gas residence time distributions in different elements of the cold model CFB rigs using a tracer injection-detection technique.

Fluid dynamic characteristics and gas dispersion data are derived from the analysis of gas RTD curves and compared with published data in similar systems.

- Chapter 7 introduces positron emission particle tracking (PEPT) as a powerful technique for the study of flow systems, and describes its application in different elements of the cold model CFB rigs. Analogously to how it was done for the gas phase, PEPT data is used for determining the residence time distribution of the solid particles and overall fluid dynamic characterisation of the CFB rigs. Solid phase dispersion data generated is compared with previously published data in similar systems.

- Chapter 8 gives guidelines for the development of models that make use of the residence time distribution data generated in previous chapters, with the aim of predicting the performance of the studied CFB systems as carbon capture units.

- Chapter 9 provides final conclusions, recommendations and suggestions for future work.

2 Literature review

In this chapter previous research efforts in the field are reviewed, emphasising those results and observations that are relevant for discussion and justification of this work.

The scope of this survey is restricted to the most innovative aspects of this study, namely:

- Experimental or theoretical work on TSA post-combustion carbon capture processes using 1) low-temperature sorbents, in particular solid amines, and 2) CFB technology, containing any combination of co-current and counter-current contact elements (Section 2.1).

- Lab- or bench-scale counter-current gas-solid contactors, in particular those featuring dilute flow of solids (trickle flow) and/or inclined baffles or orifice plates (Section 2.2).

2.1 TSA post-combustion carbon capture processes using low-temperature sorbents and CFB technology

2.1.1 Lab/bench-scale

- *Veneman et al. (2012):*

The authors use a CFB with an adsorber section that seems to be a bubbling or turbulent fluidised bed (size: 40 mm ID×500 mm height, flue gas: 5.9 l/min at 40°C) and solids conveyed to the top via a riser 15 mm ID×1900 mm height. The regenerator section is a bubbling fluidised bed 50 mm×30 mm×1000 mm, operating at a temperature of 110°C. The solids tested were silica gel and acrylic particles with particle sizes ranging 250-500 μm and 300-600 μm respectively, impregnated with a methanol solution of tetra-ethylenepentamine (TEPA). Adsorption isobars of the sorbents were determined by applying temperature ramps of 0.1°C/min to samples exposed to atmospheres at different constant CO_2 partial pressures. The acrylic-based sorbent showed potentially higher working capacities than the silica gel-based at the above operating conditions, although the authors acknowledge that the results for the latter sorbent are possibly biased due to mass transfer limitations.

Fluidisation tests at regeneration conditions in the early stages of process development are suggested by the investigators in view of their experience with the acrylic-based sorbent, which formed particle aggregates at high temperature that plugged the equipment. A similar experience is reported by Krutka et al. (2013) in a pilot-scale carbon capture process with solid amines. Continuous carbon capture in the CFB system was therefore carried out only with the silica gel based solvent. These experiments were performed with pure N_2 as regenerator sweep gas and in pure CO_2.

For experiments with N_2 as sweep gas, the authors found that the CO_2 recovery increased from 24% to 61% when the regenerator temperature was increased from 65°C to 100°C. This, however, could not be associated with a proportional increase in the sorbent working capacity, which presented a maximum at a temperature of 85°C. The investigators suggested the increase in process performance to be due to an increase in the solids circulation rate with temperature. Indeed, the calculated solids flow rate from reported data at regeneration temperature of 100°C (CO_2 recovery 61%, sorbent working capacity 0.4 mol/kg and CO_2 injected 0.8 l/min) is 0.79 g/s, 18% higher than the reported value of 0.67 g/s.

Continuous carbon capture with regeneration in pure CO_2 yielded a CO_2 recovery of 56% (the CO_2 concentration of the flue gas decreased from 6.7% to 2.1%). From the adsorption isobars, this does not seem possible as the working capacity calculated from the CO_2 concentrations at adsorber and regenerator outlet conditions is negative. This highlights the importance of generating correct equilibrium data in the sorbent characterisation stage. CO_2 purity in the regenerator was 90%, associated to dilution from gas flowing from the seal loop. A better gas sealing design should yield higher CO_2 purities although, according to the authors, in larger-scale processes the leak effects would be less detrimental.

- *Zhao et al. (2013):*

The investigators carried out continuous TSA carbon capture experiments with solid amines as part of their thermal stability study of the sorbents. Four silica gel-based sorbents were prepared by impregnation with polyethylenimine (PEI) and TEPA

solutions of different molecular weights. The CFB system consisted of a bubbling fluidised bed adsorber 50 mm ID×260 mm height, a regenerator 50 mm ID×692 mm height, and associated riser (20 mm ID×1720 mm height) and loop seals.

The reported CO_2 recoveries at regenerating conditions of pure N_2 and 120°C were in the range 73-82%. Fluctuations in the values of CO_2 recovery were associated to fluctuations in regenerator temperature caused by mixing of cold and hot sorbent in the regenerator. The authors explain that the CO_2 recovery depended on the solids circulation rate and working capacity, the latter dependent on regeneration temperature and particle residence time in adsorber. After at least 140 minutes of continuous operation, sorbent samples from the CO_2 carbon capture system were analysed by TGA showing no decrease of values of maximum CO_2 loading and amine content with respect to fresh material.

The CFB system used by the investigators is deemed to have been conceived in the context of development of materials and not of processes, but is nevertheless included in this literature review as an example of a continuous TSA process using solid amines.

- *Pröll et al. (2016):*

A dual-loop CFB concept for TSA carbon capture using low-temperature sorbents is proposed and evaluated from a thermodynamic point of view. Both adsorber and regenerator (which uses steam as sweep gas) consist of a multi-stage fluidised bed, technology that presents the advantages of 1) allowing counter-current contact between the solid and gas phases, which the authors prove (see below) to require lower solids circulation rate and regenerator heat duty than a single-stage system; 2) heat removal (in the adsorber) and addition (regenerator) can effectively be achieved thanks to fluid dynamics of bubbling fluidised beds and the possibility to embed heat transfer surfaces. The investigators also point out that the use of downcomers for solid flow between stages makes the multi-stage fluidised bed more operationally flexible and stable than other counter-current contactors like “trickle flow reactors with horizontal perforated plates”, although the latter are simpler in design.

Completing each of the two CFB loops in the system there is a riser conveyor with a bottom dense phase, an L-valve-like solids feeder, a cyclone-like solids separator and a recirculation gas compressor. A lean/rich heat exchanger between the dense phase of the risers is proposed to further reduce the energy consumption of the process. The dual-loop design makes gas sealing devices between both loops unnecessary as long as the conveying (in the riser) and purge (in the L-valve) gases are compatible with both the inlet gas in the counter-current contactor of the same loop and the outlet gas in the respective other loop. Proposed gases are CO_2 as both conveying and purge gas in the adsorber loop, whereas in the regenerator loop "clean flue gas" is used as conveying gas in the riser and steam as purge gas.

The carbon capture process is modelled using experimental adsorption equilibrium data of a solid amine studied by Fauth et al. (2012) and taking the following idealisations: 1) fast kinetics (equilibrium-controlled process) both in adsorber and regenerator, 2) trays 100% efficient, 3) sorbent 100% selective to CO_2 (the authors admit that no co-adsorption of H_2O is a strong assumption, but they take it for simplicity and lack of data), and 4) isothermal process within each of the contactors. The results for 5 stages in both adsorber and regenerator, temperature swing from 75°C to 120°C and 0.75 kg/kg CO_2 of steam as sweep gas are: CO_2 purity of 35%, solids working capacity of 1.9 mol CO_2/kg, solids circulation rate of 12 kg/kg CO_2, and energy requirement without the lean/rich HX of 3.9 MJ/kg (with such device the energy consumption could go down to 3.5 MJ/kg). If only one stage is used in both adsorber and regenerator, these values would be: CO_2 purity of 8%, solids working capacity of 0.2 mol CO_2/kg, solids circulation rate of 250 kg/kg CO_2, and energy requirement without the lean-rich HX of 18 MJ/kg. Given these values and the thermodynamic characteristics of their design, the investigators consider their process as a promising technology that "seems to satisfy all of the requirements of an efficient solid sorbent post combustion CO_2 capture process".

Indeed, the values of (theoretical) regeneration energy reported make the process competitive to the benchmark MEA scrubbing process. A visible challenge to overcome is the unavoidable high pressure drop characteristic of (multi-stage) fluidised beds. The dual-loop system proposed also implies the use of two conveying

lines and gas compressors with the consequent capital and operational expenditure, which could be low given the expected low solids circulation rate.

- *Veneman (2015) and Veneman et al. (2016):*

The authors carry out an experimental and modelling study of a trickle flow counter-current contactor 21 mm ID and 1300 mm high with horizontal perforated plates (no details are reported about the geometry of the internals) as an adsorber for post-combustion carbon capture. This contactor is claimed to have a low pressure drop, which the investigators believe is one of the key characteristics to aim for in carbon capture processes (together with counter-current contact in the adsorber), given the very large volumetric flow rates of flue gas in commercial-scale applications.

The system is completed with a multi-stage fluidised bed (5 stages) regenerator, a conveying riser and a cyclone. The solids circulation rate is controlled by rotary valves located at the regenerator inlet and outlet. The flue gas is a mixture of CO_2 and N_2 at around 30°C of inlet temperature, and the regeneration is carried out in pure N_2 at 90-120°C. The solid sorbent is a commercially available ion exchange resin functionalised with primary benzyl amine groups.

For modelling the investigators considered possible heat and mass transfer limitations. Experimental data fitting suggested that external mass transfer was fast compared to adsorption kinetics. The reported CO_2 recovery of two capture experiments at similar conditions was 58%. The low process performance is attributed to too short residence times in the adsorber since full regeneration of the solid sorbent was expected from preliminary tests (regeneration in pure N_2). Low working capacities due to external and/or intra-particle heat transfer limitations could also have played a role, since the model predicted a much higher temperature increase in the adiabatic adsorber than the one measured experimentally (60 K compared to 3 K). Another possible culprit could be an excessive deviation from the assumed plug flow for one of the phases, in particular the solid phase (see Chapter 3), although this was not acknowledged or realised by the authors.

It was also pointed out by the authors that the sorbent material presented higher adsorbing properties for water, and mentioned that this is a common feature of CO_2 sorbents being studied (zeolite 13X among them). Water adsorption is shown to be beneficial in the adsorption of CO_2 but implies higher regeneration energy consumption.

The process energy consumption reported is as low as 1.9 GJ/tCO_2, compared to 2.7-4.3 GJ/tCO_2 of the conventional MEA scrubbing.

2.1.2 Pilot-scale

- *Sjostrom et al. (2011), ADA (2011):*

Environmental solutions provider ADA carried out an extensive TSA post-combustion carbon capture research project (DE-NT0005649) funded by the US Department of Energy (DOE) National Energy Technology Laboratory (NETL), in which 1) a large number of solid sorbents were characterised using thermogravimetric analysis, and 2) the most promising materials were tested in a 1 kWe-equivalent pilot-scale facility using a slipstream of actual flue gas. The sorbents were: 87 supported amines, 31 carbon based materials, 6 zeolites, 7 supported carbonates and 10 hydrotalcites. The selected materials for the pilot testing were four supported amines; these materials showed a better overall performance than the rest in terms of CO_2 capacity, cyclic stability, poisoning resistance and theoretical regeneration energy.

In their optioneering study to select the 1 kWe equipment, ADA initially considered several technologies including fixed beds, circulating fluidised beds and counter-current contactors. The prevailing criterion was operational flexibility in view of "testing materials that had highly varied physical properties, which was an important concern because laboratory-scale sorbent screening was conducted concurrently with the 1 kW equipment design and construction". A CFB consisting of a riser (25.4 mm ID, 12.2 m long) as the adsorber and a bubbling fluidised bed as the regenerator was therefore chosen. Four supported amines were tested in such system, using actual flue gas from two different coal-fired power facilities. One of these materials could not be fluidised due to its very small particle size (10 μm), and was discarded from

further evaluation. In the remaining three cases, continuous CO_2 recovery at 90% was not possible "due primarily to the combination of a co-current adsorption system with a fluidized bed for regeneration, a combination which did not provide an adequate driving force to maintain an acceptable working CO_2 capacity". Two of the sorbents (labelled "R" and "AX") presented a continuous CO_2 removal of 20%, this value being 40% for the third material (labelled "BN"). ADA acknowledged the lack of overall process performance and associated it to poor sorbent regeneration, but considered their 1 kWe CFB to be a useful piece of equipment in evidencing the differences in overall kinetics between materials R (or AX) and BN. This can be called into question since, in equal conditions of regeneration, the higher value of continuous CO_2 recovery for material BN could be due to the higher working capacity that ADA reported for this material in their preliminary characterisation.

- *Krutka et al. (2013), DOE NETL (2016):*

In a follow-up DOE NETL project (DE-FE0004343) managed by ADA, a 1 MWe-equivalent pilot-scale system was designed and constructed where lessons learnt from operation of their previous 1 kWe co-current system were implemented. In particular, ADA realised that counter-current contact between phases in the adsorber section was necessary to increase the working capacity of the sorbent, which in turn could lead to reasonable values of process performance. ADA considered initially a "dilute phase trickle down" adsorber, but discarded it in favour of a multi-stage fluidised bed. Despite the higher pressure drop compared to a dilute solids flow system, a multi-stage fluidised bed allowed inclusion of heat transfer surface in the system for efficient removal of the heat of adsorption, promoted good gas-solid contact in overall counter-current mode and was commercially-proven technology. The counter-current contact was not needed for the regenerator as the driving force for desorption was merely the temperature swing and not the partial pressure of CO_2 (regeneration in pure CO_2). The sorbent used is an ion exchange resin functionalised with primary benzyl amine groups (similarly to Veneman et al., 2016).

The results of the operation of the 1 MWe pilot plant were shown in a project closeout presentation (DOE NETL, 2016). The system was designed for 90% CO_2 recovery, flue gas flow rate of 51 m^3/min with initial CO_2 concentration of 13.1%

and solids circulation rate of 3.9 kg/s. Actual operating conditions were gas flow rate 11-23 m^3/min and solids circulation rate 1.3-2.6 kg/s. Achieved CO_2 recoveries at these conditions were in the range 20-80%, the actual value being proportional to the solids-gas ratio. The main cause of poor process performance according to ADA was a combination of 1) reduction of the effective sorbent working capacity due to adsorption of CO_2 by the lean sorbent in the transfer line between regenerator and adsorber, and 2) solids circulation rate limitations due to changes in the flowing properties of the sorbent at elevated temperatures. The reason for conveying the solids from regenerator to adsorber using CO_2 is the degradation of the sorbent in a hot atmosphere containing oxygen, therefore forbidding the use of air or CO_2-depleted flue gas for such task. A possible solution might lie in shifting part of the cooling duty of the uppermost bed in the adsorber to a lean/rich heat exchanger or solids cooler located between the regenerator and the adsorber. This, of course, would incur an increase of the capital cost that needs to be assessed against the cost of other solutions.

- *Hornbostel (2015):*

SRI International, through DOE NETL funded programme DE-FE00013123, have investigated the use of carbon physisorbent microbeads (particle size 100-300 μm) that they claim have excellent properties for TSA carbon capture, namely: high CO_2 capacity (0.2 g CO_2/g solid at a CO_2 partial pressure of 1 atm), rapid kinetics of both adsorption and desorption, low heat of adsorption (-28 kJ/mol), low heat capacity, high thermal conductivity, high fluidity (spherical shape), high resistance to attrition, and low cost. The sorbent was first characterised in the lab and subsequently tested in a lab-scale cold model rig. The adsorber concept used by SRI is the dilute-phase counter-current flow through a commercial structured packing. The packing provides a zig-zag path for the solids to fall downwards and be in intimate contact with the upflowing flue gas, and at the same time allowing its homogeneous distribution throughout the adsorber cross section and a low pressure drop (low pressure drop is one of the main advantages of this system as SRI consider pressure drop to increase the cost of CO_2 capture). After successful fluid dynamics of the lab-scale rig were obtained, a complete system for carbon capture 0.5 MWe-equivalent was designed

and constructed. The pilot-scale system used real flue gas from a coal-fired power production facility (12.5% CO_2) at the US National Carbon Capture Center (NCCC). The rapid adsorption-desorption kinetics allowed for a compact design in which a single tower integrates the adsorber, regenerator and solids cooling section. The solids, collected at the bottom, are pneumatically transported to the top of the column into the adsorber section and descended driven only by gravity. Carbon capture efficiencies and CO_2 purity of 67% and 93% respectively are reported. Higher performance was claimed to be possible by decreasing the temperature and increasing the height of the adsorption section.

2.2 Lab/bench-scale counter-current gas-solid contactors

Claus et al. (1976) studied the gas-solid flow through a bed of Raschig ring-like packing made of wire mesh, reporting analogies with the gas-liquid system, in particular the existence of dense and dilute (trickle flow) phases, the "preloading" and "loading" zones, and flooding. In the preloading zone, the solids holdup 1) is almost entirely supported by the packing, and therefore the pressure drop due to solid suspension in the gas stream is negligible; 2) does not change with gas velocity, but is linearly proportional to the solids flow rate. The latter implies that the solids velocity in the preloading zone is constant, calculated to be 16.2 cm/s. Increasing gas velocity further from the loading region causes the column to flood, with the subsequent sharp rise of pressure drop and solids holdup.

Roes and van Swaaij (1979a) list the characteristics to feature by gas-solid counter-current contactors: 1) low axial dispersion of both phases, 2) high capacity, 3) low pressure drop, and 4) good heat and mass transfer properties, both interphase and with heat exchange surfaces. The authors give examples of contactors previously used in industry and/or investigated at the lab-scale, praising the qualities of the diluted-phase zig-zag contactor over denser-phase ones: high solids flow rates can be used with low pressure drop. Their investigation concerned the hydrodynamics of counter-current contact of a Geldart A-type solid with air in a bed of Pall rings. They obtained similar qualitative results to Claus et al. (1976). The fraction of dynamic holdup suspended on the gas phase (10% to 50% of the total dynamic holdup) is the main contributor to pressure drop apart from the packing. It increases with increasing

gas flow rate and decreasing solids flow rate. The overall trend of the pressure drop, however, was to increase with increasing both gas and solid flow rates since the increase in dynamic holdup with solids flow rate dominates. They found a trickle velocity of 15 cm/s, similar to Claus et al. (1976). They realised that the static holdup in gas-solid systems is determined by system geometry and angles of repose and internal friction of the solids (whereas in gas-liquid systems it is determined by capillary forces; in this aspect, non-wettable systems like mercury flowing on metal packing present a similar relationship between static holdup and flow rate of the dispersed phase than gas-solid systems). The authors concluded that, despite the comparable hydrodynamic behaviour between gas-solid and gas-liquid systems, data generated in gas-liquid should not be used for prediction of gas-solid systems.

Noordergraaf et al. (1980) investigated the hydrodynamics and axial dispersion of a dilute flow zig-zag contactor. The investigators chose this geometry because of its low pressure drop and axial dispersion, suitable for adsorption systems. The gas-solid contact is best at the zones between baffles, where the solids cross the gas path. Gas dispersion was found to increase with solids flow rate at low gas velocities, which the authors associated to gas entrainment by the solids trickles. At higher gas velocities, gas dispersion is less severe, and also less sensitive to the solids flow rate. Solids dispersion is not sensitive to the gas flow except at velocities close to the terminal velocity of the solids, and decreases when increasing solids flow.

Large et al. (1981) studied the trickle flow of sand through the same Pall ring packing as Roes and van Swaaij (1979a), but with larger bed diameters (320 mm instead of 70 mm) and particle sizes and densities (190 μm and 2650 kg/m^3 instead of 70 μm and 830 kg/m^3), and lower solids flux (0.7-1.7 kg/s/m^2 instead of 0-6 kg/s/m^2). The authors found that channelling and gas-solid segregation occurred at gas velocities around the solids terminal velocity value rather than flooding, which they found analogous to encountering channelling in large-diameter dense beds rather than the slug flow typical of smaller-diameter ones. Furthermore, the researchers found that for their system the gas flow rate had a higher influence in the solids flow than for Roes and van Swaaij (1979a): a higher fraction of suspended

solids holdup (60 % of the total, compared to 10% - 50% found by the latter authors) increased the pressure drop in the column but also the residence time of the particles.

Verver and van Swaaij (1986) tested a structured packing with improved hydrodynamics (claimed to have lower static holdup and pressure drop than the random packing used in previous works) with several types of solid particles ranging from FCC catalyst to steel shot 0.9 mm in diameter. The authors found that the solids slip velocity and pressure drop in the column strongly depended on the ability of the particles to agglomerate or form clusters, calling this effect "particle shielding". Smaller, less dense particles exhibit a slip velocity higher than the terminal velocity of the single particle as the solids flow rate increases and form larger entities than the single particle. By the same phenomenon, the fraction of suspended solids holdup decreases with increasing solids flow rate in small particles. Larger and/or denser particles, on the other hand, tend to behave according to the 'single-particle flow model' developed by the authors.

Verver and van Swaaij (1987) studied the fluid dynamics of a structured packing trickle bed column featuring two zig-zag channels in parallel, making this contactor a hybrid between their previous version (Verver and van Swaaij, 1986) and that of Noordergraaf et al. (1980). Cold-model experiments with FCC catalyst showed similar hydrodynamic features than for their original structured packing, i.e. higher particle velocities when increasing the solids flow rate, which again were associated to particle agglomeration. Mass transfer data was obtained through experiments in which a reaction with fast kinetics (oxidation of H_2S with SO_2 to produce elemental sulphur) was carried out. The authors concluded that mass transfer limitations were concentrated at the interphase between bulk gas and solid trickle rather than at the single particle surface.

Westerterp and Kuczynski (1987a) investigated the effect of type of packing and gas properties on the hydrodynamics of gas-solids trickle flow contactors. They introduced the concept of "trickle void fraction", and found that "a solid particle in a trickle drags along about 15 times its own volume as gas in the trickle", contributing to gas axial mixing. The authors found that for random packing, the size of the trickles increased linearly with solids flow rate at gas flow rates below the flooding

point. This indicated, similarly to for Claus et al. (1976) and Roes and van Swaaij (1979a), that the solids linear velocity was constant in such operating region, with values of 12-17 cm/s. This value was considered the average between the solids velocity in the trickle and sliding on the packing surface. On the other hand, for a commercial structured packing with a zig-zag path the solids velocity decreased with increasing gas velocity. They associated this difference to the absence of trickles (free falling particles) in the structured packing.

Westerterp and Kuczynski (1987b) conducted a study of the methanol synthesis from CO and H_2 in a "gas-solid-solid trickle flow reactor". In such a device, the solid packing acted as the reaction catalyst, whereas the trickling powder enhanced the reaction conversion by adsorbing the product. In the authors' literature survey, they mention that the idea of counter-current gas-solid contact in a packed bed was first published in a DSM 1948 patent. From 1965 to 1976, the idea of "raining packed bed" for heat recovery was patented by Compagnie de Saint-Gobain.

Kiel et al. (1993), as part of their research in SO_x and NO_x removal from flue gases, looked into the mass transfer between gas and mm-sized particles in a counter-current contactor with a similar structured packing to that of Verver and van Swaaij (1986), where the packing elements were stacked cylindrical (rather than diamond-shaped cross section) rods. Their mass-transfer process was adsorption of water in 640 μm and 2200 μm size molecular sieve particles. The researchers developed a simple plug flow model that was used to compare experimental values of the overall mass transfer coefficient to that calculated using correlations for a single sphere. They obtained, for the particle sizes used, values of the overall mass transfer coefficient 40-80% of the corresponding to the single sphere, much higher than 1% reported by previous studies using FCC catalyst. The authors confirmed in this way the observations made by Verver and van Swaaij (1986) about the "particle shielding" phenomenon and how it could be reduced by increasing the solid particle size.

Kannan et al. (1994) studied the operational characteristics of a column staged with horizontal perforated plates, determining the operational stability regions as a

function of flow rates of both phases, solid characteristics and plate geometry (open area and orifice diameter). The authors found that gas velocities at the plate holes needed to be 0.9-1.1 times the particle terminal velocity to prevent solids from "dumping" through the plate holes and form a layer on the plate surface. They also observed two modes of operation, namely dilute and dense phase flow, similar to other counter-current gas-solids systems (Claus et al., 1976). A wider operating range for gas velocity (between the minimum required to prevent "dumping" of the particles and the transition from dilute- to dense-phase flow) was promoted by using lower flow rates of larger and denser particles: this is, again, in line with the "particle shielding" effect described by Verver and van Swaaij (1986).

Nagata et al. (1994a) investigated the hydrodynamics of trickle flow of sand 0.42 mm particle size in a rectangular cross section contactor with inclined baffle plates similar to those used by Verver and van Swaaij (1987). Loading and flooding regimes were found. They report an increase of solids holdup and residence time at gas velocities above the loading point.

Nagata et al. (1994b) used inclined plates (without orifices) that create a zig-zag path for the particles. Loading and flooding regimes were found, as well as an increase of solids holdup and residence time at gas velocities above the loading point. The authors use photographs and hot-wire anemometry to obtain the 2-dimensional gas flow field. They also depict the single-particle trajectory when flowing from the edge of a baffle across the gas flow path: small particles ($u_g > u_t$) are dragged upwards, whereas large particles ($u_g < u_t$) take downward trajectories. For a given gas velocity, there is a value of particle size that makes the particulate recirculate in the space between two consecutive baffles.

Nagata et al. (1998) investigated the use of inclined plates (without orifices) for counter-current gas-solid contact, where the solid was in a dense-phase state. Such flow regime was called by the authors "moving-fluidised flow". They claimed enhanced gas-solid contact with respect to either moving or fluidised beds due to the zig-zag path and the combination of the hydrodynamics of the two more conventional solid flow regimes.

Guo and Tokuda (2002) also worked with a hybrid moving-fluidised solid flow regime for counter-current dense-phase gas-solid contact. The authors called their device "Z-path fluidised-moving bed with inclined perforated plates", which in practice is similar to a conventional multi-stage fluidised bed, but with inclined gas distributors. The angle of inclination of the plates is smaller than the angle of repose of the solids, so a minimum gas velocity is required to make the solids move over the surface of the plate. A maximum gas velocity value exists above which stable operation is hindered due to accumulation of solids on the plates. The range of stable operation was found to be narrower and shifted to lower velocities with increasing plate angles. The reported pressure drop per unit height of solids bed is smaller than for both packed and fluidised beds. A (counterintuitive) result reported by the authors is an increase in solid bed height on the plates and particle residence time with the plate angle.

Veneman (2015) and *Veneman et al. (2016)* studied a countercurrent G-S trickle flow contactor for carbon capture. The system was a column with horizontal orifice trays, the CO_2 sorbent being a commercial ion exchange resin with primary benzyl amine groups. The authors studied the cold-model fluid dynamics of the trickle flow column, and behaviour and performance of the carbon capture system formed by coupling the adsorber to a multi-stage fluidised bed regenerator and a solids recirculation line. The cold-model trickle flow adsorber presented similar features to previously studied packed contactors: relatively constant particle linear velocity at moderate values of gas velocity (24 cm/s, 48% higher than for Claus et al. (1976) and Roes and van Swaaij (1979a)), and flooding. The researchers found that bulk-to-particle heat and mass transfer resistances were small for the ranges of gas and solids flow rates used, so the adsorber efficiency was determined by the adsorption kinetics.

2.3 Summary tables

Table 2.1 and Table 2.2 compile the system characteristics (contactor geometry and dimensions, type of solids) and experimental conditions (gas velocity and solids flux) at which the works described in this literature review and the one described in this thesis are carried out.

Table 2.1. Works in continuous TSA carbon capture using upflowing co-current contactors and solid amines

Author	**Contactor characteristics**	**Solids**	**d_p (μm)**	**U_g (m/s)**	**G_s (kg/m^2/s)**
Veneman et al. (2012)	Turbulent bed (40 mm ID×500 mm) + riser (15 mm ID×1.9 m)	Silica gel (ρ_s not given, u_t not given)	250-500 300-600	0.13 (turbulent bed) 0.91 (riser)	2.8-4.7
Zhao et al. (2013)	Turbulent bed (50 mm ID×260 mm) + riser (20 mm ID×1.7 m)	Silica gel (ρ_s not given, u_t not given)	150-300	0.15 (turbulent bed) 0.96 (riser)	Not given
Sjostrom et al. (2011), ADA (2011)	Riser (25.4 mm ID×12.2 m)	Porous silica (ρ_s = 646 kg/m^3, u_t not given) Porous silica (ρ_s not given, u_t not given)	155-185 191-212	4.7	9.9
This work	Riser (26.5 mm ID×2.5 m)	Sand (ϕ_s = 0.85, ρ_s = 2650 kg/m^3, u_t = 1.0 m/s)	152	2.6-4.1	50-94
This work	Riser (50.1 mm ID×2.5 m)	Sand (ϕ_s = 0.85, ρ_s = 2650 kg/m^3, u_t = 1.0 m/s)	152	5.1-6.2	10-86

Table 2.2. Works in lab/bench-scale gas-solid counter-current contactors

Author	Contactor characteristics	Solids	d_p (μm)	U_g (m/s)	G_s (kg/m^2/s)
Claus et al. (1976)	Cylindrical screen packing (2×2 cm, 1.04 mm mesh, 0.5 mm SS wire). 92 mm ID×3m	Sand (ϕ_s = 0.64, ρ_s = 2650 kg/m^3, u_t = 1.79 m/s)	235	0-u_t	0-42
Roes and van Swaaij (1979a, 1979b)	Pall rings (1.5×1.5 cm). 75.5 mm ID×1m	FCC catalyst (ρ_s = 813 kg/m^3, u_t = 0.15 m/s)	70	0-u_t	0-6
Noordergraaf et al. (1980)	Zig-zag (19 mm×40 mm×600 mm, 45° baffles, interval 40 mm)	FCC catalyst (ρ_s = 813 kg/m^3, u_t = 0.15 m/s)	70	0-u_t	0-21
Large et al. (1981)	Pall rings (1.5 cm×1.5 cm). 320mm ID × 2 m	Sand (ρ_s = 2650 kg/m^3, u_t = 1.4 m/s)	190	0.4-1.7	0.7-1.7
Verver and van Swaaij (1986)	Diamond-cross-section stacked packing (20 mm, 24 layers). 100 mm×100 mm×480 mm	FCC catalyst (ρ_s = 810 kg/m^3, u_t = 0.11 m/s)	70	0-0.18	0-0.8
		Fine sand (ρ_s = 2650 kg/m^3, u_t = 2.0 m/s)	255	0-1.4	0-2.5
		Coarse sand (ρ_s = 2650 kg/m^3, u_t = 3.3 m/s)	425	0-1.4	0-2.5
		Fine steel shot (ρ_s = 7800 kg/m^3, u_t = 4.9 m/s)	310	0-5.4	0-4.5
		Coarse steel shot (ρ_s = 7800 kg/m^3, u_t = 12.3 m/s)	880	0-5.4	0-4

Table 2.2 (cont.)

Author	System	Solids	d_p (μm)	U_g (m/s)	G_s (kg/m^2/s)
Westerterp and Kuczynski (1987a, 1987b)	Glass Raschig rings (7 mm× 7 mm×1 mm) + catalyst pellets (5 mm×5 mm) Ceramic Raschig rings (8 mm×8 mm×3 mm) Sulzer Kerapak structured packing (25 mm ID × 0.5 m)	FCC catalyst (ρ_s = 813 kg/m^3, u_t = 0.46 m/s)	30-150	0-0.3	0-2
Kiel et al. (1993)	Circle-cross-section stacked packing (10 mm, 27 layers). 60 mm×60 mm×270 mm	Molecular sieve (ρ_s = 1533 kg/m^3, u_t = 3.4 m/s) Molecular sieve (ρ_s = 1270 kg/m^3, u_t = 8.6 m/s)	640 2200	0.3-1 0.4-2.6	0.11-0.92 0.43-1.43
Kannan et al. (1994)	Horizontal perforated plates (5 stages, orifice diameter 1.5-3 mm, free area 15%-45%, thickness 1.5 mm). 58 mm×580 mm	Silica gel (ϕ_s = 0.7, ρ_s = 670 kg/m^3) Resin (ϕ_s = 1, ρ_s = 1480 kg/m^3) Sand (ϕ_s = 0.76, ρ_s = 2650 kg/m^3) Ilmenite (ϕ_s = 0.84, ρ_s = 4300 kg/m^3)	315-500 315-500 500-630 125-200 200-315 315-500 125-200 200-315	(0.2-6.66)u_t	0.1-11

Table 2.2 (cont.)

Author	System	Solids	d_p (μm)	U_g (m/s)	G_s (kg/m^2/s)
Nagata et al. (1994a)	Double 45°-slope baffle plates (28.3 mm×10 mm, interval 42 mm×45 mm). 168 mm×50 mm×1080 mm	Sand (ρ_s = 2650 kg/m^3, u_t = 2.42 m/s)	420	0-1.3	0-2.4
Nagata et al. (1994b)	Inclined baffle plates (40-45°). 170 mm×50 mm×1500 mm	Sand (ρ_s = 2650 kg/m^3, u_t = 0.29 to 5.79 m/s)	50-1000	0.2-1.3	0-3
Nagata et al. (1998)	Inclined orifice plates (5 plates, 5°-20°). 170 mm×50 mm×1500 mm. Moving-fluidised *dense* solid phase.	Sand (ρ_s = 2650 kg/m^3)	370	0.1-1.2	0.1-2.7
Guo and Tokuda (2002)	Inclined perforated plates (40-45°). 300 mm×70 mm×1200 mm. Moving-fluidised *dense* solid phase	Rice Millet Iron ore	- - -	0.7-1.9 0.48-0.9 0.46-0.9	- 2.4-6.9 -
Veneman (2015), Veneman et al. (2016)	Horizontal perforated plates (5 stages). 21 mm×1300 mm	Polystyrene-based ion exchange resin (ρ_s = 880 kg/m^3, u_t = 2.5 m/s)	688	(0-0.32)u_t	0-3.16
This work	Inclined orifice plates (3 plates, 45°). 0.142 mm hydraulic ID × 0.65 m. Orifices: 6 mm ID	Sand (ϕ_s = 0.85, ρ_s = 2650 kg/m^3, u_t = 1.0 m/s)	152	0-0.65	0-3.3

2.4 Scalability challenges in counter-current contactors

The main characteristic sought in counter-current contactors is their higher separation (or heat transfer) efficiency compared to co-current contactors, as the former systems are not equilibrium-limited. In the context of TSA post-combustion carbon capture, counter-current contactors allow the use of sorbents with lower affinities for CO_2 at low partial pressures, or lower sorbent circulation rates for a given sorbent, than those used in a co-current contactor. This is explained in detail in the thermodynamic-kinetic study presented in Chapter 3.

One weakness of counter-current systems that becomes evident when comparing their typical operating conditions with those of co-current systems is their lower maximum gas velocity, which directly translates into a larger footprint. The great majority of works in counter-current separators presented in this literature review are conducted at gas velocities below the terminal velocity of the solid particles to prevent flooding. This limit of operation is transcended only when very small particle sizes are used, which is explained by particle agglomeration or "shielding" (Verver and van Swaai, 1986). This is however of little practical use since, even if gas velocity could be doubled or tripled with respect the terminal velocity, the absolute value of gas velocity when using small particles would still be low to cope with the very large volumetric flow rates of flue gas typical of post-combustion carbon capture. A more realistic approach to overcome this limitation would be to increase the sorbent particle size, and hence the maximum value of gas velocity before flooding.

The above can be visualised using flow regime maps like the one by developed by Grace (1986), illustrated in Figure 2.1. The abscissa and ordinate are the dimensionless particle size (d_p*) and gas superficial velocity (U_g*):

$$d_p^* = d_p\left[\rho_g\left(\rho_s - \rho_g\right)g/\mu^2\right]^{1/3} \tag{2.1}$$

$$U_g^* = U_g\left[\rho_g^2/\mu g\left(\rho_s - \rho_g\right)\right]^{1/3} \tag{2.2}$$

where d_p is the particle size, U_g the gas superficial velocity, ρ_g the gas density, ρ_s the solid particle density, μ the gas viscosity and g the acceleration of gravity.

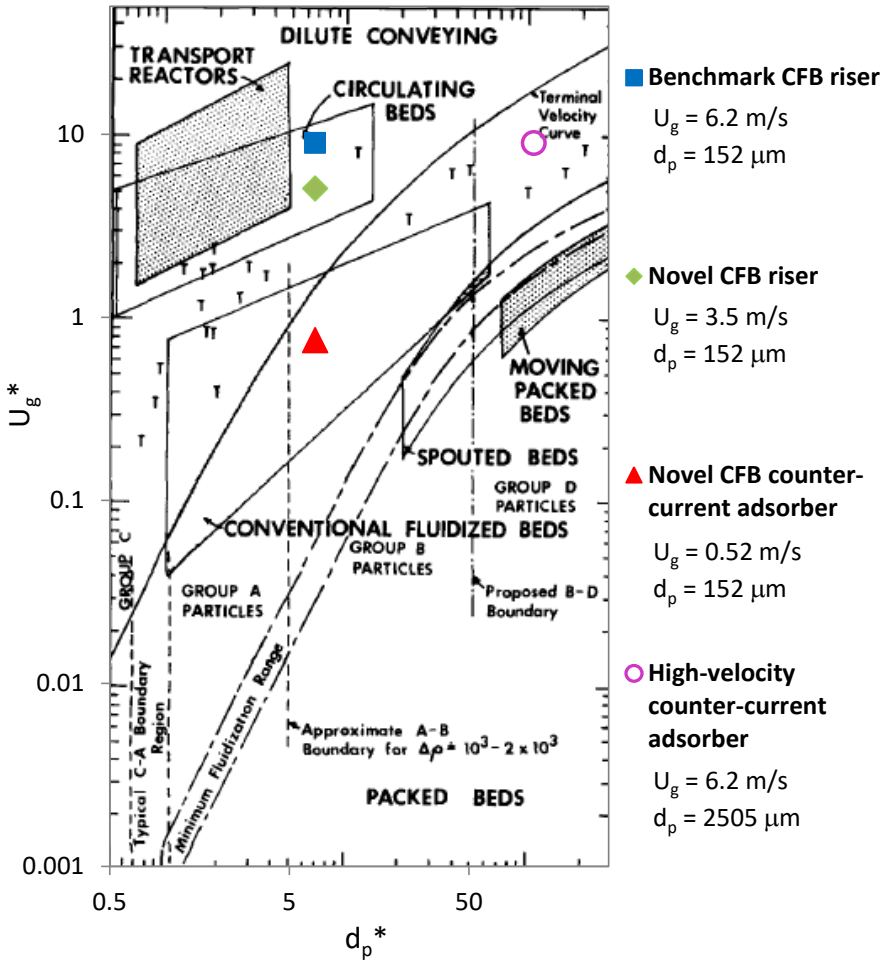

Figure 2.1. Flow regime map (Grace, 1986, reproduced with permission) representing the conditions of the systems studied in this work and a hypothetical high-velocity counter-current adsorber.

The solid symbols in the diagram represent the conditions of the two risers and the counter-current adsorber studied in this work, all using the same solid particles (sand, d_p = 152 μm, ρ_g = 2650 kg/m^3). It can be seen how the risers are located well above the "terminal velocity curve", within the "circulating beds" region. The counter-current adsorber, on the other hand, lies below such curve but at a short distance. As it will be seen in Chapter 7, the counter-current adsorber is in these conditions being operated at the maximum gas velocity recommended for stable operation, corresponding to 52% of the particle terminal velocity, or U_g/u_t = 0.52. Assuming the

same value of the ratio U_g/u_t applies at higher particle sizes and gas velocities, the particle size that could be used in a hypothetical high-velocity counter-current adsorber operating at the same gas velocity that the benchmark CFB riser is 2505 μm (represented in the regime map by an empty circle). This is a very plausible particle size that corresponds to a Geldart D-type material. The challenge for process scale-up would then be passed onto sorbent developers, who would have to design materials with faster intra-particle mass and heat transfer capabilities.

As a concluding remark, it is worth noting that gas-solid counter-current contactors operating at low gas velocity could still be considered for carbon capture in industrial plants, which typically have an associated lower gas volumetric flow rates to decarbonise than power stations (Global CCS Institute, 2016c).

3 Thermodynamic-kinetic evaluation of CFB configurations for TSA carbon capture

3.1 Introduction

The novel CFB configuration presented here is assessed, from a thermodynamic-kinetic point of view, as a carbon capture process against a benchmark CFB configuration. A basis of calculations is defined first to set the adsorption equilibrium parameters and process specifications (Section 3.2). Then, the tools to carry out the assessment are developed and described (Sections 3.3 to 3.5). These tools are used in Section 3.6 to come up with sensitivity study cases in which the impact of key process parameters is quantified for both CFB configurations.

3.2 Basis of calculations

The first step is to define the basis of calculations upon which the comparative assessment of the CFB configurations can be done. The base sorbent material, adsorption conditions, flue gas composition (CO_2 concentration) and process CO_2 recovery are given in Table 3.1. The regeneration conditions are left open, as part of the study.

Table 3.1. Basis of calculations

Flue gas		
y_{in}	0.15	CO_2 conc. (% vol.) typical from coal-fired power plants
Adsorption conditions		
T	50	Temperature (°C)
P	1	Pressure (bara)
	90%	CO_2 recovery
Isotherm: Langmuir-type		
q_{max}	0.17	Sorbent maximum loading (kg CO_2/kg solids)
b_0	10^{-8}	Langmuir pre-exponential factor (bar^{-1})
ΔH_{ads}	−60	Heat of adsorption (kJ/mol)

The sorbent isotherm chosen is Langmuir-type, as done in previous theoretical analyses of TSA carbon capture systems using CFB technology (Berger and Bhown, 2011; Pirngruber et al., 2013; Pröll et al., 2016). The values of b_0 and ΔH_{ads} for the sorbent isotherm are taken from Pirngruber et al., (2013), which the authors found would lead to a minimal loss of power production when the sorbent is used to

decarbonise a 600 MW-equivalent coal-fired power plant using a co-current CFB system. Regarding q_{max}, it was decided to take an optimistic (but not unrealistic) value to ensure that differences in carbon capture performances between the CFB systems here studied result from their differences in contact mode and not from limitations in sorbent capacity. The value chosen (0.17 kg CO_2/kg) is the highest obtained by ADA (2011), corresponding to their supported amine referenced as "R". The isotherm graph at different temperatures is shown in Figure 3.1.

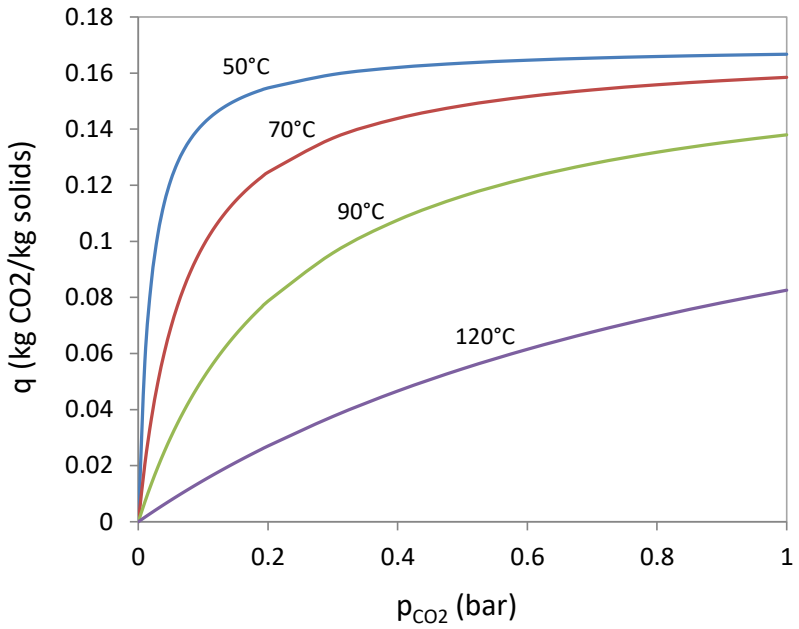

Figure 3.1. Adsorption isotherm of the sorbent used in the basis of calculations

3.3 Mass balance

The mass balances in the CFBs are presented next. In the calculations to follow, the concentration of CO_2 in the gas phase and CO_2 loading in the solid sorbent will be expressed in CO_2-free basis. In this way, the mass flow rate (in kg/s) of CO_2 in a gas stream will be given by the product F_gY, where:

$$F_g \equiv \frac{\text{mol } CO_2\text{-free gas}}{\text{s}} \cdot 0.044 \frac{\text{kg } CO_2}{\text{mol } CO_2} \tag{3.1}$$

$$Y \equiv \frac{\text{mol } CO_2}{\text{mol } CO_2\text{-free gas}} \tag{3.2}$$

Equally, the mass flow rate (in kg/s) of CO_2 in the solid phase is $F_s q$, where:

$$F_s \equiv \frac{\text{kg } CO_2\text{-free sorbent}}{\text{s}} \tag{3.3}$$

$$q \equiv \frac{\text{kg } CO_2}{\text{kg } CO_2\text{-free sorbent}} \tag{3.4}$$

The values of F_g and F_s are independent of composition since it is assumed that CO_2 is the only adsorbable species.

The flow diagrams in Figure 3.2 show schematically how the gas and solids streams are distributed in the two CFB configurations studied.

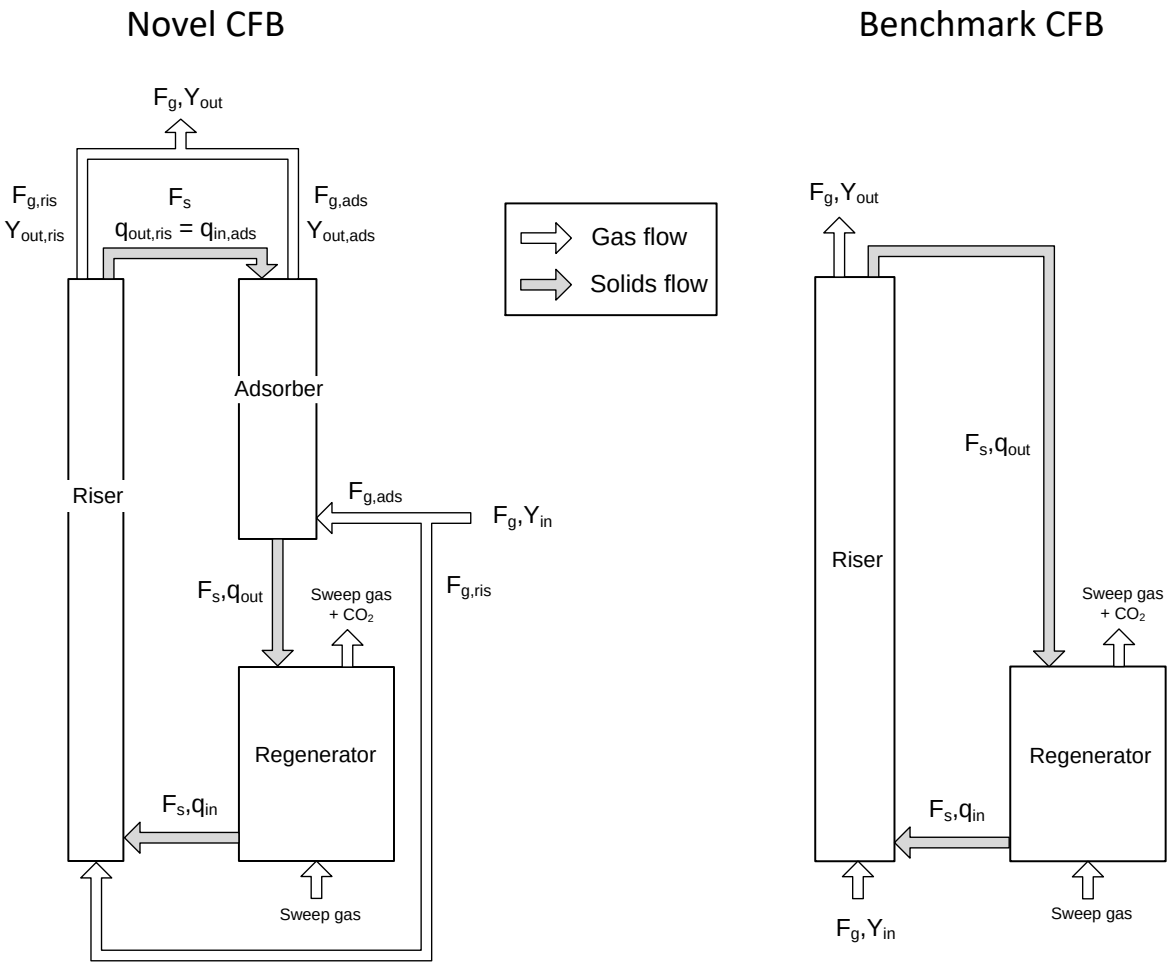

Figure 3.2. Mass balance of the novel (left) and benchmark (right) CFB configurations

Whereas in the benchmark CFB adsorption takes place in a single co-current step, the novel CFB features two adsorption steps (in series for the solids phase and in parallel for the gas phase), each with a different contact mode (co-current in the riser, counter-current in the adsorber).

3.4 Calculation of minimum solids circulation rate

The minimum solids circulation rate for 90% CO_2 recovery can be determined by solving the mass balance in combination with the equilibrium equation. The McCabe-Thiele diagram (McCabe and Smith, 1976) can be used for this purpose in analogy with gas-liquid systems (Ruthven, 1984; Ruthven and Ching, 1989). Figure 3.3 and Figure 3.4 show the corresponding McCabe-Thiele diagrams for pure co-current and counter-current adsorption. It is easy to realise from the diagrams the impact of the shape of the isotherm upon the maximum attainable value of the solids CO_2 loading.

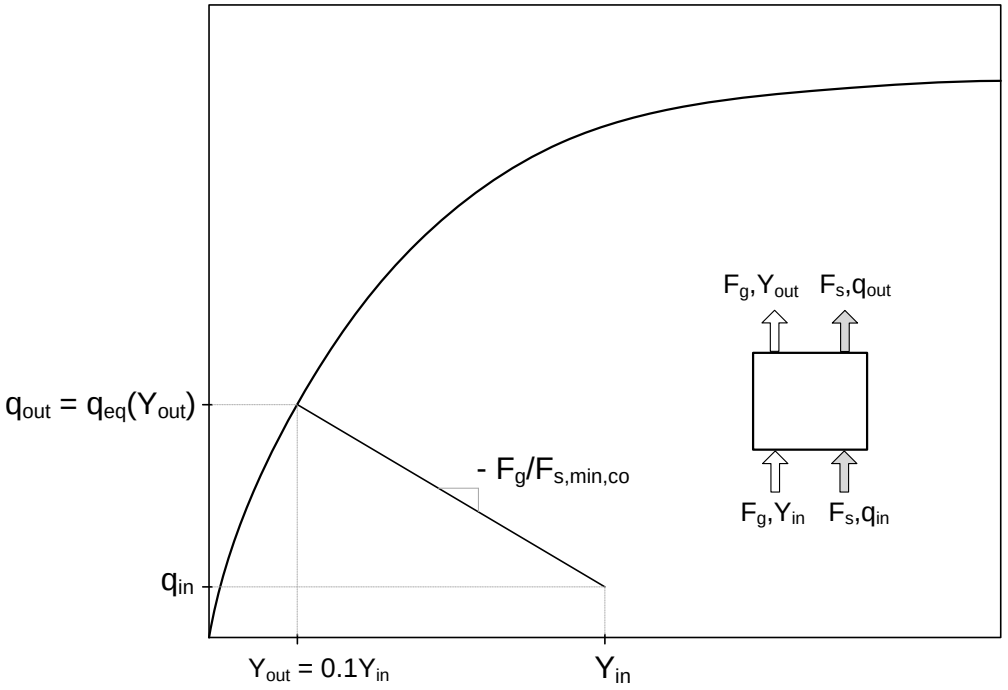

Figure 3.3. McCabe-Thiele diagram of co-current adsorber

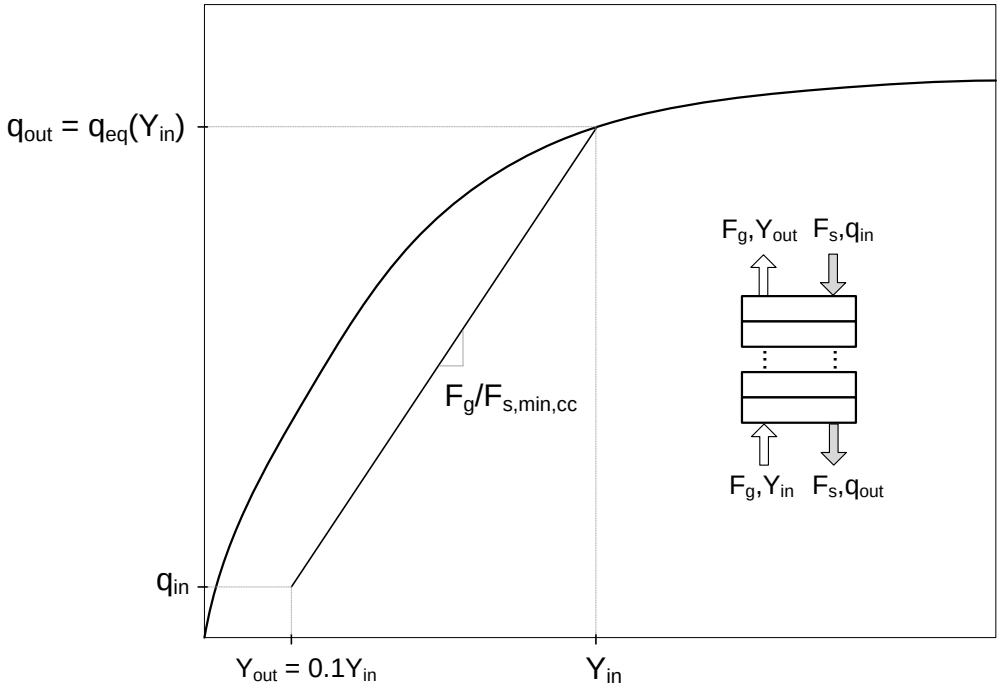

Figure 3.4. McCabe-Thiele diagram of multi-stage counter-current adsorber

For the combined co-current/counter-current arrangement in the novel CFB, the value of the minimum solids circulation rate varies between that for pure counter-current ($F_{s,min,cc}$) and pure co-current ($F_{s,min,co}$), and is function of the fraction of flue gas fed to the riser ($F_{g,ris}/F_g$ when expressed in sorbate-free basis):

$$\begin{cases} F_{s,min} = F_{s,min,cc} & \text{for} \quad 0 \le \dfrac{F_{g,ris}}{F_g} \le \dfrac{F_{s,min,cc}}{F_{s,min,co}} \\ F_{s,min} = F_{s,min,co}\dfrac{F_{g,ris}}{F_g} & \text{for} \quad \dfrac{F_{g,ris}}{F_g} > \dfrac{F_{s,min,cc}}{F_{s,min,co}} \end{cases} \tag{3.5}$$

Figure 3.5 shows an example of equation (3.5) for a particular case.

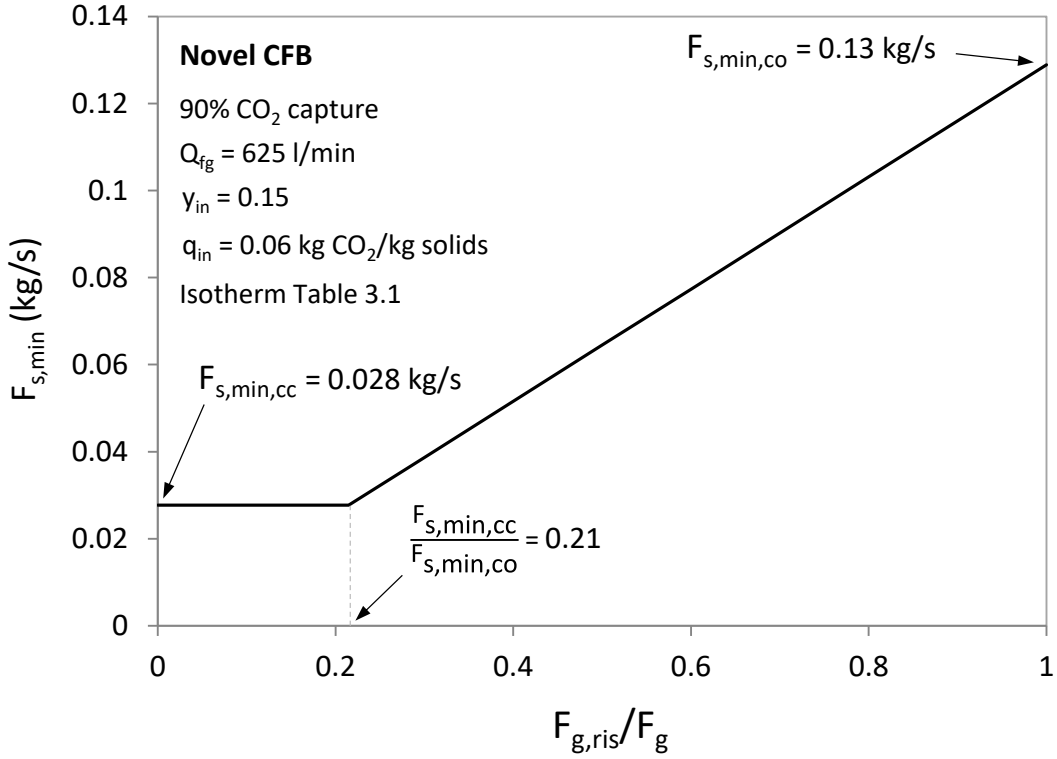

Figure 3.5. Minimum solids circulations rate in novel CFB configuration as a function of the fraction of flue gas fed to the riser

Figure 3.6 to Figure 3.8 show the McCabe-Thiele diagrams for the hybrid co-current/counter-current case, which can be grouped in three generic cases depending on the value of $F_{g,ris}/F_g$:

- $F_{g,ris}/F_g = F_{s,min,cc}/F_{s,min,co}$:

The adsorption duties of both riser and adsorber are such that the recovery achieved in both CFB sections is 90% ($Y_{out,ris} = Y_{out,ads} = Y_{out} = 0.1Y_{in}$). In this case, the adsorber is pinched at both ends (the gas and solids in contact at both ends of the adsorber are in equilibrium).

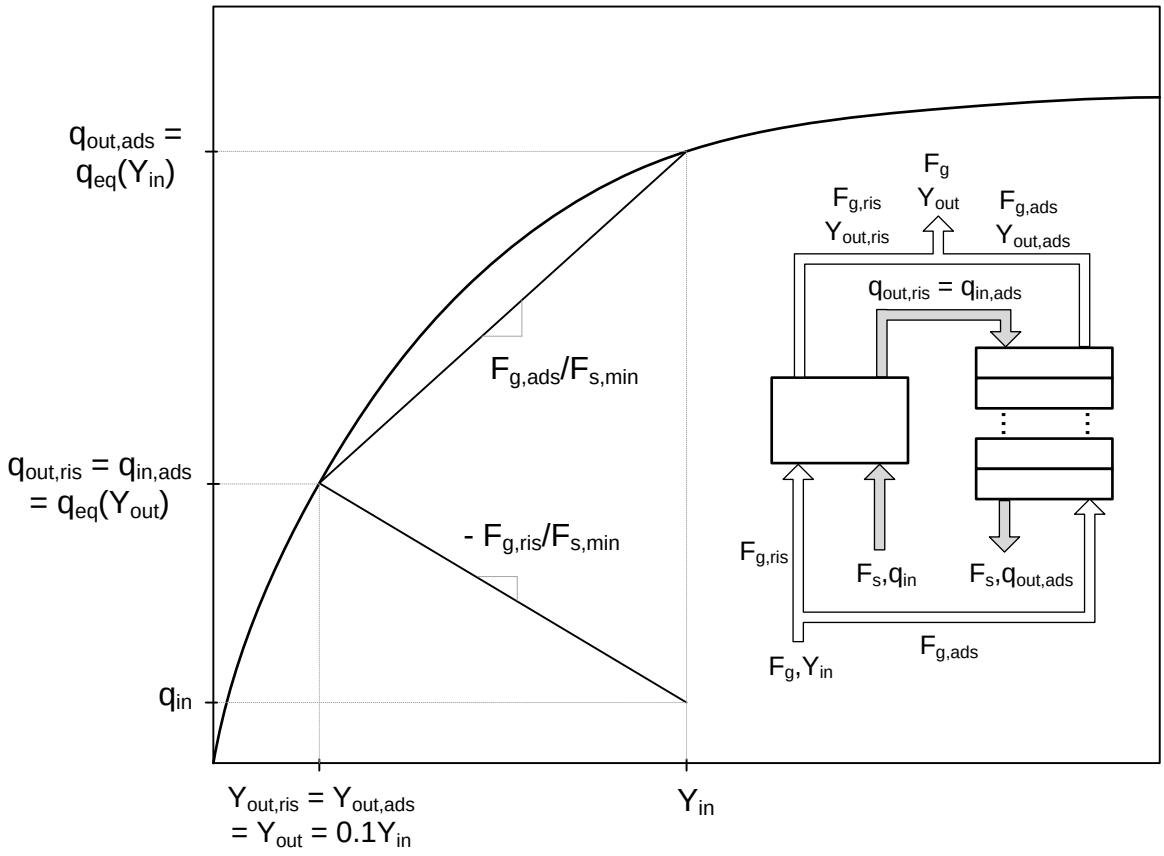

Figure 3.6. McCabe-Thiele diagram of the novel CFB configuration for the case $F_{g,ris}/F_g = F_{s,min,cc}/F_{s,min,co}$

• $F_{g,ris}/F_g < F_{s,min,cc}/F_{s,min,co}$:

In this operating region the adsorption duty is displaced to the counter-current adsorber, causing the recovery in this element of the CFB to be lower than 90% ($Y_{out,ads} > 0.1Y_{in}$). This is compensated by a CO_2 recovery in the riser higher than 90% ($Y_{out,ris} < 0.1Y_{in}$), in such a way that the total recovery is exactly 90% ($Y_{out} = 0.1Y_{in}$). It can be seen how the adsorber is pinched at the bottom end (gas inlet and solids outlet streams are in equilibrium).

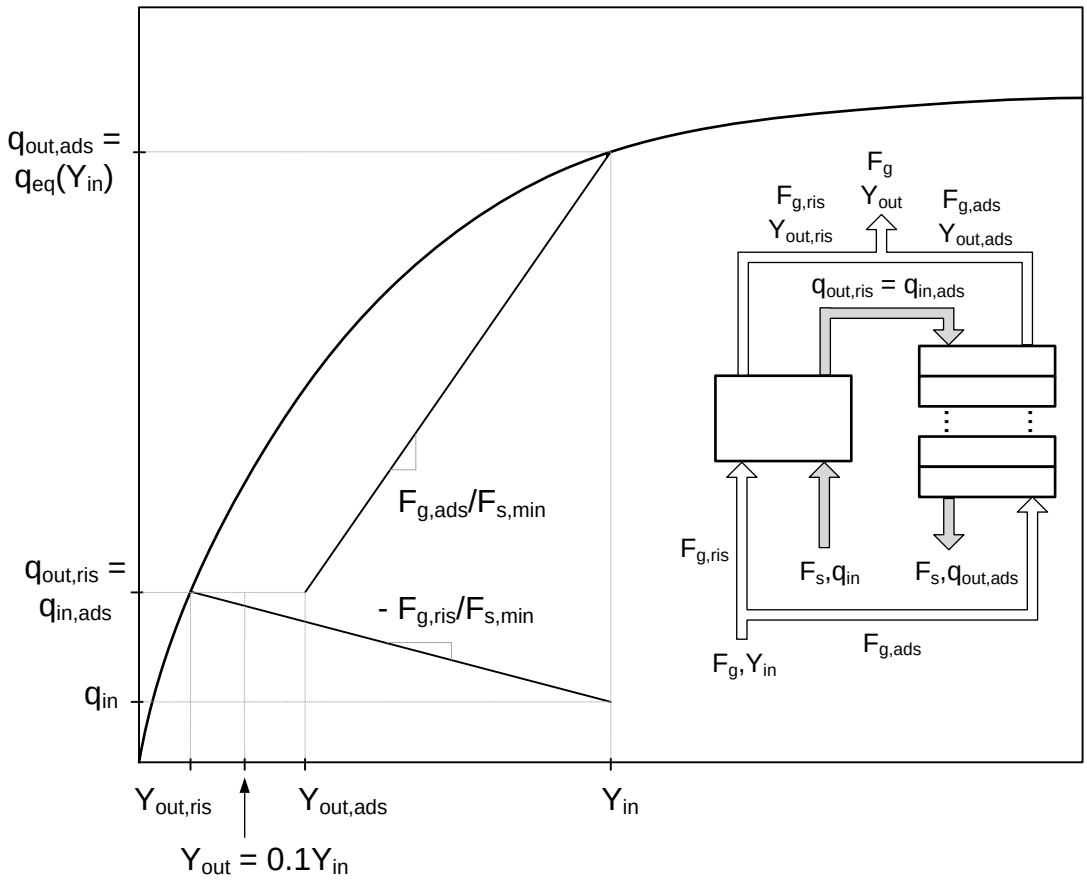

Figure 3.7. McCabe-Thiele diagram of the novel CFB configuration for the case $F_{g,ris}/F_g < F_{s,min,cc}/F_{s,min,co}$

• $F_{g,ris}/F_g > F_{s,min,cc}/F_{s,min,co}$:

In this case the adsorption duty is displaced to the riser. The CO_2 recovery in the riser is, however, constant at 90% since the minimum solids circulation rate increases linearly with the fraction of gas fed to the riser, as shown in Figure 3.5. Graphically, this corresponds to a constant value of the slope of the riser operating line. Note that in this case it is the streams at the adsorber top end (gas outlet and solids inlet) the ones in equilibrium.

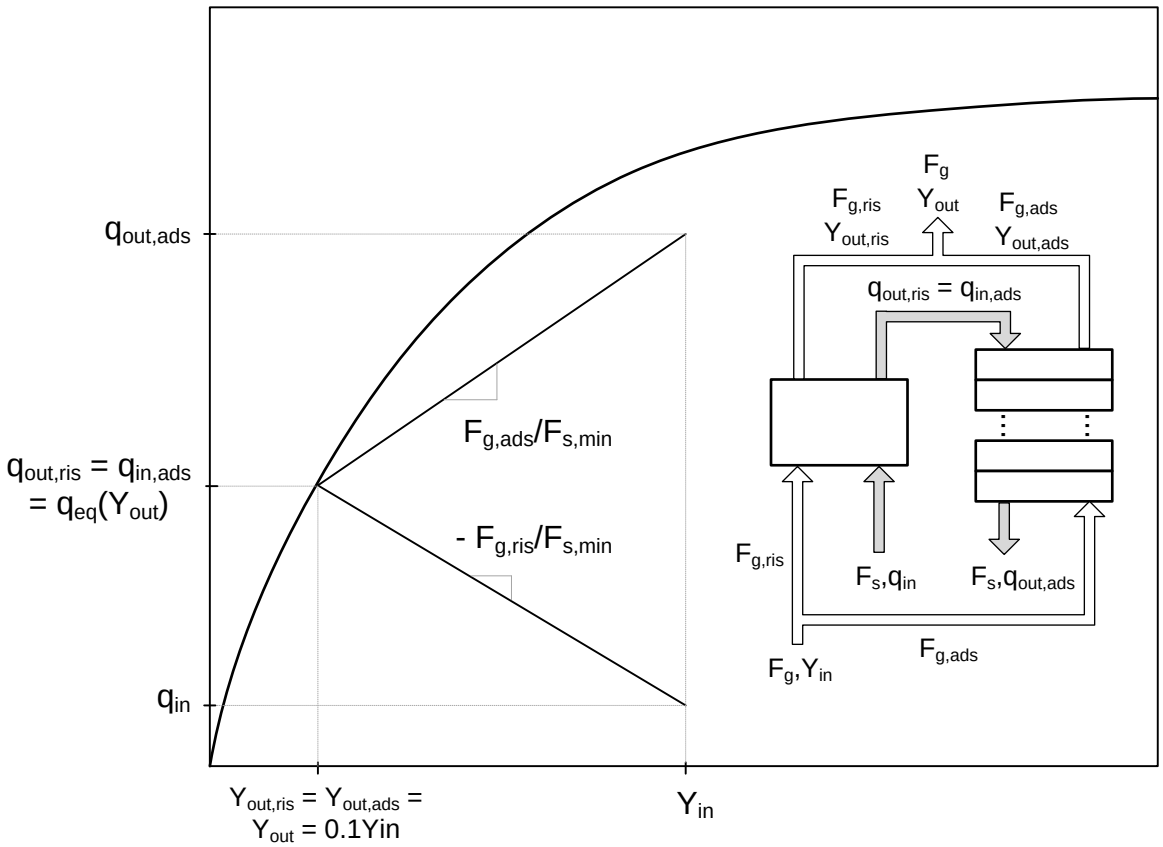

Figure 3.8. McCabe-Thiele diagram of the novel CFB configuration for the case $F_{g,ris}/F_g > F_{s,min,cc}/F_{s,min,co}$

The values of minimum solids circulation rate per unit mass of flue gas treated can be plotted against the lean sorbent loading for a particular sorbent material, adsorption temperature and CO_2 concentration in the flue gas, to form the chart shown in Figure 3.9. This type of chart could be used as a tool by TSA process designers and sorbent developers as it provides key information about the interaction between process and sorbent in a visual way. For instance:

• In case of regeneration in pure CO_2, the minimum regeneration temperature can be easily worked out from the maximum lean sorbent loading value ($q_{in,max}$), directly given in the chart. For the base case presented later in this chapter (Section 3.6.1), $q_{in,max}$ = 0.079 kg CO_2/kg solids, corresponding to a minimum regeneration temperature of 122°C for a partial pressure of CO_2 in the regenerator of 1 bar. If the regeneration temperature needs to be lower or a lower lean sorbent loading is desired, the amount of sweep gas can also be readily determined.

• The minimum solids circulation rates for pure co-current, pure counter-current and hybrid adsorbers are easily compared with each other, facilitating the selection of the most appropriate contact mode for given sorbent properties and/or inventory. For example, for q_{in} = 0.04 kg CO_2/kg the minimum solids circulation rate in a pure co-current adsorber is 0.1 kg/s per standard cubic meter per second of flue gas with 15% CO_2. If a pure counter-current adsorber is chosen instead, this value drops to a third, 0.036 kg/s. As an alternative, a hybrid adsorber like the one studied in this work can be used, in which case the fraction of flue gas fed to the counter-current section needs to be only 64% of the total to benefit from using just the minimum solids flow rate required in a pure counter-current system.

• If charts are made for a set of different sorbent materials, adsorption temperatures and/or CO_2 concentration in the flue gas, a choice of the most promising one to use with a particular adsorber design can be facilitated following the reasoning above.

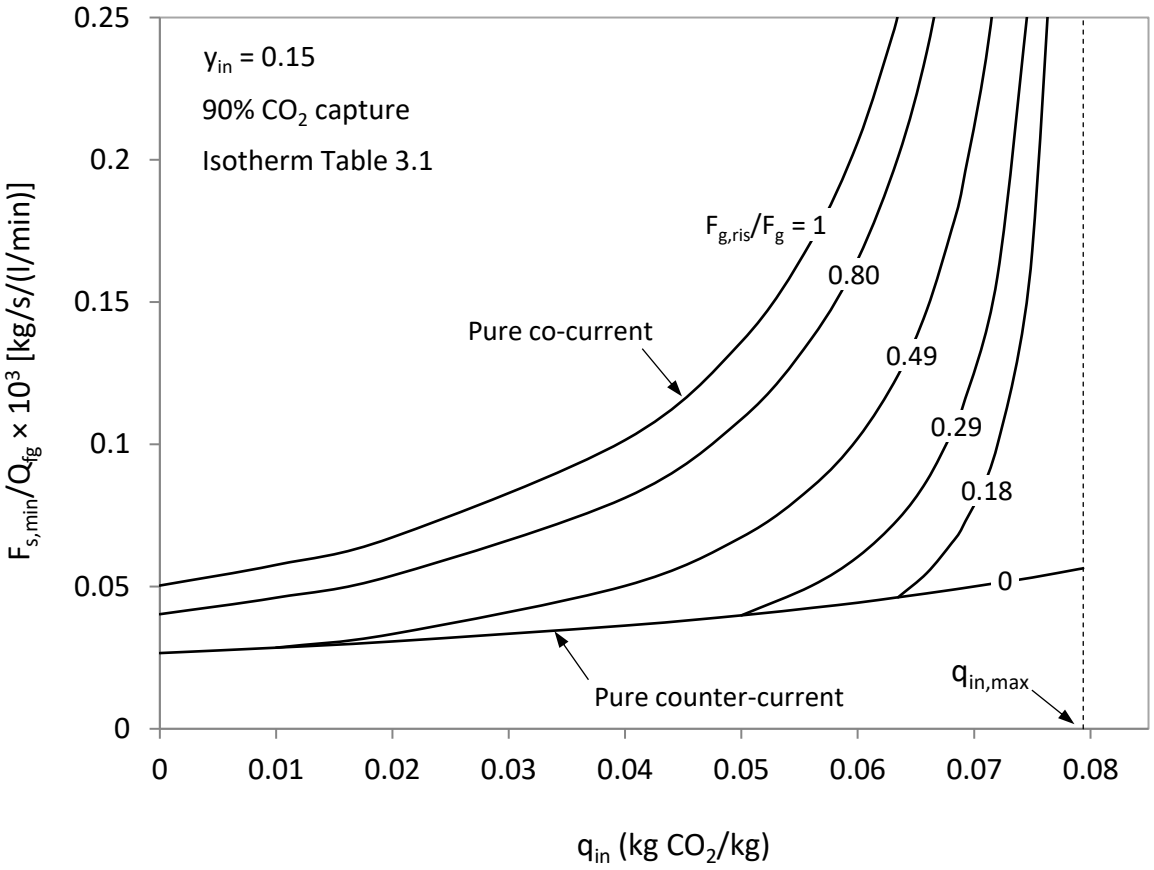

Figure 3.9. Minimum solids circulation rate per unit flue gas flow rate for the novel CFB configuration as a function of lean sorbent loading and fraction of flue gas fed to the riser

3.5 Adsorber model

The discussion in Section 3.4 considers only equilibrium and contact mode in the assessment and comparison of different CFB configurations, and as such no account of the actual sizing and geometry was taken for a required process performance. An attempt to do so is made by means of the adsorber model presented in this section.

A 1-dimensional, two-phase flow model for a generic adsorber of length L (Figure 3.10) is set up. The flue gas and the solid sorbent are in contact and flowing in the z-direction at velocities u_g and u_s respectively, in analogy to rate-based models in unit operations (McCabe and Smith, 1976). At position z in the adsorber, the gas has a CO_2 molar fraction y, the solid sorbent a mass CO_2 loading q, and the cross-sectional area perpendicular to the flow direction is A. The voidage is ε and the solids volumetric fraction $\varepsilon_s = 1-\varepsilon$. The values of the above variables are at this stage all assumed to be dependent on z.

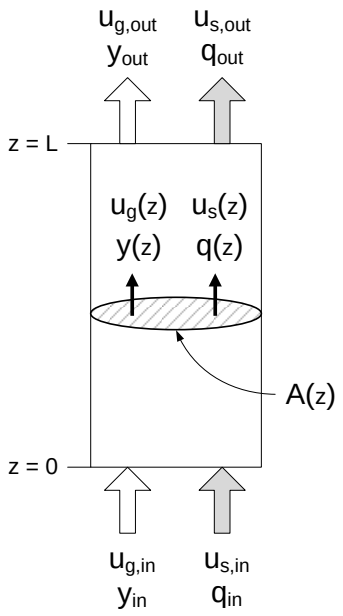

Figure 3.10. Adsorber 1-D model

The differential equations that define the model are derived from the mass balance of CO_2 in a slice of the adsorber extending from z to z+Δz. It will be assumed that both phases flow according to the axially-dispersed plug flow model (Ruthven, 1984):

- *Gas phase* (Figure 3.11.):

$$\varepsilon A u_g c_T My\Big|_z + \left(-D_g \varepsilon A c_T M \frac{\partial y}{\partial z}\right)\Big|_z - \varepsilon A u_G c_T My\Big|_{z+\Delta z} - \left(-D_g \varepsilon A c_T M \frac{\partial y}{\partial z}\right)\Big|_{z+\Delta z} -$$

Rate of CO_2 in by convection | Rate of CO_2 in by dispersion | Rate of CO_2 out by convection | Rate of CO_2 out by dispersion

$$-a\varepsilon_s A\Delta z N - A\Delta z \frac{\partial(\varepsilon c_T My)}{\partial t} = 0 \qquad (3.6)$$

Rate of CO_2 from gas to solid | Rate of CO_2 accumulation

Differentiating equation (3.6) with respect to z yields:

$$\frac{\partial}{\partial z}\left(\varepsilon A u_g c_T y\right) + \frac{\partial}{\partial z}\left(-D_g \varepsilon A c_T \frac{\partial y}{\partial z}\right) + \frac{a\varepsilon_s AN}{M} + A\frac{\partial(\varepsilon c_T y)}{\partial t} = 0 \qquad (3.7)$$

where:

D_g is the *axial dispersion coefficient* for the gas phase (m^2/s)

a is the surface area per unit volume of particle available for adsorption (m^{-1})

N is the adsorption rate of CO_2 per unit area of solid phase (kg $CO_2/m^2/s$)

c_T is the molar density of the flue gas (mol gas/m^3). For a real gas $c_T = P/ZRT$, where Z is the compressibility factor of CO_2 at pressure P and temperature T

M is the molecular weight of CO_2 (0.044 kg/mol)

The gas-to-solid mass flux is given by the following expression:

$$N = \rho_s k_m \left(q_{eq} - q\right) \qquad (3.8)$$

where:

ρ_s is the sorbate-free particle density (kg/m^3).

k_m is the overall mass transfer coefficient (m/s).

q_{eq} is the sorbent loading in equilibrium with a molar fraction of CO_2 y in the gas phase (kg CO_2/kg solids).

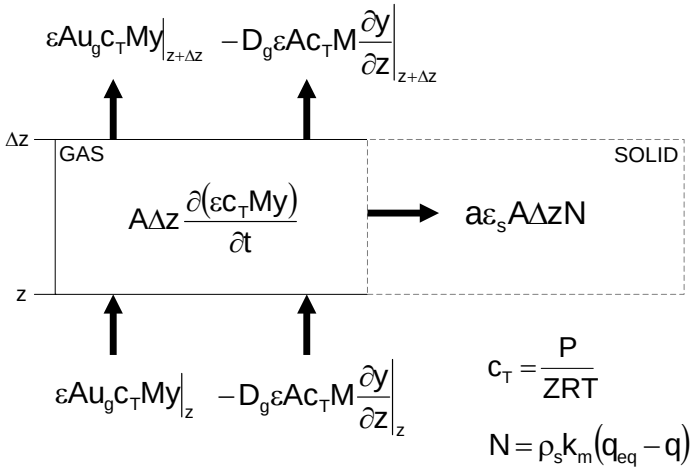

Figure 3.11. Mass balance of gas-phase CO_2 in a differential slice of the adsorber

- *Solid phase* (Figure 3.12):

$$\varepsilon A u_s \rho_s q\big|_z + \left(-D_s \varepsilon_s A \rho_s \frac{\partial q}{\partial z}\right)\Big|_z - \varepsilon A u_s \rho_s q\big|_{z+\Delta z} - \left(-D_s \varepsilon_s A \rho_s \frac{\partial q}{\partial z}\right)\Big|_{z+\Delta z} +$$

Rate of CO_2 in by convection | Rate of CO_2 in by dispersion | Rate of CO_2 out by convection | Rate of CO_2 out by dispersion

$$+ a\varepsilon_s A\Delta z N - A\Delta z \rho_s \frac{\partial(\varepsilon_s q)}{\partial t} = 0 \qquad (3.9)$$

Rate of CO_2 from gas to solid | Rate of CO_2 accumulation

Differentiating equation (3.9) with respect to z yields:

$$\frac{\partial}{\partial z}\left(\varepsilon A u_g q\right) + \frac{\partial}{\partial z}\left(-D_s \varepsilon_s A \frac{\partial q}{\partial z}\right) - \frac{a\varepsilon_s A N}{\rho_s} + A\frac{\partial(\varepsilon_s q)}{\partial t} = 0 \qquad (3.10)$$

where D_s is the *axial dispersion coefficient* for the solid phase (m^2/s).

Definition and units of the other parameters in eq. (3.10) and variables are given in the mass balance for the gas phase.

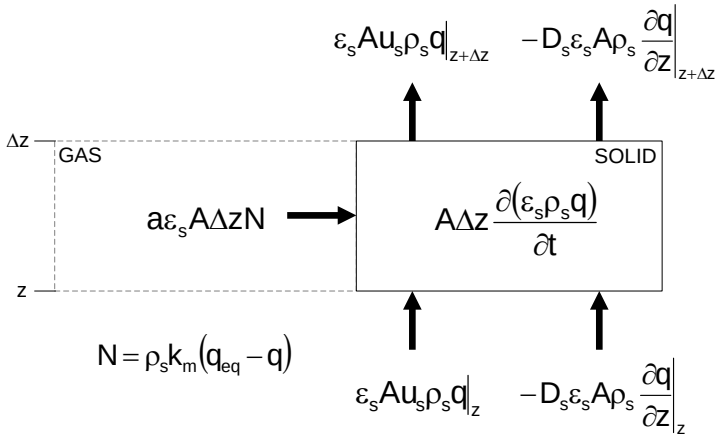

Figure 3.12. Mass balance of solid-phase CO_2 in a differential slice of the adsorber

3.5.1 Simplified adsorber model

A simplified version of the reactor model that allows easy numerical implementation can be obtained under the following assumptions:

- Steady state operation
- Isothermal process
- No pressure drop
- Ideal gas
- One sorbate species (CO_2) only
- Dilute system: no variation of gas velocity due to CO_2 removal from the gas phase
- Constant values of cross-sectional area, solids fraction, and overall mass transfer and dispersion coefficients

Under this set of assumptions the differential equations (3.7) and (3.10) become:

$$-D_g \frac{d^2 y}{dz^2} + u_g \frac{dy}{dz} + \frac{\varepsilon_s}{1-\varepsilon_s} \frac{RT}{P} \frac{\rho_s}{M} a k_m (q_{eq} - q) = 0 \qquad (3.11)$$

$$-D_s \frac{d^2 q}{dz^2} + u_s \frac{dq}{dz} - a k_m (q_{eq} - q) = 0 \qquad (3.12)$$

where the product ak_m is the so-called *lumped* mass transfer coefficient (s^{-1}) and q_{eq} is given by the Langmuir isotherm:

$$q_{eq} = q_{max}\frac{bPy}{1+bPy} \quad ; \quad b = b_0\left(\frac{-\Delta H_{ads}}{RT}\right) \tag{3.13}$$

Equations (3.11) and (3.12) can be integrated between 0 and L applying the boundary conditions for closed systems (Danckwerts, 1953):

$$y\Big|_{z=0} - \frac{D_g}{u_g}\frac{dy}{dz}\bigg|_{z=0} = y_{in} \quad ; \quad \frac{dy}{dz}\bigg|_{z=L} = 0 \tag{3.14}$$

$$q\Big|_{z=z'} - \frac{D_s}{u_s}\frac{dq}{dz}\bigg|_{z=z'} = q_{in} \quad ; \quad \frac{dq}{dz}\bigg|_{z=z''} = 0 \tag{3.15}$$

where:

$z' = 0$, $z'' = L$ if $u_s > 0$ (co-current)

$z' = L$, $z'' = 0$ if $u_s < 0$ (counter-current)

It is important to remark that any results obtained using (3.11) and (3.12) must be taken as a first approximation only, due to the simplifications introduced in the general adsorber model, equations (3.7) and (3.10). Fortunately, most of these simplifications are mild for the systems here studied (for example, pressure drop in high-velocity risers and counter-current adsorbers is low given the low concentration of solids) or tend to become a reality as technology evolves (sorbents highly selective towards CO_2).

3.6 Sensitivity analysis

The information presented and discussed in the previous sections of this chapter is now used to assess the two CFB configurations as CO_2 adsorbers. In the approach followed here, the simplified adsorber model presented in Section 3.5.1 is used in a sensitivity study to identify key variables and parameters and quantify their impact on CO_2 recovery. The model is implemented in Matlab, using the bvp4c solver routine to integrate the set of differential equations (Veneman et al., 2016). As explained below, the model is fed with dimensions and experimental data from the cold models, leaving the lumped mass transfer coefficient as a parameter.

3.6.1 Base case

Table 3.2 presents the values of variables and parameters for the base case from which study cases can be generated.

Both CFB configurations, whose dimensions are those of the cold models (Chapter 4), are fed with the same flue gas stream (Q_{fg} = 625 l/min, 15% vol. CO_2). The solids circulation rate F_s used is 1.3 times the minimum ($F_s = 1.3F_{s,min}$); this value has been chosen arbitrarily between 1.2 and 1.5, according to the rule of thumb in the design of separation processes (Perry et al. (Ed.), 1997). The minimum solids circulation rate is, in turn, function of the lean sorbent loading (q_{in}) and the CFB configuration, as explained in Section 3.4. The value of q_{in} = 0.06 kg CO_2/kg chosen for the base case gives actual solid circulation rates of 0.17 kg/s and 0.036 kg/s for the benchmark and novel CFB configurations respectively (see Figure 3.13).

Fluid dynamics are represented by the solids velocity (u_s), solids fraction (ε_s) and axial dispersion coefficient of both phases (D_g and D_s). The values of u_s and ε_s are calculated using experimental correlations obtained from the cold models (Chapter 5), whereas the values of D_g and D_s have been assumed to be very low for the base case, so plug flow for both phases is obtained. The impact of deviation from plug flow on CO_2 recovery is investigated as part of the sensitivity study.

Table 3.2. Base case for the evaluation of the CFBs as CO_2 adsorbers

	Benchmark CFB	Novel CFB		
		Overall	Riser	Adsorber
Q_{fg} (l/min)	625	625	115	510
y_{in} (mol CO_2/mol)	0.15	0.15	0.15	0.15
q_{in} (kg CO_2/kg)	0.06	0.06	0.06	*
$F_{s,min}$ (kg/s)	0.129	0.0277	**	**
$F_s/F_{s,min}$	1.3	1.3	1.52	1.3
F_s (kg/s)	0.168	0.036	0.036	0.036
L (m)	2.5	**	2.5	0.65
D (m)	0.051	**	0.0265	0.142
V (l)	5.1	11.4	1.4	10.0
V/Q_{fg} (s)	0.49	1.09	0.73	1.18
u_g (m/s)	5.2	**	3.6	0.52
u_s (m/s)	3.0	**	1.4	0.14
L/u_s (s)	0.83	**	1.8	4.6
ε_s	0.012	**	0.016	0.0061
D_g (m^2/s)	10^{-5}	10^{-5}	10^{-5}	10^{-5}
D_s (m^2/s)	10^{-5}	10^{-5}	10^{-5}	10^{-5}

*depending on value of ak_m; **not applicable

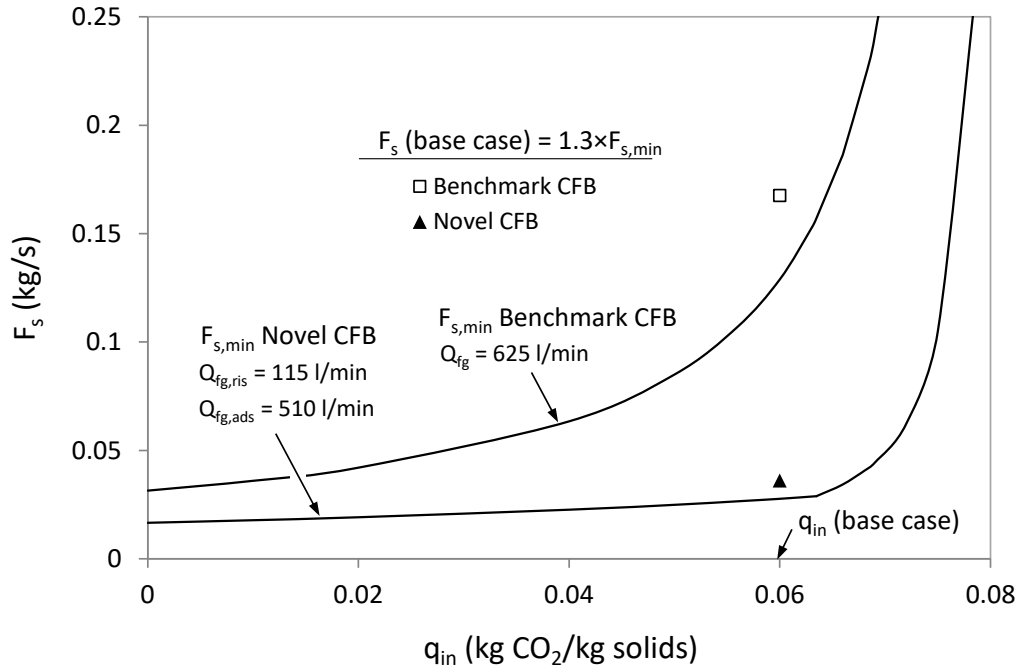

Figure 3.13. Minimum and actual solids circulation rates for the base case

The CO_2 recovery for the base case as a function of ak_m is shown in Figure 3.14. Both CFB configurations are able to achieve CO_2 recoveries higher than 90% at

equilibrium, which is an expected result since the solid circulating rates used are greater than the minimum. It can also be seen that the benchmark configuration requires a lower value of ak_m to attain 90% recovery than the novel, 0.36 s^{-1} and 0.40 s^{-1} respectively, for the given CFB dimensions. This makes the benchmark CFB a better option if the selection is solely based on the criterion of achieving 90% CO_2 recovery at the lowest possible value of ak_m. Other two criteria that can heavily influence the choice of adsorber configuration in the context of this analysis are the equipment size (whether footprint, volume or both) and the solids circulation rate. The volume of the benchmark CFB is less than half of the novel configuration, the height being the same, again making the former a better option. However, the solids circulation rate in the benchmark CFB is 4.7 times that of the novel (0.168 kg/s compared to 0.036 kg/s) as a direct consequence of the equilibrium limitations characteristic of any co-current contactor. This constitutes a huge disadvantage for the overall carbon capture process since the higher the solids circulation rate, the higher the energy demand in the regenerator in the form of sensible heat. Other undesirable consequences of high solids circulation rate are the higher flue gas compression power required and higher erosion of inner walls and internals. It is worth noticing that, in some cases, knowledge of the adsorption equilibrium alone can be sufficient to estimate whether the needed solids circulation rate for a specific separation is above a reasonable value. For instance, for the hypothetic sorbent with isotherm given in Section 3.2, regeneration in pure CO_2 at 124°C would yield a lean sorbent loading of at least 0.075 kg CO_2/kg. The corresponding minimum solids circulation rate is 0.57 kg/s, 17 times the corresponding value for a pure counter-current process. This is a strong argument against the use of a pure co-current adsorber in terms of minimizing the overall energy efficiency of a carbon capture process.

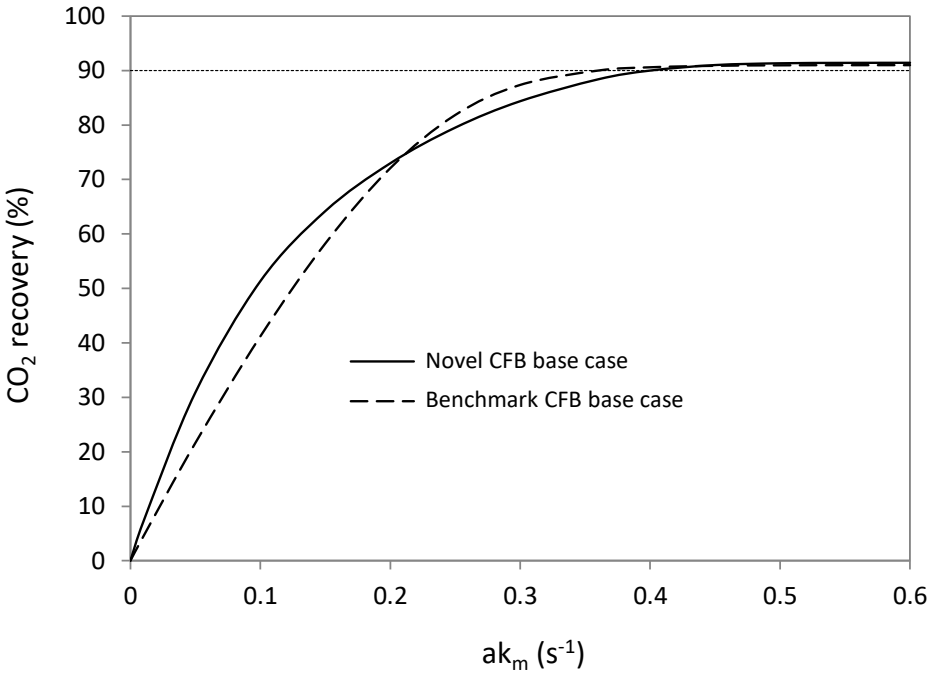

Figure 3.14. CO_2 recovery-ak_m curves for the base case

It can be observed in Figure 3.14 that although the slope of the curve is steeper for the novel CFB at low values of ak_m, its value decreases quickly at $ak_m > 0.15\ s^{-1}$. The slope of the curve corresponding to the benchmark CFB, on the other hand, only flattens appreciably when very close to the equilibrium CO_2 recovery value. This different behaviour stems from the evolution of the corresponding adsorber axial CO_2 profiles with ak_m. Such profiles are plotted in Figure 3.15 for three different values of ak_m. It can be seen how equilibrium is reached in the riser of the novel CFB at low values of ak_m, between 0.1 and 0.2 s^{-1} (corresponding to overall CO_2 recovery values of 50% and 70% respectively). This is not surprising since the high solids-to-gas ratio in the novel CFB riser (the amount of flue gas fed to the riser is just a portion of the total, 18.4% for the base case) implies that a relatively large amount of particle surface area is available for mass transfer. The riser, therefore, does not contribute in achieving higher CO_2 recoveries when increasing the value of ak_m in the novel CFB.

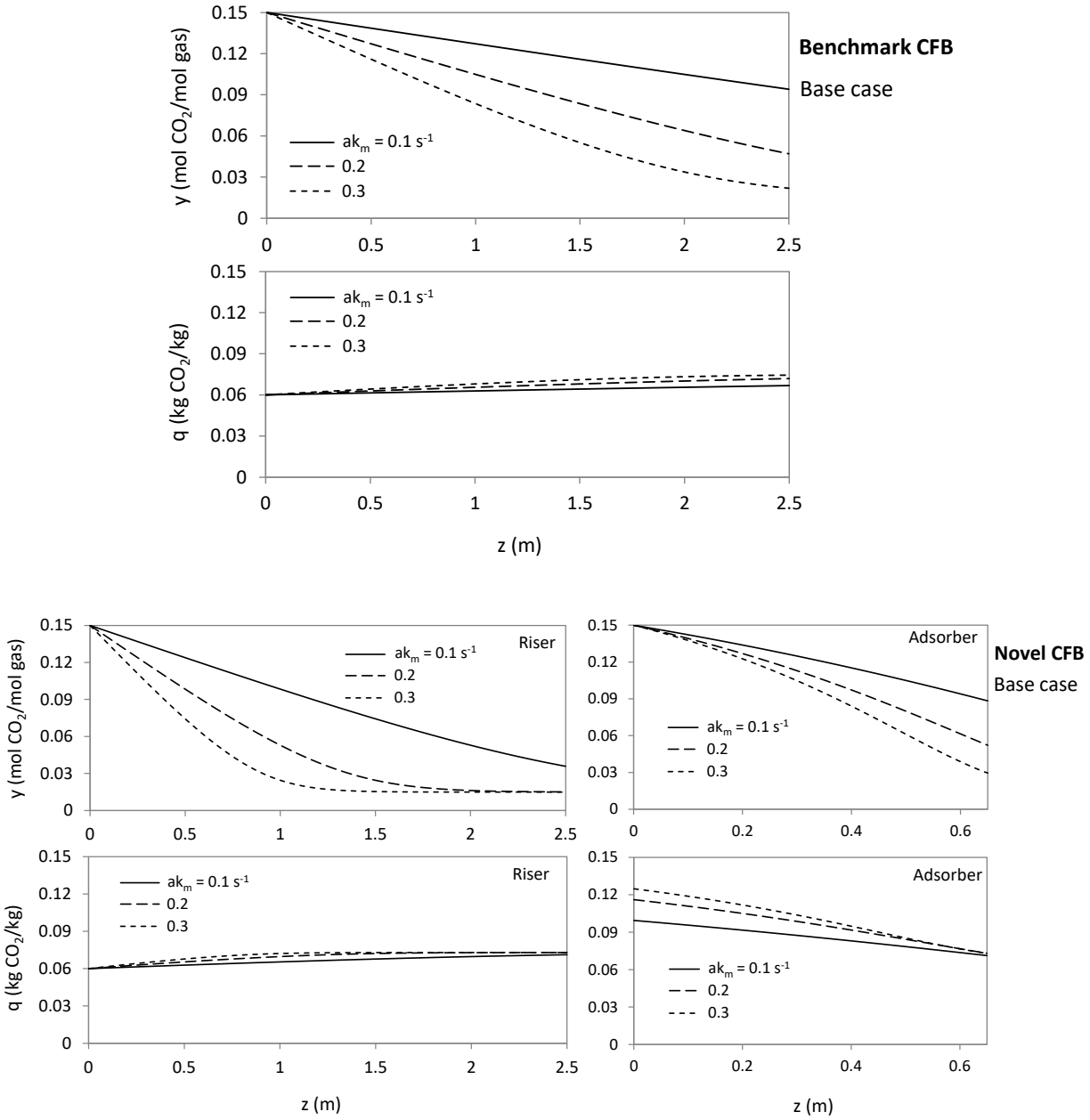

Figure 3.15. CFB axial profiles of gas-phase CO_2 concentration and sorbent loading for the base case

3.6.2 Study cases

Study cases can be derived from the base case to identify and quantify key characteristics of the CFB configurations studied in this work regarding their performance as carbon capture processes. The study cases are presented as recovery-ak_m curves, plotted together with the base case curve so the impact of the varied variable/parameter on the CO_2 recovery can be easily visualised.

- *Impact of CFB length:*

Assessing the impact of the equipment size on CO_2 recovery must be done carefully since fluid dynamics can vary greatly, influencing operability and performance. For example, increasing riser diameter can choke the flow of solids if the gas velocity value falls below a minimum (see Chapter 5). It is therefore paramount that knowledge of fluid dynamics with different system sizes and geometries is gained before predicting process performance. Nevertheless, an attempt to do so is carried out here by calculating CO_2 recoveries for CFBs of different lengths.

It will be assumed that the average solid fractions do not change with equipment length. This is more likely to be true for the counter-current adsorber than for the risers since the former CFB element is fitted with internals that control the flow of solids (this is revealed by particle tracking experiments, see Section 7.6.2).

• Benchmark CFB:

Figure 3.16 shows the CO_2 recovery in function of ak_m for equal length increments of 1.25 m (0.5 times the initial height) from the base case. The gain in CO_2 recovery decreases as the length of the CFB increases. A graph illustrating the length required to achieve 90% recovery as a function of ak_m is presented in Figure 3.19.

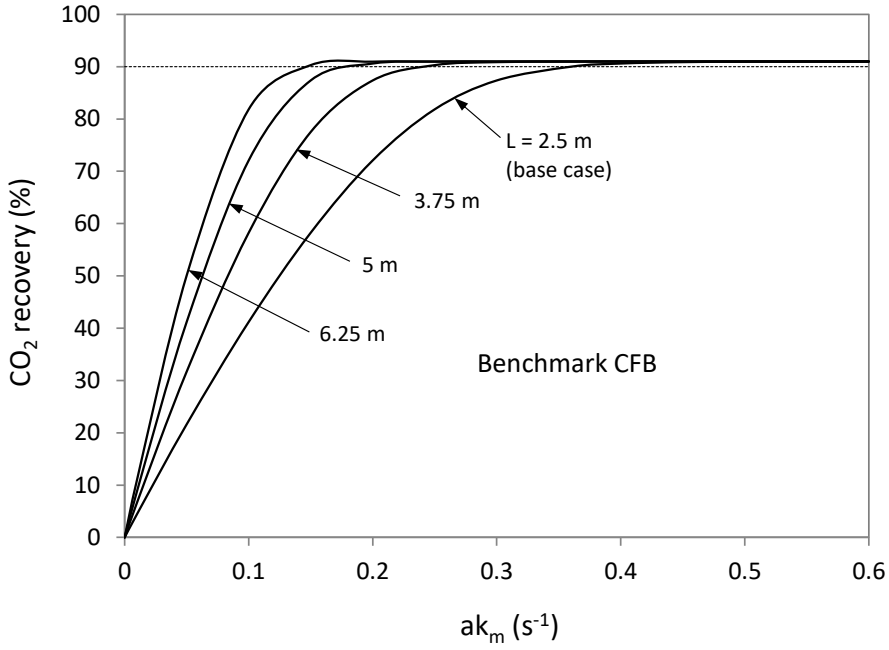

Figure 3.16. CO_2 recovery-ak_m curves showing the impact of changes in equipment length on CO_2 recovery. Benchmark CFB

• Novel CFB:

In the novel CFB, changes in the length of the riser and the counter-current adsorber are more constrained than for the benchmark due to their mutual spatial arrangement. In particular, the maximum length of the adsorber is limited to the distance between the riser top and the regenerator top. However, the study of both riser and adsorber can be done separately and later combined.

Figure 3.17 shows CO_2 recovery-ak_m curves for the novel CFB when only the riser length is changed. The riser plays an auxiliary role as a CO_2 adsorber in this CFB configuration, so the impact on the overall CO_2 recovery can be visualized by using the theoretical limits of zero and infinite length. In case of zero length, the portion of flue gas fed to the riser is untreated (bypassed from inlet to outlet) and mixed with the adsorber outlet gas stream. The overall CO_2 recovery suffers as a consequence a penalty that depends on the fraction of flue gas fed to the riser. This fraction is 18.4% of the total for the base case, which, if bypassed, would incur a CO_2 recovery drop of 15 percentage points, from 91.4% to 76.5%. On the other hand, using a riser of

infinite length would not bring any benefits in CO_2 recovery (refer to the discussion about the adsorber axial profiles presented in Figure 3.15).

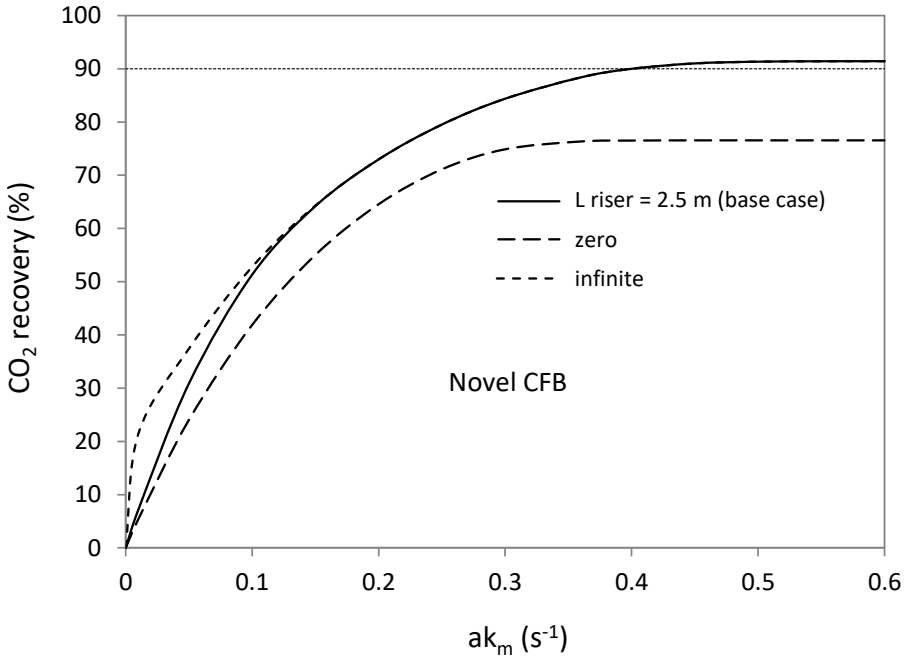

Figure 3.17. CO_2 recovery-ak_m curves showing the impact of changes in equipment length (riser) on CO_2 recovery. Novel CFB

Figure 3.18 shows CO_2 recovery-ak_m curves for the novel CFB when only the length of the counter-current adsorber is changed. The length increment used is 0.17 m, the height of an adsorber module of the cold model (see Section 4.3.3). Like for the benchmark configuration, gains in CO_2 recovery for a given value of ak_m are progressively smaller as the total length increases. It is therefore increasingly difficult, in terms of adsorber length needed, to achieve 90% CO_2 recovery. This is clearly visualised in Figure 3.19. The counter-current adsorber requires around just a third of the length of the benchmark CFB, although values can get prohibitively high when $ak_m < 0.05\ s^{-1}$. As an example of application, the counter-current adsorber is estimated to require a length of 7.8 m if $ak_m = 0.034\ s^{-1}$, value obtained for the counter-current adsorber of Veneman et al. (2016). This value was calculated using the authors' experimental data in the adsorber model presented in this work.

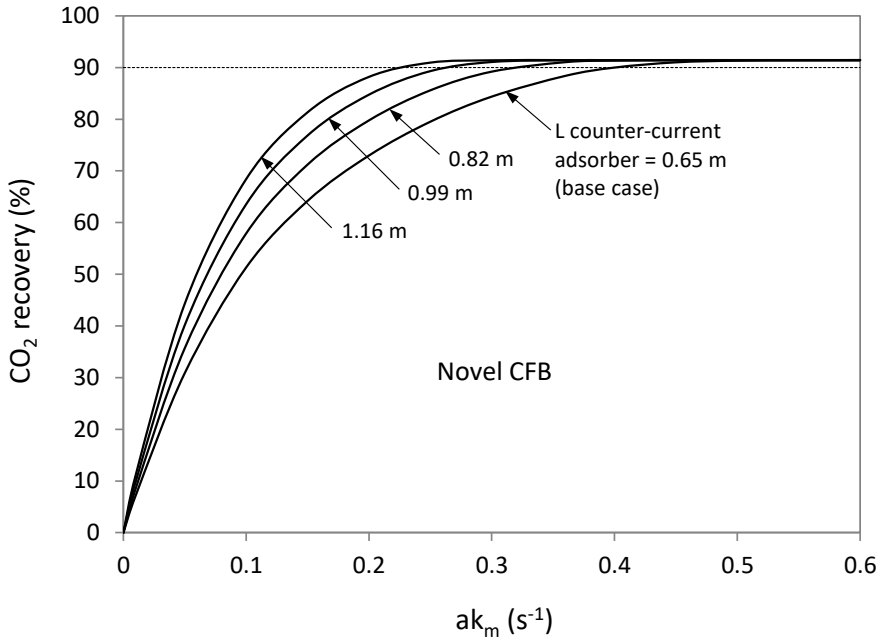

Figure 3.18. CO_2 recovery-ak_m curves showing the impact of changes in equipment length (adsorber) on CO_2 recovery. Novel CFB

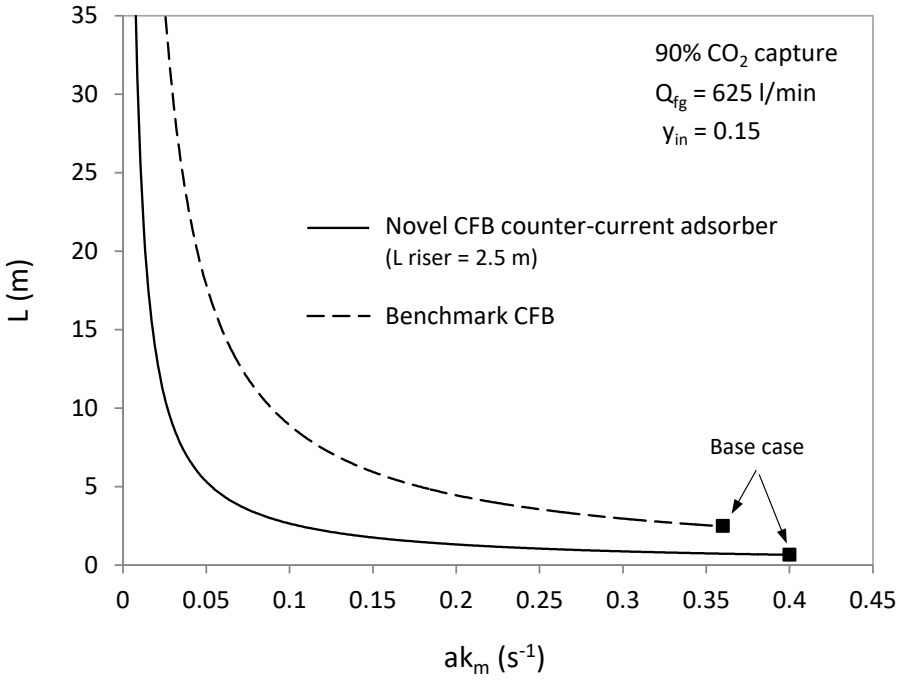

Figure 3.19. Equipment length as a function of ak_m

- *Impact of solids circulation rate:*

Figure 3.20 and Figure 3.21 show the impact of changing the solids circulation rate on the CO_2 recovery in each of the CFB configurations. Increasing the solids circulation rate has a positive impact in both systems, bringing down the value of ak_m at which 90% CO_2 recovery is achieved. The impact on recovery seems to be inversely proportional to the absolute value of the solids flow rate, and therefore the novel CFB benefits more than the benchmark from the same increment in the solids flow rate. It can be argued that this is due to a larger relative increase in the driving force for adsorption (coming from the flattening of the solids loading axial profile) and mass transfer area (due to an increase in solids fraction) at low solids flow rates.

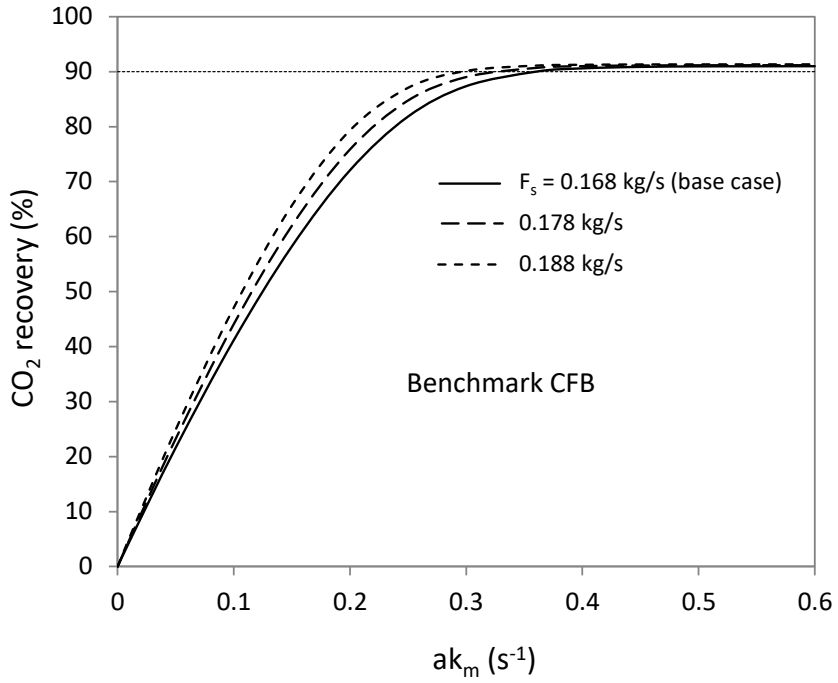

Figure 3.20. CO_2 recovery-ak_m curves showing the impact of changes in solids circulation rate on CO_2 recovery. Benchmark CFB

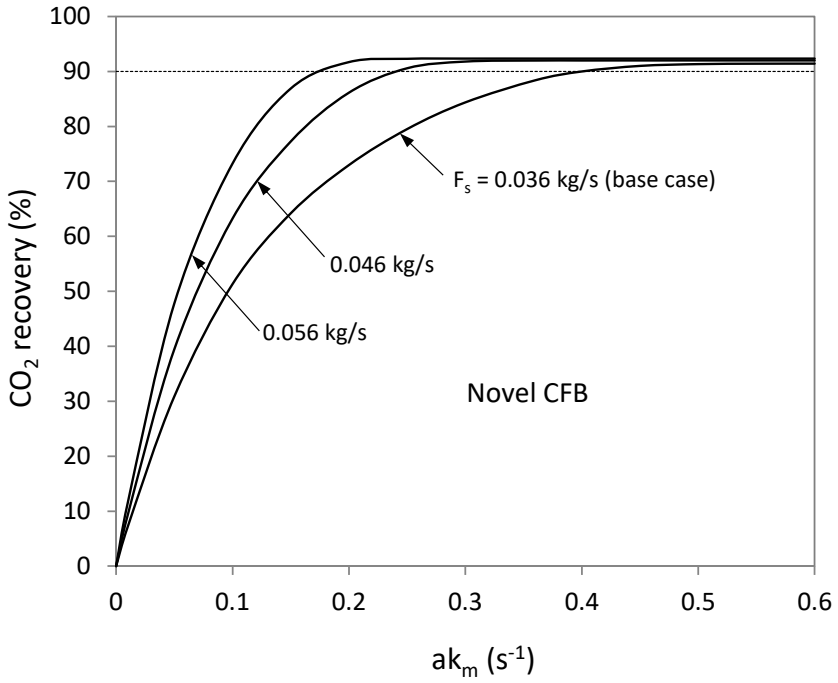

Figure 3.21. CO_2 recovery-ak_m curves showing the impact of changes in solids circulation rate on CO_2 recovery. Novel CFB

- *Impact of fraction of flue gas fed to the riser (novel CFB only):*

The main function of the riser in the novel CFB configuration presented in this work is to transport the solids from the regenerator to the counter-current adsorber, and therefore the amount of flue gas fed to the riser is primarily decided upon operational considerations. However, its secondary role as a co-current CO_2 adsorber needs to be properly considered to make sure the overall performance of the system is not compromised. The value of the fraction of flue gas fed to the riser is chosen so: 1) the operating conditions lie within the operational window, and 2) the solids flow rate is higher than the minimum. This is illustrated in Figure 3.22.

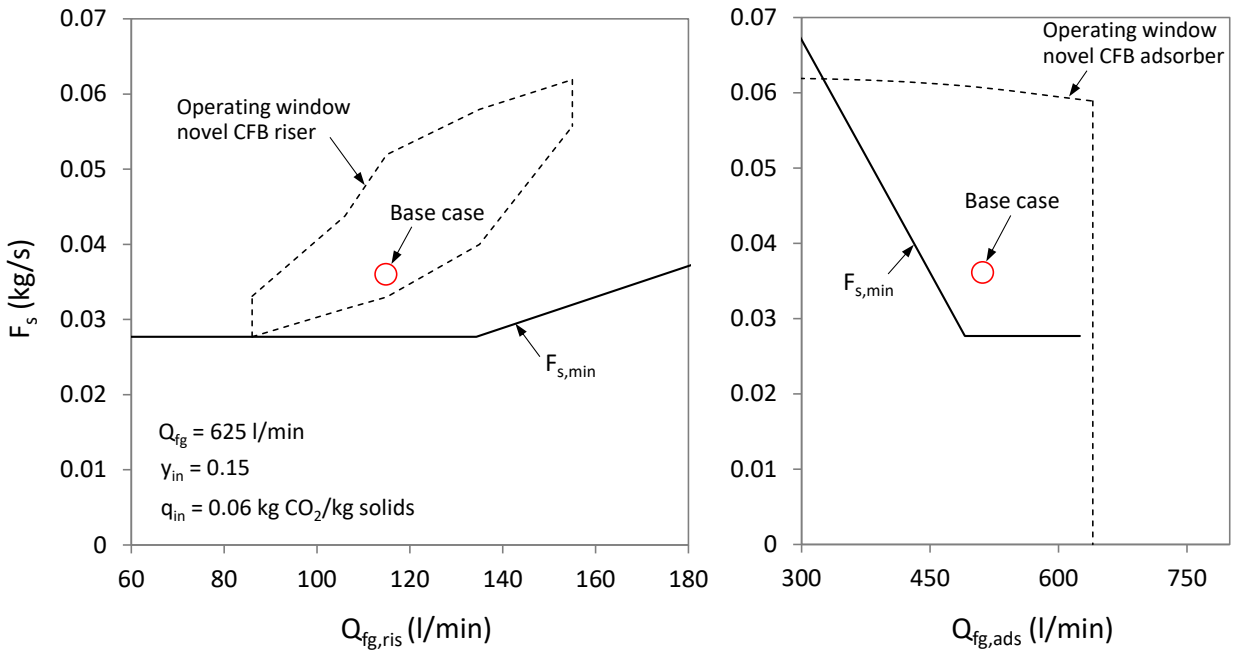

Figure 3.22. F_s-Q_{fg} diagrams showing the position of the base case with respect to the operating windows and minimum solids circulation rate line of the novel CFB. The CFB operating windows are presented and described in Chapter 5

Figure 3.23 shows the recovery-ak_m curves for the base case and two other values of fraction of flue gas fed to the riser. The values chosen for this case study are 0/625 and 150/625. These values are not practicable in the actual cold model rig while keeping constant the solids circulation rate (such operating conditions lie out of the operating window), but perfectly possible physically; a fraction 0/625 would be equivalent to feeding the whole of the flue gas to the counter-current adsorber, solids circulation then achieved by using a carrier gas or a mechanical conveying device. As it can be seen in the graph, the curve corresponding to a fraction 0/625 represents an upper bound for CO_2 recovery under the conditions of the base case, evidencing the superior performance of the counter-current adsorber compared to any co-current/counter-current combination.

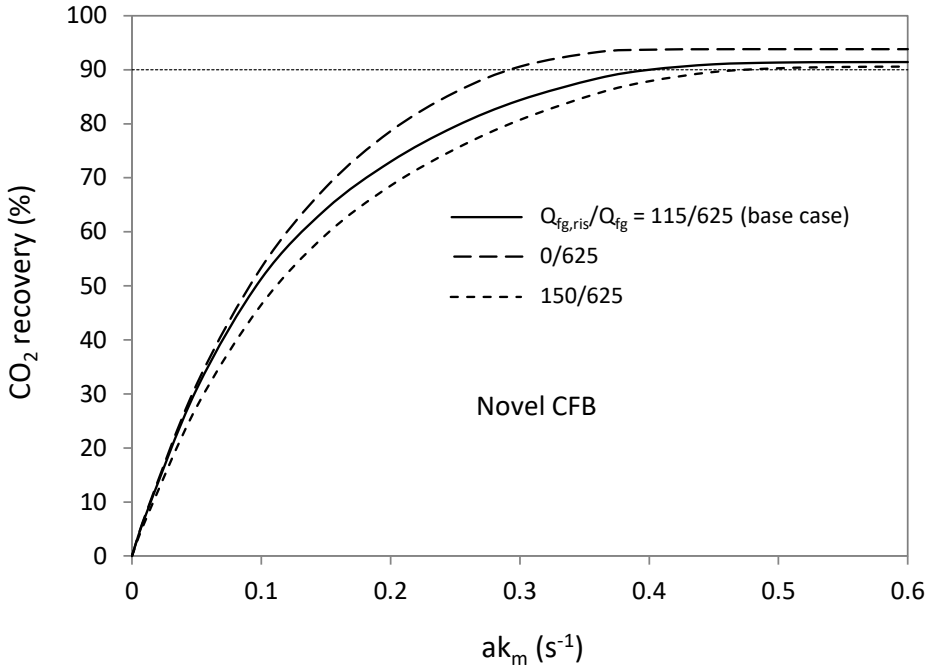

Figure 3.23. CO_2 recovery-ak_m curves showing the impact of changes in the fraction of flue gas fed to the riser on CO_2 recovery (novel CFB only)

- *Impact of axial dispersion:*

The effect of axial dispersion in either the solid or gas phase on the CO_2 recovery can be explored by modifying the values of the dispersion coefficients D_s and D_g in the adsorber model. Plug flow was considered for the base case by giving a very small number to these coefficients (10^{-5} m^2/s).

Figure 3.24 shows the CO_2 recovery for the base case as a function of the axial Péclet number. Such number is defined as:

$$Pe = Lu/D \tag{3.16}$$

where L is the length of the system, u the linear velocity and D the axial dispersion coefficient. In the context of this study, a Péclet number for each phase applies:

$$Pe_s = Lu_s/D_s \quad \text{for the solid phase} \tag{3.17}$$

$$Pe_g = LU_g/D_g \quad \text{for the gas phase} \tag{3.18}$$

For the benchmark CFB, solids dispersion at the conditions of the base case causes a negligible drop in CO_2 recovery: at state of complete mixing ($Pe_s = 0$), the CO_2 recovery drops 0.8 percentage points, from 90% to 89.2%. Looking at the CO_2 axial profiles (Figure 3.15), it can be observed that the sorbent loading does not vary much along the CFB, and therefore it is already similar to the flat profile of a well-mixed system. Gas dispersion, however, causes an initially much steeper gas CO_2 concentration to flatten, reducing the overall driving force for adsorption and therefore the CO_2 recovery in a higher degree than mixing of the solid phase. The CO_2 recovery for complete mixing of the gas phase in the benchmark CFB can drop more than 11 percentage points (from 90% to 78.6%).

Dispersion of both gas and solids in the riser of the novel CFB has a negligible impact (in conditions of the base case) in the overall CO_2 recovery of the novel CFB configuration, even in case of complete mixing of both phases. This is due to a combination of factors given its auxiliary role as a CO_2 adsorber: a) a large solids-to-gas ratio; b) a small portion of the total flue gas to treat, and c) a sufficient length.

The novel counter-current adsorber, on the other hand, shows a higher sensitivity to axial dispersion than the CFB risers due to its lower solids-to-gas ratio. The combined effect of dispersion on both phases at $Pe_s = Pe_g = 25$ is already enough to cause a drop in the overall CO_2 recovery of 2.2 percentage points, and 5.2 percentage points if $Pe_s = Pe_g = 10$. If both phases are well mixed, the CO_2 recovery drops 24 percentage points, from 90% to 66%.

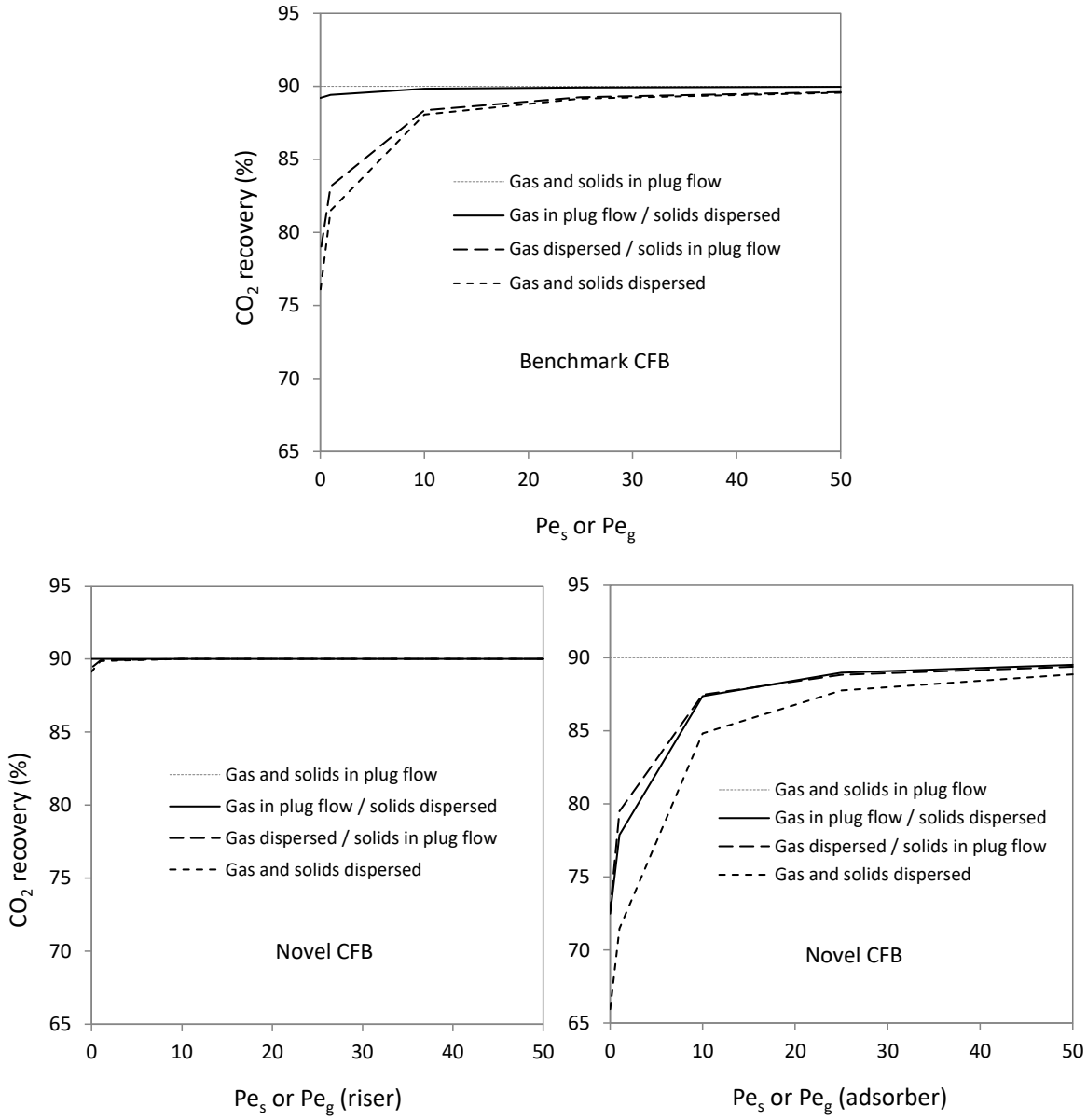

Figure 3.24. CO_2 recovery as a function of the axial Péclet number of both gas and solid phases

3.7 Conclusions

The thermodynamic-kinetic evaluation of the CFB configurations carried out in this chapter shows the clearly superior performance of the novel CFB system here presented with respect to a conventional (benchmark) co-current CFB as a TSA carbon capture process. Knowledge of the adsorption equilibrium alone is sufficient to realise that the latter system may incur a higher energy consumption associated to minimum solids circulation rates several times higher than for counter-current systems. This is especially the case when low lean sorbent loadings cannot be achieved due to temperature limitations in the regeneration step and/or regeneration in pure CO_2.

The sensitivity analysis using a simplified adsorber model and operating conditions, dimensions and fluid dynamics from cold model CFB rigs allowed the quantification of the impact of several variables/parameters on the CO_2 recovery. The key findings of such analysis are the following:

- Increase in performance (higher CO_2 recovery for a given value of the lumped mass transfer coefficient, ak_m) can be achieved in both CFB configurations by increasing either the solids circulation rate or the length of the equipment. An increase in solids circulation rate is not advisable for the benchmark CFB since CO_2 recovery is less sensitive to the (already high) solids circulation rate, but would be much more noticeable in the novel CFB.

- If an increase in equipment length is chosen to achieve higher recoveries, this is done for the novel CFB by increasing the length of the counter-current adsorber; the riser length will increase accordingly as dictated by the spatial arrangement of both elements. However, the contribution of the riser to the increment in CO_2 recovery is much more limited than that of the counter-current adsorber, and in fact it does not contribute at all when the goal CO_2 recovery is higher than about 70%.

- At the operating conditions of the base case and 90% CO_2 capture, ak_m values higher than 0.05 s^{-1} are required for equipment length to be smaller than 15 m (benchmark CFB riser) and 5 m (novel CFB counter-current adsorber). Lower

values of ak_m would most likely lead to excessively long pieces of equipment, especially in the case of the benchmark CFB (see Figure 3.19).

- The fraction of flue gas fed to the riser in the novel CFB should be as low as possible to benefit from the superior performance of the counter-current adsorber. However, a minimum value is needed for the circulation of solids at the required rate within operational constraints.

- Adequate design of the counter-current adsorber is required to achieve flow conditions as close as possible to plug flow, given the high sensitivity of overall CO_2 recovery with the degree of back-mixing of both phases in this CFB element. On the other hand, process performance is insensitive to axial dispersion of either phase in the novel CFB riser; this is a very convenient result since high solids and gas axial dispersion are expected in the riser as it will be shown in Chapters 6 and 7.

4 Description of experimental equipment

4.1 Introduction

In this chapter the materials, instruments and methods that constitute the experimental CFB cold model systems used in this work are described. The solids representing the CO_2 sorbent in the real carbon capture process are characterised first (Section 4.2). The cold model CFB rigs are described next (Section 4.3) in terms of materials of construction, dimensions, geometry and design features. The instrumentation installed for the measurement of air flow rates and pressures at different points of the CFBs and the data acquisition system are described in Section 4.4. The technique used for the measurement of the solids circulation rate is described in Section 4.5. Finally, the measures implemented against static electricity generation and accumulation in the CFB rigs are described in Section 4.6.

4.2 Solids characterisation

The particulate solid used in this work is a silica sand that was available from previous research works in bubbling fluidised beds (Glass et al., 2009). A microscope image of a sample of particles is shown in Figure 4.1.

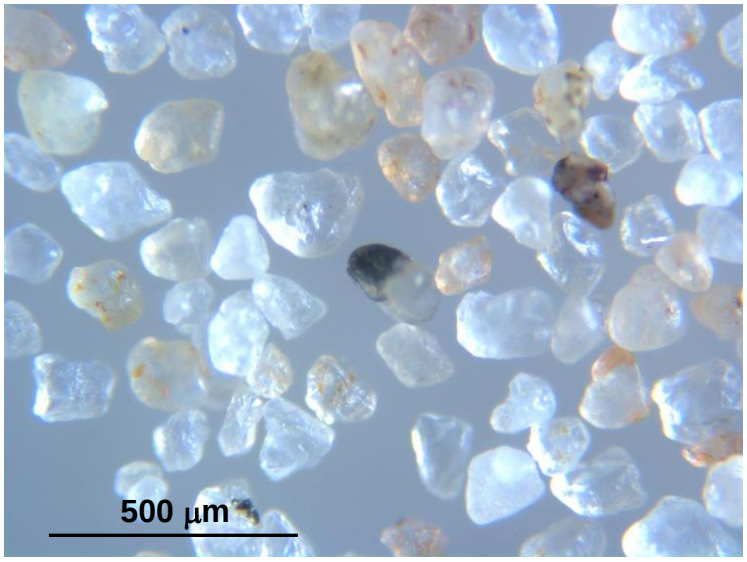

Figure 4.1. Microscope image of the particulate solid (silica sand) used in this work

Table 4.1 presents the solids properties of concern in this work. The methods and calculations used in the solids characterisation are described next.

Table 4.1. Characteristics of the solids used in this work

Sand		Denomination
d_p	152	Mean particle size (μm)
ρ_s	2650	Particle density (kg/m^3)
B		Geldart classification group
ϕ_s	0.85	Particle sphericity
$U_{g,mf}$	0.033	Minimum fluidising velocity (m/s)
u_t	1.0	Terminal velocity (m/s)
$\varepsilon_{s,mf}$	0.54	Volumetric fraction at minimum fluidising conditions
$\varepsilon_{s,c}$	0.60	Volumetric fraction of compacted bed
$\varepsilon_{s,l}$	0.56	Volumetric fraction of loose bed

- *Particle size distribution, mean particle size:*

The particle size distribution (Figure 4.2) was determined by sieving. A sample of ~100 g of sand was placed in the top sieve of a stack with nominal openings of 500 μm, 300 μm, 250 μm, 150 μm and 106 μm, and shaken for 10 min using a lab shaker. The mean particle size is defined to yield the same total surface area in the sample (Kunii and Levenspiel, 1991), equation (4.1):

$$\text{Mean}\, d_p = \frac{1}{\sum w_i / d_{p,i}} \tag{4.1}$$

where w_i is the normalized weight of the fraction i of the sample with a mean particle size $d_{p,i}$. The value of $d_{p,i}$ is calculated as the average opening size each two consecutive sieves.

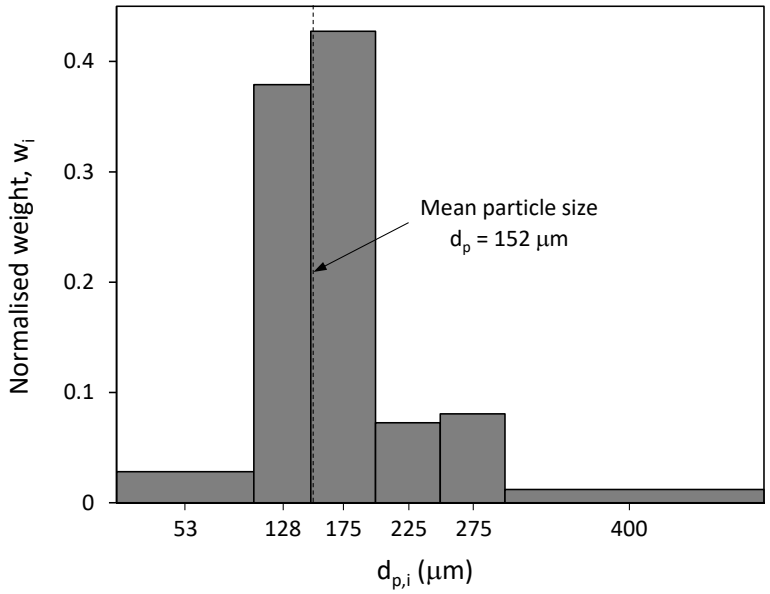

Figure 4.2. Particle size distribution and mean particle size of the solids used in this work

- *Particle density, ρ_s:*

The particle density was determined by water displacement. A weighed amount of sand (~50 g) was slowly poured into a 100-ml graduated cylinder initially containing a weighed amount of water at room temperature. The cylinder was then topped up with a weighed amount of water to a total of 70.0 ml. This procedure was carried out three times and results averaged. The water was assumed to have a density of 1000 kg/m^3.

- *Geldart classification group:*

The solids fall into the B group of the Geldart classification (Geldart, 1973), as it can be seen in the particle size – density diagram in Figure 4.3. Group B solids typically present good fluidising behaviour. The formation of bubbles occurs from the onset of the fluidised regime, which can grow large and promote good mixing of particles (Kunii and Levenspiel, 1991).

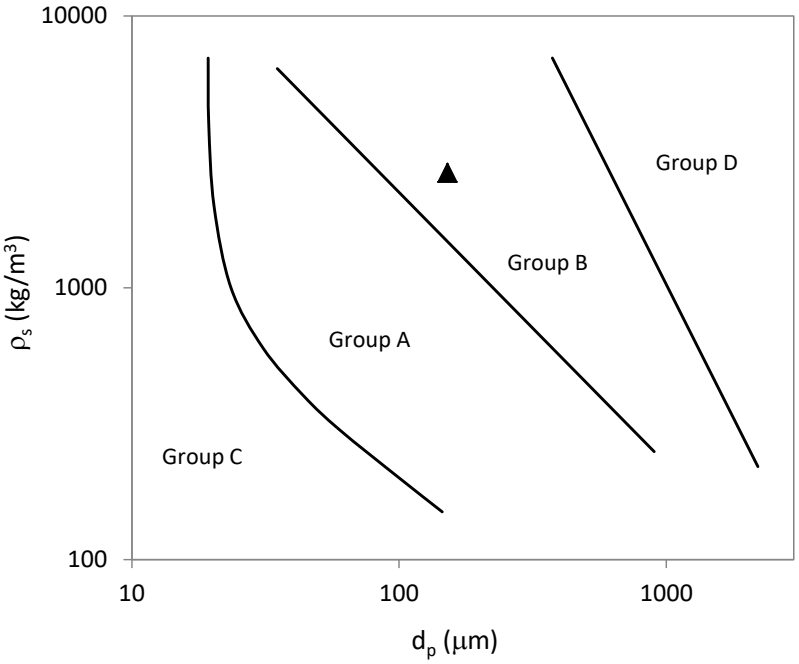

Figure 4.3. Location of the solids used in this work (solid triangle) in the Geldart classification diagram (adapted from Geldart, 1973)

- *Pressure drop – gas velocity diagram:*

A small fluidised bed setup (sketched in Figure 4.4) 52 mm ID was built to determine the fluidisation characteristics of the sand. A sand sample of 400.0 g was poured into the vessel (open to air) to form a bed with an initial height of 11.8 cm. The pressure drop – gas velocity diagram shown in Figure 4.5 was obtained by recording the pressure drop of the sample while the air flow rate was slowly increased from zero to a value where the sample was fully fluidised (vigorous bubbling), and returned back to zero. The air flow rate was measured with a calibrated orifice flow meter, and the pressure drop of the sample (after subtraction of the pressure drop of the gas distributor) was determined with a differential pressure transducer. Both instruments, which are described in Section 4.4, are the same as those used to measure air flow rates and pressures in the CFB rigs.

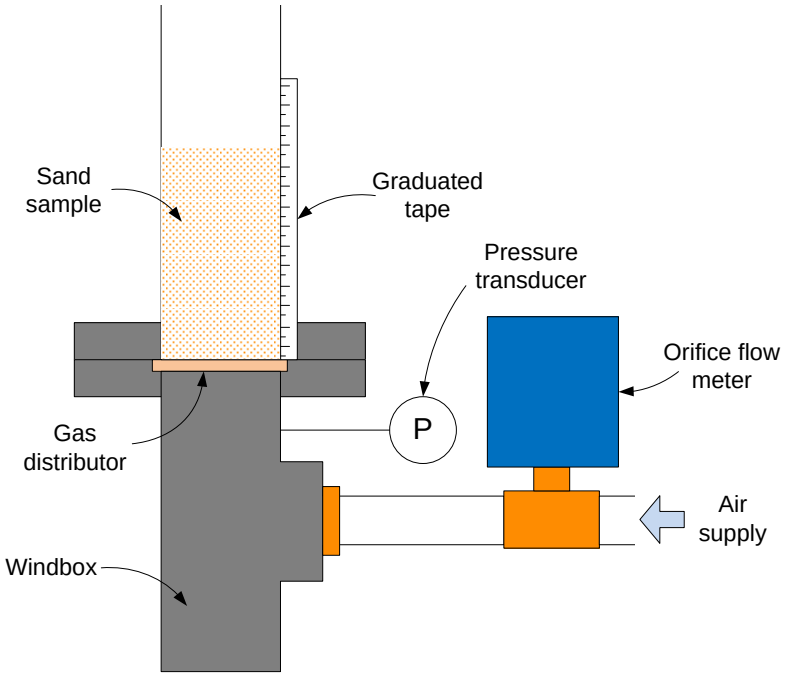

Figure 4.4. Setup for determining the fluidisation characteristics of the solids used in this work

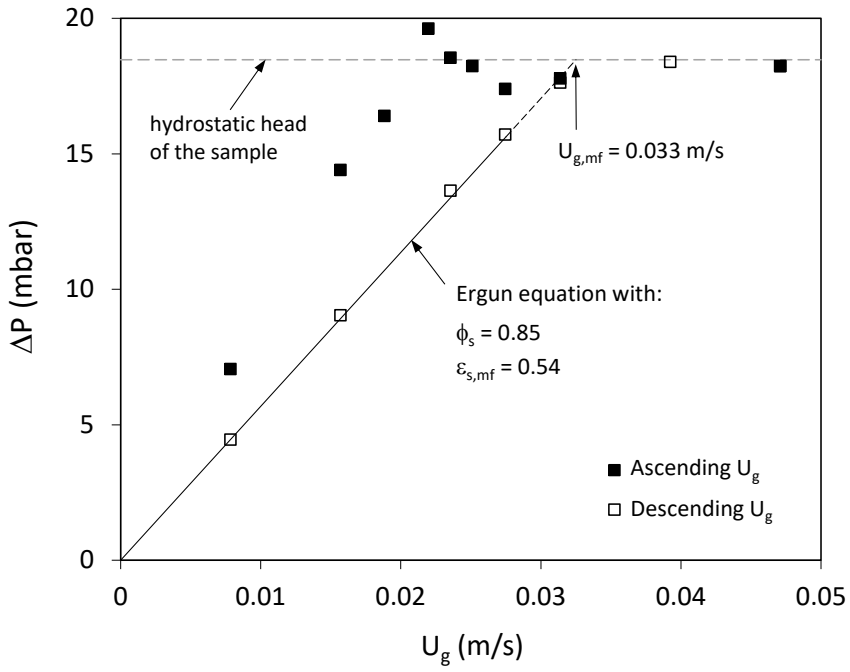

Figure 4.5. Pressure drop – superficial gas velocity diagram for the solids used in this work

- *Minimum fluidisation velocity, $U_{g,mf}$:*

It can be determined from Figure 4.5 as the intersection between the horizontal branch of the curve (bed fully fluidised) and the straight line corresponding to the fixed bed after defluidisation.

- *Volumetric fraction at minimum fluidising conditions, $\varepsilon_{s,mf}$:*

From the definition of volumetric fraction of solids:

$$\varepsilon_s = \frac{\text{volume of solids in the bed}}{\text{bed volume}} = \frac{\text{mass of particles in the bed/particle density}}{\text{bed volume}} = \frac{m_s/\rho_s}{V} \tag{4.2}$$

Applying (4.2) to the bed of solids used to determine the graph in Figure 4.5:

$$\varepsilon_{s,mf} = \frac{m_s/\rho_s}{h_{mf} A} \tag{4.3}$$

where h_{mf} the height of the bed after defluidisation and A the bed cross-sectional area.

- *Particle sphericity, ϕ_s:*

The effective value of ϕ_s for pressure drop purposes can be calculated using the Ergun equation for a fixed bed whose particle volumetric fraction is known (Kunii and Levenspiel, 1991). The Ergun equation for the just defluidised bed of solids in Figure 4.5 is:

$$\frac{\Delta P}{h_{mf}} = 150\frac{\varepsilon_{s,mf}^2}{(1-\varepsilon_{s,mf})^3}\frac{\mu U_g}{(\phi_s d_p)^2} + 1.75\frac{\varepsilon_{s,mf}}{(1-\varepsilon_{s,mf})^3}\frac{\rho_g U_g^2}{\phi_s d_p} \tag{4.4}$$

where μ and ρ_g are the air viscosity and density respectively. The value of ϕ_s is obtained by fitting equation (4.4) to the defluidisation data in Figure 4.5.

- *Solids volumetric fraction of compacted and loose beds, $\varepsilon_{s,c}$ and $\varepsilon_{s,l}$:*

The values of $\varepsilon_{s,c}$ and $\varepsilon_{s,l}$ were calculated from the volume occupied by a weighed sample of solids in a slender graduated cylinder (25 mm ID) and applying equation (4.2). The loose bed was formed by slowly pouring the sand into the cylinder, whereas to obtain the compacted bed the cylinder was gently tapped until the bed volume could not be further reduced. Note that the solids fraction of a loose bed is higher than that at minimum fluidising conditions (see Table 4.1).

- *Particle terminal velocity, u_t:*

It is calculated using equations (4.5) and (4.6) (Haider and Levenspiel, 1989, cited in Kunii and Levenspiel, 1991):

$$u_t = \left[\frac{18}{(d_p^*)^2} + \frac{2.335 - 1.744\phi_s}{(d_p^*)^{0.5}}\right]^{-1}\left[\frac{\rho_g^2}{\mu(\rho_s - \rho_g)g}\right]^{-1/3} \qquad 0.5 < \phi_s < 1 \tag{4.5}$$

$$d_p^* = d_p\left[\frac{\rho_g(\rho_s - \rho_g)g}{\mu^2}\right]^{1/3} \tag{4.6}$$

4.3 Description of the cold model CFB rigs

The two cold model CFB rigs studied in this work are separated entities, and therefore are described individually. The regenerator, however, is a shared element and is described first. The descriptions given in this chapter concern the physical features of the pieces of equipment. The operating characteristics of the systems are described in Chapter 5.

4.3.1 Regenerator

The hardware used in this work as the regenerator is a cylindrical container that originally was designed as a setup for a bubbling fluidised bed (Glass et al., 2009). As such, it initially featured a windbox, a horizontal bed support plate, a main body and a lid as its main components. The main body is of modular design, allowing flexibility in body height and number and position of inlet/outlet ports and internals,

like banks of horizontal heat exchange tubes. All parts are made of Perspex except the support plate, which is made of steel.

The configuration used in this work contains parts from the original setup, whereas others were modified or created for this application. The main components of the regenerator as used here are the following (see Figure 4.6 and Figure 4.7 for reference):

- A windbox, fitted with a pressure tap and an air inlet port.
- A cylindrical main body 279 mm ID and 744 mm high, made up of several modules of different heights, with a horizontal solids outlet pipe at the bottom module.
- A lid fitted with a vertical solids inlet pipe, an air outlet port (fitted with a filter bag, described in Section 4.3.3) and a filling port.
- A Valterra slide valve (manually operated) 38 mm ID, fitted to the upper end of the solids inlet pipe.
- A set of 6 “fingers” simulating horizontal heat exchange tubes, located roughly half way along the regenerator main body and extending most of its cross section. The fingers diameter and pitch are 20 cm and 43 mm respectively.
- An inclined (45°) air distributor made out of a 6-cm thick porous plastic sheet. More details are given below.
- A nozzle for injection of lube air into the solids outlet pipe. More details are given below.

- *Regenerator air distributor:*

It is a 6-cm thick porous polyethylene sheet from SPC Technologies, reference PE10060, inclined with an angle of 45 degrees. It is placed in the regenerator so the lowest point of the sheet lies at the bottom of the solids outlet pipe. The initial reasoning behind using an inclined air distributor was trying to promote a narrower solids residence time distribution by creating a funnel-like path towards the outlet pipe (particle tracking experiments determined that the effect achieved was actually the opposite, see Chapter 7). Most of the plastic porous sheet is covered on both sides

by aluminium adhesive tape, in such a way that only a section 10 cm wide (measured along the sheet long axis) at its lower side was left open to gas flow. This open section acts as the actual gas distributor, while the rest of the plastic sheet serves merely as the bed support (no aeration through). This was a necessary measure to prevent the air flow from entering the bed only through the shallowest side (Figure 4.8). The empty volume created between the inclined plastic sheet and the windbox was filled with a piece of upholstery high-density foam, which is supported on a horizontal steel plate. This steel plate allows the air flow through holes made only underneath the permeable section of the plastic sheet (Figure 4.9). The absence of such foam block is detrimental for the gas residence time distribution experiments as the empty volume left underneath the porous plastic sheet would create a "trap" for the tracer gas.

- *Lube air nozzle:*

A nozzle to inject so-called lube air directly into the solids outlet pipe was installed with the aim of promoting the overall solids flow. The nozzle is inserted into the regenerator main body right above the solids outlet pipe and then redirected bending it 90 degrees twice (Figure 4.9). The tip of the nozzle lies close to the bottom of the pipe, sticking 3 mm into it from the regenerator inner wall. This was meant to prevent the lube air from flowing into the regenerator main body. The flow pattern of lube air in the solids outlet pipe and its influence in the operation of the CFB rigs are described in detail in Chapter 5.

Figure 4.6. Regenerator front view (left) and 3D CAD model (right)

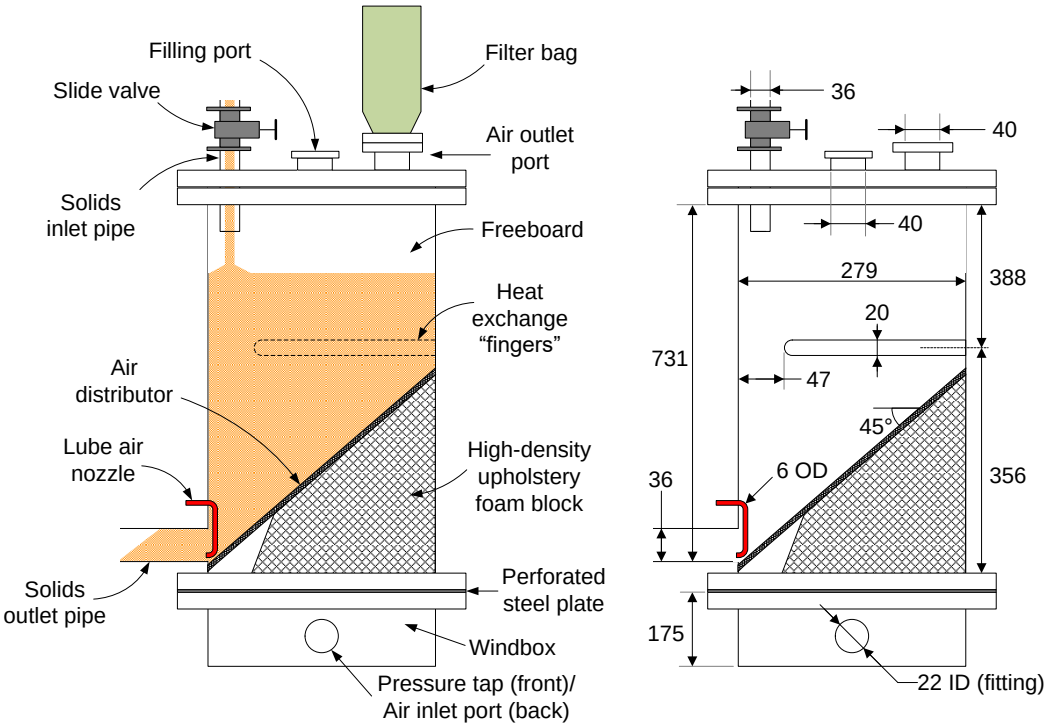

Figure 4.7. Regenerator main components (left) and dimensions (right). Dimensions in mm. Drawings not to scale

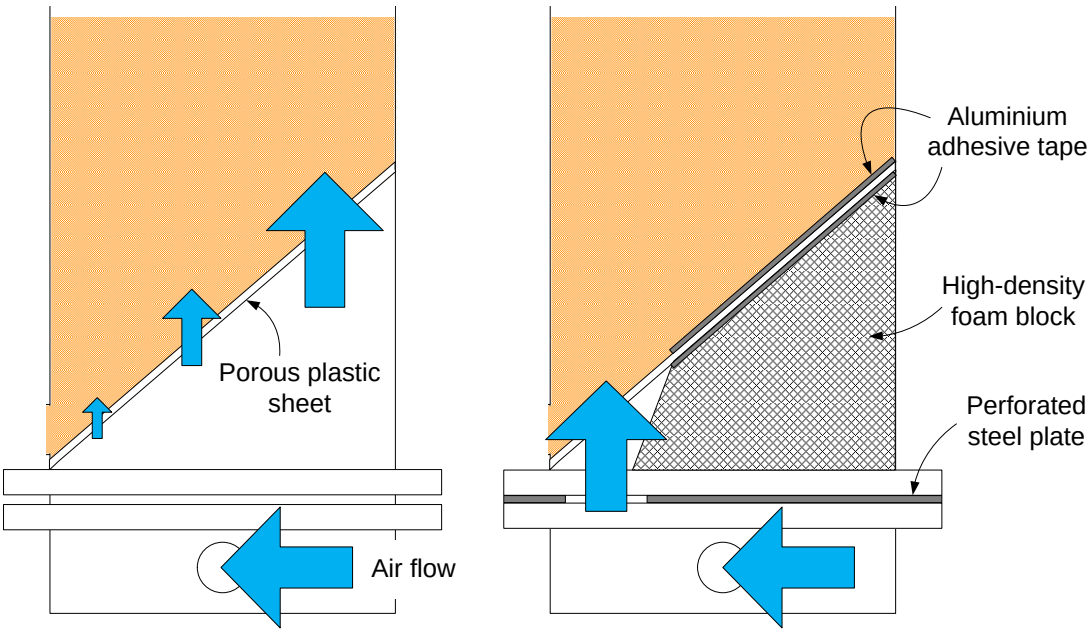

Figure 4.8. Air flow maldistribution due to inclination of air distributor (left) and measures to prevent it (right)

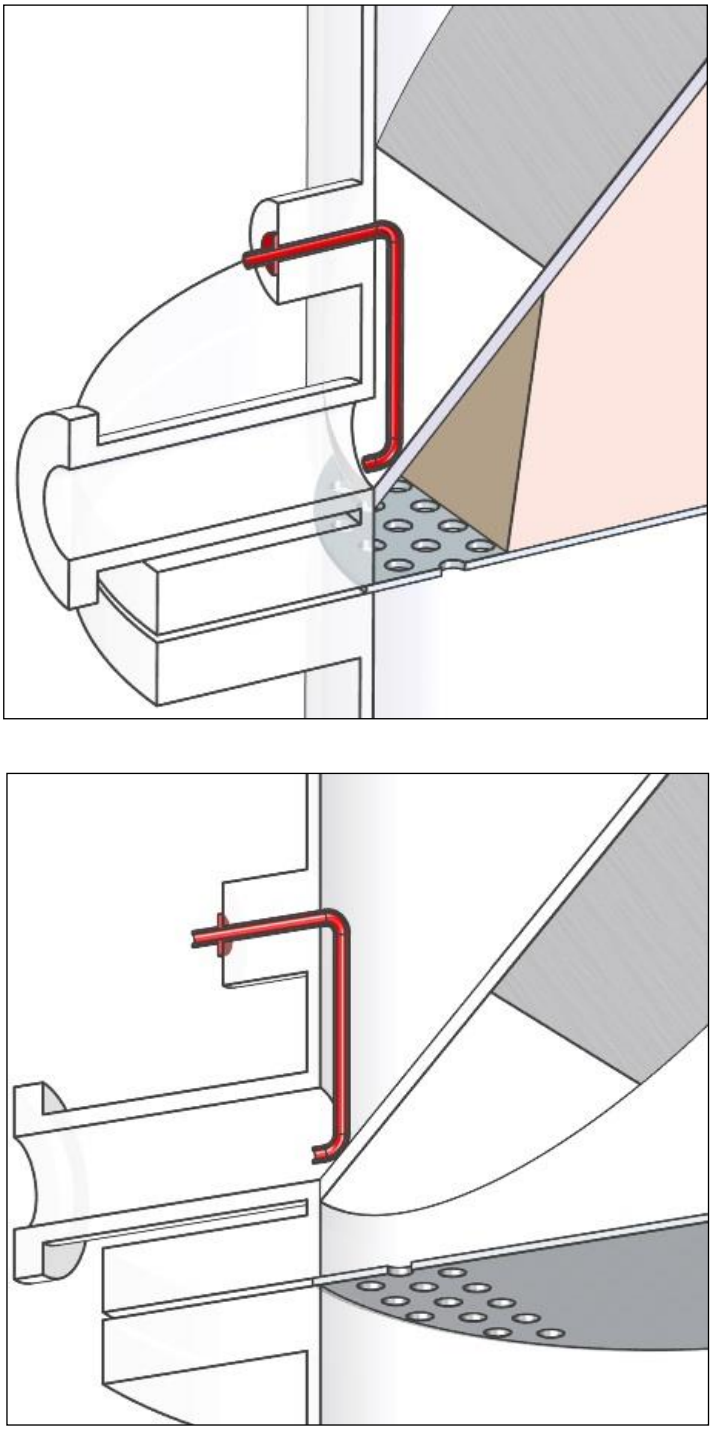

Figure 4.9. 3D model high-angle (top) and low-angle (bottom) close-up view of the regenerator lower section. The foam block has been removed in the bottom image to show the aluminium adhesive tape covering part of the lower surface of the inclined air distributor.

4.3.2 Benchmark CFB

The benchmark CFB (Figure 4.10 and Figure 4.11) is a simple co-current system that is made up of three main elements, namely the riser, the cyclone and the regenerator. In this section only the first two elements are described since the regenerator was already described in Section 4.3.1.

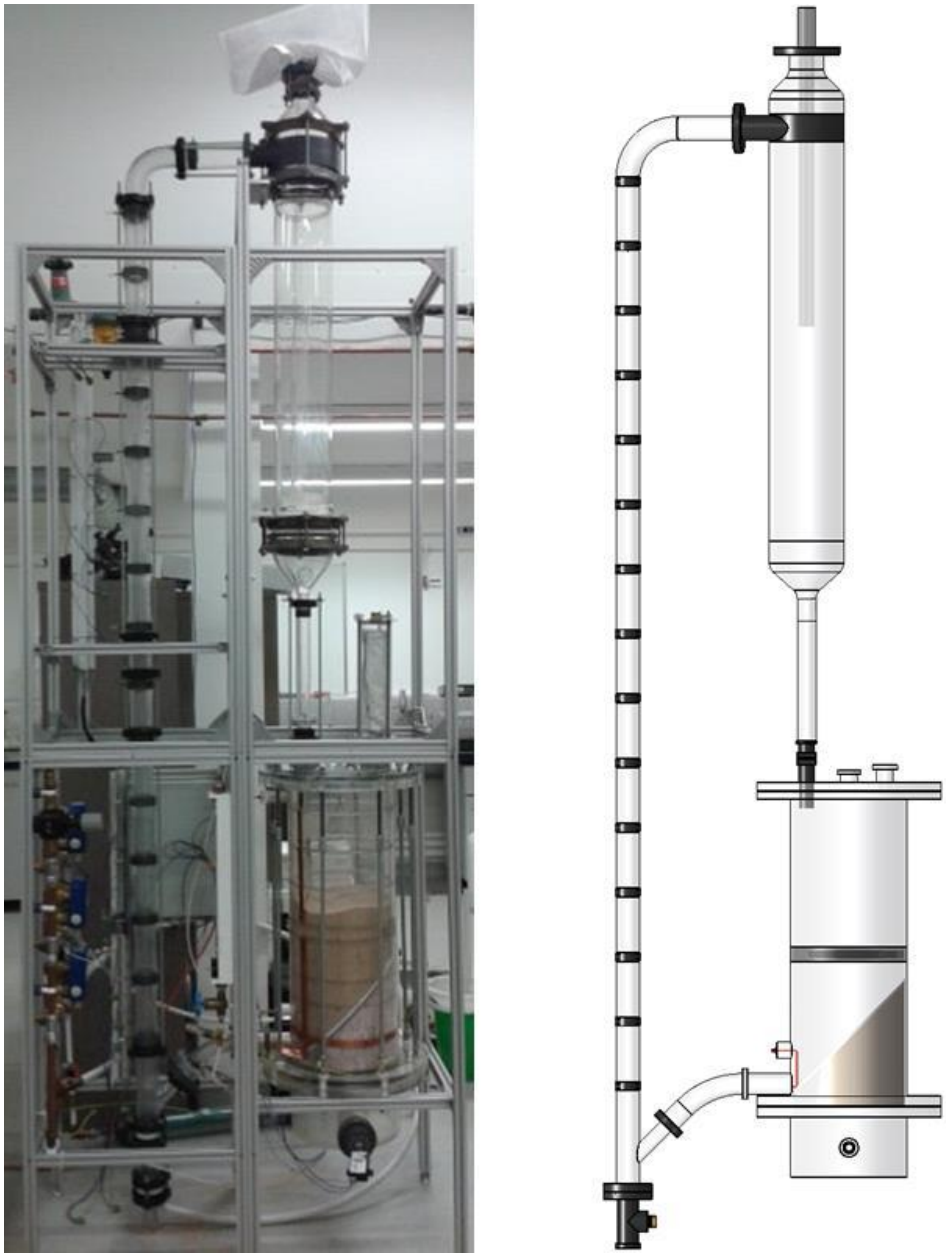

Figure 4.10. Front view (left) and 3D CAD model (right) of the benchmark CFB

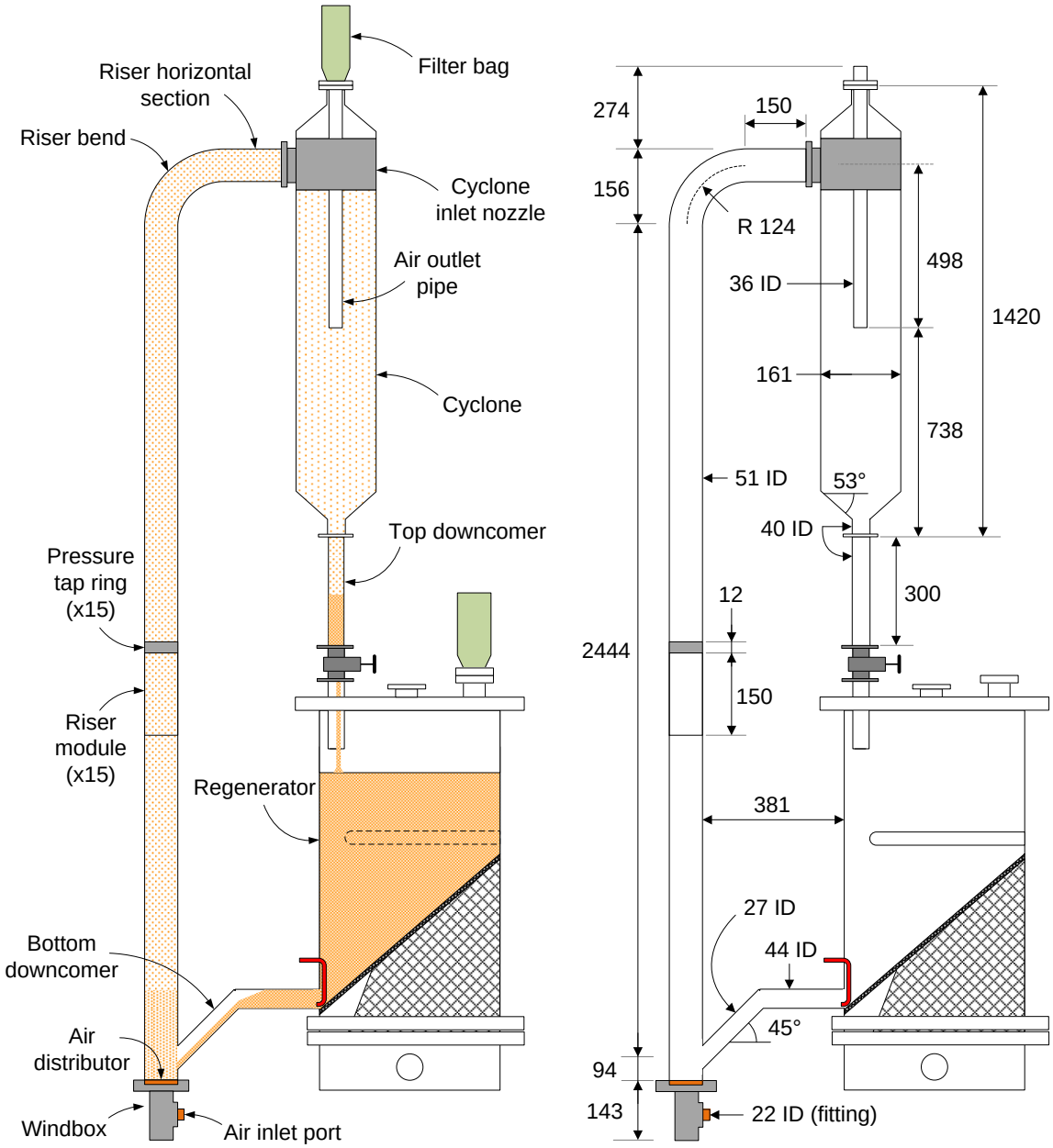

Figure 4.11. Main components (left) and dimensions (right) of the benchmark CFB. Dimensions in mm. Drawings not at scale

- *Benchmark CFB riser:*

The riser of the benchmark CFB has an inner diameter of 51 mm, and is composed of a main body, a bottom section, a windbox, a gas distributor and a top section.

The riser main body is made up of 14 cylindrical modules of borosilicate glass 150 mm long and 3 mm wall thickness from De Dietrich Process Systems. PVC cylindrical rings are installed between the modules acting as joints/holders of the glass modules (Figure 4.12) and allowing the installation of pressure taps. Details about the pressure taps are given in Section 4.4.

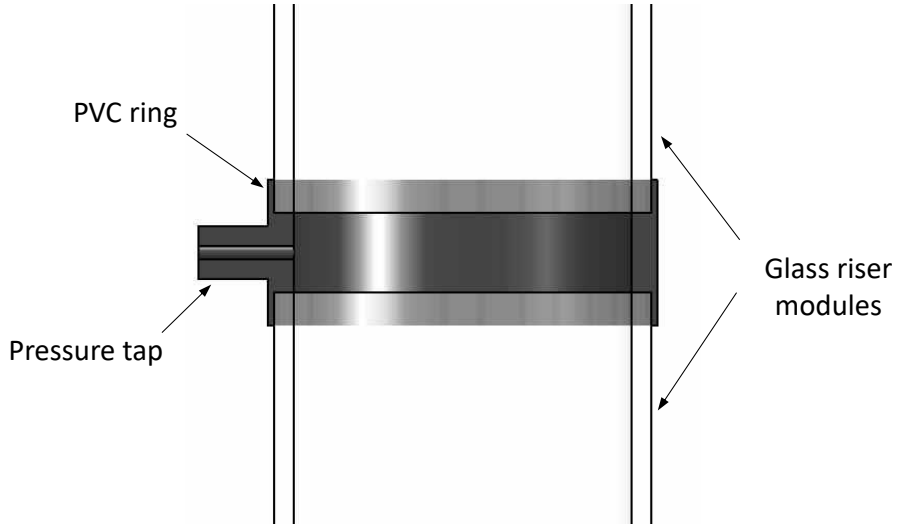

Figure 4.12. Section front view of a segment of the benchmark CFB riser, showing the connection between the glass modules and the PVC rings. A more detailed sketch of the pressure taps is shown in Figure 4.24

The riser bottom section (Figure 4.13) is similar to the glass cylindrical modules described above but slightly longer and fitted with a 45-degree branch that acts as the solids inlet port. The solid inlet port is connected to the regenerator solids outlet pipe by a long-radius 45° bend glass pipe denominated bottom downcomer.

The riser windbox (Figure 4.13) is made of PVC, and is equipped with a 22 mm ID brass fitting for connection with the air supply line, a head containing the air distributor and a pressure tap. The windbox is a common element to both CFB risers, but the head is interchangeable to accommodate for the different riser diameters and air distributors. In case of the benchmark CFB, the air distributor is a disc 60 mm

diameter cut out of a 5-mm thick sintered bronze porous sheet Porvair grade BRM 45. This material has a mean pore diameter of 67 μm and a permeability of 205×10^{-12} m^2. The disc pressure drop curve after installation in the windbox can be found in Appendix 3.

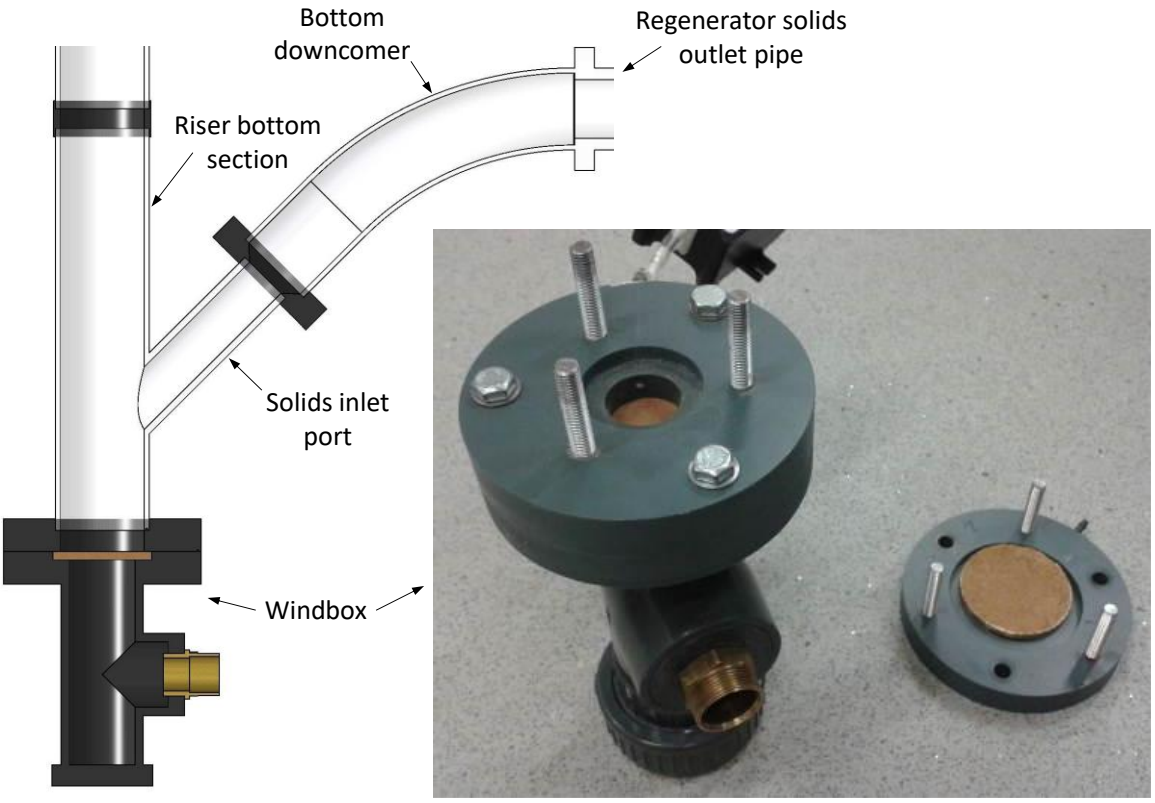

Figure 4.13. Benchmark CFB riser bottom. The installed windbox head in the photograph corresponds to the novel CFB riser, the one on the floor to the benchmark CFB

The riser top section (Figure 4.14) is composed of a 90° glass bend with a radius-to-inner diameter ratio of 2.4, connected to the cyclone inlet port by one riser glass module placed horizontally. Given the tangential orientation of the cyclone inlet port, the horizontal part of the riser top is slightly angled (7 degrees) with respect to the front plane of the rig.

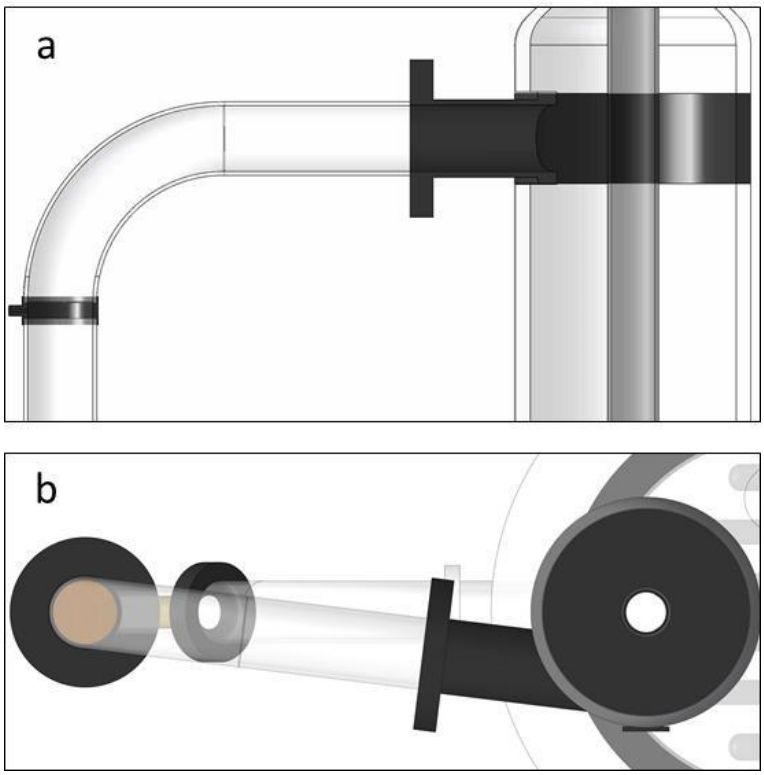

Figure 4.14. Front (a) and top (b) views of the benchmark CFB riser top section

- *Benchmark CFB cyclone:*

The benchmark CFB cyclone (Figure 4.15) is a crude gas-solids separator whose main components are a tangential inlet port (made of PVC), a cylindrical main body (glass), two conical ends (glass) and an air outlet pipe (Perspex). The inlet port is the only bespoke element, the rest being spare parts from previous experimental setups within the School of Engineering. As such, the separation performance is not optimized but relies basically on a drastic reduction on the air velocity to just 10% of the value in the riser, combined with solids agglomeration and wall friction due to the initial tangential trajectory of the incoming two-phase stream. Entrained solids are captured in the filter bag (described in Section 4.3.3) fitted at the upper end of the gas outlet pipe.

The element connecting the cyclone bottom to the regenerator solids inlet pipe is denominated the top downcomer. The solids flow and the height of solids in the top downcomer is controlled manually using the slide valve located between the top downcomer and the regenerator solids inlet pipe.

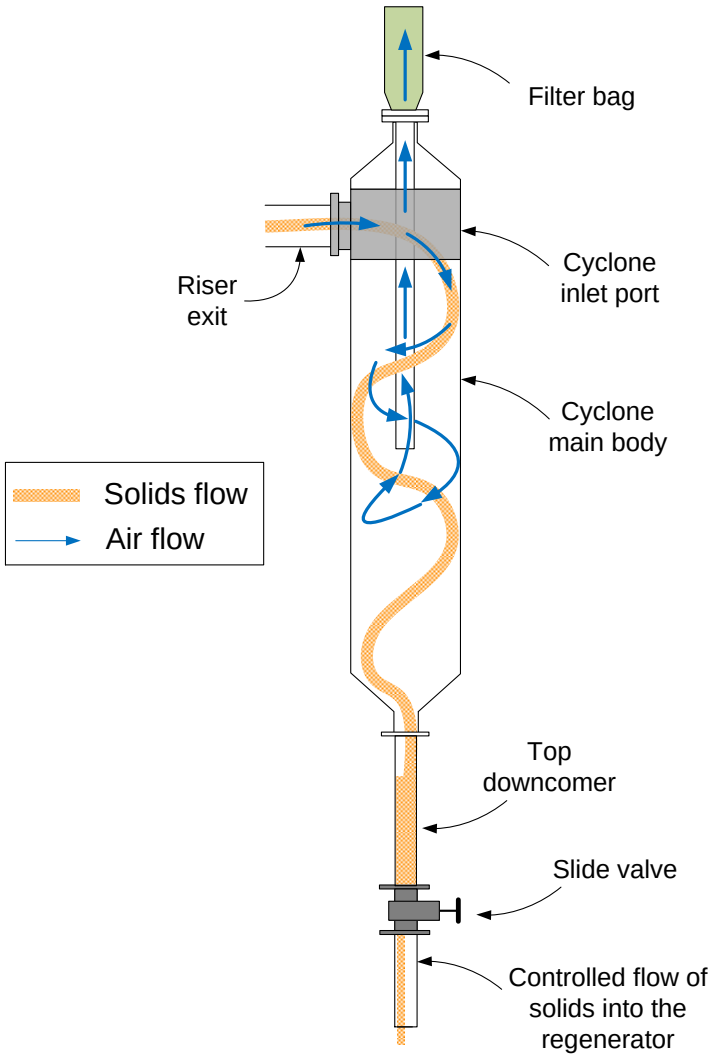

Figure 4.15. Schematic diagram of the benchmark CFB cyclone

4.3.3 Novel CFB

The main elements of the novel CFB (Figure 4.16 and Figure 4.17) are the riser, the counter-current adsorber and the regenerator. In this section only the first two elements are described since the regenerator was already described in Section 4.3.1.

Figure 4.16. Front view (left) and 3D CAD model (right) of the novel CFB

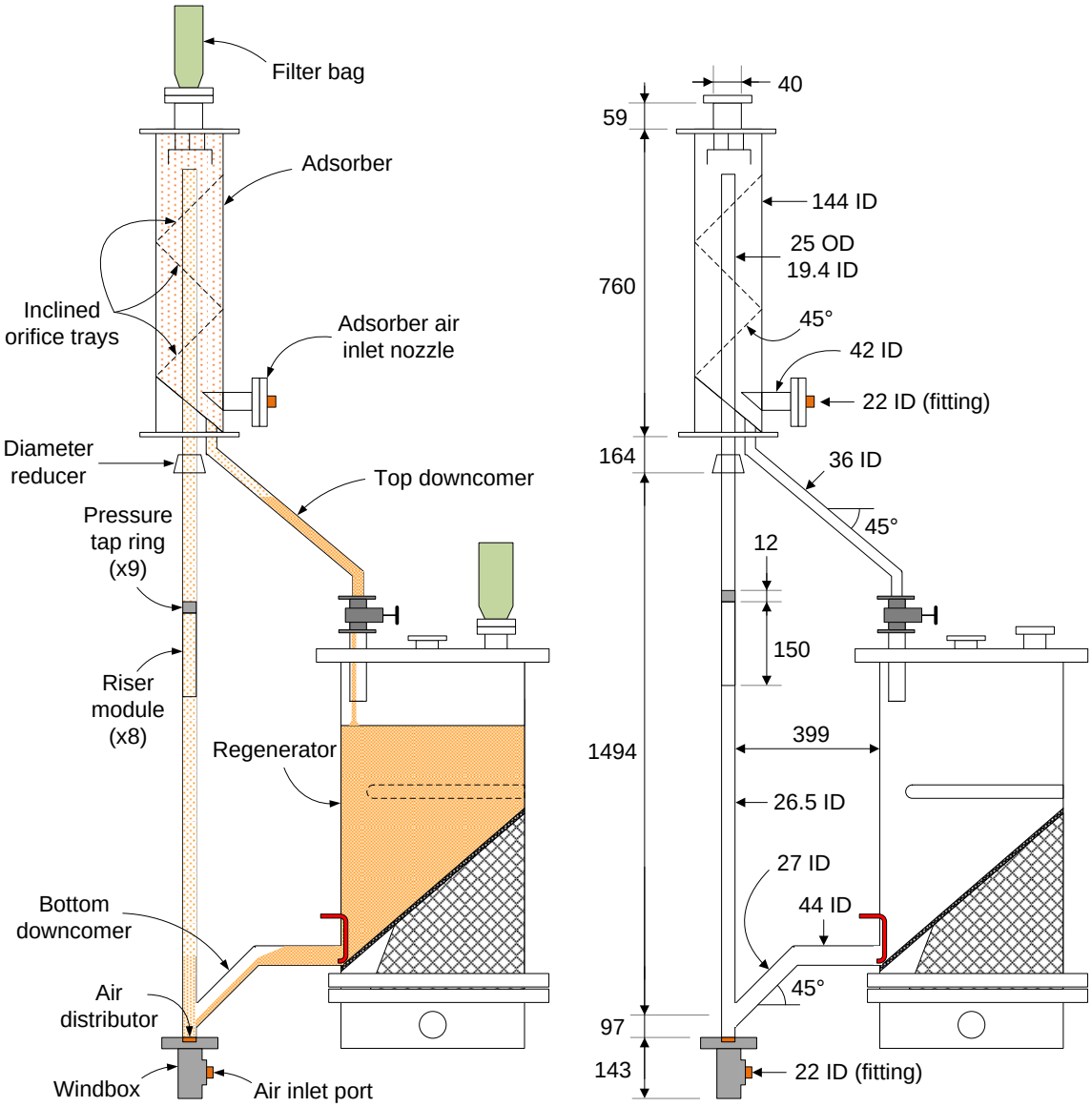

Figure 4.17. Main components (left) and dimensions (right) of the novel CFB. Dimensions in mm. Drawings not to scale

- *Novel CFB riser:*

The riser of the novel CFB is made up of a lower and an upper part (Figure 4.18). The lower part runs from the bottom of the rig to a few centimetres below the adsorber. It has an inner diameter of 26.5 mm and is made of glass modules and PVC rings in the same way as the riser of the benchmark CFB. The bottom downcomer and the windbox are the same as those used in the benchmark CFB; in this case, the windbox uses a head with a narrower hole to adapt to the smaller riser outer diameter (shown in Figure 4.13). The air distributor is a porous disc 60 mm diameter and 3 mm thick made of sintered bronze Porvair grade BRM 30. This material has a mean pore diameter of 35 μm and a permeability of 30×10^{-12} m^2. The disc pressure drop after installation in the windbox can be found in Appendix 3.

The upper riser is a Perspex tube with an outer diameter of 25 mm and inner diameter of 19.4 mm. It runs coaxially into the counter-current adsorber from the top of the lower riser. Linking the two riser parts is a small Perspex hollow cylinder machined to provide a smooth transition from lower to upper riser. The main reason for using a tube as the upper riser is to facilitate the riser-adsorber assembly (the riser is simply inserted into the adsorber). The tube inner diameter used is the closest lower than the diameter of the lower riser available in the Mechanical Workshop at the moment of construction.

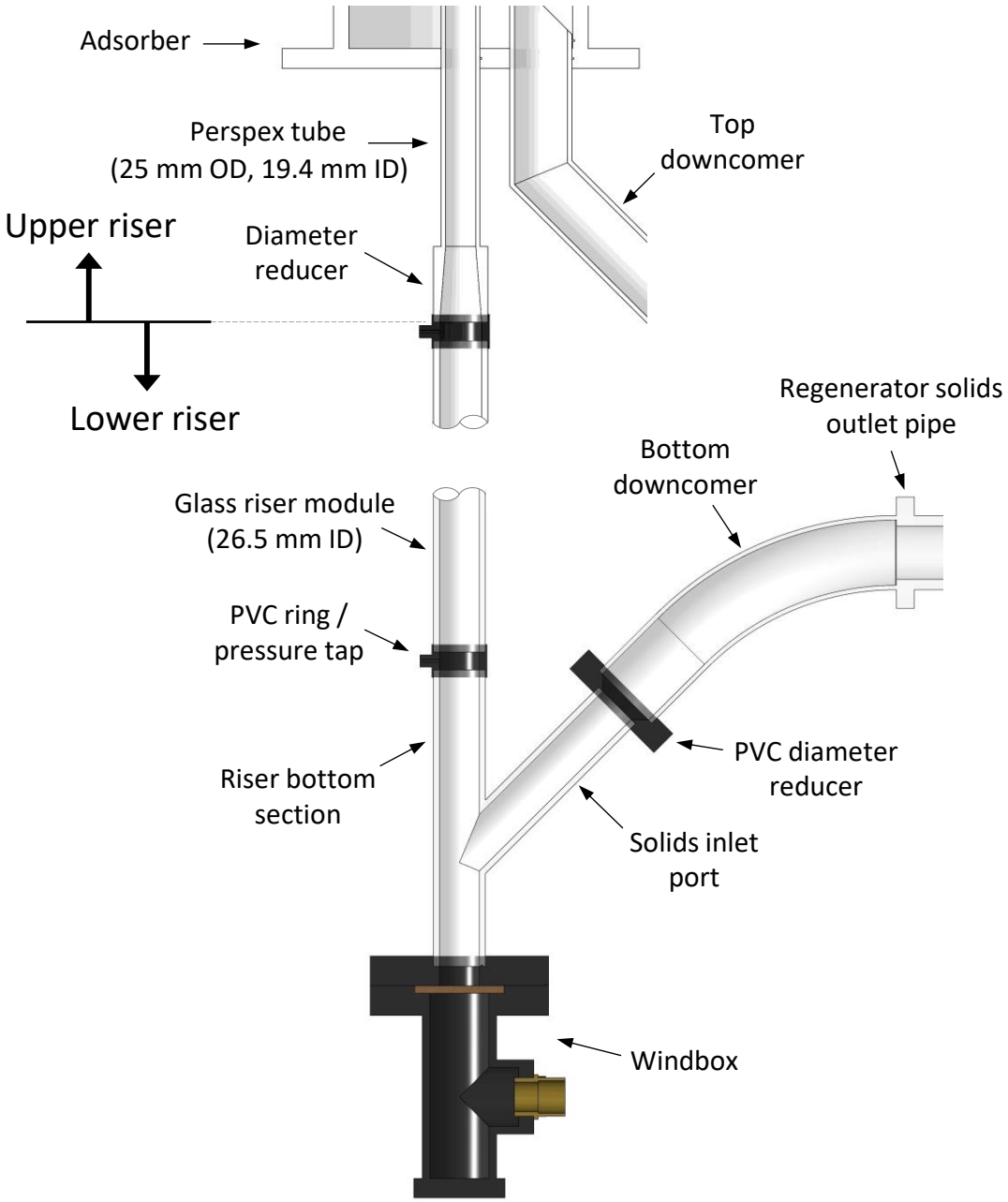

Figure 4.18. Section front view of the novel CFB riser

- *Novel CFB adsorber:*

The counter-current adsorber (Figure 4.19 and Figure 4.20) is the most complex element, in terms of geometry, of the CFB rigs. It is composed of cylindrical modules made of Perspex forming the adsorber main body, a bottom section and a head. All parts are drilled along their axis for assembly with the upper riser.

The adsorber tray modules are the functional units of the system in terms of gas-solid contact. For this study three tray modules were used, although they can be stacked in any number. Each module contains a 45° inclined orifice tray (Figure 4.21) 5 mm thick glued to the cylindrical wall. Each tray has 198 orifices 6 mm in diameter, drilled perpendicular to the tray plane. The orifice area represents 25.1% of the total tray surface. The orifices are arranged in a square pattern with a pitch of 10 mm for most of the tray surface; only two orifice rows, to both sides of the tray short axis, are arranged in a staggered pattern. This orifice pattern was chosen for ease of construction.

The adsorber head plays the double role of adsorber lid and gas-solid separator. It contains on its lower side a rimmed "impingement plate" against which the gas-solid mixture from the riser is discharged. After impact, the solids rain down whereas the air makes its way out through the filter bag fitted at the top outlet port (Figure 4.22). The filter bags used in this work are HEPA-like, which should retain between 90% and 99% of particles sizing 0.3 μm (Walters, 2004).

The adsorber bottom section contains an inclined "discharge plate" to facilitate the flow of solids falling from the lowermost tray module into the top downcomer. Air is introduced horizontally into the adsorber bottom via the air inlet nozzle. This nozzle has a slot next to the tube fitting to allocate a porous disc that can be used as a backup method to measure the air flow rate through (see Section 4.4.2).

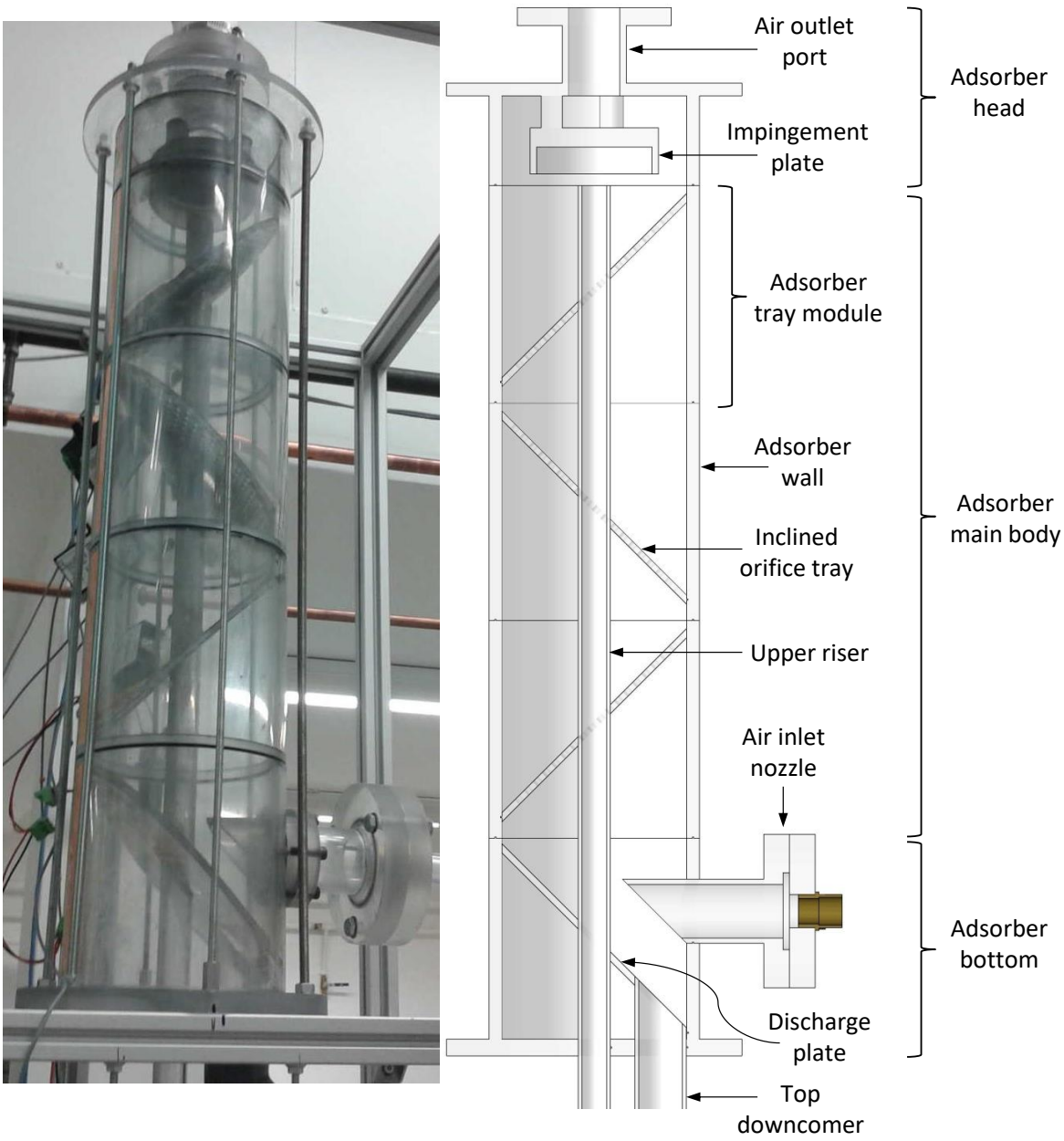

Figure 4.19. Low-angle photograph (left) and 3D CAD section front view (right) of the novel CFB adsorber. Each adsorber tray module is fitted with a pressure tap above the inclined orifice tray (not shown)

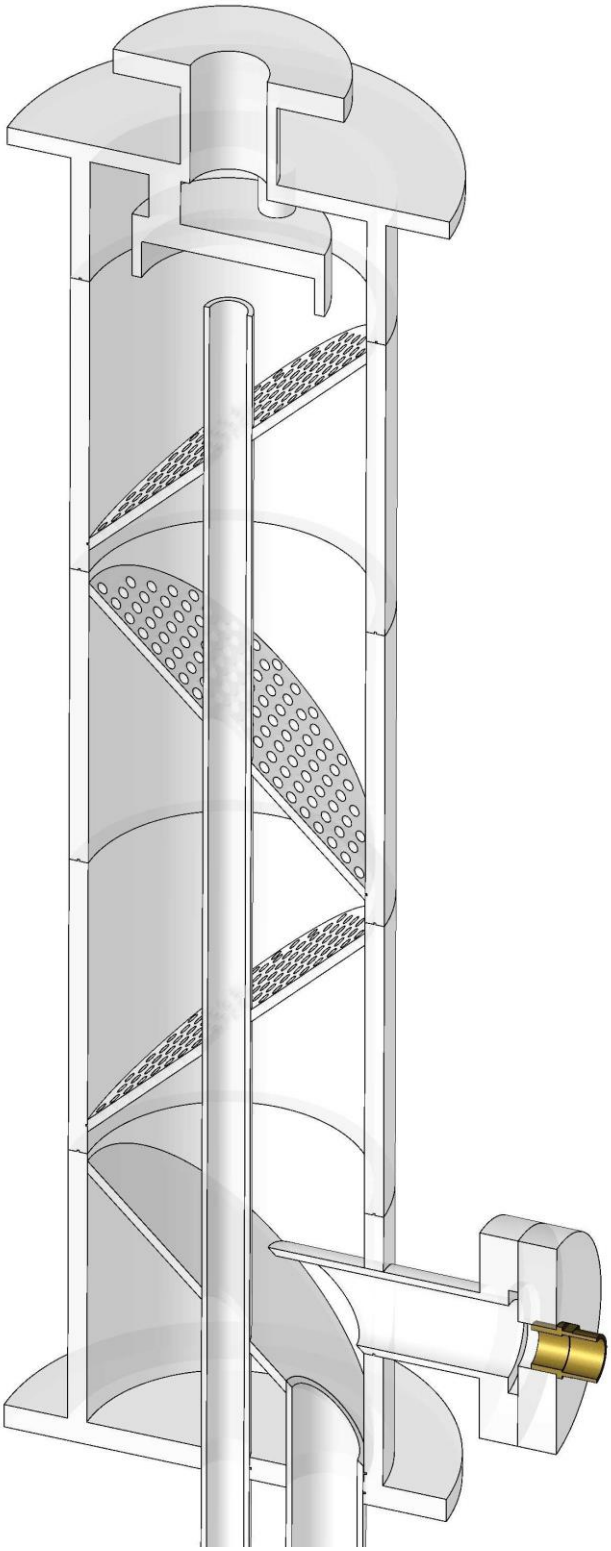

Figure 4.20. High-angle 3D CAD section view of the novel CFB adsorber

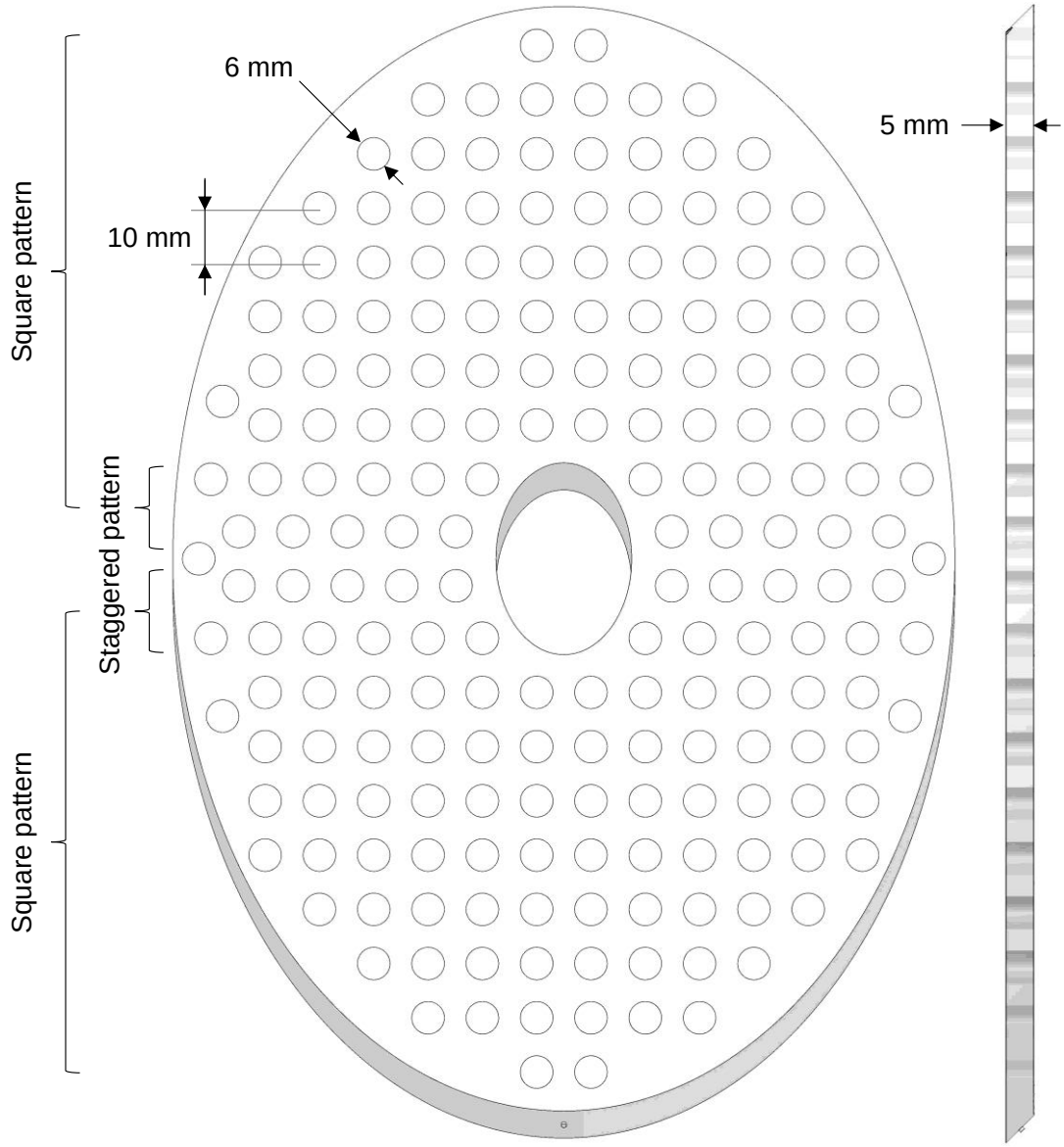

Figure 4.21. Front (left) and side (right) views of the inclined orifice trays of the novel CFB adsorber

Figure 4.22. Filter bag fitted to the air outlet port of the novel CFB adsorber. A similar filter is used in the air outlet ports of the regenerator and the benchmark CFB cyclone

4.4 Instrumentation

This section concerns the instruments, auxiliary materials and methods to measure, read and log values of gas flow rates and pressures in the CFB rigs and other small setups used in this work (for example, the small fluidised bed for solids characterisation sketched in Figure 4.4). Instruments and methods used in the determination of residence time distributions of gas and solids are described in Chapters 6 and 7 respectively.

4.4.1 Measurement of pressure

Pressures are measured using differential transducers Autotran model 851 4P 18D (Figure 4.23). This instrument has a selectable pressure range between ±0.25 psi and ±2 psi with an accuracy of ±1% of the full-scale output, or 0.02 psi (~1.4 mbar). The device output is an analog voltage 1-10 VDC.

Figure 4.23. Differential pressure transducer Autotran model 851 (image taken from the manufacturer's website, with permission)

The value of pressure read by the transducer is the difference between its two pressure ports, and can therefore be positive or negative. For gauge pressure readings, the high pressure port is used whereas the other is left open to air. In this work, the terms "gauge" and "1-port" are interchangeable when referred to pressure, and so are the terms "differential" and "2-port".

PVC pressure taps 2 mm ID (depicted in Figure 4.24) were installed at multiple points of the systems. Schematic drawings showing the approximate location of pressure taps in the CFB rigs are given in Appendix 1. 2 mm ID flexible tubes were used for connection between the pressure taps and the pressure transducer ports. The tube length varied depending on the location but was generally very short: 1-2 cm for 1-port connections and 7-10 cm for 2-port connections. Particles were prevented from entering the tubes by using cotton plugs on the pressure side of the taps, which were not too compacted and did not damp the pressure signal as demonstrated in preliminary tests. Dimensions of the pressure taps and tube connectors are well within recommended values for this application (see van Ommen et al., 1999).

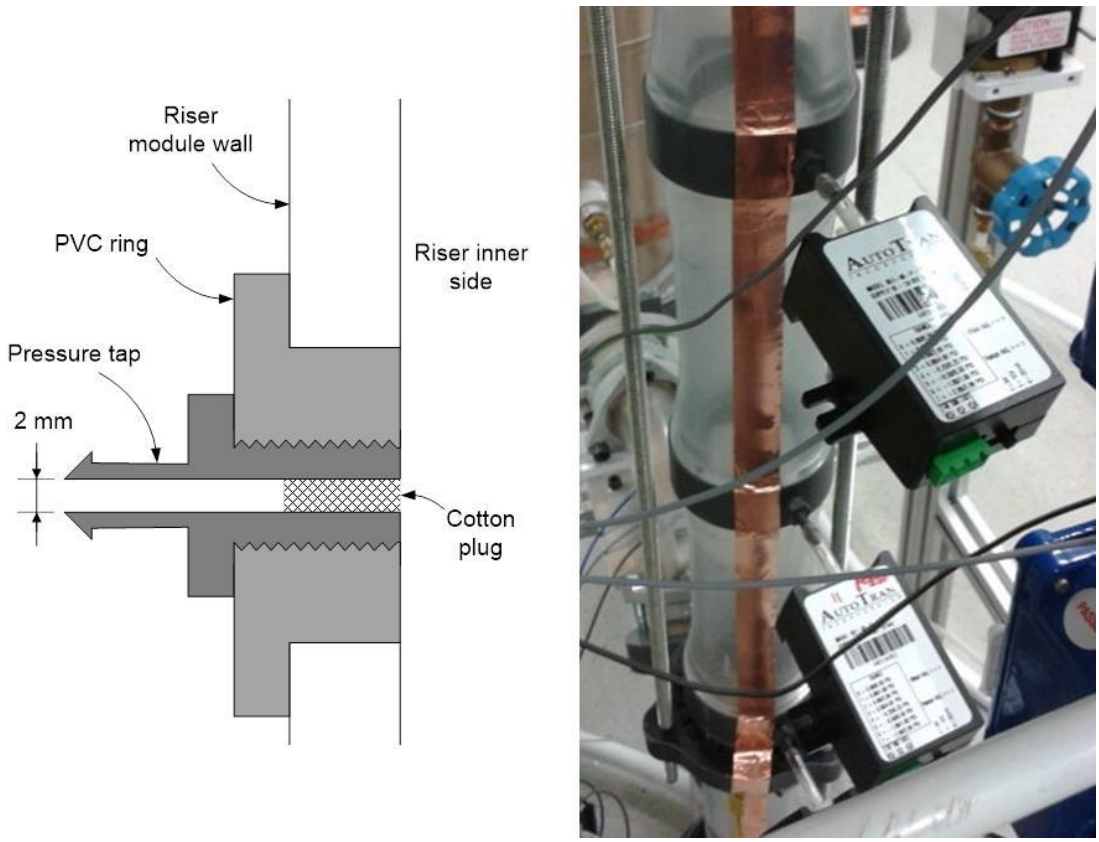

Figure 4.24. Sketch showing the pressure taps installed in the CFB risers (left) and example of installed pressure transducers in the benchmark CFB (right)

4.4.2 Measurement of air flow rate

Table 4.2 presents the instruments that were installed or temporarily used for the measurement of air flow rates in the different sections of the CFB rigs or other small experimental setups used in this work.

The first choice for measuring air flow rates was the use of orifice flow meters, given their simplicity and relative low cost. Several Eletta R-series, model GL flow meters (Figure 4.25) were acquired to measure the different air flow ranges in the different sections of the CFB rigs. These instruments consist of two main parts, namely the pipe section and the control unit. The pipe section contains the orifice disc, and is female-threaded for installation in the flow line. The control unit is mounted on top of the pipe section, and contains a rubber diaphragm that bends under the pressure difference at both sides of the orifice. This diaphragm acts in turn on a potentiometer,

modifying the value of the instrument output linearly with the flow. The flow meter output is an analog current 4-20 mA.

Figure 4.25. Orifice flow meter Eletta R-Series, model GL

After acquisition and preliminary testing, it was realised that the Eletta flow meters were calibrated at a higher pressure than the required (2.5 barg instead of 0 barg), with the consequent systematic error in the readings that could be (depending on the measured range) as large as 100% of the expected values. Moreover, new orifices received from the manufacturer and calibrated at the assumed right pressure presented even larger departures from the expected values. The possible reasons behind this were discussed with the manufacturer but no clear conclusions were reached. After much discussion, and in view of the still useful linear relationship between meter output and air flow rate, it was decided that the overall best solution was to keep the flow meters and use them after calibration with other air flow rate measuring instruments available at the School of Engineering in Edinburgh.

The instruments used for calibration of the orifice flow meters were (Figure 4.26):

- A mass flow controller Cole-Parmer model OU-32907-75 with a measuring range of 1-100 l/min and accuracy ±0.2% of full-scale reading (±0.2 l/min).

- Two rotameters KDG Mobrey, with measuring ranges 30-300 l/min and 400-4000 l/min (measured at 15°C and 1013 mbara) and accuracy 2.5% of full-scale reading (±4 l/min and ±50 l/min respectively).

In addition to the instruments above, the air distributors of both CFB risers can be used as a backup using the correlation between pressure drop and air flow rate through (given in Appendix 3). The same backup method is available for the novel CFB adsorber air inlet flow rate by inserting a porous disc in the slot made in the air inlet nozzle for this purpose.

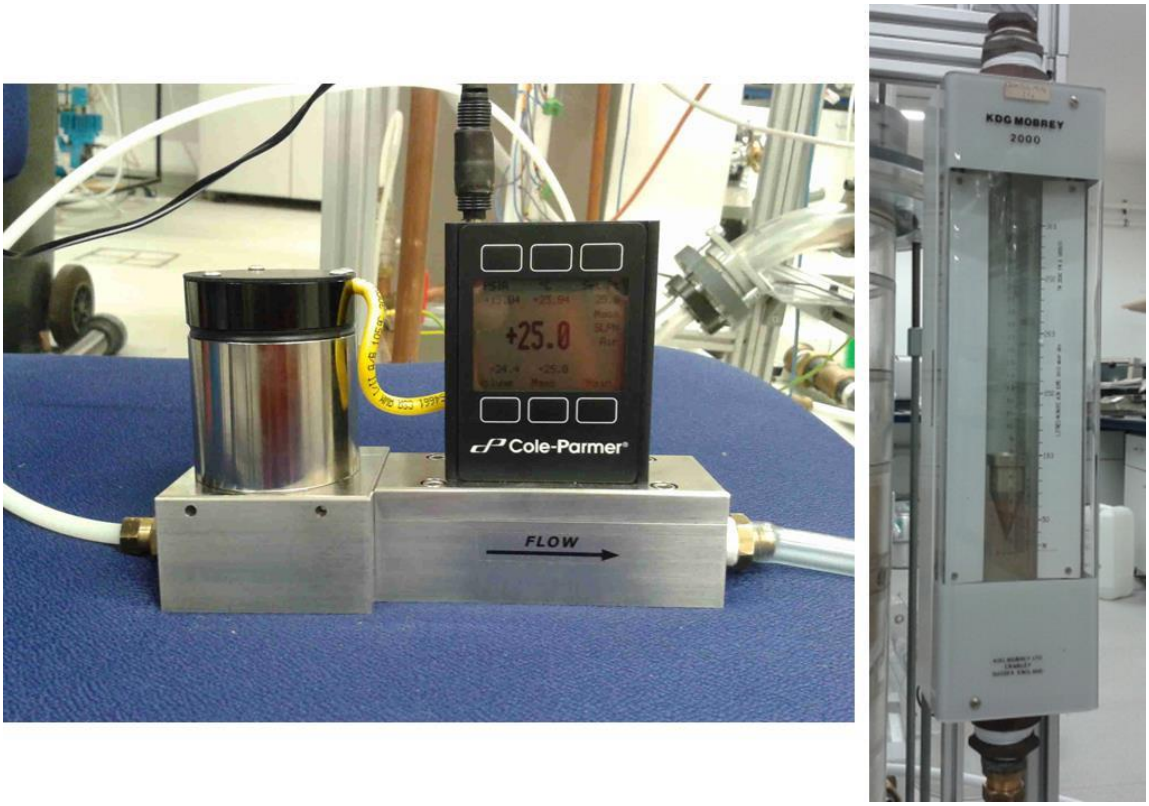

Figure 4.26. Mass flow controller Cole-Parmer 1-100 l/min (left) and a rotameter KDG Mobrey 30-300 l/min (right) used for calibration of the orifice flow meters

Table 4.2. List of instruments used for measurement of air flow rates

Reference	Air stream	Air flow rate range (l/min)	Comments
Calibrating instruments			
Mass flow controller		1-100	
Rotameter 3		30-300	
Rotameter 4		400-4000	
Calibrated instruments			
Rotameter 1	Lube air (regenerator)	5-50	Calibrated* with mass flow controller
Rotameter 2	CO_2 pulse detection sample	8-32	Calibrated* with mass flow controller
Orifice flow meter 1	Regenerator inlet	5-27	Calibrated* with mass flow controller
Orifice flow meter 2	Regenerator inlet	16-36	Calibrated* with mass flow controller
Orifice flow meter 3	Novel CFB riser inlet	84-156	Calibrated* with rotameter 3
Orifice flow meter 4	Benchmark CFB riser inlet Novel CFB adsorber inlet	400-800	Calibrated* with rotameter 4
Backup instruments			
Pressure drop in air distributor	Novel CFB riser inlet	0-185	Calibrated** with mass flow controller (1 to 100 l/min) and rotameter 3 (100 to 200 l/min)
Pressure drop in air distributor	Benchmark CFB riser inlet	0-800	Calibrated** with mass flow controller (1-100 l/min), rotameter 3 (100-300 l/min) and rotameter 4 (400-800 l/min)
Pressure drop in porous disc	Novel CFB adsorber inlet	0-800	Same material and size as the benchmark CFB riser air distributor (see Section 4.3.2) Calibrated** with mass flow controller (1-100 l/min), rotameter 3 (100-300 l/min) and rotameter 4 (400-800 l/min)

*Calibration curve available in Appendix 3 **Pressure drop curve available in Appendix 2

4.4.3 Data acquisition system

Data acquisition is achieved using the 3-level system schematised in Figure 4.27. The first level is composed of the physical instruments installed in the CFB rigs; the second level is the core of the system, formed by a CompactRIO real-time controller from National Instruments (see description below) that receives the analog signals from the physical instruments and stores the data; this information can be accessed via Ethernet using a computer (the third level of the data acquisition system) locally by direct connection to the CompactRIO or remotely via the university local network.

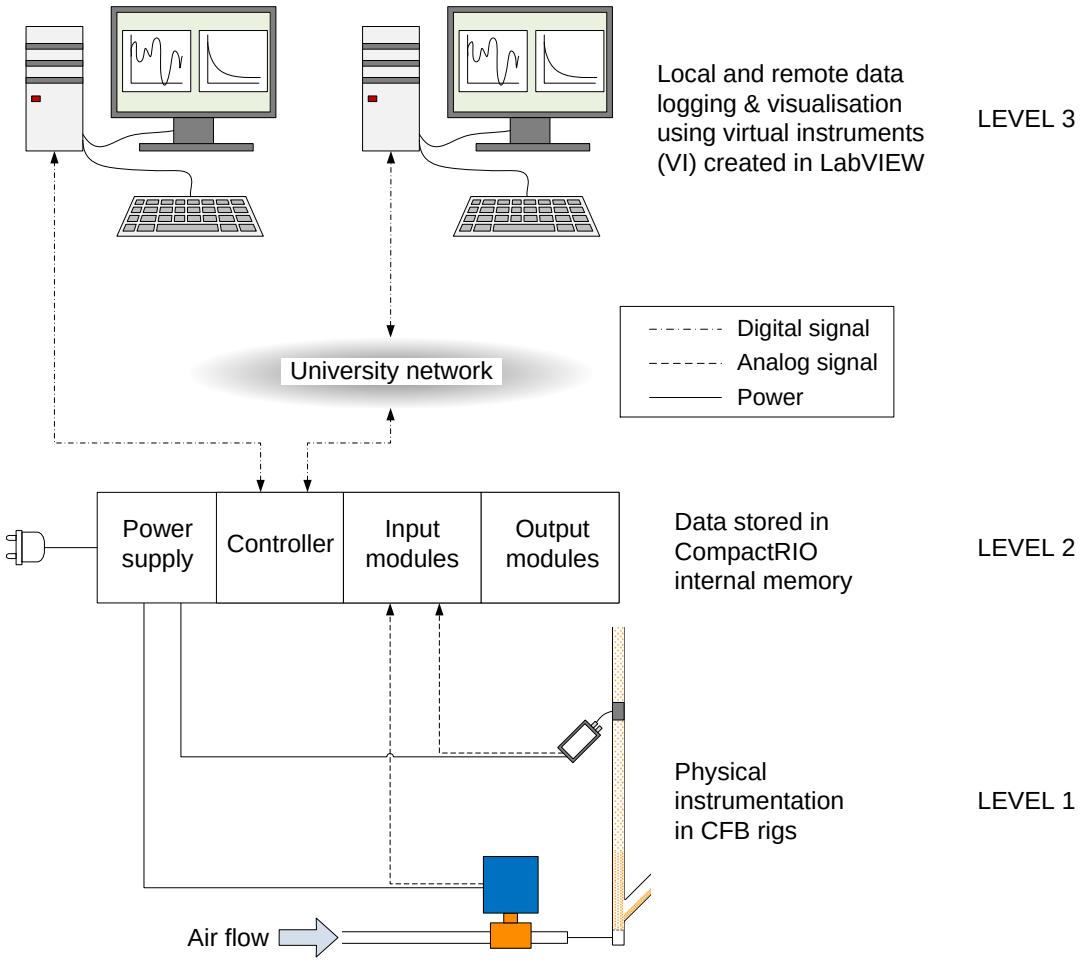

Figure 4.27. 3-level data acquisition system used in this work

The CompactRIO package (Figure 4.28) consists of a controller and a number of input/output modules assembled together in a configurable chassis. The package used

here was formed by a controller model CRIO-9022, two analog ±10 V input modules model NI 9205 and one thermocouple input module model NI 9213.

Figure 4.28. Generic CompactRIO package composed of the controller unit (large block on the left) and several input/output (I/O) modules mounted on a reconfigurable chassis. Image taken from National Instruments' website (with permission).

For generation of data from the input signals, the CompactRIO is programmed in the dataflow graphic language LabVIEW (National Instruments). The program used here allows recording values of voltage from the pressure transducers and orifice flow meters with a frequency of 19 Hz, value deemed high enough to capture the main characteristics of the gas-solid flow in the CFBs. According to van Ommen et al. (2011), "the dominant frequencies in most fluidised bed systems are of the order of 1-5 Hz".

LabVIEW is also used to create virtual instruments (VI) for visualization of the data as it is generated. The front panel (the part actually visible in the computer screen) of an example VI created for this purpose is shown in Figure 4.29.

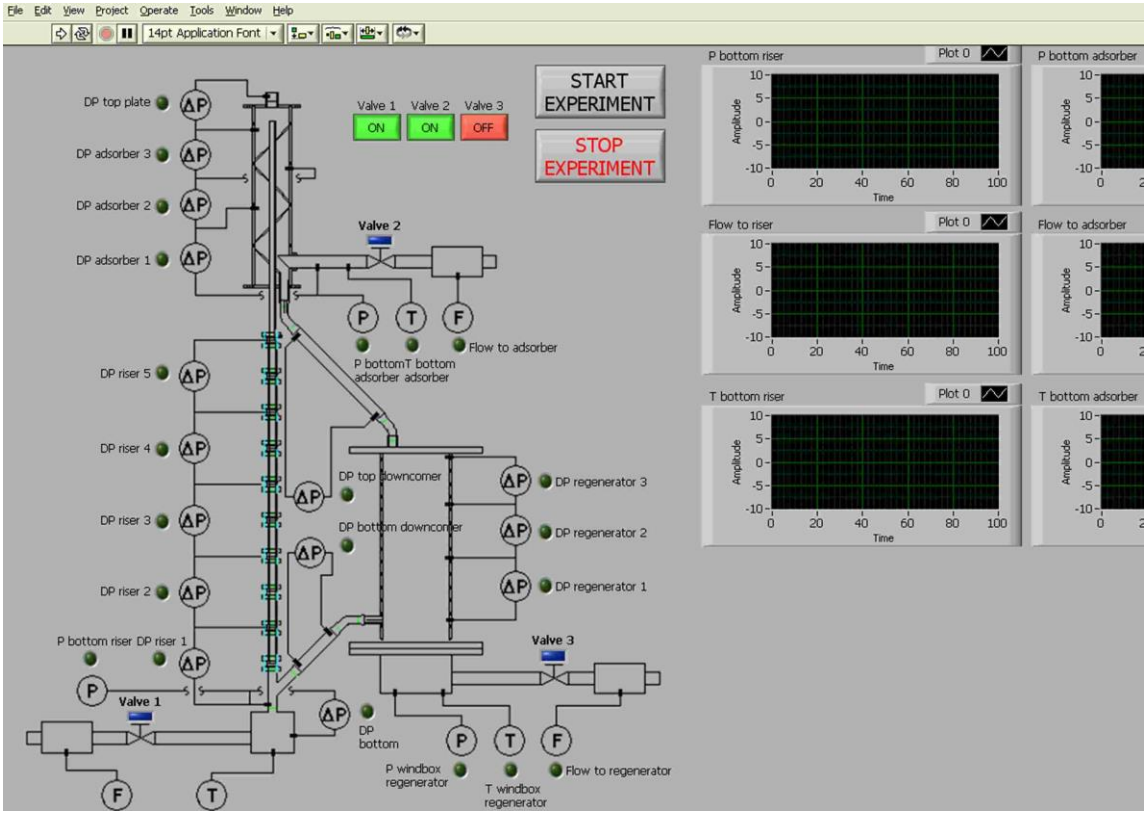

Figure 4.29. Front panel of a LabVIEW virtual instrument (VI) for visualization and logging control of the generated data in the novel CFB

4.5 Measurement of the solids circulation rate

The solids flow rate in both CFB rigs is determined by closing the regenerator slide valve and measuring the solids accumulation in the top downcomer. In normal conditions, the solids level in the top downcomer is kept close to the upper end as a gas sealing measure between the counter-current adsorber (novel CFB) or cyclone (benchmark CFB) and the regenerator. When carrying out the measurement of the solids circulation rate, the following procedure is followed (see Figure 4.30 for reference):

1) Increase the opening of the slide valve so the solids level in the top downcomer goes down, near the downcomer lower end.

2) Close the slide valve, making sure the flow of solids into the regenerator is completely interrupted. This step turned out to be difficult at times as the solids

easily prevent the valve to close 100%. The best practice is to shut the valve quickly with a sudden move of the handle.

3) Register the time taken for the solids level to rise between two planes previously marked on the downcomer. The lower plane is always in the same position, whereas the position of the upper plane can be varied to accommodate (if possible) the filling time to 10-12 s and/or a distance between planes around 15-20 cm.

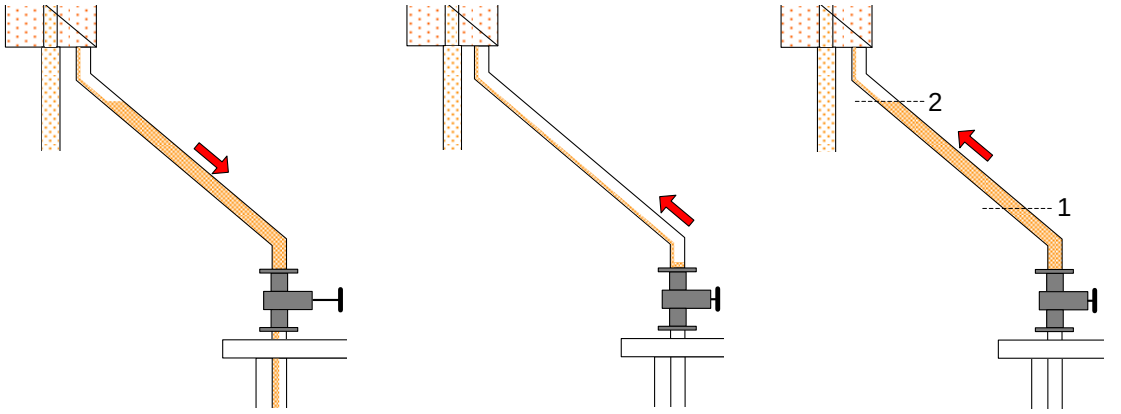

Figure 4.30. Procedure for measuring the solids circulation rate in the CFB rigs. Although the sketch corresponds to the novel CFB, the procedure is identical in both CFB configurations

The value of the solids circulation rate F_s given the distance d_f between downcomer planes (in the direction of the downcomer axis) and filling time t_f is calculated as:

$$F_s = \frac{\varepsilon_{s,l} A_{dc} d_f \rho_s}{t_f} \tag{4.7}$$

where A_{dc} is the cross-sectional area of the top downcomer. The solids fraction in the downcomer corresponds to that of a loose bed, $\varepsilon_{s,l}$ (see Section 4.2). This was determined experimentally in preliminary tests by manually filling the downcomer with weighed samples.

4.6 Measures for static electricity control

The first solids circulation trials after construction of the CFB rigs showed that strong electrostatic discharges (sparks) and particle agglomeration (Figure 4.31) occurred especially at high rates of both phases, and therefore measures to minimise these highly undesirable phenomena were implemented.

Static electricity generation and accumulation in gas-solid flowing systems is caused by interaction of the solid particles with 1) the walls, 2) the fluidising gas, and 3) themselves (Park et al., 2002; Klinzing, 2003). Effective measures for static electricity control must act upon these three types of interaction.

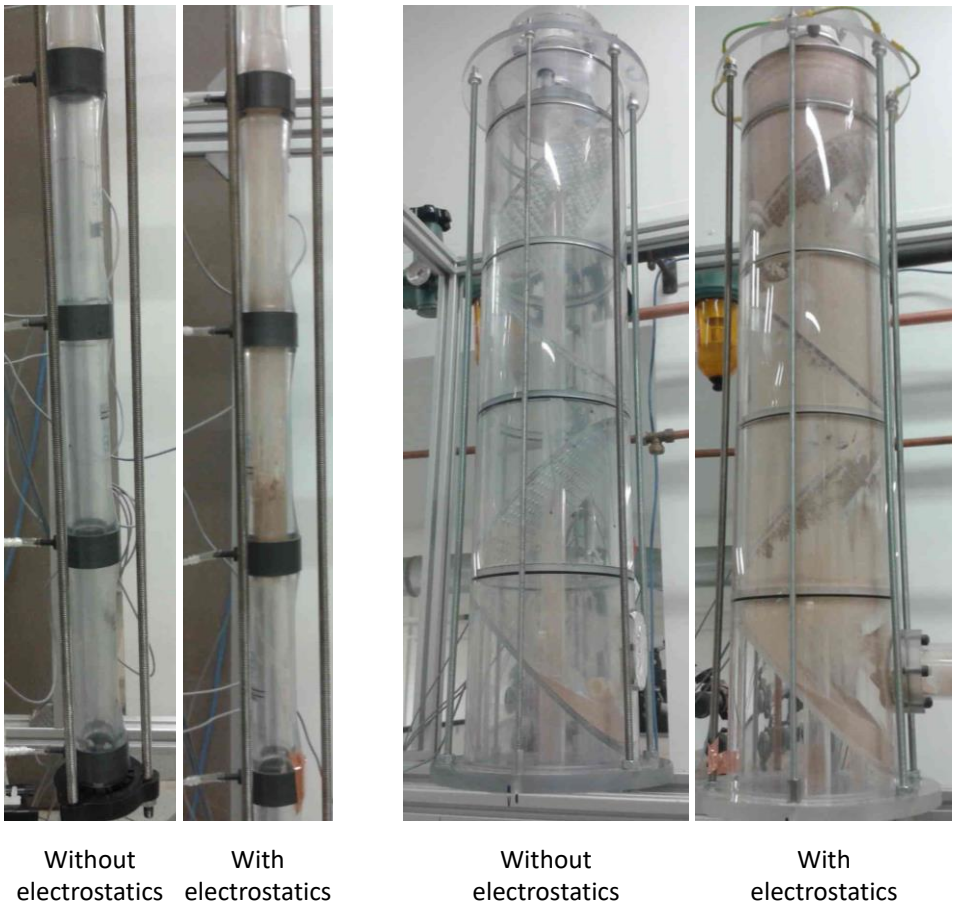

Figure 4.31. Effect of static electricity in novel CFB riser (left) and adsorber (right)

- 1st measure: adhesive copper tape:

The earliest measure adopted to prevent static electricity accumulation and violent discharge in form of sparks was the application of copper tape 15 mm wide with conductive adhesive from 3M (reference 1181) on the external surface of the different CFB elements (Figure 4.32). The copper tape was applied forming a net that was connected to the ground terminal of the setup. While effective reducing the formation of sparks, this measure did not, by itself, prevent the solid particles from agglomerating and sticking to the walls. This suggests that although draining of static electricity from the CFB walls was (up to a certain degree) achieved, further measures against statics were needed.

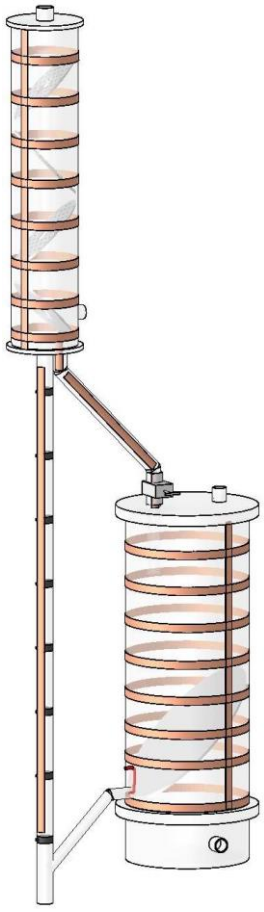

Figure 4.32. 3D CAD model of the novel CFB with copper adhesive tape used for grounding

- 2nd measure: anti-static spray:

The second measure implemented was the application of an anti-static spray to all surfaces (inner and outer) of all non-metal parts of the CFB rigs, including rubber gaskets and o-rings. This did not include the external surfaces of the riser glass modules bought on purpose for this project since they already had a conductive polymer layer. The anti-static product used was a Licron Crystal spray from Techspray, which formed an impact-resistant urethane-based transparent dissipative coating. This product did not require thermal curing and worked right after complete evaporation of the solvent.

The application of the anti-static spray was successful in preventing particle agglomeration at low solids flow rates (up to approx. 0.02 kg/s in the novel CFB, where the spray was first tried). Statics at higher solid flow rates could still be felt, assumed to be generated by strong particle-particle interaction.

- 3rd measure: graphite powder (trial) and air humidification:

Further anti-static electricity measures needed to address the generation or accumulation of statics at the particle-particle interaction level. This can be achieved by increasing the conductivity of the surface of the particles (Bafrnec and Beña, 1972; Park et al., 2002; Klinzing, 2003). Two methods were tried: 1) coating the sand particles with graphite powder (Hagyard and Sacerdote, 1966; Bafrnec and Beña, 1972), and 2) humidifying the air flow.

For the first method, micron-sized graphite powder was added to a batch of sand large enough to perform solids circulation tests in the novel CFB. The amount of graphite was 0.14% of the weight of the sand (Bafrnec and Beña, 1972). Although statics were substantially reduced, graphite powder turned to be a very dirty material that darkened the transparent walls of the rigs. Besides, it was realised it could be released into the lab atmosphere due to its small particle size and low density. Indeed, inspection of the filter bags revealed that a large amount of graphite was covering their inner side.

It should be noted that graphite powder was tried as a particle coating substance in absence of another much-tried powder in the literature for statics dissipation, Larostat 519 (Chang and Louge, 1992; Glicksman et al., 1993; Zhang et al., 1996; Wang, 1997; Yao et al., 2006; Moughrabiah et al., 2012). This substance is a quaternary ammonium salt that, in virtue of its hydrophilic nature, increases the water concentration on the particle surfaces and therefore their conductivity (Klinzing, 2003).

Air humidification, despite being “a well-know” (Park et al., 2002) and “the most convenient” (Klinzing, 2003) method to combat static electricity in gas-solid flow systems, was tried late in this study because 1) it was thought that it could affect the flowability of the sand, and 2) air humidifiers for the flow rates used here were too expensive. Fortunately, house-made humidifiers were devised and constructed using spare parts from the Mechanical Workshop (Figure 4.33).

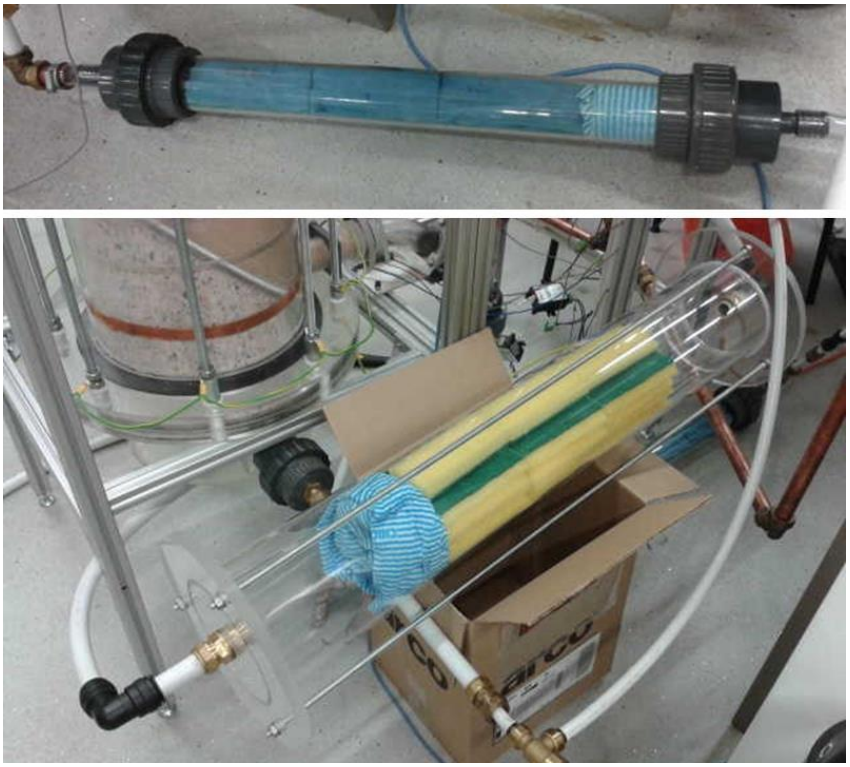

Figure 4.33. Low flow rate (top) and high flow rate (bottom) air humidifiers

The humidifiers were merely closed cylindrical containers where the air could flow through and collect moisture from soaked sponges. Water droplets were retained using thin cleaning cloths wrapped around a metal mesh structure that fitted tight in the cylinders. The pressure drop was low as the sponges did not occupy the whole cross section of the humidifiers but left longitudinal channels for the air to flow.

The air humidity was measured in a one-off basis using a humidity sensor Honeywell model HIH-4000-004, mounted in a small metal case as shown in Figure 4.34. The air relative humidity after flowing through each of the humidifiers is shown in Figure 4.35. The air flow rates are those corresponding to the CFB risers. In both cases the initial relative humidity is high (>90%), corresponding to the air volume that initially fills the humidifiers. This initial value leads to a lower value corresponding to steady state operation. After a certain time, the sponges start to dry out, with the consequent decrease in air relative humidity. The high flow rate humidifier can achieve 80% relative humidity for at least an hour, whereas for the low flow rate version the value is 60% for 30 minutes. Nevertheless, values of relative humidity higher than 40% (sufficient according to Park et al., 2002) can be maintained for at least 80 m of uninterrupted operation in the low flow rate humidifier, and for more than 140 m in the high flow rate version.

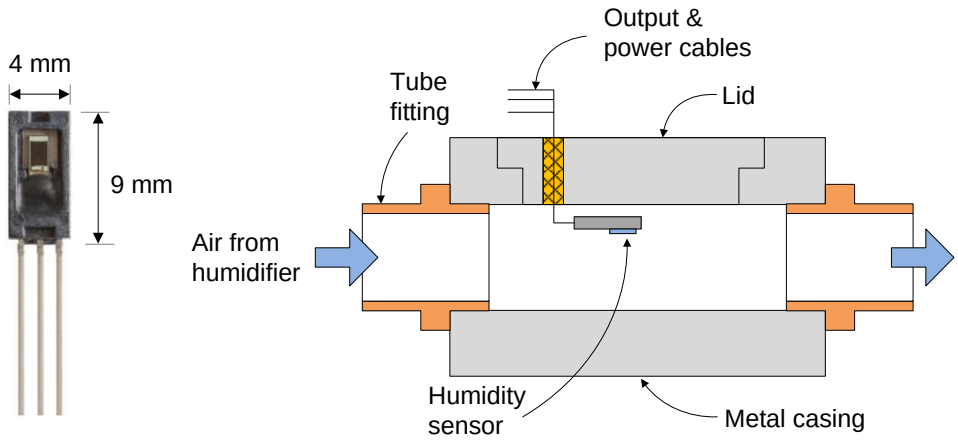

Figure 4.34. Humidity sensor Honeywell model HIH-4000-004 (left) and mounted on a case for air humidity measurements (right). Image taken from the manufacturer's website (permission pending)

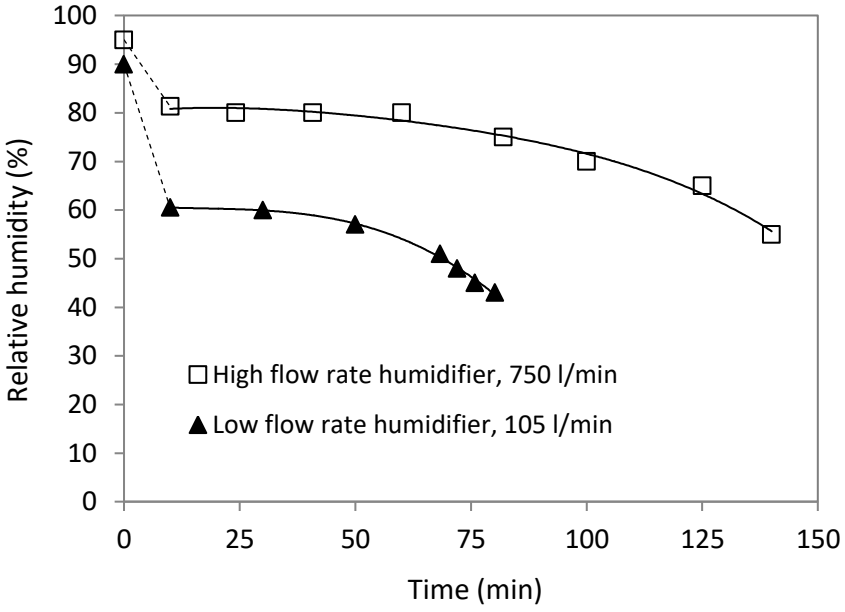

Figure 4.35. Air relative humidity versus time after flowing through the humidifiers

Air humidification proved to be the best measure to keep static electricity to a minimum, although it has not been tested on its own but together with the other measures described previously. It has also been observed that, with all anti-static measures in place, the undesirable effects of static electricity are more likely to be encountered when the rigs are "dirty", i.e. dirt particles from the ambient air and sand fines accumulate in the system. These particles might act as initiation points for the electrostatics to grow. Equipment disassembly, cleanup and reassembly greatly contribute to reduce or delay the generation and accumulation of static electricity.

The elimination of inner surfaces with an angle lower than the angle of repose of the solids is also highly recommended. Solids pockets, in the presence of static electricity act as a "magnet" for other particles and can grow until completely filling the system. The novel CFB adsorber is especially prone to experience this phenomenon given the geometry of the internals, as illustrated in Figure 4.36.

Figure 4.36. Examples of sand pockets in the novel CFB adsorber and growth due to accumulation of static electricity

5 Operating characteristics of the cold model CFB rigs

5.1 Introduction

The CFB rigs are described and analysed in this chapter in terms of operating characteristics and the underlying phenomena governing them. An explanation of the mechanisms that allow solids circulation in CFB systems is given first (Section 5.2). Description of the operating features of the rigs follow, starting with the regenerator (Section 5.3) as the truly operational "heart" of the CFB systems in its role of solids feeder. The operational interaction between the regenerator and the riser is described in detail in Section 5.4, providing the foundations to understand the operating capabilities and limitations of the CFB rigs as integral units, which can be expressed graphically in form of operating windows for easy visualisation (Sections 5.5 and 5.6).

5.2 CFB solids circulation and pressure loop

Solids circulation in a CFB can be explained by analogy with water circulation in a loop (Basu, 2006). Figure 5.1 depicts such a system. In absence of aeration, water would not circulate; aeration provided to one of the columns lowers its hydrostatic head due to the lower density of the air-water mixture, triggering the water circulation by pressure difference at the base of the columns (points 1 and 2).

The mechanical energy balance between points 1 and 2 of the water loop in Figure 5.1 is (Kunii and Levenspiel, 1991):

$$P_2 - P_1 + \rho_{12} g\left(h_2 - h_1\right) + \Delta P_{12} = 0 \qquad (5.1)$$

where P_1 and h_1 are the pressure and height, respectively, at point 1 (idem for point 2), and ρ_{12} and ΔP_{12} the density and pressure drop due to friction, respectively, between points 1 and 2.

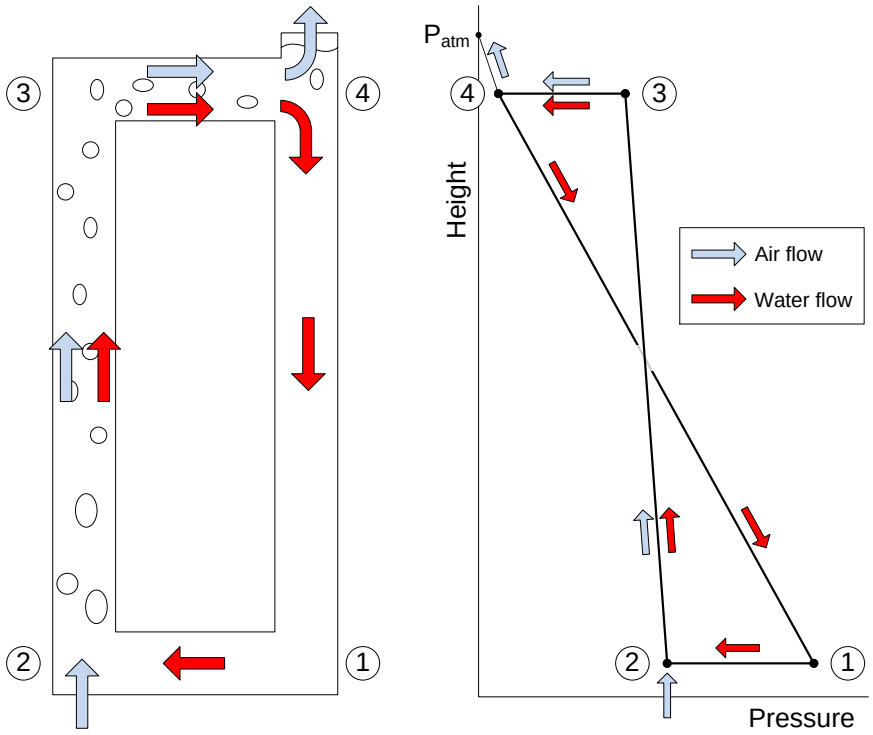

Figure 5.1. Water circulation by aeration (adapted from Basu, 2006) (left) and corresponding pressure loop (right)

Similarly, for the other three branches of the water loop in Figure 5.1:

$$P_3 - P_2 + \rho_{23} g(h_3 - h_2) + \Delta P_{23} = 0 \tag{5.2}$$

$$P_4 - P_3 + \rho_{34} g(h_4 - h_3) + \Delta P_{34} = 0 \tag{5.3}$$

$$P_1 - P_4 + \rho_{41} g(h_1 - h_4) + \Delta P_{41} = 0 \tag{5.4}$$

Taking into account that $h_1 = h_2$ and $h_3 = h_4$ and adding up all equations (5.1) to (5.4):

$$\rho_{23} g(h_3 - h_2) + \rho_{41} g(h_1 - h_4) + \Delta P_{12} + \Delta P_{23} + \Delta P_{34} + \Delta P_{41} = 0 \tag{5.5}$$

The equation above can be expressed in a more revealing form:

$$\rho_{41} gh = \rho_{23} gh + \sum \Delta P \quad ; \quad \text{where } h = h_3 - h_2 = h_4 - h_1 \tag{5.6}$$

Equation (5.6), corresponding to the whole pressure loop, states that the hydrostatic head of the dense vertical branch (left-hand side term) equals the sum of the

hydrostatic head of the aerated vertical branch (first term on the right-hand side) plus the friction losses of all branches (second term on the right-hand side). The value of water flow rate is (implicitly) defined in equation (5.6) through the relationship between the term $\Sigma\Delta P$ and fluid velocity.

Figure 5.2 and Figure 5.3 present the pressure loop diagram of the benchmark and novel CFB respectively. Despite the apparent differences between the CFBs and the water circuit, as long as the solids behave as a liquid (at least partially) circulation occurs by the same principle. As explained later in Section 5.3, the regenerator is the equivalent to the "dense vertical branch" in the water circuit. It provides the head for overcoming the pressure drop in the different sections of the CFBs, and hence enabling the circulation of solids in the loop. The regenerator head can be controlled by aeration, which in turn allows control of the solids circulation rate.

It can be observed in Figure 5.2 and Figure 5.3 that, due to the geometric configuration of the CFB rigs, the pressure at the upper end of the top downcomer (point 6) is higher than at the lower end (point 7). As a consequence, air from the cyclone (in case of the benchmark CFB) and the counter-current adsorber (novel CFB) percolates into the regenerator. In the real carbon capture process, this implies that the product CO_2 stream would get diluted with clean flue gas (benchmark CFB) or flue gas (novel CFB). This must be avoided given the very restrictive specification of >95% product CO_2 purity. Measures to minimise gas percolation into the regenerator could be:

- Minimise the pressure drop in the clean flue gas exhaust (branch 6-P_{atm} in the benchmark CFB pressure loop, and 5-P_{atm} in the novel CFB).
- Keep the solids level high in the top downcomer to maximise gas flow resistance.
- Novel CFB only: minimise the pressure drop of the counter-current adsorber (branch 5-6).
- Use a steam seal in the top downcomer (Kunii and Levenspiel, 1991).
- Increase the pressure in the regenerator by throttling the desorbed CO_2 exhaust (branch 7-P_{atm}). This is not advised because 1) it creates instabilities in the solids

circulation flow rate; 2) it would (in the real carbon capture process) increase the partial pressure of CO_2 in the regenerator, reducing the extent of sorbent regeneration and therefore the sorbent working capacity.

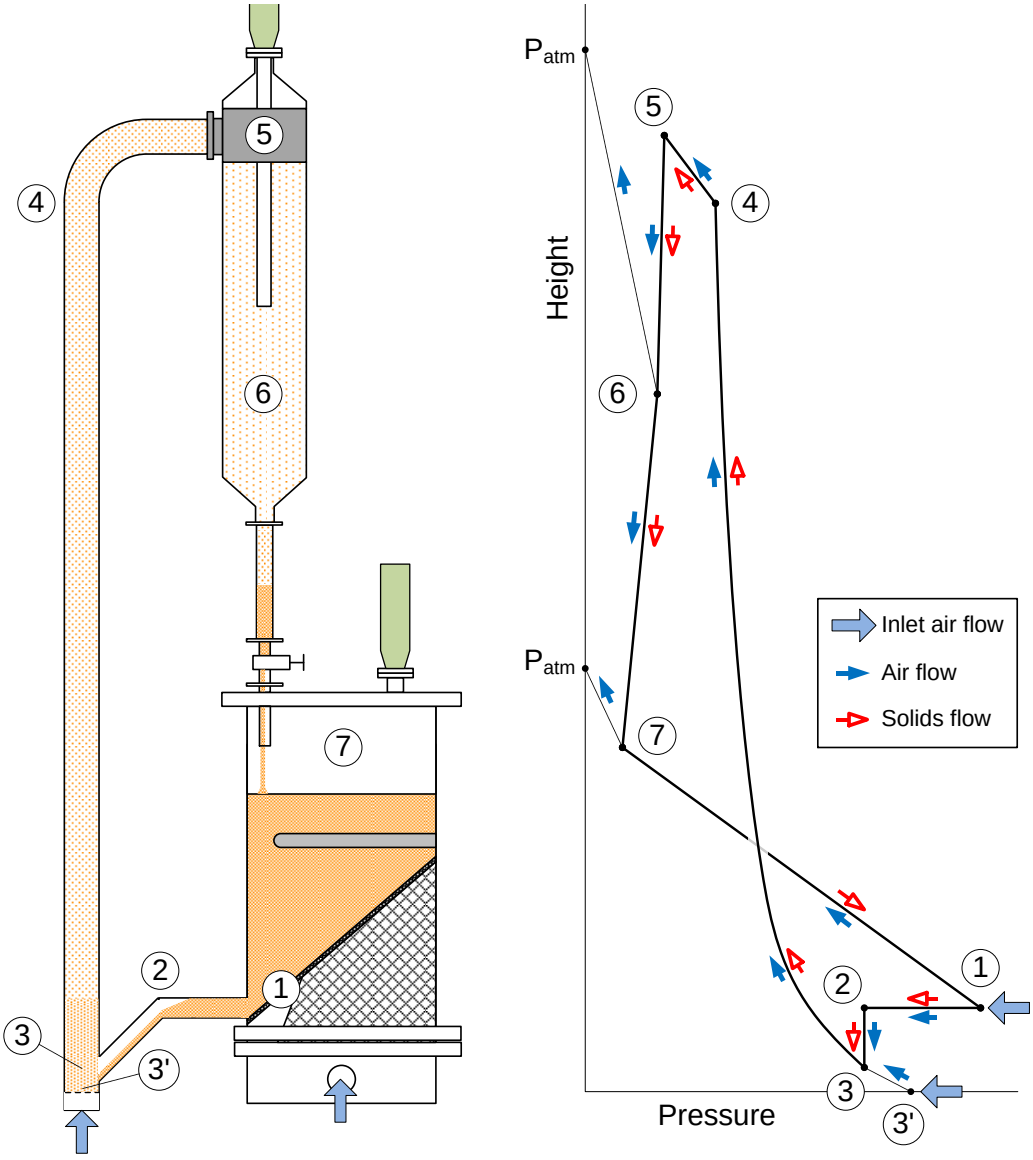

Figure 5.2. Pressure loop diagram of the benchmark CFB. The magnitude of pressure at different points is given for illustration purposes only

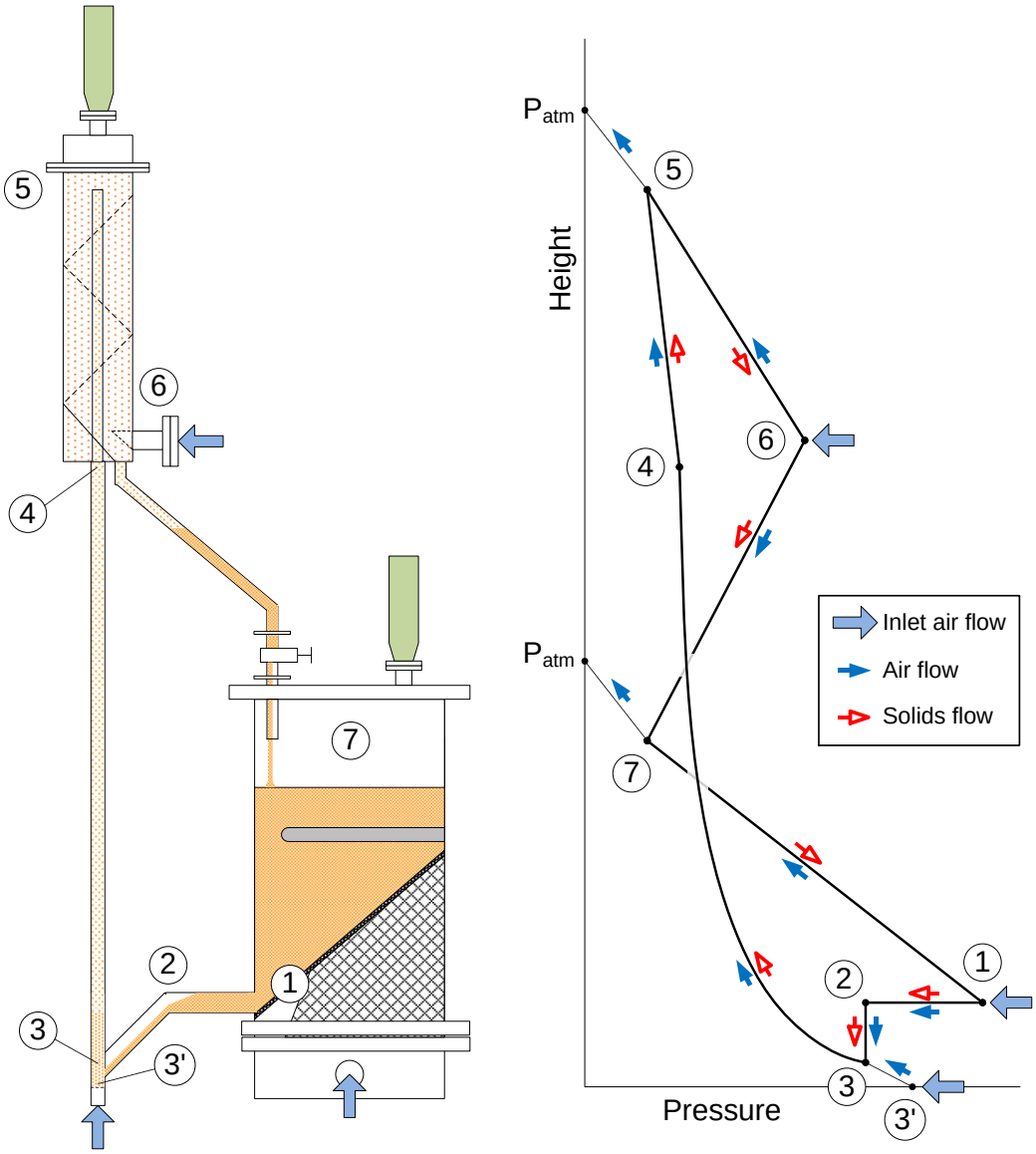

Figure 5.3. Pressure loop diagram of the novel CFB. The magnitude of pressure at different points is given for illustration purposes only

5.3 Regenerator

The description of the operating features of the regenerator as the solids feeder of the CFB rigs is approached by first studying it as a stand-alone system. This will set the foundations to later describe the operating characteristics of the regenerator as an integral part of a CFB system, as well as those of the CFB system itself. Note that, in the real carbon capture process, regenerator and solids feeder are two separate components of the CFB system and therefore the following operating description does not apply directly.

Consider the regenerator as a container open to atmosphere with the shape depicted in Figure 5.4. A bed of solids sits on the inclined support, with a height h_{reg} measured from the bottom of the solids outlet pipe. In the absence of aeration, the solids will not flow but only penetrate a short distance into the outlet pipe, equal to $l_r = D_{feeder}/\tan \theta_r$, where D_{feeder} is the inner diameter of the outlet pipe and θ_r the angle of repose of the solids.

Flow of solids is promoted by aeration at the bottom of the regenerator. Air can be introduced via the gas distributor (*primary air*) and through a dedicated nozzle (*lube air*). These forms of aeration are not equivalent and have different impacts upon the solids flow and system operation, as explained in Sections 5.3.1 and 5.3.2.

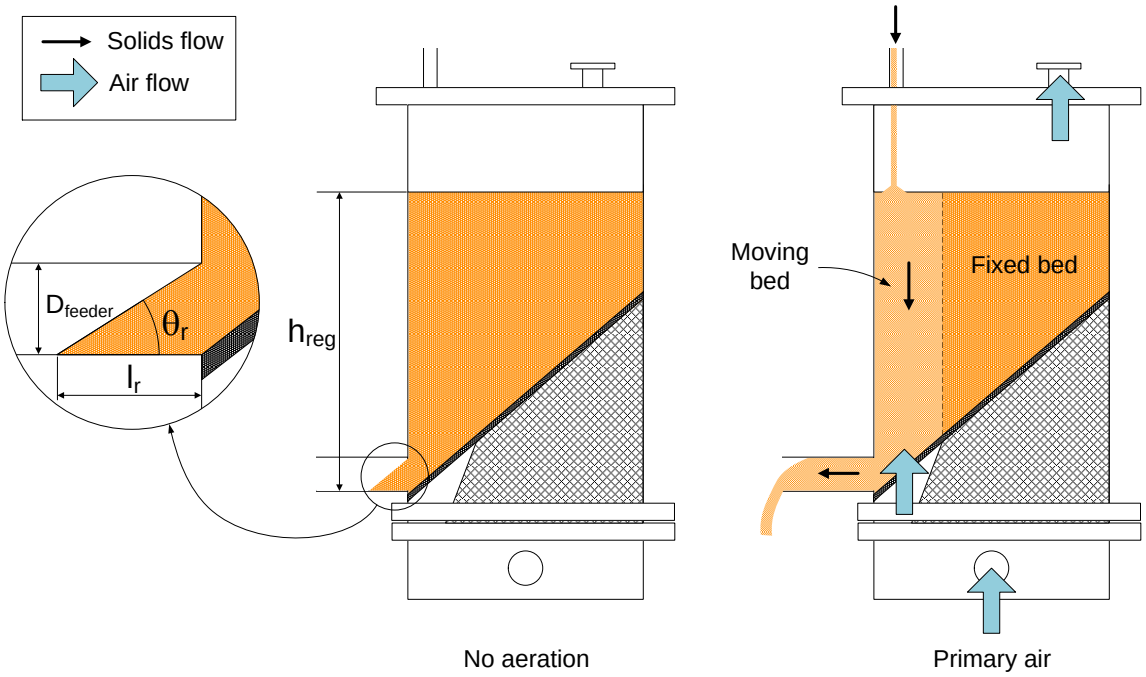

Figure 5.4. CFB regenerator without aeration (left) and aeration with primary air (right)

5.3.1 Aeration with primary air only

When aeration is provided to the regenerator with primary air only, solids start to flow in moving bed regime once the air flow rate is increased above a threshold value. Visual observation of the solid particles at the regenerator walls and bed surface reveals that the moving bed does not occupy the whole regenerator cross section but only a fraction adjacent to the solids outlet pipe; the rest apparently remains in fixed bed regime (Figure 5.4b). A detailed analysis of the solids flow in the regenerator main body using the PEPT technique is presented in Section 7.6.3.

The solids flow pattern in the outlet pipe was observed visually and is sketched in Figure 5.5. The particles flow in layers with decreasing horizontal velocities from top to bottom. A layer of stagnant solids is present at the bottom of the pipe, which becomes thinner as the solids flow rates increases.

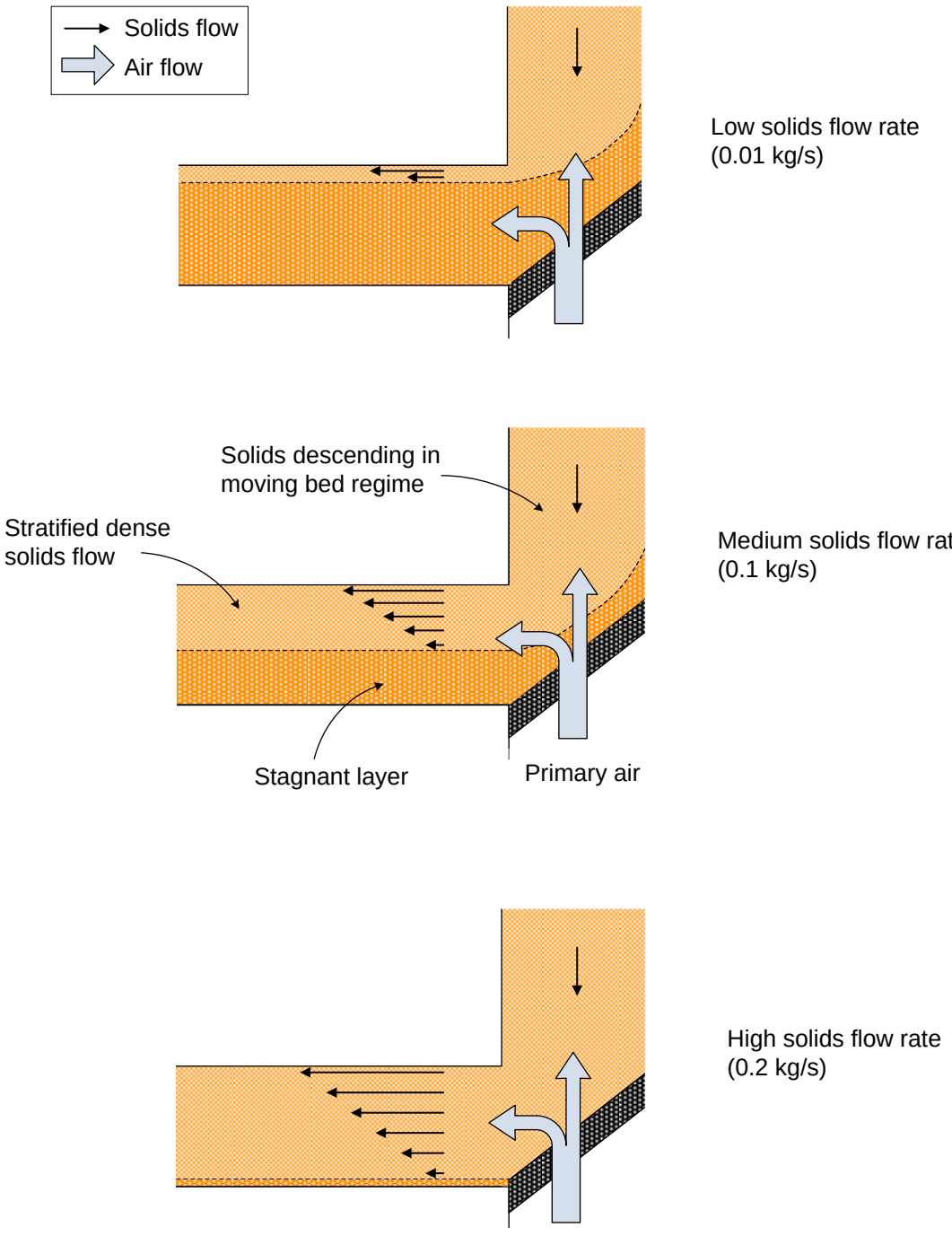

Figure 5.5. Solids flow pattern in regenerator solids outlet pipe. Aeration with primary air only

The pressure at the bottom of the regenerator ($P_{reg,bot}$) increases as the primary air flow rate increases. Figure 5.6 shows how the solids flow rate and $P_{reg,bot}$ vary with primary air flow rate for two different values of solids bed height in the regenerator. Note that the value of $P_{reg,bot}$ was not obtained directly but as the difference between

the pressure at the windbox and the pressure drop of the air distributor. The latter can be found in Appendix 2.

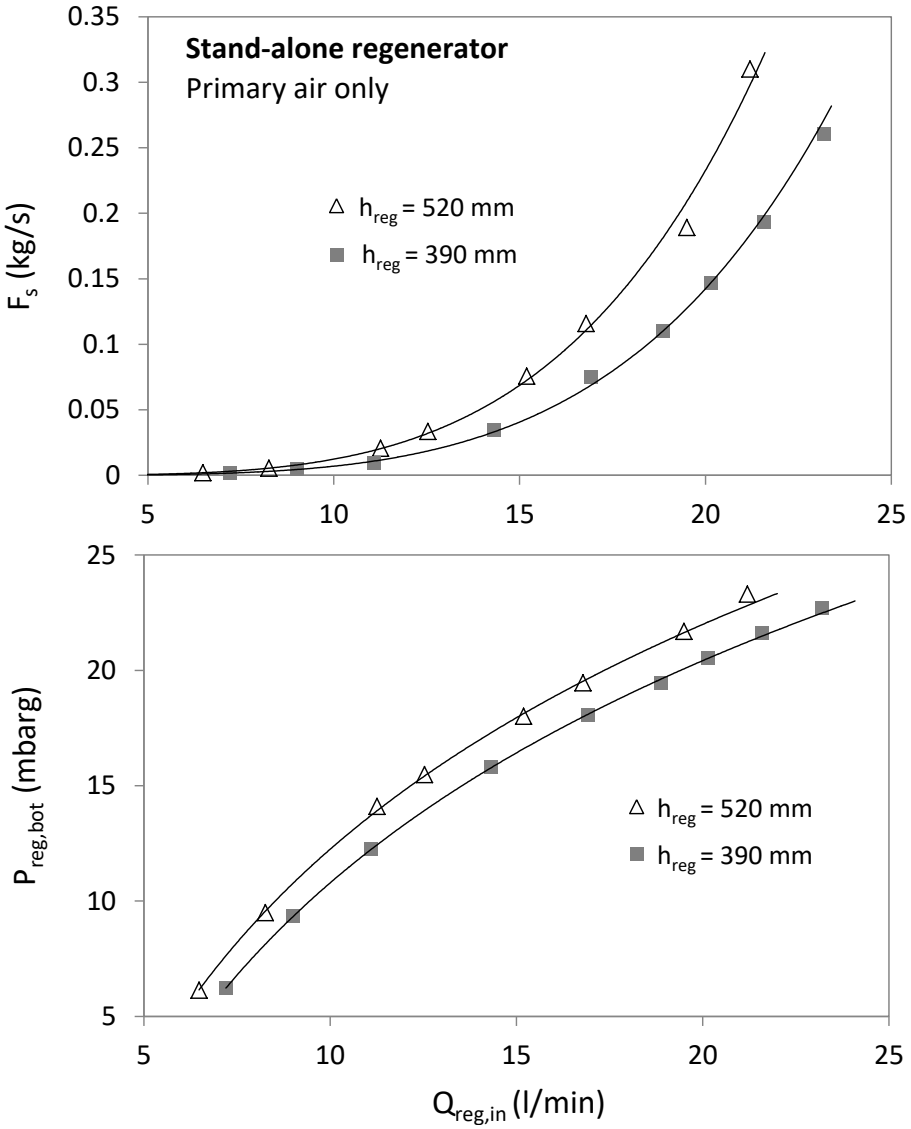

Figure 5.6. Solids flow rate (top) and regenerator bottom pressure (bottom) as a function of primary air flow rate and solids bed height. Stand-alone regenerator

The shape of the curves in Figure 5.6 and the solids flow pattern in the horizontal solids outlet pipe (Figure 5.5) are very similar to those of an L-valve (Knowlton and Hirsan, 1978). The comparison side by side between the regenerator and a typical L-valve/standpipe arrangement shown in Figure 5.7 reveals that both systems share similar features. This implies that the phenomena governing the working principles of the L-valve and the regenerator are likely to be similar as well.

Knowlton and Hirsan (1978) determined experimentally that, for a given L-valve geometry, the pressure drop of the lower branch of the L-valve (from the aeration point to the end of the horizontal pipe) is function of the solids flow rate and independent of the height of solids in the standpipe. The authors expected this result as they concluded from their observations that the solids flow rate was a function of the relative gas-solids velocity in this branch of the L-valve and, therefore, also function of the pressure drop. The role of the column of solids in the standpipe is merely to assist the L-valve providing the pressure needed at the aeration point. Should this observations be valid for the regenerator, combination of data in Figure 5.6 into an F_s-$P_{reg,bot}$ plot would yield a single line. This is indeed the case, as shown in Figure 5.8.

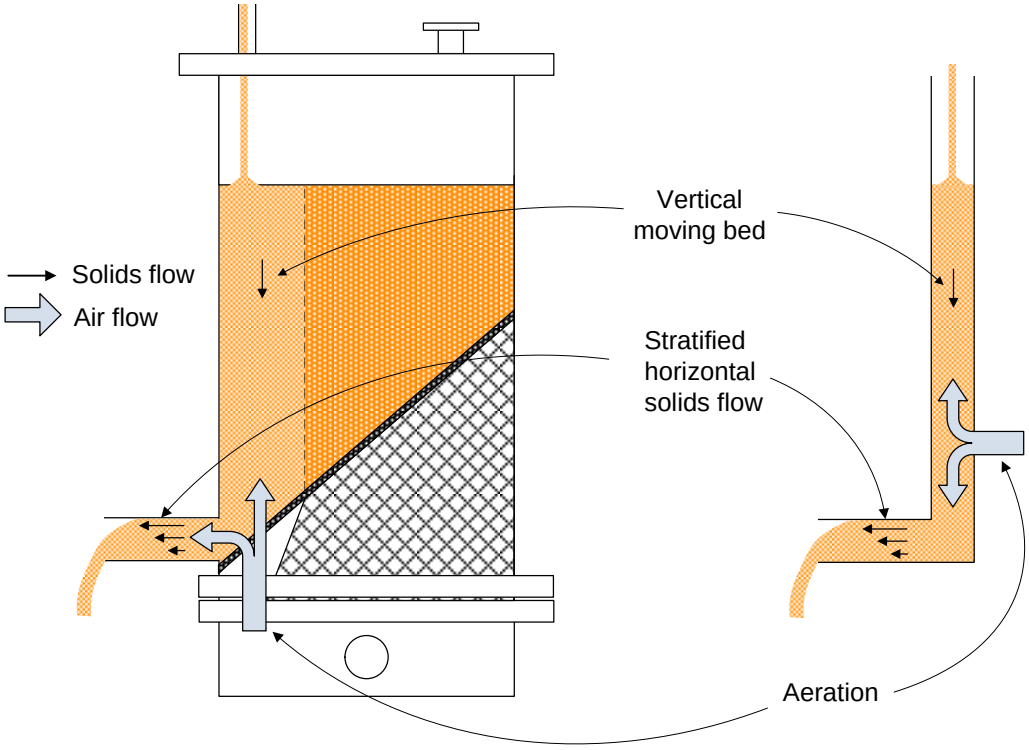

Figure 5.7. Comparison between the stand-alone regenerator (left) and an L-valve/ standpipe assembly (right)

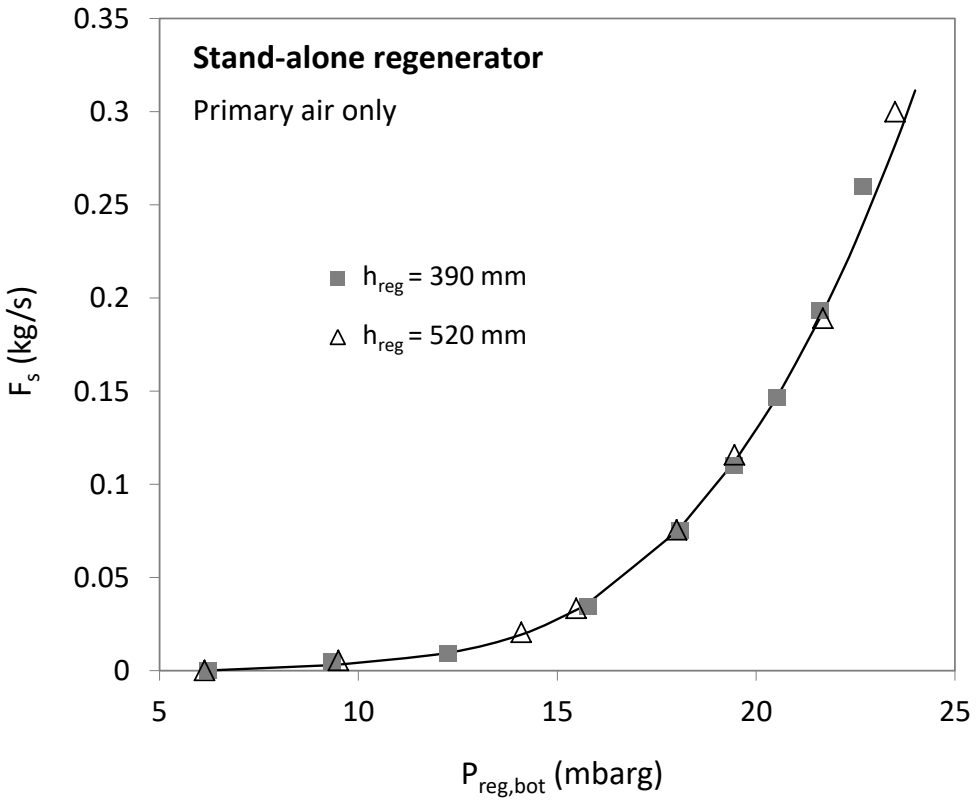

Figure 5.8. Solids flow rate as a function of regenerator bottom pressure. Stand-alone regenerator (primary air only)

5.3.2 Aeration with primary and lube air

The addition of air directly into the regenerator solids outlet pipe (lube air) facilitates the flow of solids by reducing the pressure needed at the bottom of the regenerator to deliver a given value of solids flow rate. Figure 5.9 shows the curve F_s-$P_{reg,bot}$ when 10 l/min of lube air is used in combination with primary air.

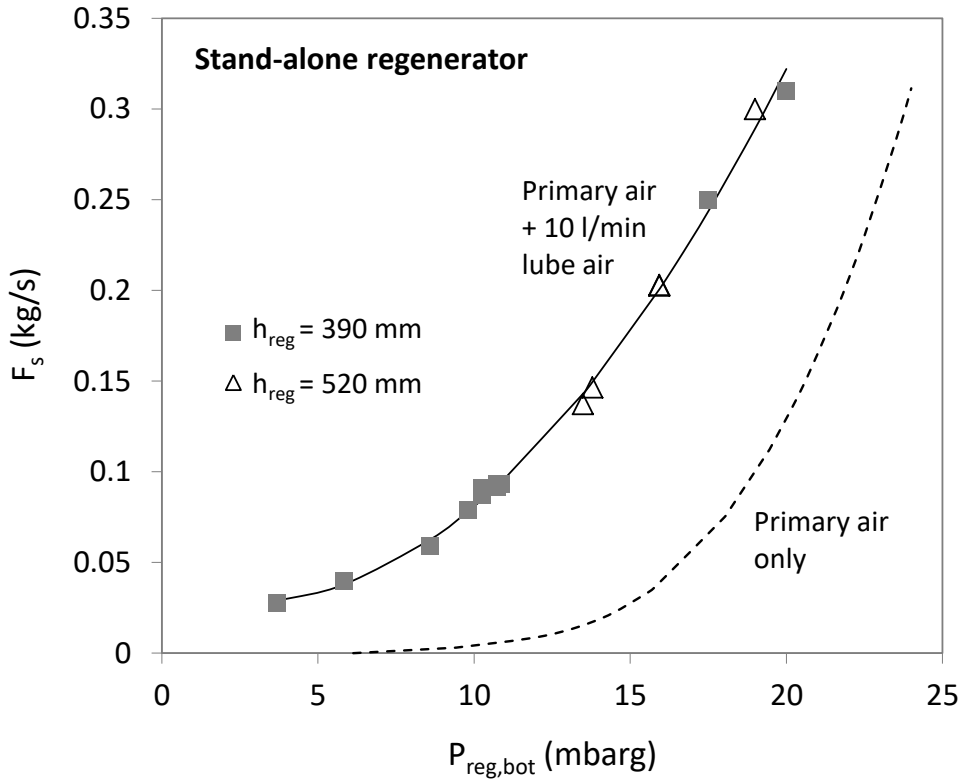

Figure 5.9. Solids flow rate as a function of regenerator bottom pressure. Stand-alone regenerator (primary air + 10 l/min of lube air)

The gas-solids flow pattern through the solids outlet pipe differs considerably from when only primary air is used for aeration, as illustrated in Figure 5.10. Lube air tends to segregate from the solids and flow in elongated, shallow bubbles along the top of the pipe. The sand pockets in between bubbles move at much higher velocity than the denser phase at the bottom of the pipe, which flows in a similar fashion as described in Section 5.3.1 for aeration with primary air only.

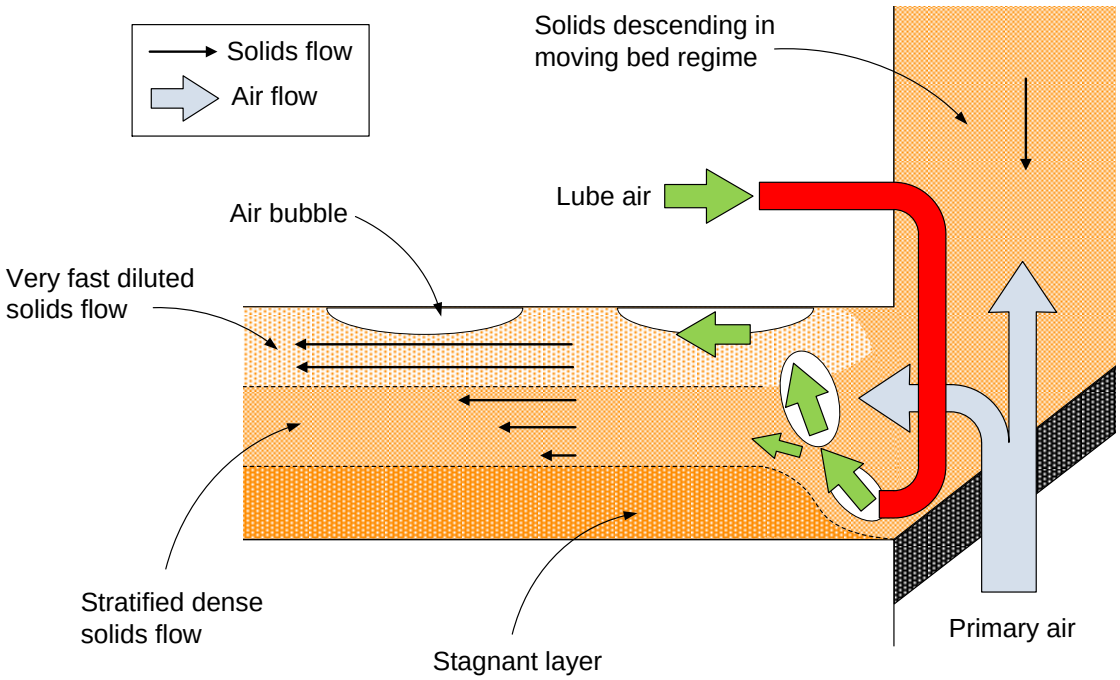

Figure 5.10. Air and solids flow pattern in regenerator solids outlet pipe. Aeration with primary air and lube air

5.3.3 Air flow distribution

The primary air stream (with a flow rate $Q_{reg,in}$) splits in two as it enters the regenerator, namely the fraction that leaves with the solids through the outlet pipe (Q_{Lv}) and the one flowing through the bed of solids in the regenerator main body (Q_{reg}). The mass balance dictates that:

$$Q_{reg,in} = Q_{Lv} + Q_{reg} \tag{5.7}$$

The value of Q_{Lv} is obtained for L-valves using eq. (5.7) and the Ergun equation adapted for moving beds to estimate the value of Q_{reg} (Knowlton and Hirsan, 1978). This is not a reliable approach in case of the regenerator since solids and (presumably) gas flow patterns are very different from those in a standpipe. Values of Q_{Lv} and Q_{reg} were instead determined experimentally using the setup depicted in Figure 5.11. The setup was run in steady-state for different values of primary air flow rate by keeping the height of the solids bed constant. The corresponding solids flow rates were obtained by weighing the amount of solids collected in a determined

period of time, ranging from very low values (0.004 kg/s) to the discharge rate limit of the solids reservoir (~0.3 kg/s).

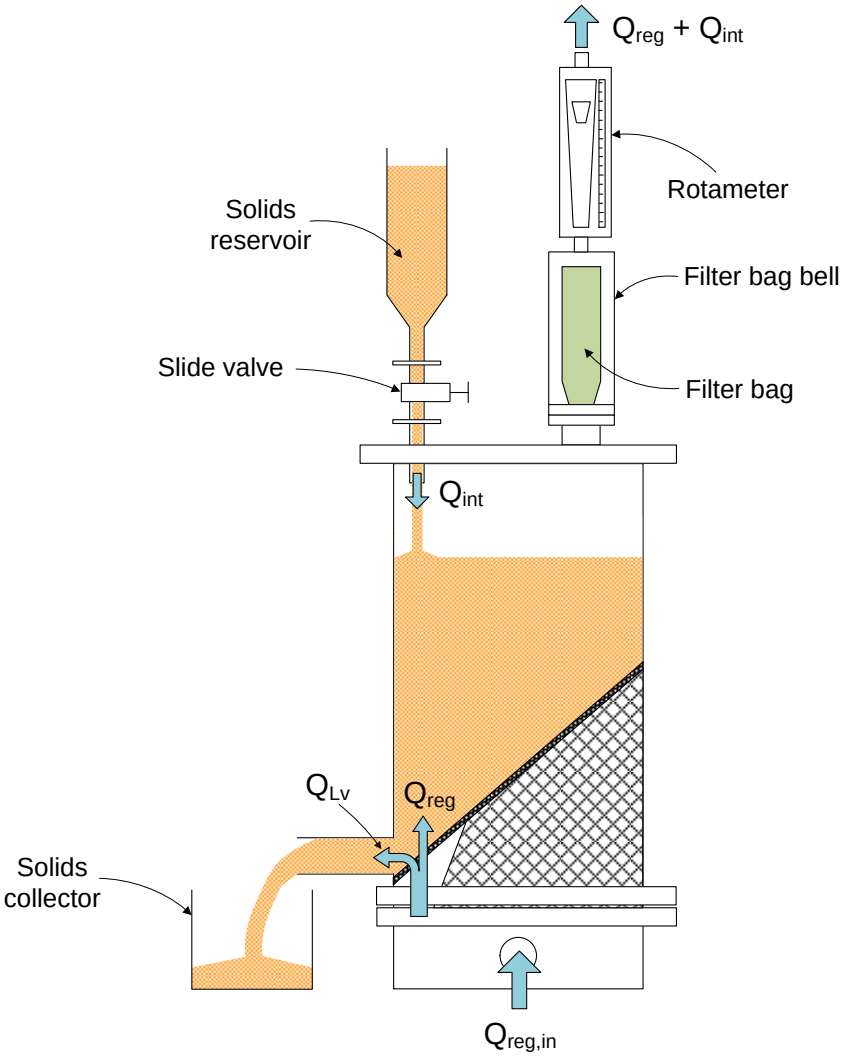

Figure 5.11. Setup for determination of the air flow distribution in the regenerator

The air mass balance for the setup in Figure 5.11 is:

$$Q_{reg,in} + Q_{int} = Q_{Lv} + \left(Q_{reg} + Q_{int}\right) \tag{5.8}$$

where Q_{int} is the flow rate of interstitial air from the solids reservoir, whose value can be estimated from the expression below:

$$Q_{int} = \frac{F_s}{\rho_s} \frac{\left(1 - \varepsilon_{s,int}\right)}{\varepsilon_{s,int}} \tag{5.9}$$

The value of $\varepsilon_{s,int}$ is estimated as the average between the solids fraction determined experimentally for compacted ($\varepsilon_{s,c}$) and loose bed ($\varepsilon_{s,l}$) (Tong, 2003):

$$\varepsilon_{s,int} \approx \frac{\varepsilon_{s,c} + \varepsilon_{s,l}}{2} = \frac{0.60 + 0.56}{2} = 0.58 \tag{5.10}$$

Figure 5.12 shows the curves F_s-Q_{Lv} for the regenerator operated with primary air and primary air + 10 l/min lube air.

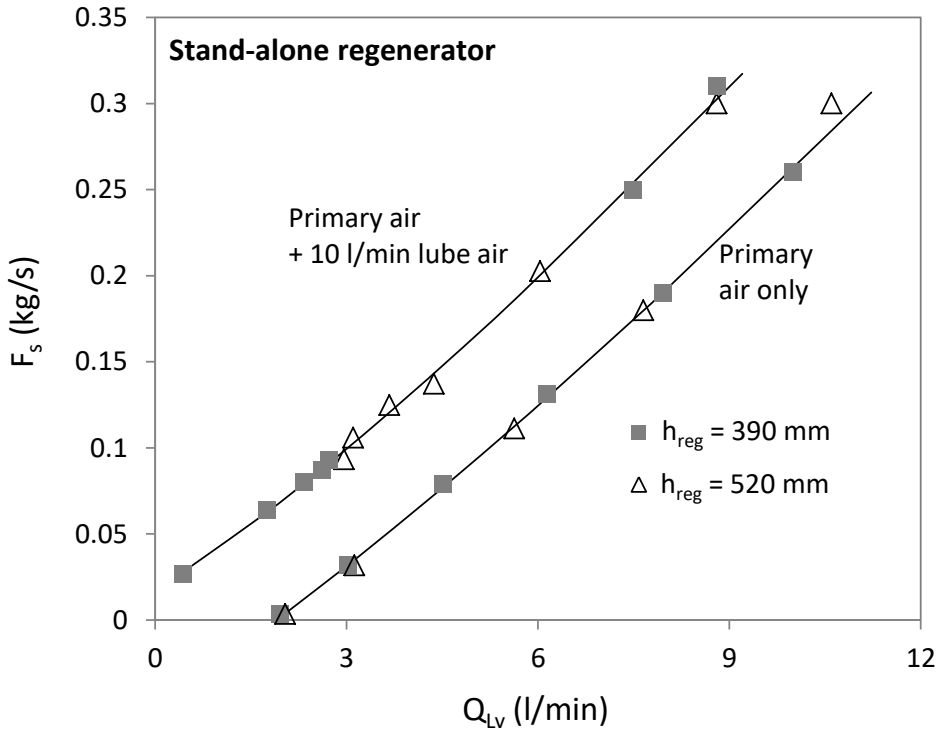

Figure 5.12. Solids flow rate as a function of gas flow leaving with the solids. Stand-alone regenerator

5.3.4 Limit of operation

Operation of the regenerator as a solids feeder must be kept within the moving bed regime as this enables control of the solids flow rate by manipulating the aeration rate and the solids bed height, as seen in Sections 5.3.1 and 5.3.2. In the fluidised state, the pressure at the regenerator bottom not only becomes insensitive with aeration flow rate, but also erratic due to the fluctuations caused by gas bubbles.

The setup depicted in Figure 5.13 was used to determine maximum stable values of $P_{reg,bot}$ achievable in the regenerator under the moving bed regime ($P_{reg,bot,max}$). The primary air flow rate was increased until vigorous bubbling was achieved in the regenerator, then slowly turned down until a constant value of $P_{reg,bot}$ was observed before it steadily decreased with the aeration rate. A slide constriction was installed in the outlet pipe to keep the solids flow rate below the discharge rate limit of the solids reservoir.

Figure 5.14 shows the values of $P_{reg,bot,max}$ obtained with the procedure above for three different values of solids bed height. These values are 70-80% of the corresponding to cylindrical beds with the same weight of solids and average cross-sectional area, similarly to what is observed in conical and tapered beds (Malek and Lu, 1965; Shi et al., 1984; Olazar et al., 1993).

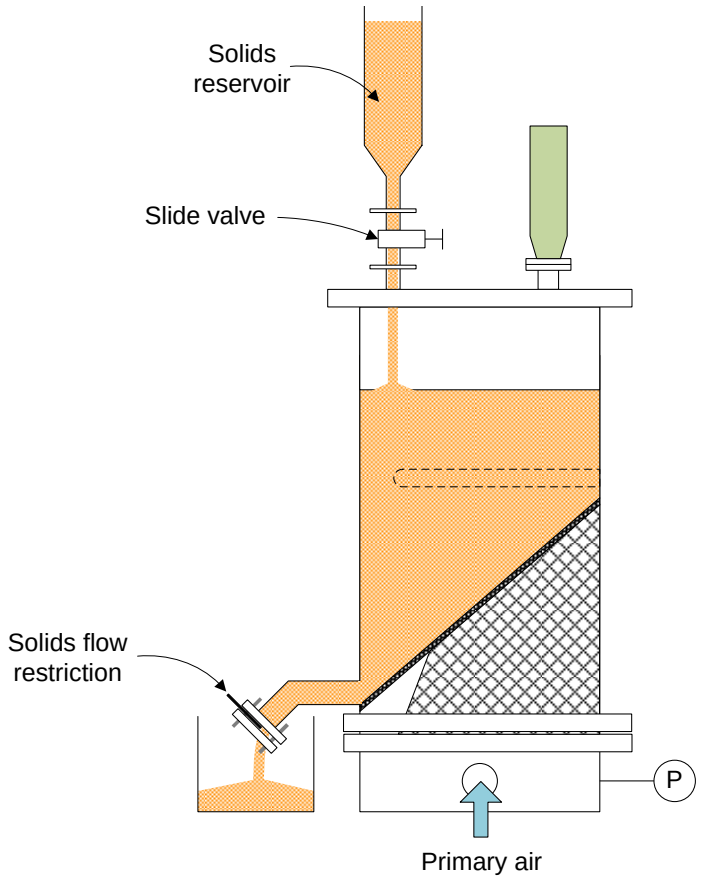

Figure 5.13. Setup for determination of the maximum pressure achievable at the regenerator bottom, $P_{reg,bot,max}$

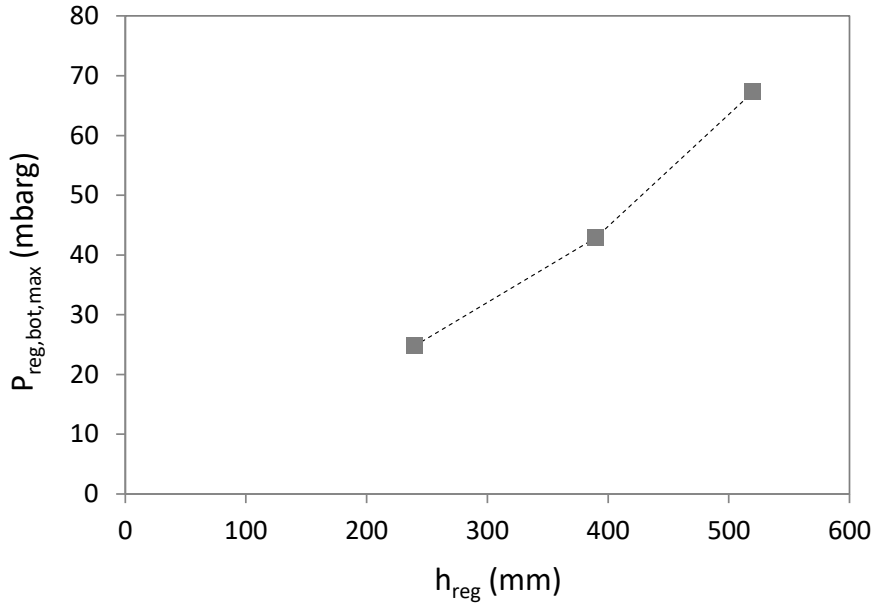

Figure 5.14. Values of $P_{reg,bot,max}$ as a function of solids bed height

5.4 Interaction regenerator-riser

The steady-state and dynamic operating behaviour of a CFB loop is ultimately the result of the interaction between the individual elements that make up the system, the most important of which is the interaction between the riser and the regenerator. The characteristics of this interaction are presented in this section.

5.4.1 Effect of primary air and lube air flow rate

Consider the CFB to be running at a certain initial steady state (point 1, Figure 5.15). Solids are discharged with a flow rate F_s from the regenerator into the riser. The superficial velocity of the upflowing air stream in the riser is $U_{g,ris}$.

Increasing the primary air flow rate increases the pressure at the bottom of the regenerator and the solids flow rate, as explained in Section 5.3. However, when regenerator and riser are integrated in the CFB system, the solids are discharged against the pressure at the riser bottom ($P_{ris,bot}$) rather than to the atmosphere. The extra pressure needed at the regenerator bottom to deliver the solids at the same flow rate is accounted for in the F_s-$P_{reg,bot}$ diagram by a shift of the curve towards higher pressures. If the air flow rate in the riser is kept constant, the gas-solid mixture in the riser becomes increasingly denser with further increase in the solids flow rate, increasing the hydrostatic head of the air-solids mixture and therefore the pressure at the riser bottom. This trend can be kept until the operating limit of either riser or regenerator is reached, i.e. classical (also called C-type, see Bi et al., 1993) choking velocity (U_{Cch}) in the riser (point 3, Figure 5.15a) or fluidisation in the regenerator (point 3, Figure 5.15b). In case the latter becomes the limiting factor in CFB operation, a fraction of primary air can be substituted by lube air to bring down the pressure at the bottom of the regenerator (point 2a, Figure 5.16) or to push the system towards higher solids flow rates (point 2b, Figure 5.16).

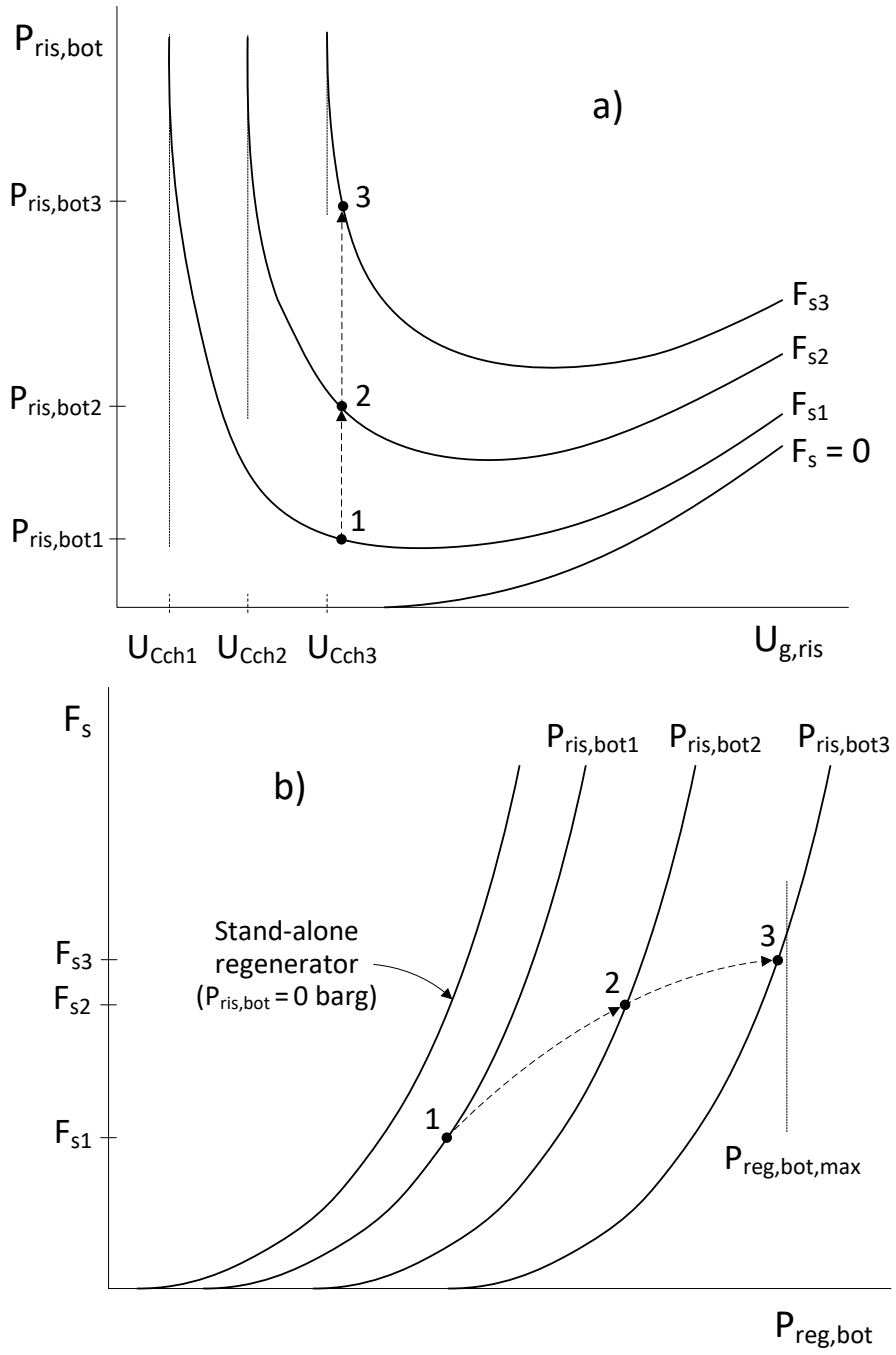

Figure 5.15. Operating diagrams of riser (a) and regenerator (b) showing the operating path resulting from the riser-regenerator interaction at increasing primary air flow rate and constant riser air velocity

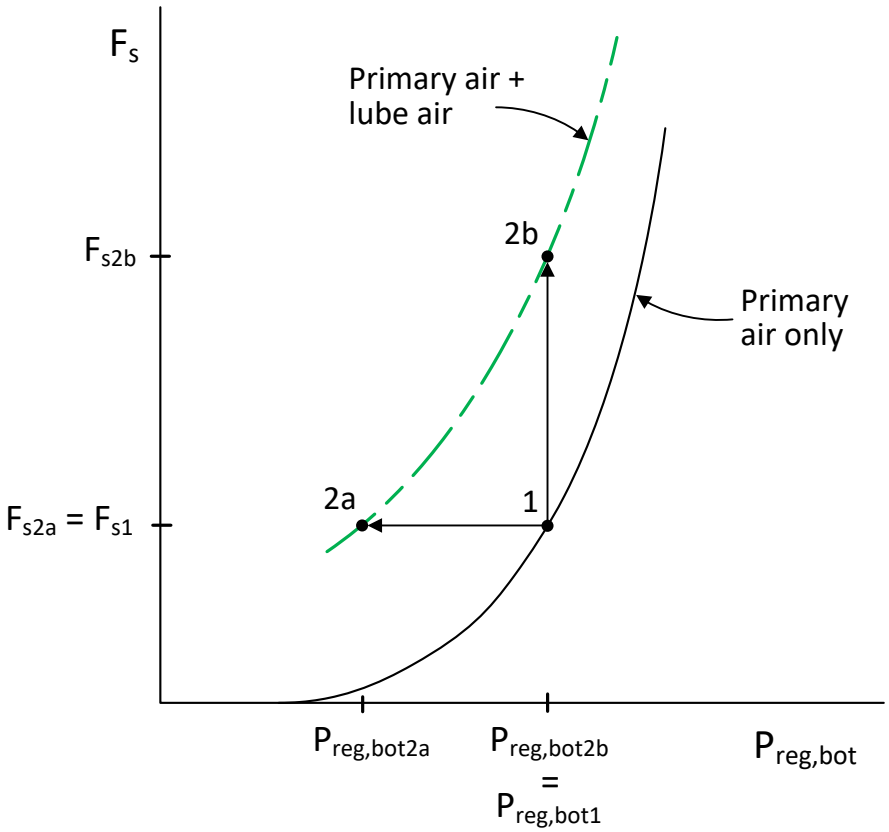

Figure 5.16. Effect of lube air in the regenerator F_s-$P_{reg,bot}$ diagram

5.4.2 Effect of riser air flow rate

Consider the CFB to be now at the initial operating point 1 in Figure 5.17. The air flow rate (or rather the air superficial velocity) in the riser is then increased while keeping constant the pressure at the regenerator bottom. The concentration of solids in the riser would tend to decrease (assuming the solids flow rate remained constant) and so would the pressure at the riser bottom due to a lower hydrostatic head of the gas-solid mixture. The higher pressure difference between regenerator and riser results in an increase in solids flow rate, counteracting the mixture dilution in the riser. These two opposite effects eventually balance out to bring the CFB to a new operating point represented by point 2 in Figure 5.17, which features a higher solids flow rate and lower pressure at the riser bottom than point 1.

This trend can be maintained for increasing values of air velocity in the riser until the gas-wall friction pressure drop starts having a greater impact than the decrease in hydrostatic head (point 3). At this precise point the solids flow rate has reached the maximum value attainable for the given constant value of $P_{reg,bot}$. Higher values of riser air velocity will increase the pressure at the riser bottom, to which the regenerator reacts by decreasing the solids flow rate (point 4).

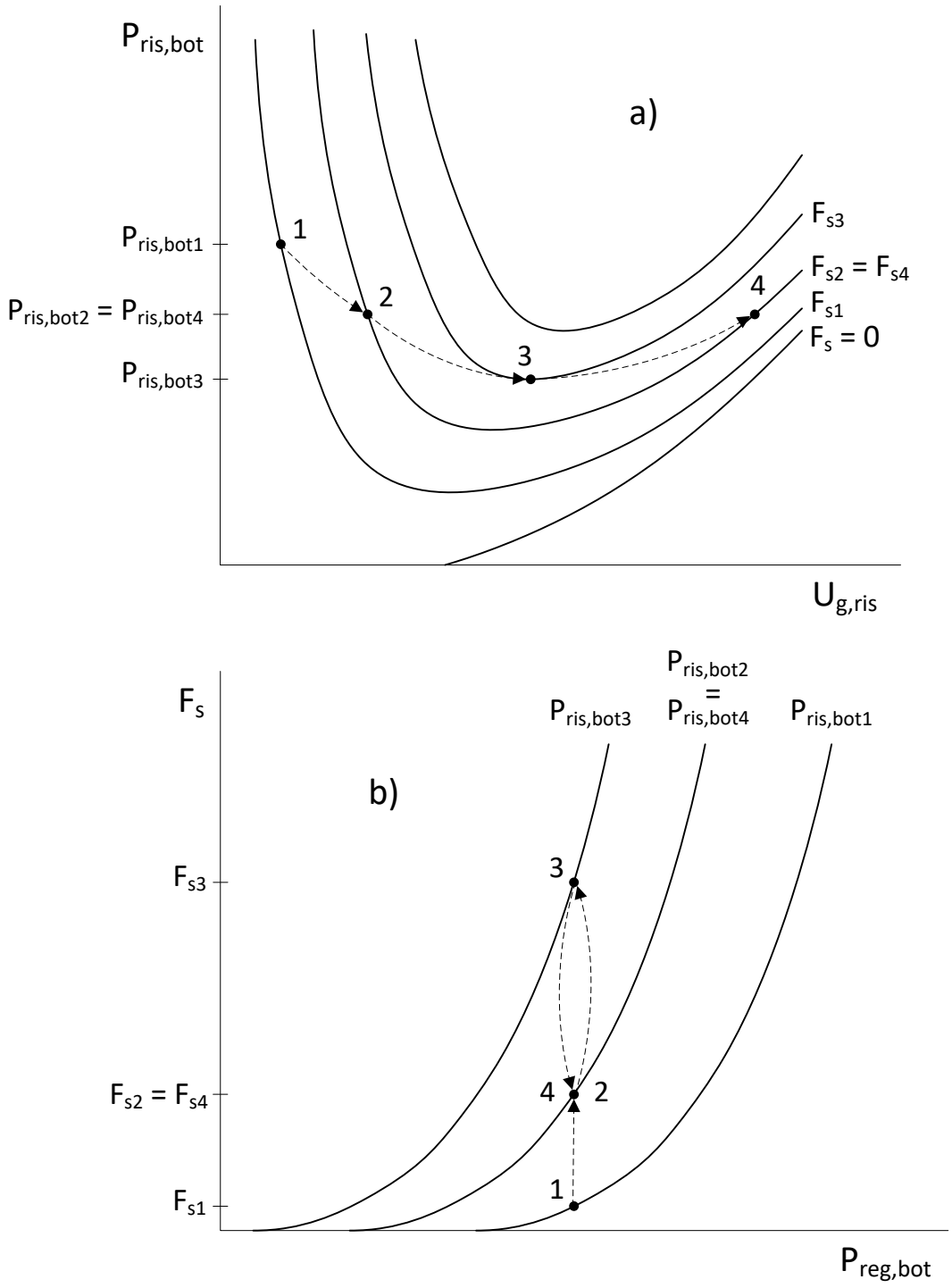

Figure 5.17. Operating diagrams of riser (a) and regenerator (b) showing the operating path resulting from the riser-regenerator interaction at increasing riser air velocity and constant regenerator bottom pressure

5.5 Benchmark CFB

5.5.1 Operating characteristics

Figure 5.18 shows the F_s-$P_{reg,bot}$ curve for two different values of riser air flow rate. The curves feature an additional pressure demand above a certain value of solids flow rate, reflected as a "jump" of the F_s-$P_{reg,bot}$ curves towards higher values of $P_{reg,bot}$. This is caused by constriction of the 2-phase flow as solids suddenly start to settle forming a dune in the horizontal section of the riser top (Harris, 2002).

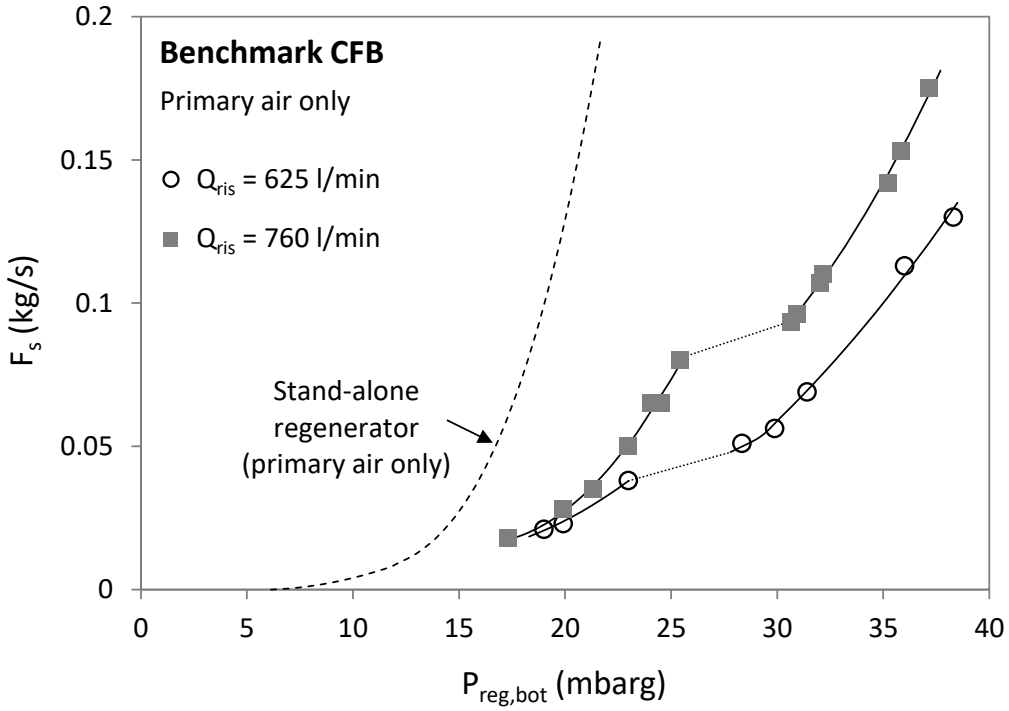

Figure 5.18. Solids circulation rate as a function of regenerator bottom pressure. Benchmark CFB

Lube air can be used to lower the pressure demand on the regenerator at high solids flow rates, as shown in Figure 5.19. For a given value of solids flow rate, the effect of lube air on reducing the required value of $P_{reg,bot}$ is more pronounced at low values of lube air flow rates (0-10 l/min), and present a maximum effect somewhere in the range 30-50 l/min (Figure 5.20). Above this value the pressure at the regenerator bottom increases again, indicating that the gas-wall friction pressure drop in the solids feeder starts to outweigh the pressure-reducing effect of lube air.

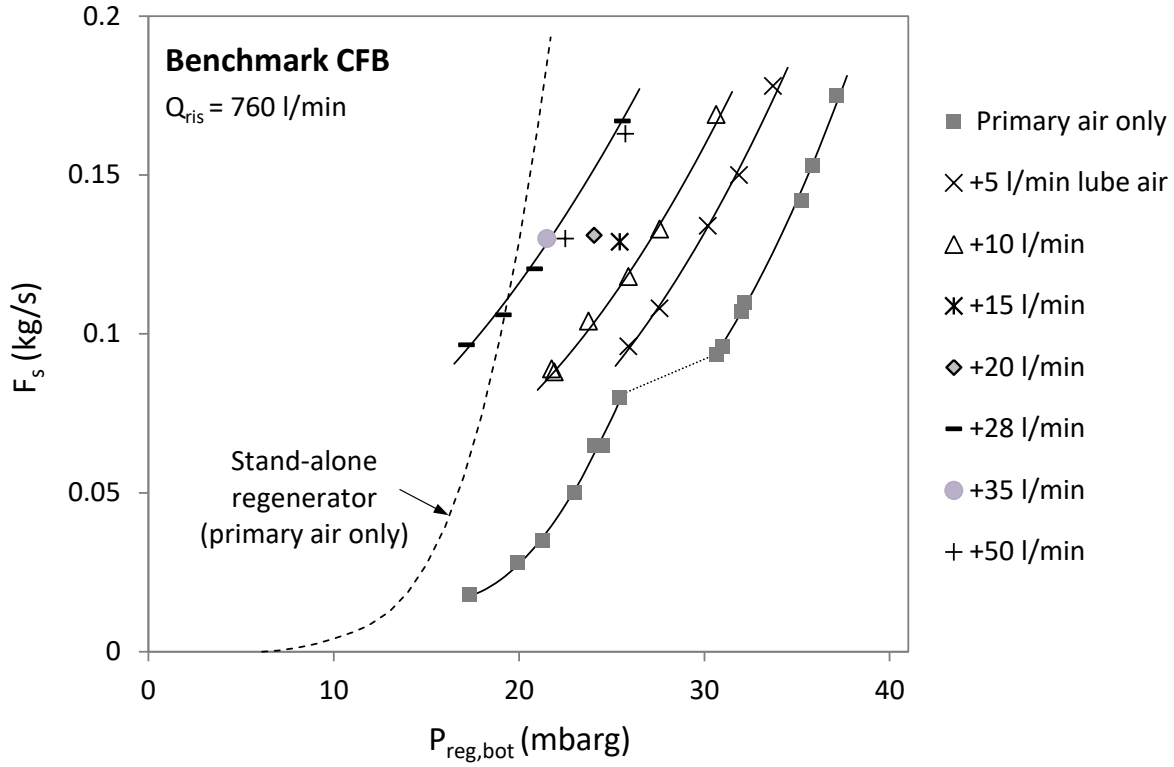

Figure 5.19. Solids circulation rate as a function of regenerator bottom pressure for several values of lube air flow rate. Benchmark CFB

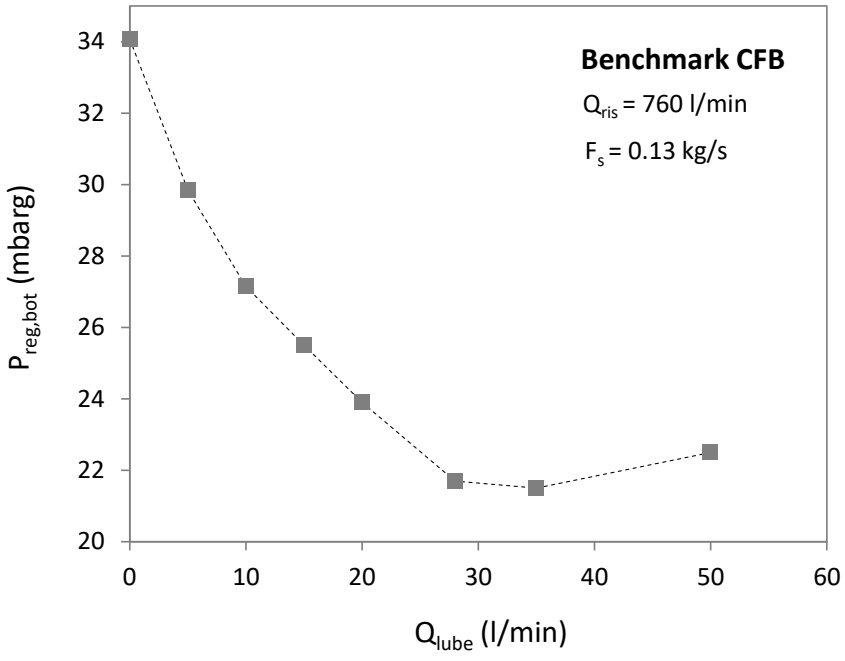

Figure 5.20. Effect of lube air flow rate on regenerator bottom pressure at constant solids circulation rate. Benchmark CFB

Figure 5.21 shows the pressure at the regenerator bottom as a function of primary air flow rate. The value of $P_{reg,bot}$ is limited to 30 mbarg to prevent low-frequency oscillations (0.1-0.4 Hz) in the solids flow rate. Visual observations suggest that these low-frequency oscillations are caused by the dynamic interaction between the riser and the solids feeder, but a thorough study has not been carried out. Zhang et al. (1998) found a similar behaviour in a CFB with a standpipe and L-valve, and postulated that the oscillations originated in the standpipe and propagated to the riser through the L-valve.

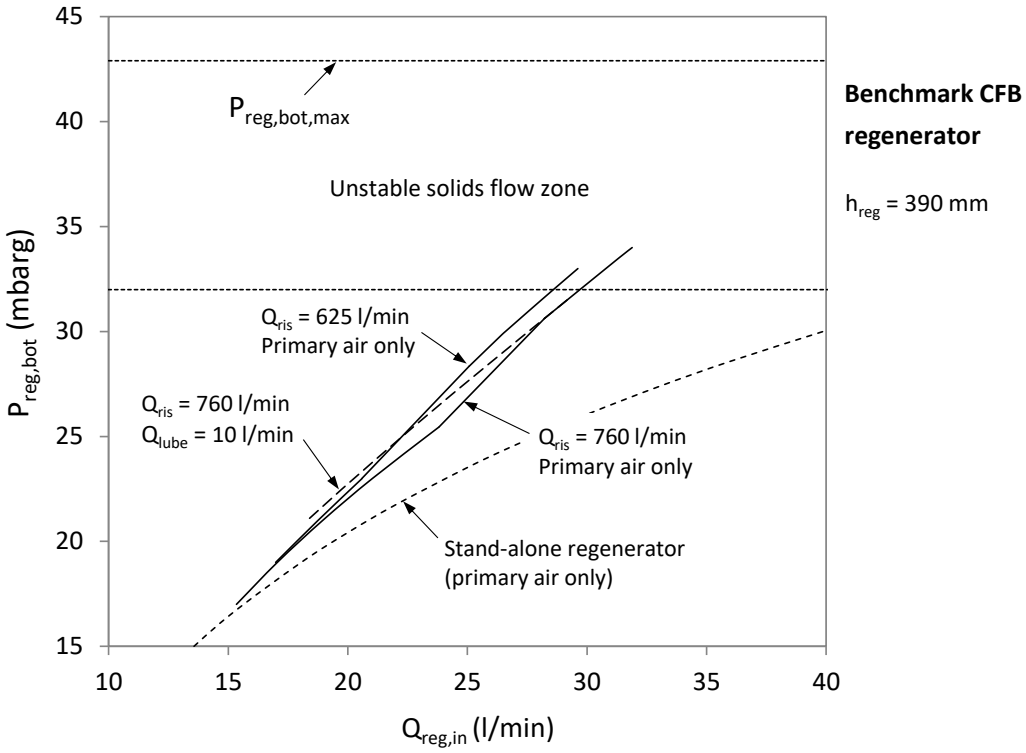

Figure 5.21. Regenerator bottom pressure as a function of primary air flow rate. Benchmark CFB

5.5.2 Operating window

Figure 5.22 presents the operating window of the benchmark CFB. The maximum air flow rate in the riser is limited to 760 l/min by the compressor, whereas a minimum value of 625 l/min is recommended in order to avoid serious blockage of the horizontal section at the riser top. The maximum solids flow rate achievable is around 0.25 kg/s.

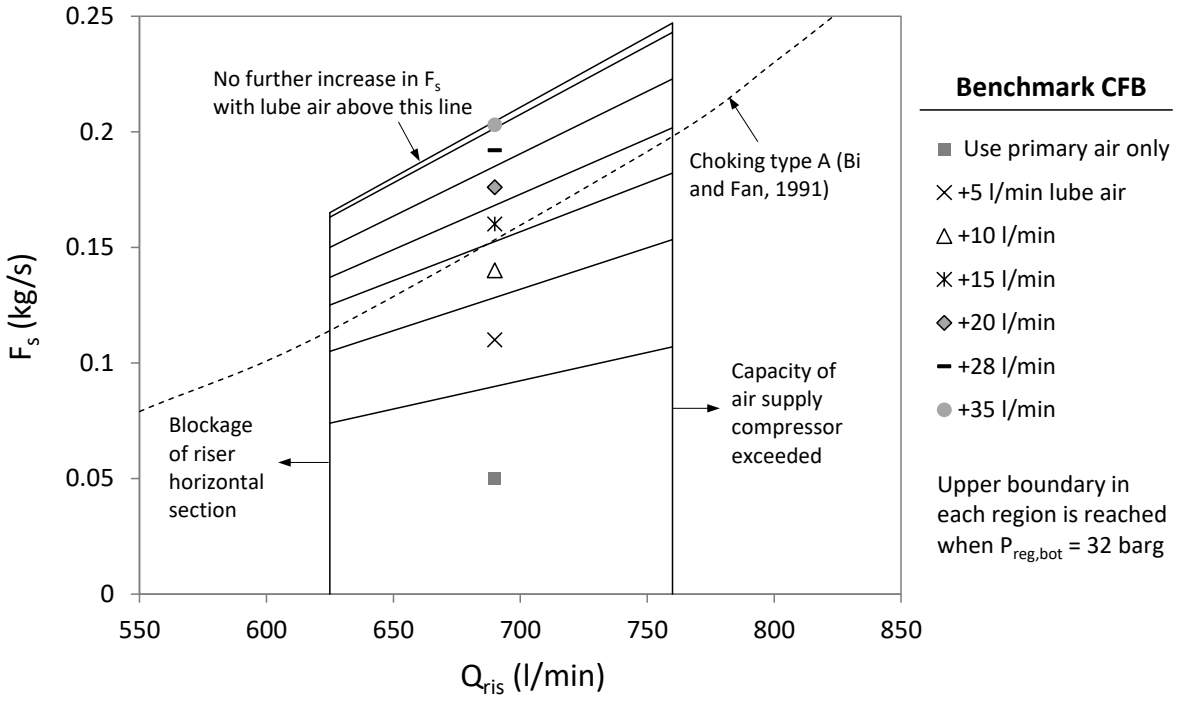

Figure 5.22. Operating window of the benchmark CFB

5.5.3 Riser pressure profiles

Figure 5.23 presents the pressure profiles for the benchmark CFB riser at different values of solid flux and air velocity. The values of pressure increase overall, especially at low gas velocity, due to the back-pressure caused by the aforementioned flow constriction in the horizontal riser section. The shape of the profiles change progressively towards higher pressures at the riser bottom when increasing solids flux and decreasing gas velocity. This is due to the combined effect of solids acceleration and the formation of a denser suspension at the bottom (A-type choking, see Bi et al., 1993), evidencing the approach to the flow regime boundary between pneumatic transport and fast fluidisation.

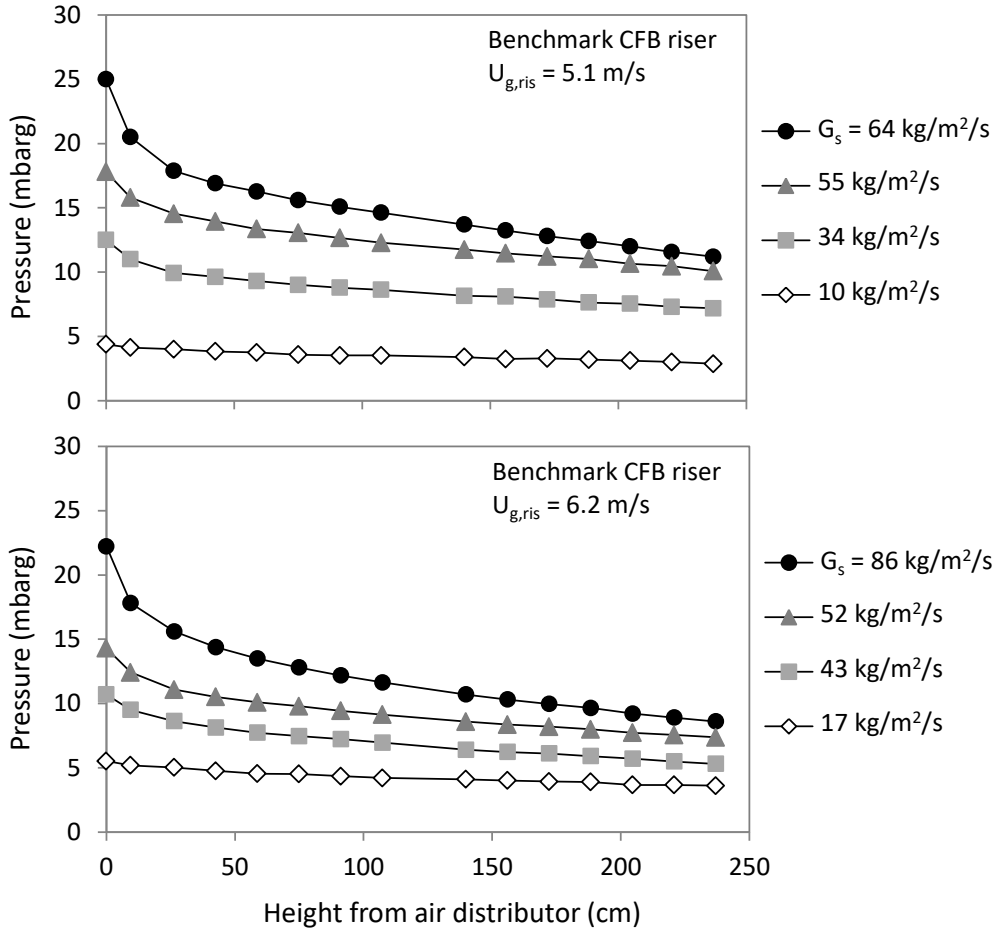

Figure 5.23. Pressure axial profiles. Benchmark CFB riser

5.5.4 Riser solids fraction profiles

The solids fraction profiles in the riser are obtained from the pressure profiles presented above. In an attempt to subtract the contribution of solids acceleration, the momentum balance of gas and solid phases in the riser is used in a similar approach to Stemerding (1962) and Weinstein and Li (1989):

In a 1-dimensional, two-phase, steady state system of constant cross section and turbulent flow, the momentum balance is (Bird et al., 1960; Brandani and Zhang, 2006):

$$\frac{d}{dz}\left(\varepsilon\rho_g u_g^2 + \varepsilon_s\rho_s u_s^2\right) = -\frac{dP}{dz} - \left(\varepsilon\rho_g + \varepsilon_s\rho_s\right)g - F_{gw} - F_{sw} - F_{ss} \qquad (5.11)$$

where F_{gw}, F_{sw} and F_{ss} are the contributions of gas-wall, solid-wall and solid-solid interactions, respectively. The value of F_{gw} is the experimental pressure drop per unit length of riser (available in Appendix 2). F_{sw}, F_{ss}, and variations of gas density and velocity are assumed negligible.

Solving (5.11) for dP/dz:

$$\frac{dP}{dz} = -\frac{d}{dz}\rho_s \varepsilon_s u_s^2 - \left(\varepsilon\rho_g + \varepsilon_s\rho_s\right)g - F_{gw} \tag{5.12}$$

Taking into account that $\varepsilon = 1 - \varepsilon_s$, multiplying by dz and integrating downwards from the riser top (z = L) to an arbitrary position z in the riser length:

$$P(z) = P_L - \rho_s\left[\varepsilon_s(z)u_s^2(z) - \varepsilon_{s,L}u_{s,L}^2\right] - \rho_g g\int_L^z\left[1-\varepsilon_s(z)\right]dz - \rho_s g\int_L^z \varepsilon_s(z)dz - F_{gw}(z-L) \tag{5.13}$$

The solids fraction and solids velocity profiles $\varepsilon_s(z)$ and $u_s(z)$ can be obtained by reconstruction of the experimental pressure profile using equation (5.13). The values of ε_s and u_s are not independent but related by the mass balance: $G_s = \rho_s\varepsilon_s u_s$. The values of $\varepsilon_{s,L}$ and $u_{s,L}$ are chosen under two conditions: 1) the slip velocity is equal or higher that the terminal velocity; 2) after integration, $u_s(0) = 0$ (solids velocity zero at the bottom of the riser).

An example of solids fraction profile before and after correction for acceleration is shown in Figure 5.24. The "original" solids fraction profile was obtained piece-wise (every two points) from the pressure balance fully attributing the pressure drop to the hydrostatic head of the gas-solid mixture. The difference between the two curves is very substantial at the very bottom of the riser, where the pressure gradient presents its maximum value. It can be argued, as done for example by Stemerding (1962) and Chan et al. (2009), that part of the contribution to the pressure gradient at the bottom of the riser could be due to the hydrostatic head of solids aggregates (i.e. annulus, streaks, clusters, etc.) that are denser than the single particle, leading to an overestimation of the contribution to pressure drop due to acceleration. This is however not detrimental in the sense that underestimated values of solids fraction

lead to conservative values of performance when used in the adsorber model presented in Chapter 3.

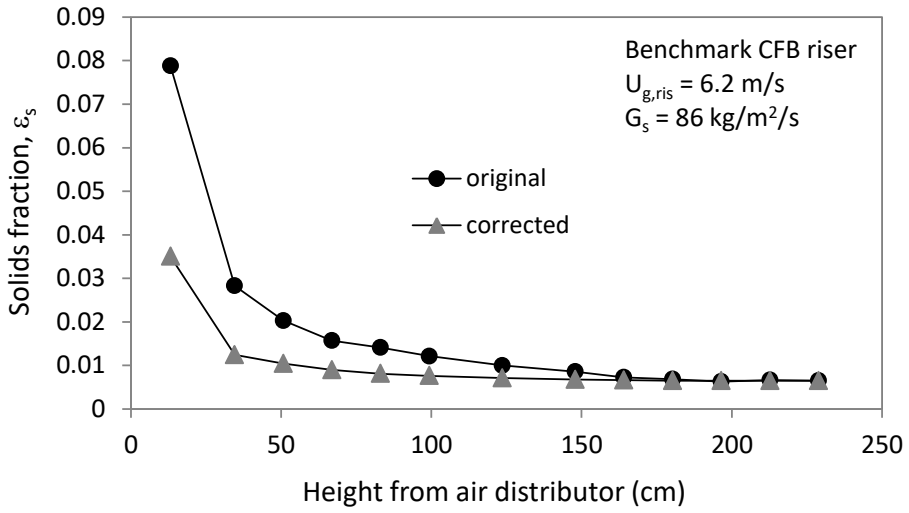

Figure 5.24. Comparison between the "original" and "corrected for solids acceleration" solids fraction axial profile. Benchmark CFB riser

Figure 5.25 shows the corrected solids fraction profiles corresponding to the pressure profiles for the benchmark CFB previously presented in Figure 5.23. The averaged values along the riser length can be correlated with the solid flux and the superficial gas velocity in form of axially-averaged slip velocities ($u_{slip,av}$). From the definition of slip velocity and the mass balance of solids along the riser:

$$G_s = \rho_s \varepsilon_{s,av} \left[\frac{U_{g,ris}}{(1-\varepsilon_{s,av})} - u_{slip,av} \right] \tag{5.14}$$

The values of $u_{slip,av}$ for the benchmark CFB are presented in Figure 5.26.

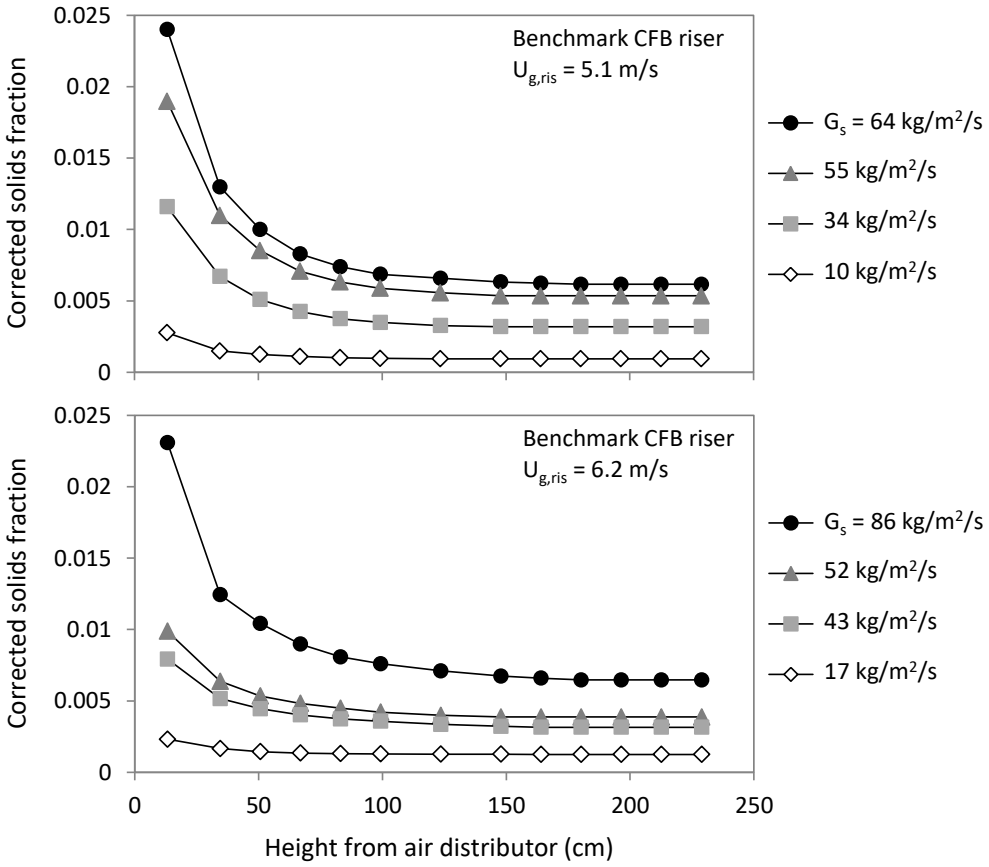

Figure 5.25. Solids fraction (corrected for solids acceleration) axial profiles. Benchmark CFB riser

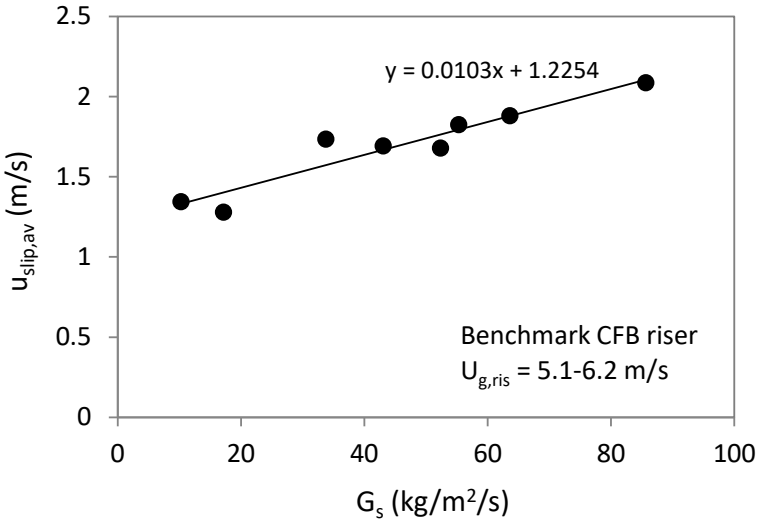

Figure 5.26. Axially-averaged slip velocity as a function of solids flux. Benchmark CFB riser

5.6 Novel CFB

5.6.1 Operating characteristics

Figure 5.27 shows the F_s-$P_{reg,bot}$ curves for several riser air flow rates, ranging from 86 l/min to 182 l/min. The slope of the curves steepens with increasing riser air flow rate, evidencing the characteristics of the steady-state interaction between riser and regenerator described in Section 5.4.1.

Most of the experimental data in Figure 5.27 were obtained in absence of air flow in the adsorber ($Q_{ads,in} = 0$) due to limitations in the air supply capacity. However, the effect of the adsorber on the rig when $Q_{ads,in} > 0$ is easy to account for as it is limited to a small increase in pressure required at the bottom of the regenerator (see data for $Q_{ads,in} = 640$ l/min in Figure 5.27). This extra pressure corresponds to the increase in pressure drop in the adsorber gas outlet (pipe + filter bag), which is only noticeable when the total air flow through exceeds 450-500 l/min. In the most demanding case (total air flow rate fed to the CFB around 840 l/min), the increase in pressure drop was around 2 mbar.

The use of lube air at low flow rates (5-10 l/min) has a positive effect in stabilising the solids circulating rate and system pressures, whereas higher flow rates of lube air introduce very little improvement (see Figure 5.28). In view of this, lube air is recommended to be used in an "on/off" fashion by using either zero or 10 l/min, rather than regulated as needed as it was explained in Section 5.5 for the benchmark CFB configuration.

Figure 5.29 shows the pressure at the regenerator bottom as a function of primary air flow rate. The value of $P_{reg,bot}$ is limited to 30 mbarg to prevent low-frequency oscillations (0.1-0.4 Hz) in solids flow rate (see discussion about this phenomenon in Section 5.5.1).

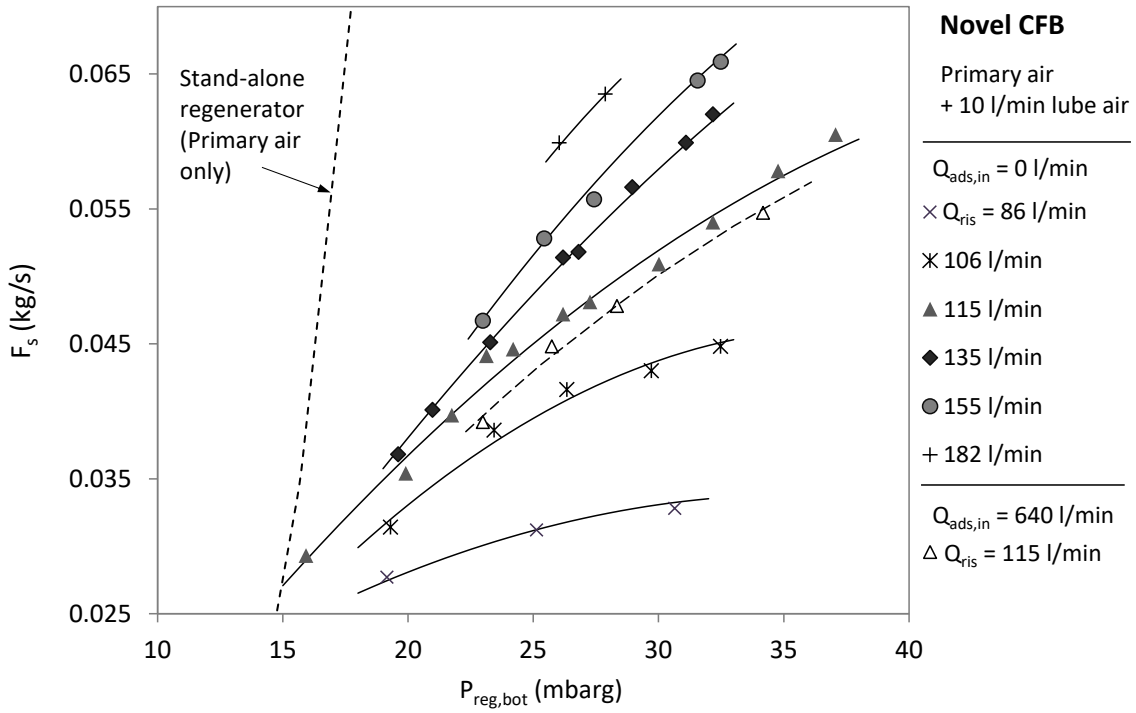

Figure 5.27. Solids circulation rate as a function of regenerator bottom pressure. Novel CFB (aeration with primary air +10 l/min lube air)

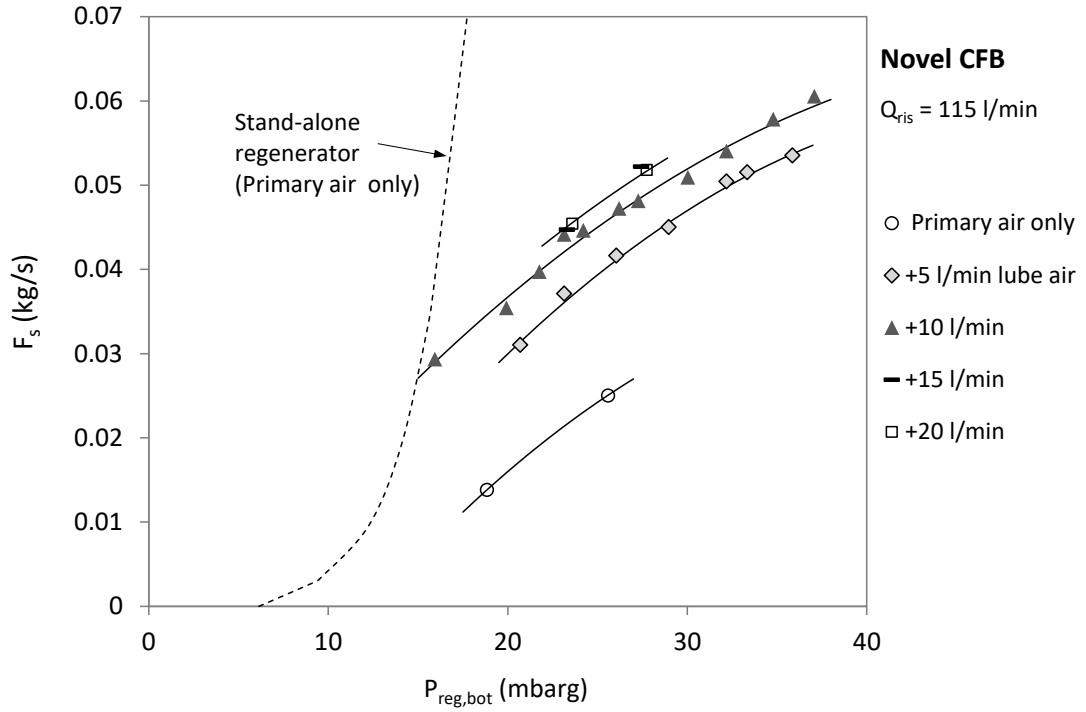

Figure 5.28. Solids circulation rate as a function of regenerator bottom pressure for different values of lube air flow rate. Novel CFB

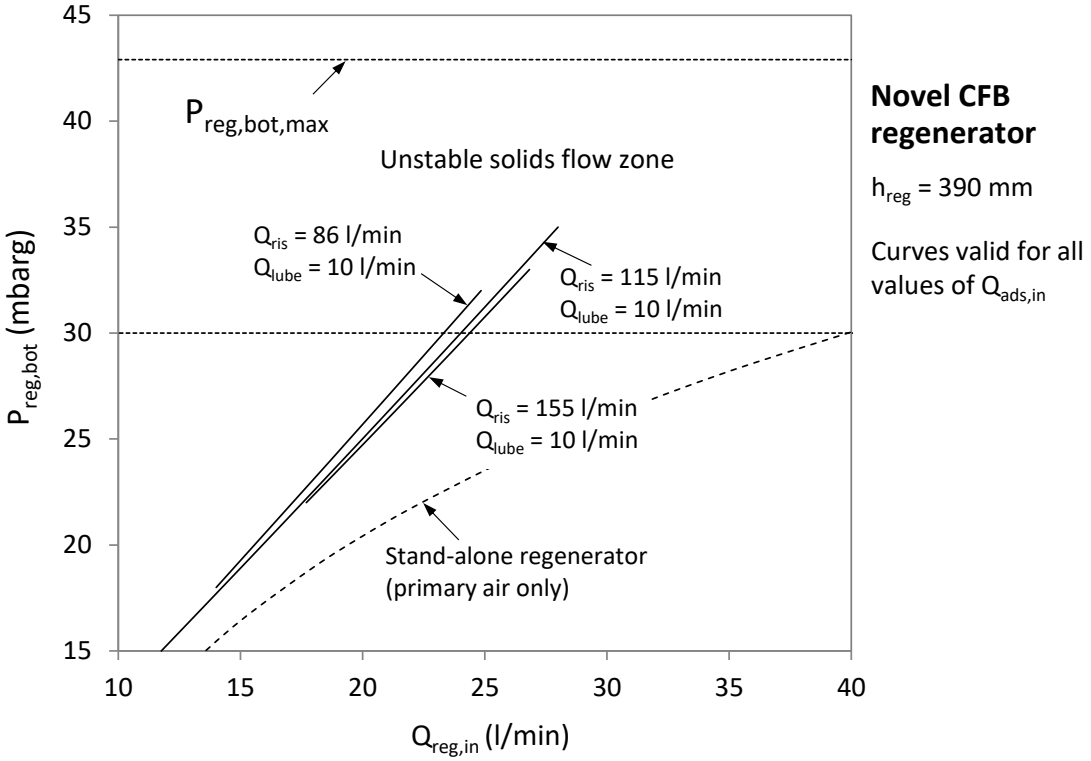

Figure 5.29. Regenerator bottom pressure as a function of primary air flow rate. Novel CFB

5.6.2 Operating window

Figure 5.30 shows the operating window of the novel CFB riser and counter-current adsorber. The interaction between riser and adsorber, from an operating point of view, is very weak as it is limited to the pressure at the top of the adsorber, as commented previously in Section 5.6.1. This makes the adsorber a very flexible element in terms of allowed combinations of air and solids flow rates, which translates into a wide operating window (Figure 5.30b). Values of $Q_{ads,in}$ are limited to around 640 l/min to prevent a high rate of solids carry-over. Note that the upper limit of solids flow rate in the adsorber is that of the riser; the solids flow capacity of the adsorber as a stand-alone system has not been determined.

The maximum air flow rate in the novel CFB riser is limited to 155 l/min as higher values lead to instability in the solids flow. A minimum value of 86 l/min is recommended to prevent C-type choking of the system. The solids flow rates are delimited within a narrow range flanked by regions of solids flow instability.

It can be argued that the greater solids flow instability in the novel CFB compared to the benchmark configuration is due to the fact that the former system is A-type choked, i.e. a dense phase is formed at the riser bottom below the solids inlet port (see Bi et al., 1993). The existence of such a dense phase exacerbates the interaction between riser and regenerator. In the worst case, pressure fluctuations at the bottom of the riser are large enough to cause peaks of negative pressure difference between riser and regenerator, with the consequent reverse gas flow (from riser bottom to regenerator).

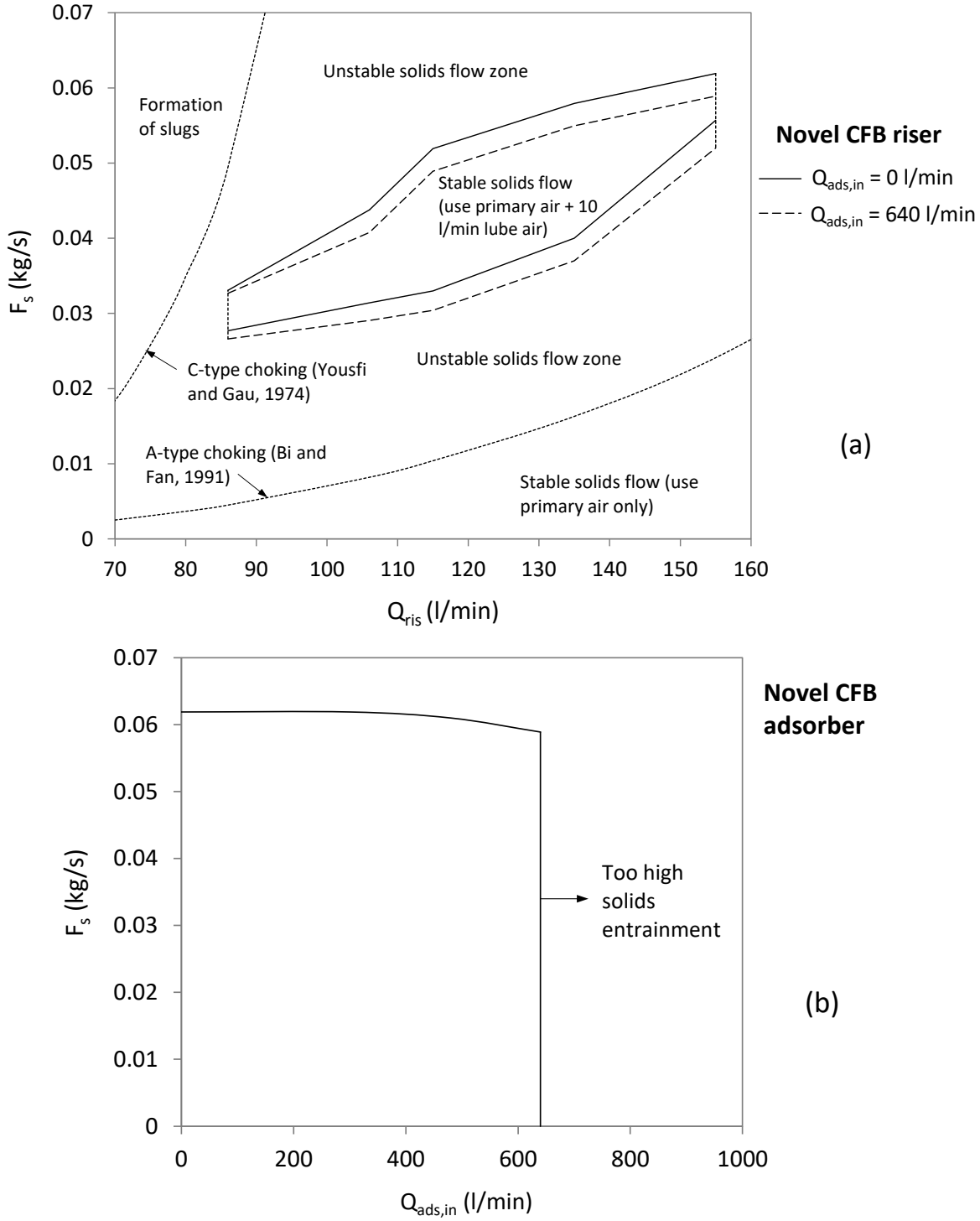

Figure 5.30. Operating window of the novel CFB riser (a) and adsorber (b). The upper limit of F_s is that of the riser and not the adsorber as a stand-alone system.

5.6.3 Riser pressure profiles

Figure 5.31 presents the pressure profiles for the novel CFB riser at different values of solid flux and gas velocities. Note that only the profile for the riser lower section (refer to Figure 4.18 where riser lower and upper sections of the novel CFB are identified) could be obtained as it was the section fitted with pressure taps.

At $U_{g,ris}$ = 2.6 m/s, the operating conditions are close to classical choking (or C-type, see Bi et al., 1993) and the height and density of the gas-solid mixture at the riser bottom rapidly increase with increasing the solids flow rate, which translates into an increase of pressure at the riser bottom. Increasing the gas velocity tends to flatten the pressure profile due to the combined effect of 1) a decrease in the hydrostatic head by dilution of the gas-solid mixture, and 2) an increasing in pressure drop in the upper riser due to increasing gas-wall friction losses.

5.6.4 Riser solids fraction profiles

Figure 5.32 shows the values of solids fraction obtained from the corresponding pressure profiles. These values were obtained analogously to those for the benchmark CFB, following the procedure described in Section 5.5.4. The correlation of the corresponding values of axially-averaged slip velocity with operating conditions is shown is Figure 5.33.

5.6.5 Adsorber pressure drop

The values of pressure drop in the novel CFB adsorber as a function of the air superficial velocity for two different values of solids flux can be found in Figure 5.34. The calculated values of pressure drop assuming the solids are fully suspended are plotted in the same graph for comparison. The solids volumetric fraction is assumed to be $G_s/\rho_s u_s$, where the value of solids velocity was determined by particle tracking experiments (Chapter 7). The gas-wall contribution to the pressure drop in the empty adsorber was found negligible and therefore was not subtracted from the experimental values shown.

Pressure drop due to solids-gas interaction increases with gas velocity, especially when approaching the value of high rate of entrainment (0.67 m/s, corresponding to

the boundary value of air flow rate in the adsorber operating window, 640 l/min), but is in all cases well below the hydrostatic head. Figure 5.35 presents the ratio of experimental to calculated pressure drop, showing that 1) the experimental pressure drop is below 20% of the hydrostatic head except at low solids flow rate and high gas velocity; 2) the fraction of supported solids by the gas decreases with solids flow rate. These results are in agreement with previous works in fluid dynamics of gas-solid trickle flow systems (Claus et al., 1976; Roes and van Swaaij, 1979a; Large et al., 1981; Verver and van Swaaij, 1986; Westerterp and Kuczynski, 1987a), and is associated to two phenomena (refer to the fluid dynamic characteristics of these systems in the literature review, Section 2.2, for reference): 1) a high fraction of the solids weight is supported on the internals of the adsorber, i.e. the inclined orifice trays; 2) the solid particles flow as dense streams (trickles), with the inner particles not subjected to drag by the gas phase. The latter phenomenon is denominated "particle shielding" in the works referenced above. Particle shielding was found to hinder mass and heat transfer, and consequently could lower the performance of the adsorber as a CO_2 capture process if these are the controlling mechanisms in the overall adsorption kinetics.

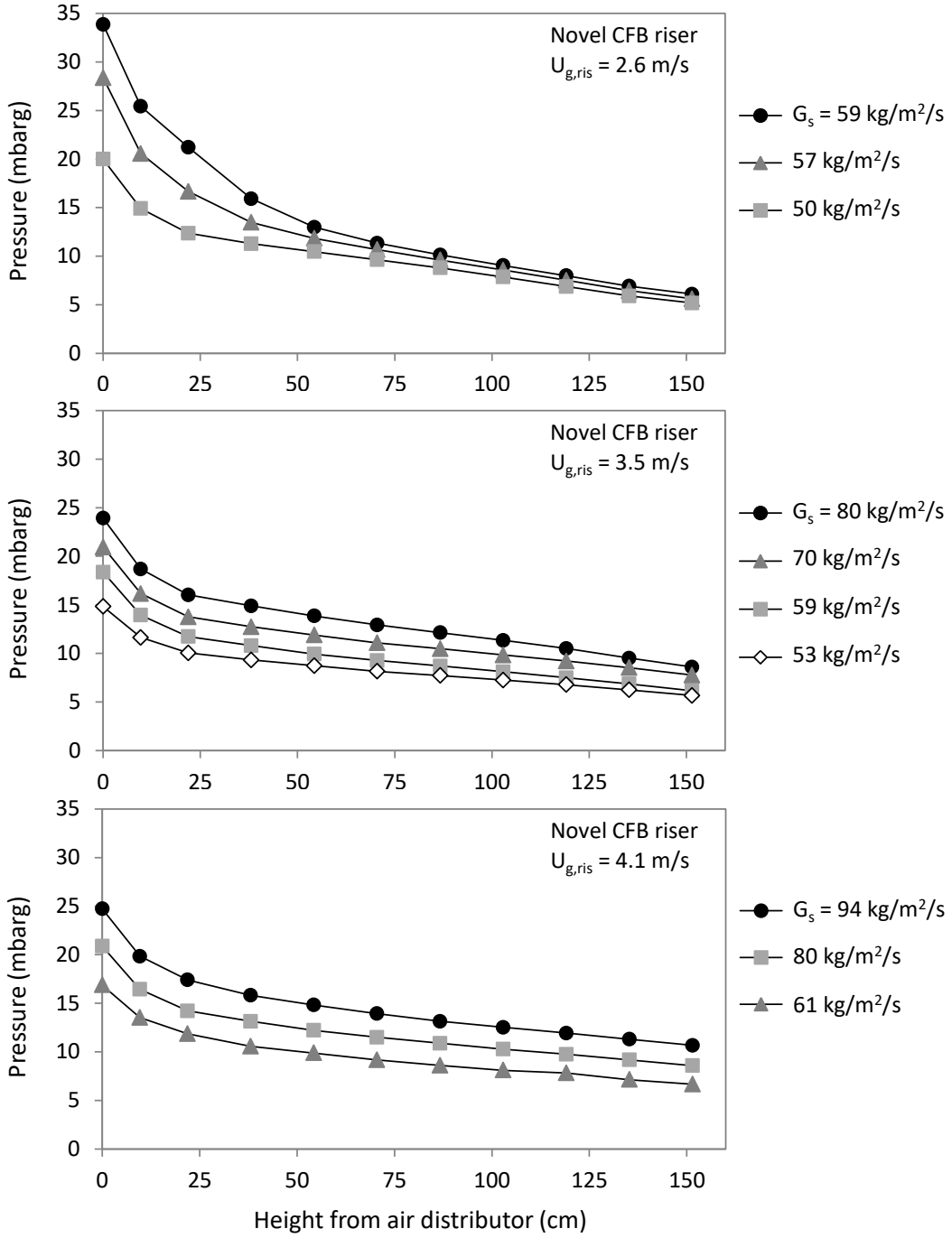

Figure 5.31. Pressure axial profiles. Novel CFB riser

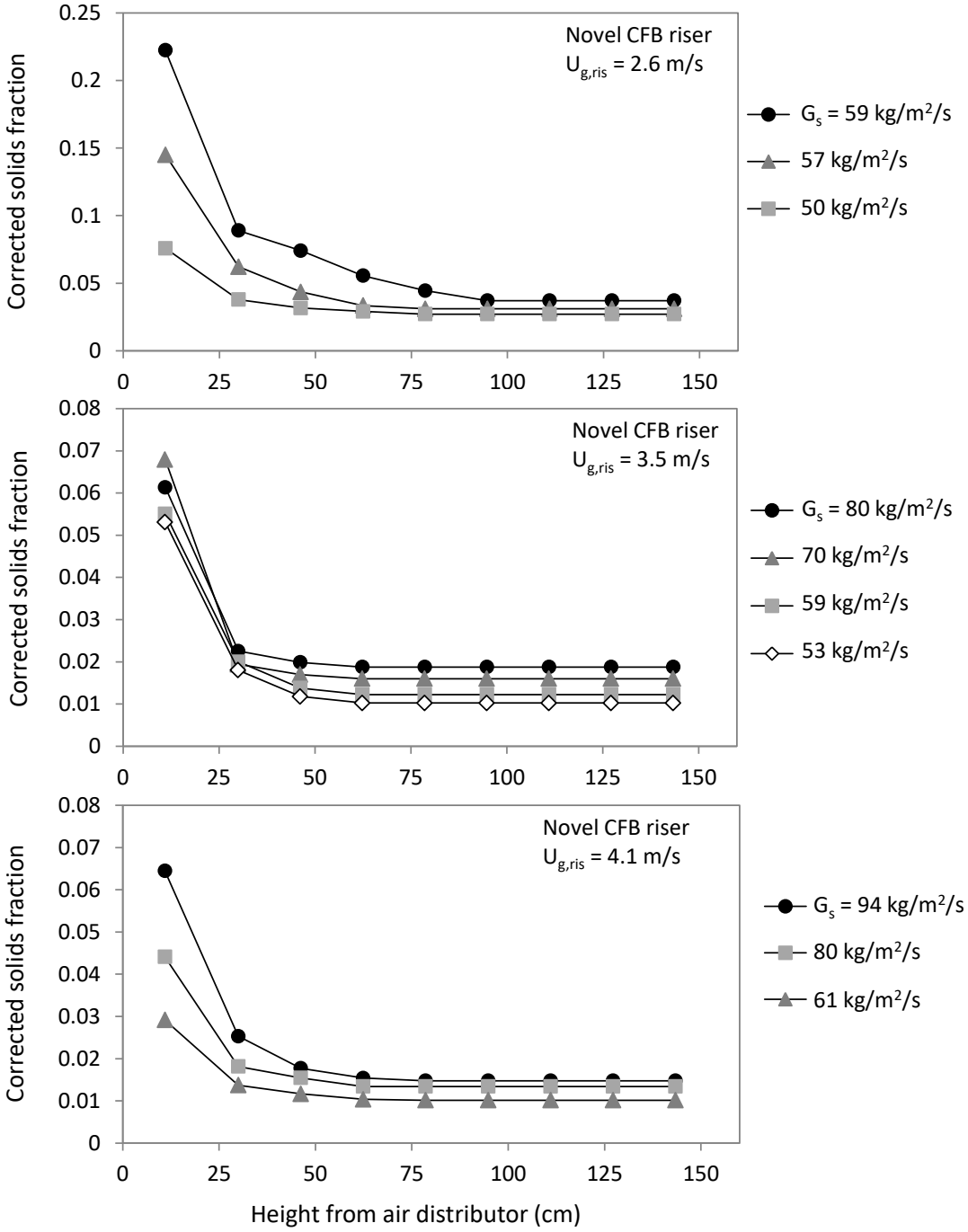

Figure 5.32. Solids fraction (corrected for solids acceleration) axial profiles. Novel CFB riser

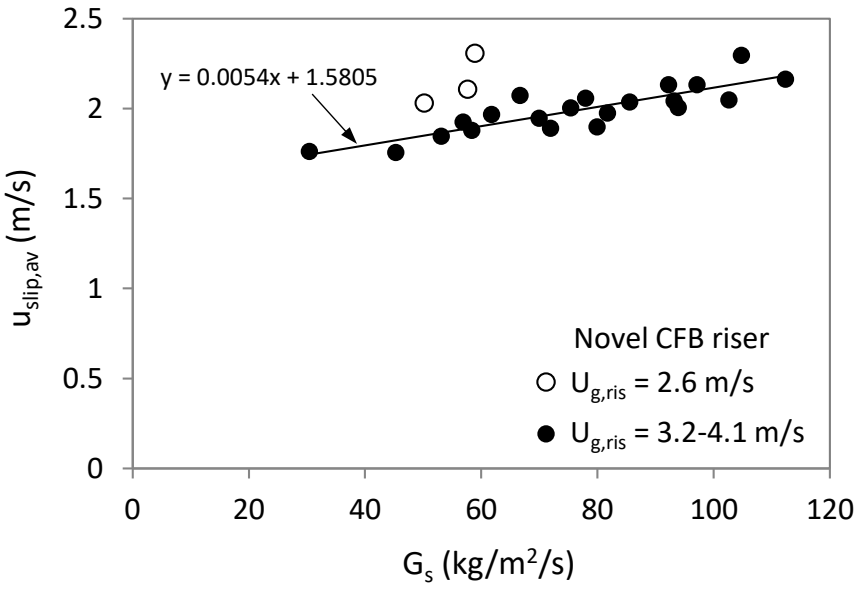

Figure 5.33. Axially-averaged slip velocity as a function of solids flux. Novel CFB riser

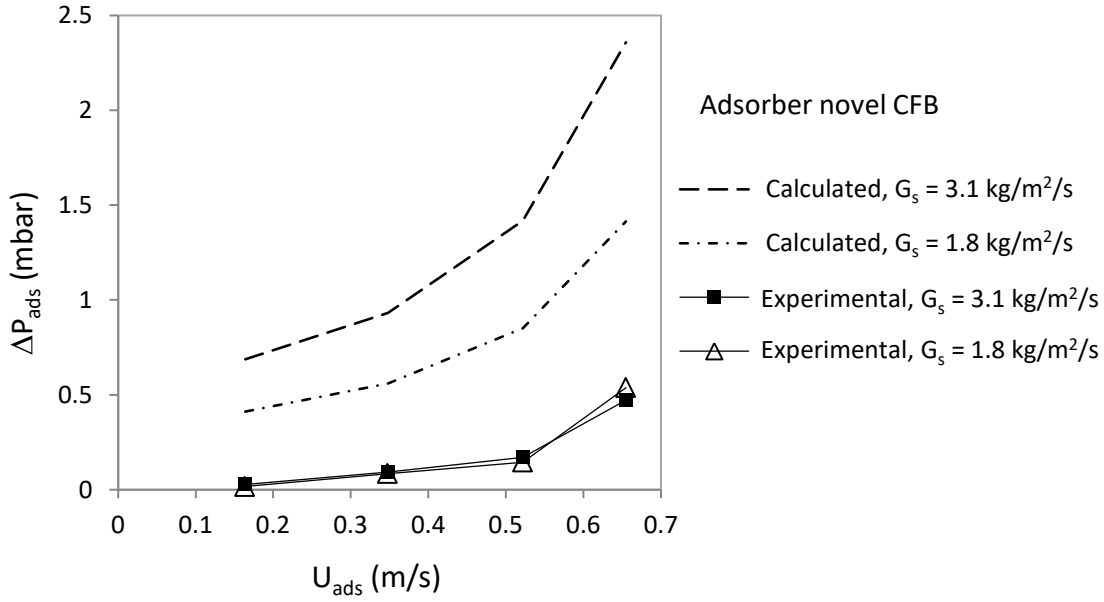

Figure 5.34. Pressure drop as a function of air superficial velocity. Novel CFB adsorber

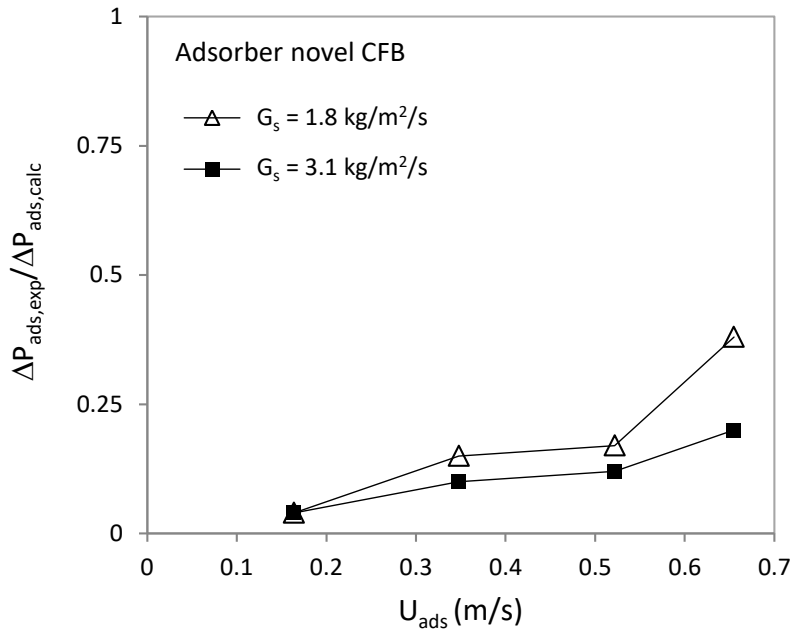

Figure 5.35. Experimental-to-calculated pressure drop as a function of air superficial velocity. Novel CFB adsorber

5.7 Conclusions

The operating characteristics of the constructed novel and benchmark cold model CFB rigs have been described at the level of whole entities (CFB loops) and as individual elements (regenerator, risers, counter-current adsorber).

Steady circulation of solids is governed by the pressure balance in the CFB loops. The regenerator is the "active" element of the loop by providing the pressure head needed to drive the flow of solids around the loop. Control of the pressure head and, in turn, of the solids circulation rate is achieved by keeping the solids flow in the regenerator in the moving bed regime and controlling the amount of aeration introduced at the regenerator bottom. Two types of aeration are made available: 1) primary air is fed via the regenerator windbox for main solids flow rate control purposes; 2) lube air can be injected into the solids outlet pipe to reduce the pressure drop in this element and, as a consequence, attain higher solids circulation rates.

The characteristics of the interaction between riser and regenerator dictate that solids circulation rate increases with increasing height of the solids bed in the regenerator and decreasing solids concentration in the riser. For given same conditions in the regenerator, the maximum achievable solids circulation rate in each CFB configuration is then related to the density of the gas-solids mixture in the riser. The benchmark CFB riser is fed with a large amount of air (corresponding to 100% of the flue gas to treat in the real carbon capture process), leading to high gas velocities (5.1-6.2 m/s), low solids fraction (0.5-0.8%, axial average) and therefore high solids flow rates (up to 0.25 kg/s). The novel CFB riser, on the other hand, is fed with just a fraction of the total air flow rate (the rest sent to the counter-current adsorber), with the subsequent lower gas velocities (2.6-4.1 m/s), higher solids fraction (2-3%, axial average) and lower solids flow rates (up to 0.06 kg/s).

In practice, operating windows of both CFB configurations are narrower than expected from the discussion above due to phenomena like: flow constrictions formed by solids settling in horizontal sections (benchmark CFB riser top) and instabilities in solids flow rate (especially in the novel CFB). Some of these phenomena could be prevented by improving the system geometry; for example, the

top of the benchmark CFB riser could be re-designed to eliminate the horizontal section, or narrowed to keep the solids velocity high. The connection between regenerator and riser in the novel CFB is also susceptible of re-shaping to test the impact on solids flow stability.

The novel CFB counter-current adsorber is a very operationally flexible element, which is due to its peculiar spatial arrangement with other elements in the CFB system. The maximum solids flow rate in the adsorber is constrained by the regenerator-riser interaction, and not by the adsorber as a stand-alone system. Conversely, the impact of adsorber operation in the solids circulation rate is very small since it is related to the increase in pressure drop in the air exhaust at the top of the rig. A more noticeable impact of adsorber operation is the percolation of air from the adsorber bottom into the regenerator top. This should be avoided in the real carbon capture process to prevent dilution of the product CO_2 below the specification of >95% purity. Preventive measures could be steam sealing or minimizing the pressure drop in the adsorber.

The pressure drop in the adsorber increases with air flow rate but does not seem to increase with solids flow rate in the operational region tested. The values correspond to only a fraction (generally less than 25% except at high air flow rates) of the hydrostatic head of the gas-solid mixture, indicating that the solids are supported on the adsorber inclined trays and/or flow in dense trickles that offer less resistance to flow. This is a sought advantage since most of the flue gas (in the real carbon capture process) would be fed to the counter-current adsorber. However, the formation of dense trickles is known in the literature to be detrimental for heat and mass transfer between the bulk gas and the trickle inner particles.

6 Determination of gas residence time distributions

6.1 Introduction

It was recognised from the sensitivity analysis carried out in Chapter 3 that knowledge of the degree of deviation from plug flow of both solid and gas phases in CFB adsorbers is necessary to predict their performance with a minimum of confidence. Recalling Figure 3.24, the estimated drop in CO_2 recovery in case of maximum deviation from plug flow is around 15 and 25 percentage points for the benchmark and novel CFB adsorbers respectively.

In this chapter, the concept of residence time distribution (RTD) and main theoretical background is introduced as a means to qualify and quantify the fluid dynamic characteristics of any flow system (Section 6.2). Measurements, tools and techniques used to obtain experimental data related to the gas RTDs in the different elements of the two CFB cold models rigs are presented (Section 6.3). These data are used to generate the gas RTDs (Section 6.4) which allow gaining insight into the fluid dynamics of the CFB rigs and obtaining values of gas dispersion parameters that can be used in the adsorber model in the prediction of CO_2 recoveries (Section 6.5).

6.2 Theoretical background

6.2.1 The concept of residence time distribution (RTD)

The residence time of an element of fluid leaving a flow system is defined as the time that such element spent within the boundaries of such flow system (Nauman, 1981, 2008). Different fluid elements would accumulate different residence times depending on their path through the system, and therefore the fluid as a whole would exhibit a distribution of residence times. Residence time distributions can be obtained experimentally performing relatively easy tracer injection-detection experiments that reveal qualitative and quantitative information about the fluid flow (Levenspiel and Smith, 1957).

6.2.2 Characterisation of RTDs

Residence time distributions can be expressed in the form of frequency functions (Wen and Fan, 1975; Westerterp et al., 1984). The one used in this work is the E(t)

function, called the *exit age distribution* (Danckwerts, 1953). The E(t) function is defined as:

E(t)dt = fraction of fluid having a residence time between t and dt (6.1)

Very often in the literature, E(t) is also denominated residence time distribution or simply RTD. In this work, E(t), its reduced-time version E(θ) (see definition in eq. (6.7)) and RTD will hereafter be used interchangeably.

As a frequency function, E(t) can be characterised by statistical parameters derived from the moments around the origin (Westerterp et al., 1984). The n-th moment around the origin is defined as:

$$\mu_n = \int_0^\infty t^n E(t)dt \tag{6.2}$$

The zero-th moment is equal to unity, which is an intrinsic property of frequency functions:

$$\mu_0 = \int_0^\infty E(t)dt = 1 \tag{6.3}$$

Of special relevance are the mean residence time τ, variance σ^2 and skewness γ, defined as:

$$\tau = \int_0^\infty tE(t)dt = \mu_1 \tag{6.4}$$

$$\sigma^2 = \mu_2 - \mu_1^2 \tag{6.5}$$

$$\gamma = \mu_3 - 3\mu_1\mu_2 + 2\mu_1^3 \tag{6.6}$$

When comparing E(t) curves at different timescales, it is convenient to transform them into their reduced-time versions, E(θ):

$$E(\theta) = \tau E(t) \quad \text{where } \theta = t/\tau \tag{6.7}$$

The symbols for the mean residence time, variance and skewness of E(θ) are τ_θ, σ^2_θ and γ_θ, respectively.

- *Combination of E(t) in series:*

The E(t) function of a combination of two flow systems in series, $E_3(t)$, can be obtained from the E(t) functions of the individual systems, $E_1(t)$ and $E_2(t)$, using the so-called convolution integral:

$$E_3(t) = \int_0^t E_2(p)E_1(t-p)dp \quad \text{or} \quad E_3(t) = \int_0^t E_1(p)E_2(t-p)dp \tag{6.8}$$

The mean residence time and variance of $E_3(t)$ are obtained by addition of those of $E_1(t)$ and $E_2(t)$:

$$\tau_3 = \tau_1 + \tau_2 \tag{6.9}$$

$$\sigma_3^2 = \sigma_1^2 + \sigma_2^2 \tag{6.10}$$

Note that these expressions only hold exactly in closed systems (see discussion in Section 6.2.4).

6.2.3 The tracer pulse injection technique

Assume that an amount M of a non-reactive, non-adsorbable tracer material is injected as a perfect pulse (δ-Dirac function) into a system of volume V and volumetric flow rate Q, which satisfies the conditions of: a) single-input and single-output; b) closed-closed boundaries; and c) constant density. Let the effluent concentration of such tracer be C_{out}. In these conditions, the following expressions hold (Levenspiel, 1999):

$$M = Q\int_0^\infty C_{out}(t)dt \tag{6.11}$$

$$\tau = \frac{\int_0^\infty tC_{out}(t)dt}{\int_0^\infty C_{out}(t)dt} = \frac{V}{Q} \tag{6.12}$$

$$E(t) = \frac{C_{out}(t)}{\int_0^\infty C_{out}(t)dt} \tag{6.13}$$

Expression (6.11) simply states the mass balance for the tracer. (6.12) can be proven from the mass balance as well (Fogler, 2006). Validity of (6.13), on the other hand, stems from the fact that all tracer molecules contributing to $C_{out}(t)$ spent exactly a time t inside the system, which, by definition, corresponds to a residence time t (provided the tracer was injected as a perfect pulse and the system boundaries are closed).

In practice, (6.13) will hold in more or less extent depending on how close the conditions of the real experiment are to the ideal. In particular, the real shape of the inlet pulse will influence the shape of $C_{out}(t)$ if the width of the inlet pulse is large compared to the value of mean residence time of the tracer (Wen and Fan, 1975; Westerterp et al., 1984; Luyben, 1990). If this is the case, the tracer concentration at both the system inlet and outlet needs to be measured to obtain E(t), and the technique is called the *imperfect* pulse test (Bischoff and Levenspiel, 1962; Bischoff, 1963). The tracer technique used in this work to obtain gas RTDs is of the imperfect pulse type. The details of the experimental arrangements involved are given in Section 6.3, whereas Section 6.4 discusses the approach followed to obtain E(t) curves from tracer concentration data.

6.2.4 Boundaries of the flow system

It has been stated previously that closed boundaries are required for the relationship between the tracer effluent concentration and the system RTD to hold exactly. This is so because only closed boundaries guarantee that the time elapsed between tracer injection and detection is identical to the time spent by the tracer molecules within boundaries. If boundaries are open, molecules are free to cross them and re-enter the system, accumulating time outside the system. As pointed out by Nauman (1981), this is an obvious observation when thinking of a fluid as a sum of “discrete entities”

(molecules, particles, etc), but created confusion in the field for several decades when applied to fluids as a continuum (Nauman, 2008).

In practice, distinction between open and closed conditions is not relevant when either: a) the level of dispersion is low, according to Levenspiel (1999) when the Péclet number is higher than 100; or b) the experimental setup is constructed in such a way that plug flow is promoted at the points of the system where tracer injection and detection are carried out (Westerterp et al., 1984). It will be seen in the following sections that neither condition is satisfied in two of the four CFB elements studied, namely the risers of both CFB configurations. In these cases it will be acknowledged that, strictly speaking, the E(t) curves and their reduced-time versions E(θ) here obtained and presented do not correspond to gas residence time distributions but to some other time distribution (Westerterp et al., 1984; Levenspiel, 1999).

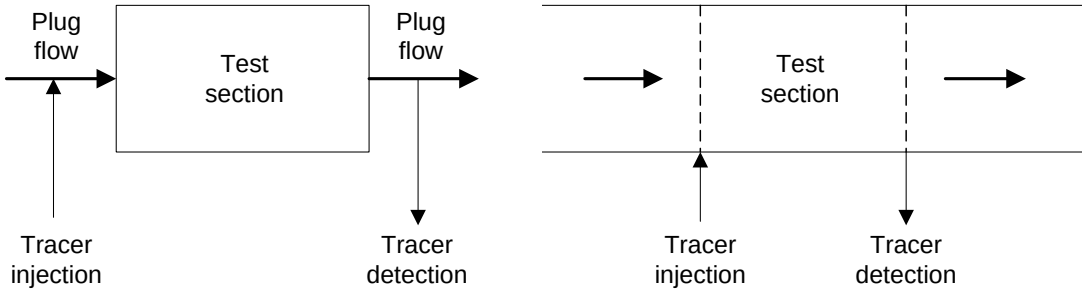

Figure 6.1. Pulse injection-detection test with closed-closed (left) and open-open (right) boundaries (adapted from Westerterp et al., 1984)

6.3 Experimental procedure

In the imperfect pulse test, a pulse of tracer of arbitrary shape is injected upstream the inlet of the studied system, and the tracer concentration detected both at the inlet and the outlet of such system (Bischoff and Levenspiel, 1962; Bischoff, 1963). The experimental methods and instruments used here for tracer injection and detection are described in Sections 6.3.1 and 6.3.2 respectively. Details of how these are used in more specific arrangements for each group of experiments are given in Section 6.3.3.

6.3.1 Tracer injection system

Typical tracer gases used in flow systems with air are CO_2, He, Ar and H_2 (Wen and Fan, 1975). The tracer gas used in this work is CO_2.

The tracer injection system is composed of three elements (Figure 6.2): the first element (a) is the supply bottle where pure CO_2 is contained under pressure (20 barg). The bottle is fitted with a pressure regulator, a safety valve and a female quick release connector. The second element (b) is the "injector", which is made of two ball valves with a tee fitting in between where a pressure gauge is connected, and a male quick release fitting at each end. The third element (c) is the injection fitting (tee + female quick release connector) placed in each of the air supply lines of the CFB rigs.

The injection of CO_2 as a pulse is achieved by purging and loading the injector at a desired pressure and subsequently releasing this batch of gas into the air supply line (see Figure 6.3 for reference). This is carried out connecting only two of the three elements at a time. In this way, direct connection between the pressurised CO_2 bottle and the CFB system is avoided.

The injector pressure is set to a value between 2 barg and 3 barg. Preliminary testing of the pulse injection/detection system showed that the quick release fittings could be easily connected and disconnected in this pressure range, and at the same time the maximum values of concentration detected by the CO_2 sensors were kept below the upper limit of detection (5%).

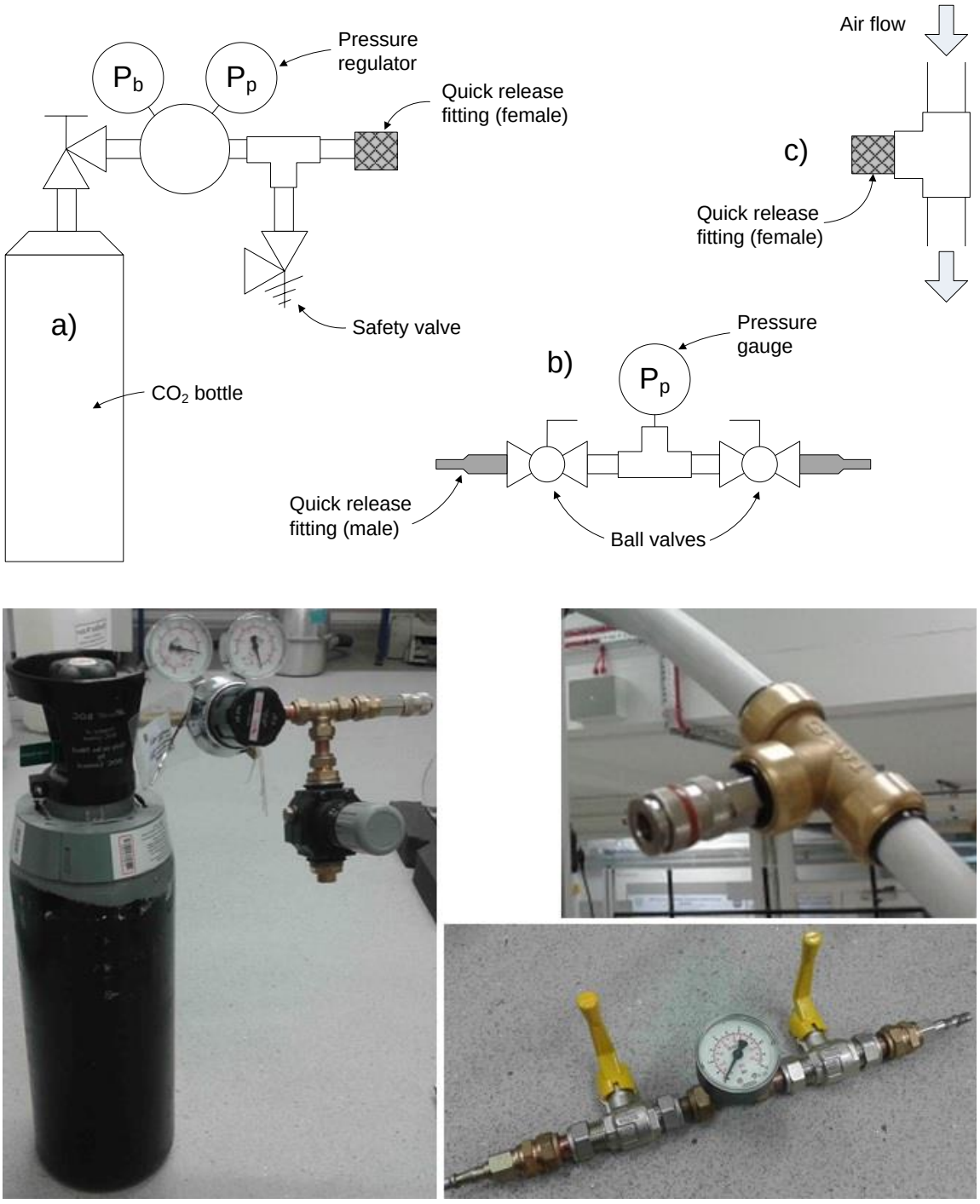

Figure 6.2. Components of the CO_2 injection system. a) CO_2 bottle, b) injector, and c) injection fitting

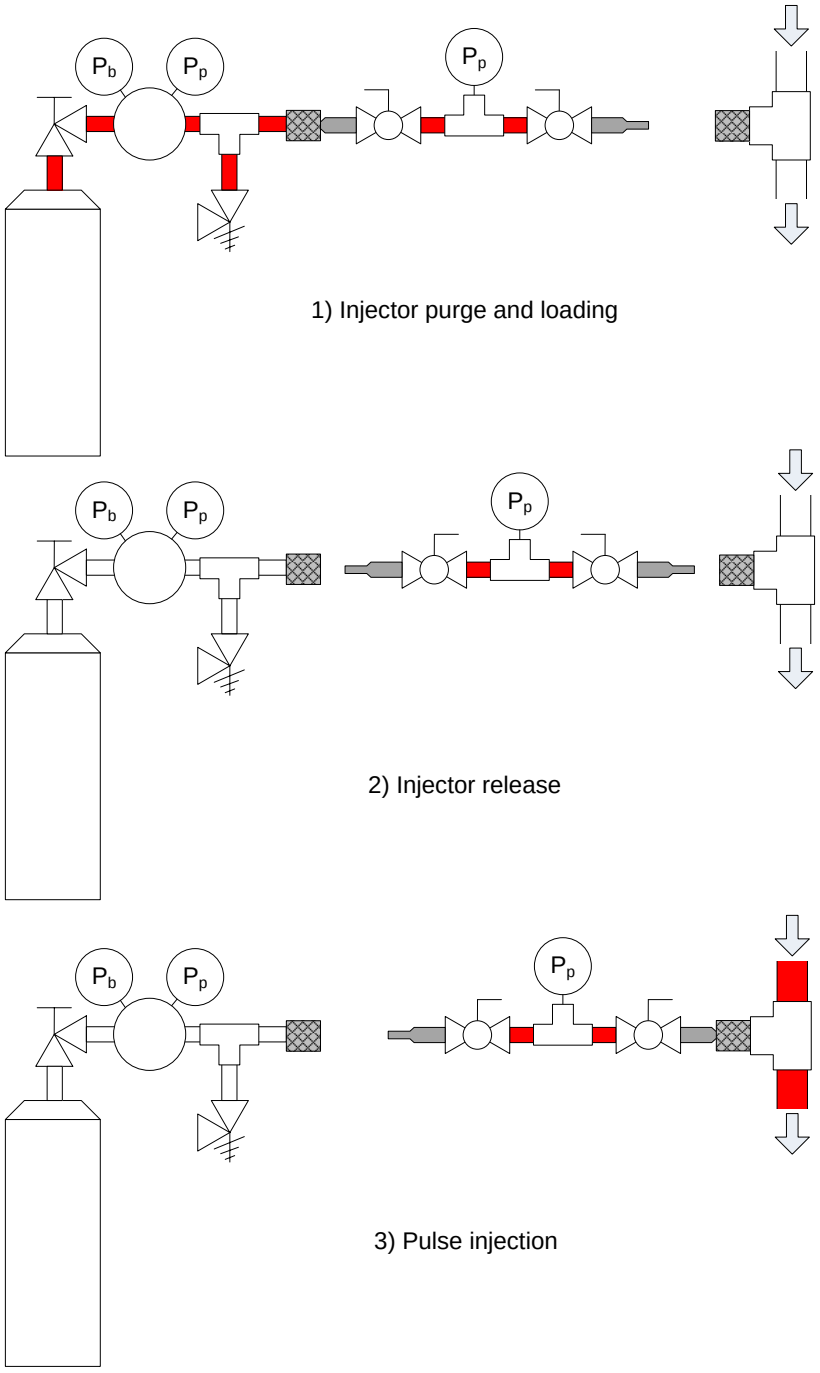

Figure 6.3. CO_2 pulse injection procedure

6.3.2 CO_2 detection system

CO_2 concentration in the air flow is measured using two infrared absorption detectors from Gas Sensing Solutions Ltd, models COZIR Wide Range and SprintIR (Figure 6.4). These two sensors are identical with the only difference being the reading rate: 2 and 20 readings/s for the COZIR and SprintIR model respectively. All experiments were carried out with the SprintIR model except CO_2 detection at the regenerator outlet, which did not require such high speed of data acquisition. The sensors readings are transmitted via a USB cable to a computer (no data acquisition device required), and recorded/visualised using a virtual instrument programmed in LabVIEW. The upper detection limit is 5% for both sensors, and the accuracy ±3% of the reading.

Figure 6.4. CO_2 sensor, model COZIR Wide Range (image borrowed from GSS's website, with permission).Model SprintIR is physically identical to the COZIR.

The sensing elements of the detectors are located inside a cylindrical casing, which is closed at the top by a fine plastic mesh for protection against solid particles. It was found by preliminary testing that this design increases the response time of the sensors due to the time taken by the gas to diffuse into the system and reach the sensing elements. To mitigate this effect, the sensor manufacturer supplies a cap that can be adapted to the cylindrical casing and helps directing the gas flow towards the sensing elements. This idea was borrowed here and a similar cap was created by the Technical Services of the University of Edinburgh (Figure 6.5).

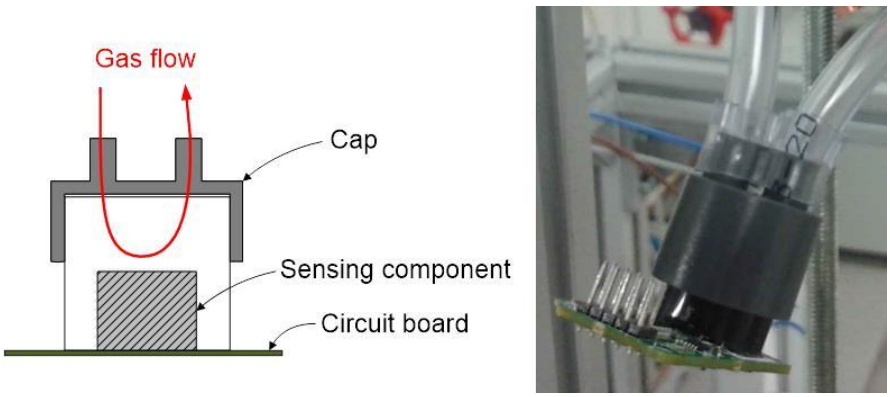

Figure 6.5. CO_2 sensor with a cap to direct gas flow towards the sensing components (idea borrowed from the sensor manufacturer)

Even when the sensor response time can be reduced with the arrangement just described, the overall combined dynamics of the sensor and the sampling line will inevitably be present and influence the shape of the measured CO_2 curve. An approach to eliminate the contribution of the detection system is to determine the transfer function of the sensor and use it to mathematically obtain the actual CO_2 concentration curves from the raw data (Baron et al., 1992). However, this is not necessary when performing imperfect pulse tests since the contribution of the detection system is present in both the inlet and outlet concentration signal and therefore is cancelled out when obtaining the characteristic E(t) curve of the studied flow system. This has been ensured by keeping the characteristics of the detection system (length and inner diameter of the sampling lines and sample flow rate) equal for all experiments.

6.3.3 Experiments

Figures 6.6 to 6.9 show the CO_2 injection-detection points for the different CFB elements analysed. Note that only one CO_2 sensor was used at a time (rather than two simultaneously as it may be suggested by the drawings) due to technical difficulties with the virtual instrument used to control the data logging from the computer. The sensor was used alternatively at inlet and outlet positions to minimise systematic errors in the data sets generated. The gas samples were taken using flexible tubes 4 mm ID and 7 cm long, the flow rate being 10 l/min in all cases, measured with a calibrated rotameter connected downstream the CO_2 sensor (Figure 6.10).

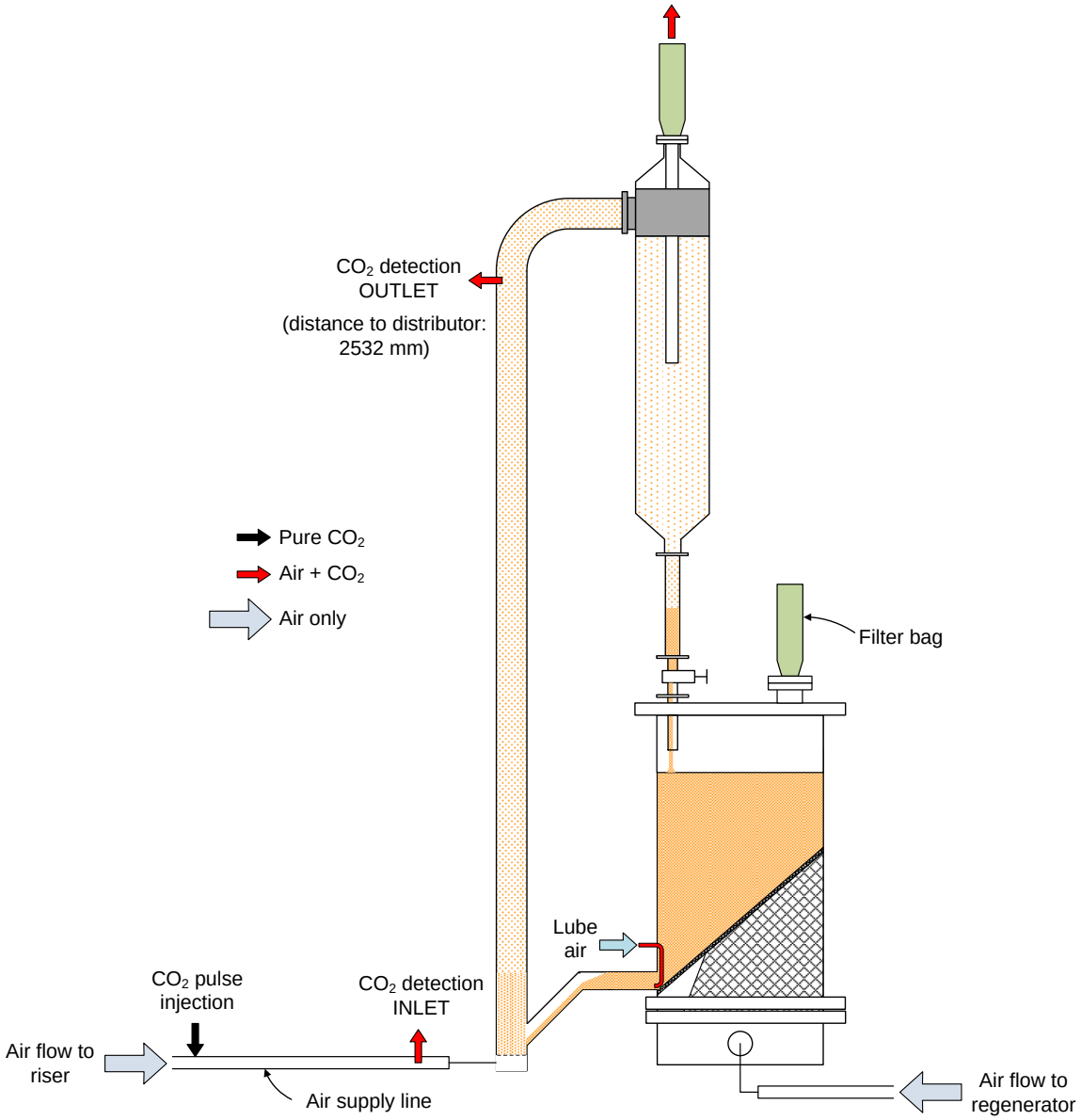

Figure 6.6. CO_2 pulse injection-detection experimental arrangements in benchmark CFB riser

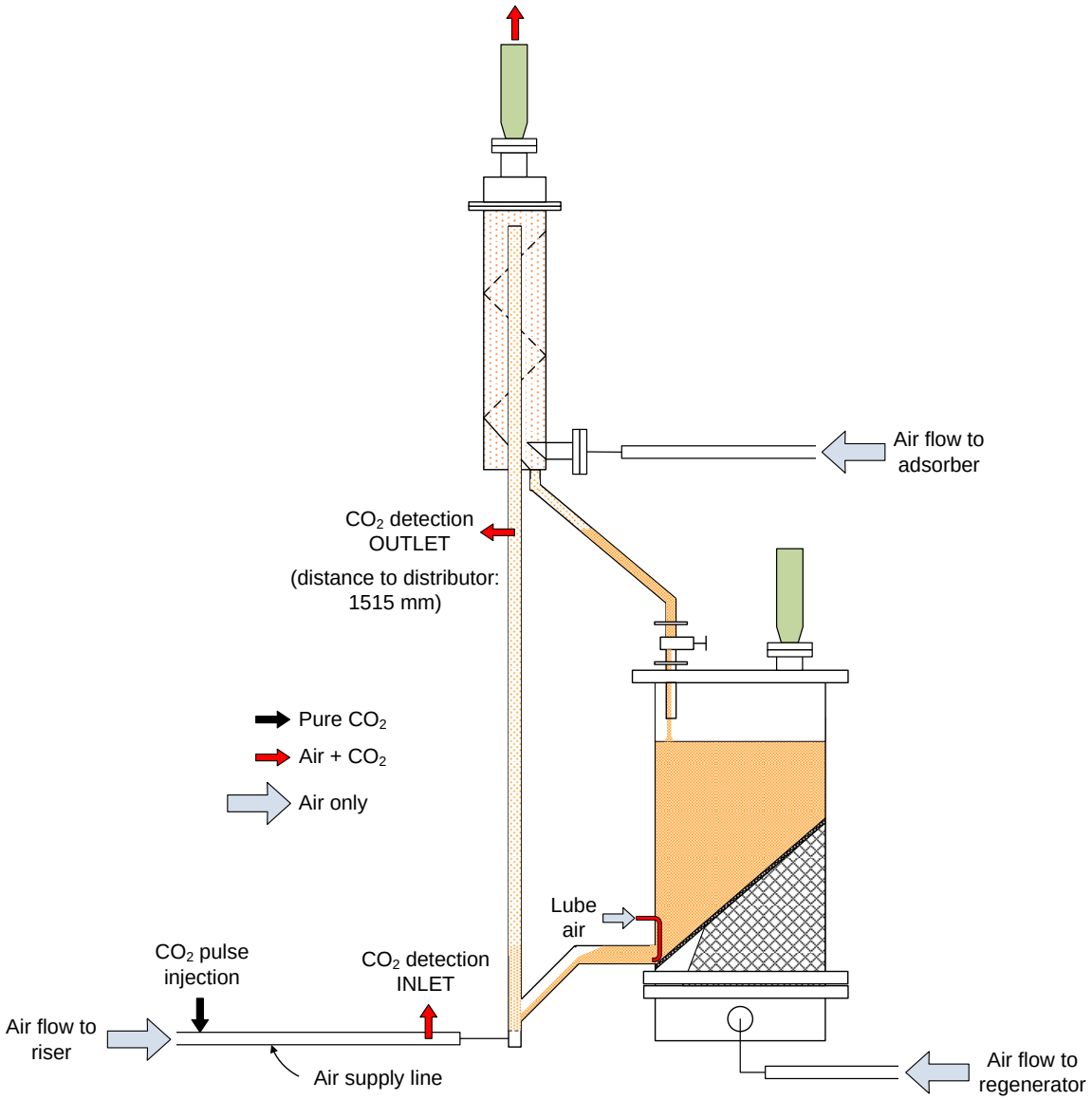

Figure 6.7. CO_2 pulse injection-detection experimental arrangements in novel CFB riser

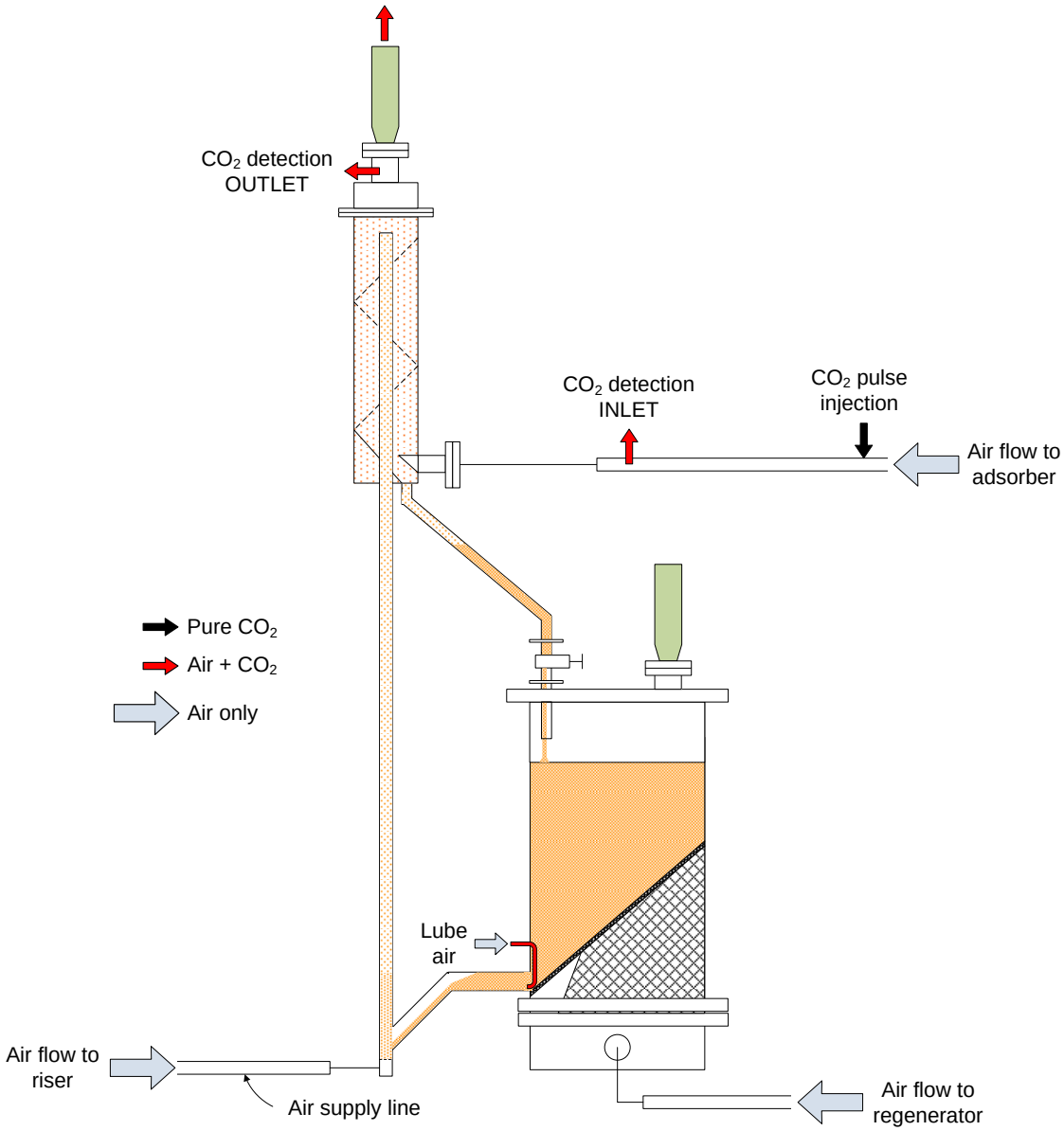

Figure 6.8. CO_2 pulse injection-detection experimental arrangements in novel CFB adsorber

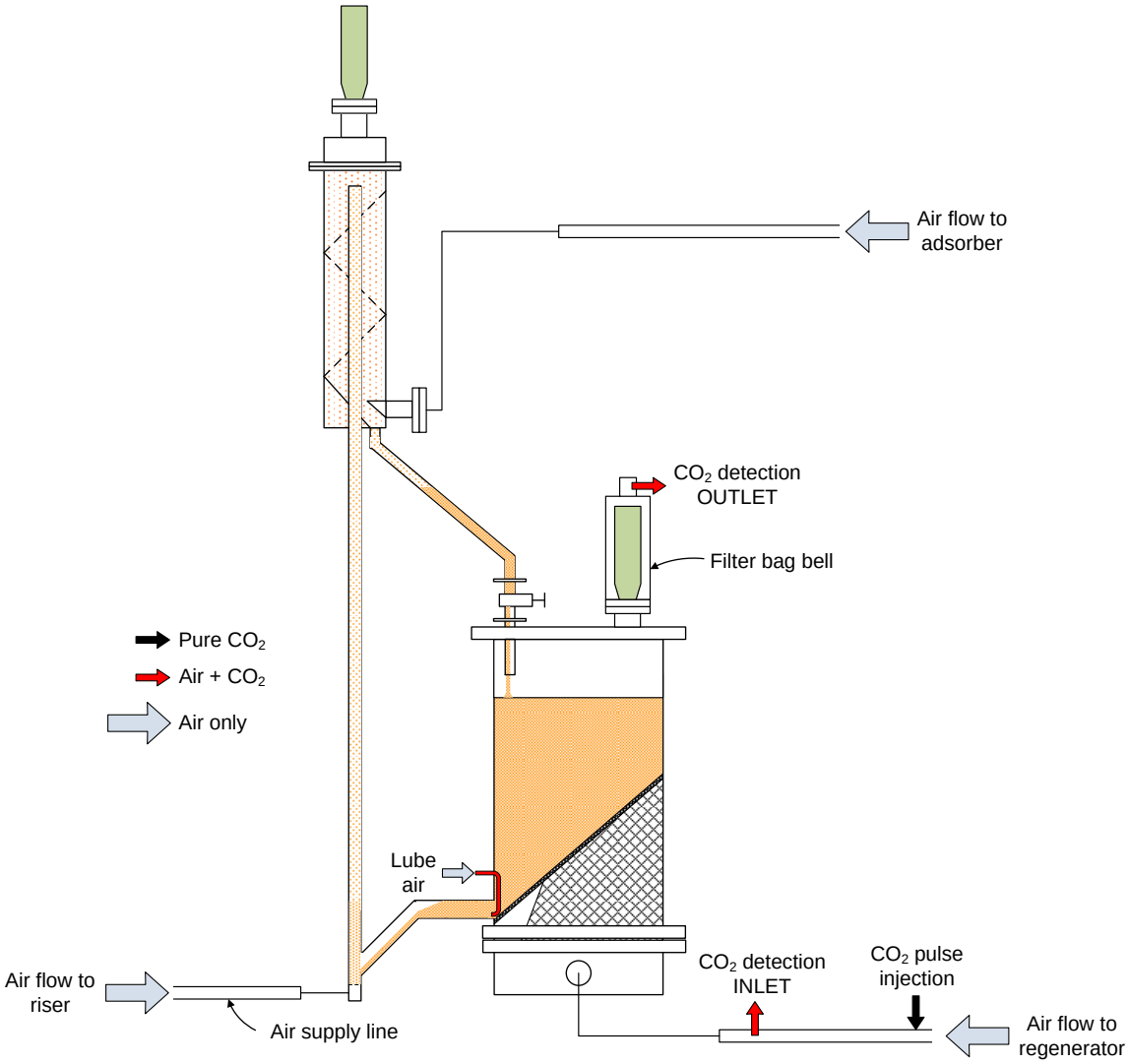

Figure 6.9. CO_2 pulse injection-detection experimental arrangements in regenerator (integrated in novel CFB)

Figure 6.10. CO_2 detection arrangement in the benchmark CFB riser

The operating conditions of the CFBs and other experimental details of the CO_2 injections are given in Tables 6.1 to 6.4. Blank experiments (zero solids flow rate) were also carried out to find out the impact of system geometry on the shape of the gas RTDs.

The experiments are referenced as below:

- RISbx_y (where x = 1 to 2 and y = 0 to 2): Benchmark CFB riser.
- RISnx_y (where x = 1 to 2 and y = 0 to 2): Novel CFB riser.
- ADSx_y (where x = 1 to 4 and y = 0 to 2): Novel CFB adsorber.
- REGx_y (where x = 1 to 3 and y = 1 to 2): Regenerator (integrated in novel CFB).

In all cases x refers to gas flow rate conditions and y to solid flow rate conditions, being y = 0 blank experiments (zero solids flow rate).

Table 6.1. CO_2 pulse experimental data and gas RTD results. Benchmark CFB riser

Exp. Ref.	CFB operating conditions					CO_2 injection	CO_2 inlet	CO_2 outlet	RTD							
	$Q_{ris,in}$ (l/min)	Q_{lube} (l/min)	$U_{g,ris}$ (m/s)	F_s (kg/s)	G_s (kg/s/m^2)	P_{inj} (barg)	$\tau_{in,exp}$ (s)	$\tau_{out,exp}$ (s)	τ_{exp} (s)	σ^2_θ	γ_θ	DPFS model			DPF_{oo} model	DPF_{cc} model
												Pe	ϕ	N	Pe	Pe
RISb1_0	625	0	5.1	0	0	3	0.38	1.0	0.81	0.057	0.0094	40.0	0.95	1	39	34
RISb1_1	613	10		0.081	39.7	3	0.38	0.99	0.61	0.094	0.024	20.0	0.95	1	25	20
RISb1_2	612	10		0.112	54.8	3	0.38	1.03	0.65	0.12	0.036	16.7	0.95	1	20	16
RISb2_0	760	0	6.2	0	0	3	0.42	0.97	0.30	0.057	0.0094	40.0	0.95	1	39	34
RISb2_1	747	10		0.097	47.5	3	0.42	0.87	0.45	0.090	0.022	25.0	0.95	1	26	21
RISb2_2	746	10		0.136	66.6	3	0.42	0.91	0.20	0.11	0.034	20.0	0.95	1	21	17

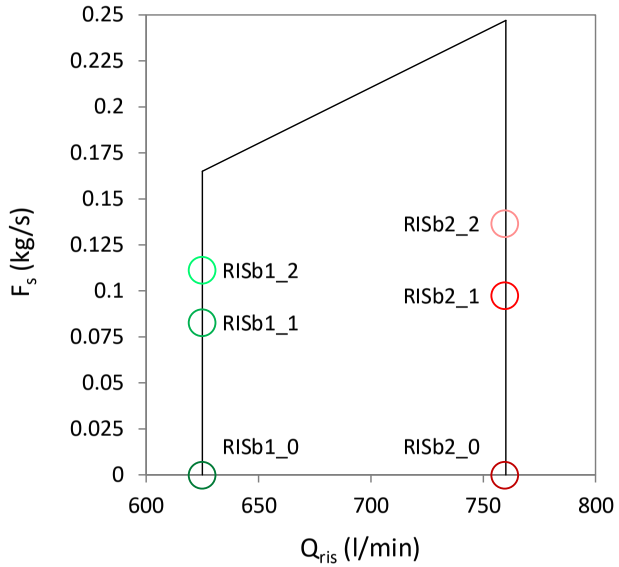

Figure 6.11. CFB operating conditions for CO_2 pulse experiments. Benchmark CFB riser

Table 6.2. CO_2 pulse experimental data and gas RTD results. Novel CFB riser

Exp. Ref.	CFB operating conditions					CO_2 injection	CO_2 inlet	CO_2 outlet	RTD							
	$Q_{ris,in}$ (l/min)	Q_{lube} (l/min)	$U_{g,ris}$ (m/s)	F_s (kg/s)	G_s (kg/s/m^2)	P_{inj} (barg)	$\tau_{in,exp}$ (s)	$\tau_{out,exp}$ (s)	τ_{exp} (s)	σ^2_θ	γ_θ	DPFS model			DPF_{oo} model	DPF_{cc} model
												Pe	ϕ	N	Pe	Pe
RISn1_0	86	0	2.6	0	0	2	0.52	1.43	0.95	0.076	0.027	65.0	0.85	1	30	25
RISn1_1	75	10		0.031	56.6	2	0.52	1.41	0.89	0.14	0.055	22.2	0.85	1	17	13
RISn2_0	115	0	3.5	0	0	2	0.60	1.30	0.50	0.076	0.027	65.0	0.85	1	30	25
RISn2_1	104	10		0.039	72.5	2	0.60	1.28	0.68	0.13	0.049	25.0	0.85	1	19	14
RISn2_2	104	10		0.051	90.7	2	0.60	1.20	0.60	0.15	0.060	20.0	0.85	1	16	12

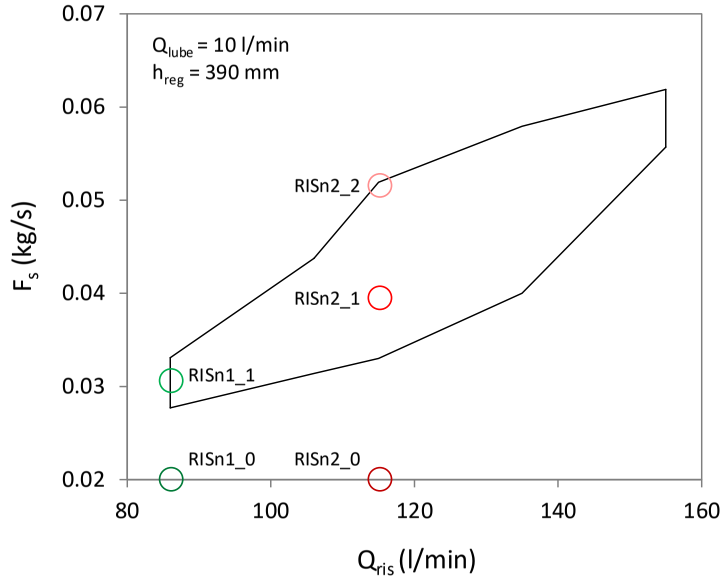

Figure 6.12. CFB operating conditions for CO_2 pulse experiments. Novel CFB riser

Table 6.3. CO_2 pulse experimental data and gas RTD results. Novel CFB adsorber

Exp. Ref.	CFB operating conditions							CO_2 injection	CO_2 inlet	CO_2 outlet	RTD							
	$Q_{ads,in}$ (l/min)	$U_{g,ads}$ (m/s)	$U_{g,tray}$ (m/s)	$Q_{ris,in}$ (l/min)	Q_{lube} (l/min)	F_s (kg/s)	G_s (kg/m^2/s)	P_{inj} (barg)	$\tau_{in,exp}$ (s)	$\tau_{out,exp}$ (s)	τ_{exp} (s)	σ^2_θ	γ_θ	DPFS model			DPF_{oo} model	DPF_{cc} model
														Pe	ϕ	N	Pe	Pe
ADS1_0	160	0.16	0.48	115	0	0	0	3	0.45	3.95	3.50	0.070	0.025	83.3	0.85	1	32	28
ADS1_1				104	10	0.027	1.70	3	0.45	4.07	3.62	0.13	0.049	25.0	0.85	1	19	14
ADS1_2				104	10	0.049	3.09	3	0.45	4.15	3.70	0.16	0.066	18.2	0.85	1	15	11
ADS2_0	340	0.35	1.01	115	0	0	0	3	0.48	2.40	1.92	0.070	0.025	83.3	0.85	1	32	28
ADS2_1				104	10	0.037	2.34	3	0.48	2.18	1.70	0.075	0.026	83.3	0.85	1	29	25
ADS2_2				104	10	0.055	3.47	3	0.48	2.59	2.11	0.087	0.030	50.0	0.85	1	26	21
ADS3_0	510	0.52	1.52	115	0	0	0	3	0.50	1.49	1.11	0.13	0.056	52.5	0.8	1	19	14
ADS3_1				104	10	0.032	2.02	3	0.50	2.03	1.41	0.12	0.052	55.0	0.8	1	21	16
ADS3_2				104	10	0.052	3.28	3	0.50	1.80	1.30	0.13	0.055	53.4	0.8	1	19	15
ADS4_0	643	0.66	1.91	115	0	0	0	3	0.50	1.51	1.01	0.12	0.053	54.5	0.8	1	21	16
ADS4_1				104	10	0.031	1.96	3	0.50	1.71	1.21	0.12	0.055	53.1	0.8	1	20	16
ADS4_2				104	10	0.051	3.22	3	0.50	1.79	1.29	0.12	0.054	53.9	0.8	1	21	16

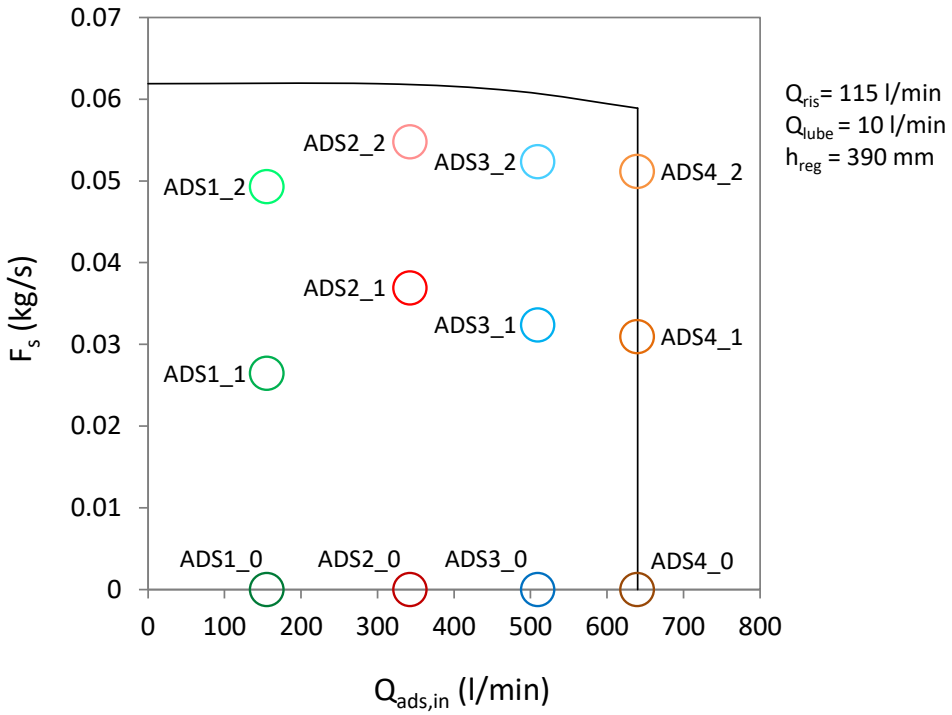

Figure 6.13. CFB operating conditions for CO_2 pulse experiments. Novel CFB adsorber

Table 6.4. CO_2 pulse experimental data and gas RTD results. Regenerator (integrated in novel CFB)

Exp. Ref.	CFB operating conditions					CO_2 injection	CO_2 inlet	CO_2 outlet	RTD							
	$Q_{reg,in}$ (l/min)	Q_{reg} (l/min)	$Q_{ris,in}$ (l/min)	Q_{lube} (l/min)	F_s (kg/s)	P_{inj} (barg)	$\tau_{in,exp}$ (s)	$\tau_{out,exp}$ (s)	τ_{exp} (s)	σ^2_θ	γ_θ	DPFS model			DPF_{oo} model	DPF_{cc} model
												Pe	ϕ	N	Pe	Pe
REG1_1	16.2	14.1	113	0	0.013	3	6.8	180	173	0.147	0.082	55.1	0.68	1.3	17	13
REG1_2		16.0	104	10	0.038	3	6.8	166	159	0.139	0.069	54.1	0.68	1.3	18	13
REG2_1	21.0	18.7	112	0	0.023	3	6.4	136	130	0.159	0.091	49.5	0.68	1.3	16	11
REG2_2		20.6	103	10	0.047	3	6.4	128	122	0.152	0.079	48.8	0.68	1.3	16	12
REG3_1	24.3	21.9	112	0	0.028	3	6.2	116	110	0.181	0.112	40.0	0.68	1.3	14	10
REG3_2		23.8	103	10	0.052	3	6.2	110	104	0.192	0.122	39.2	0.68	1.3	14	9

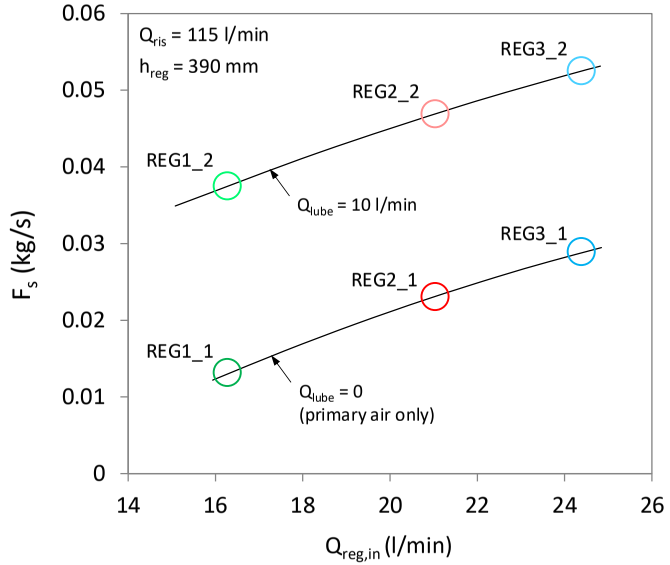

Figure 6.14. CFB operating conditions for CO_2 pulse experiments. Regenerator (integrated in novel CFB)

6.4 Determination of exit age distributions E(t)

The 3-step approach described below is followed to obtain E(t) curves from the CO_2 concentration-time data generated using the imperfect pulse injection technique:

1) Choose a flow model for which the mathematical expression of E(t) exists and assume values of the model parameters. The chosen model is not required to be a physical representation of the flow pattern since it is used here as a tool for data fitting only (Moser and Cupit, 1966, cited in Paris et al., 1971).

2) Convolute the model E(t) curve to the experimental inlet concentration-time curve using eq. (6.8).

3) Fit the convoluted curve obtained in Step 2 to the experimental outlet concentration-time curve. If the fit is satisfactory, the model E(t) curve can be taken as that of the studied CFB element. If the fit is not satisfactory, go back to Step 1 and change either the model or the value of the parameters.

The justification for this approach is to avoid deconvolution of the inlet CO_2 concentration curve from the outlet curve. Deconvolution is a complex process that yields a noisier signal than the original (Luyben, 1990). The convolute-and-fit approach here proposed is a well-established method to obtain RTD curves using the imperfect pulse injection technique (Westerterp et al., 1984; Levenspiel, 1999).

Two different 1-dimensional flow models were tested to fit the experimental data, namely the axially-dispersed plug flow with open-open boundaries (DPF_{oo}) (Levenspiel, 1999) and the axially-dispersed plug flow with stagnant zone (DPFS) as presented by Villermaux and van Swaai (1969). The DPFS model was developed to model dispersion in packed columns with gas-liquid trickle flow. It features a zone in dispersed plug flow with closed-open boundaries that exchanges material with an adjacent stagnant region. A schematic representation of both models is presented in Figure 6.15.

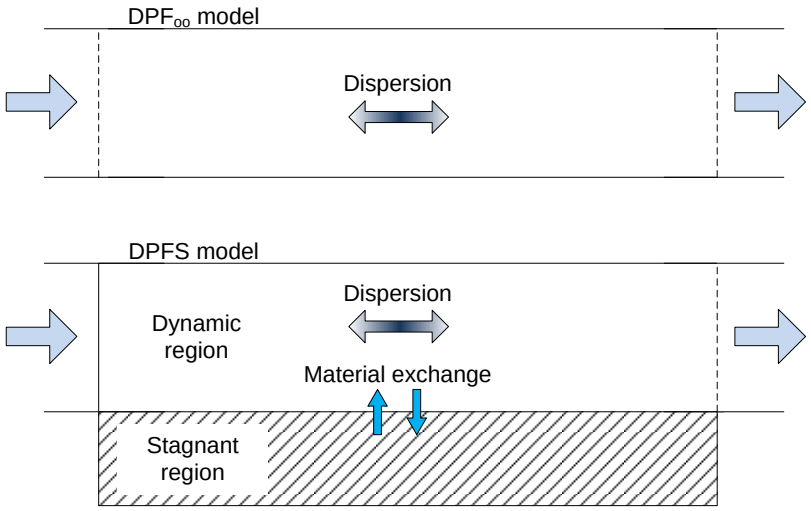

Figure 6.15. Schematic representation of the DPFS model (bottom) (adapted from Villermaux and van Swaai, 1969) compared to the axially-dispersed plug flow model with open-open boundaries (top)

The expressions of the reduced-time exit age distribution function E(θ) (transformable into E(t) using eq. (6.7)) for the DPF$_{oo}$ and DPFS models are:

- *DPF$_{oo}$ model:*

$$E(\theta) = \frac{1}{\sqrt{4\pi\theta/Pe}} \exp\left[-\frac{(1-\theta)^2}{4\theta/Pe} \right] \tag{6.14}$$

where Pe is the Péclet number, defined by equation (3.16).

- *DPFS model:*

$$E(\theta) = \exp\left(-\frac{N\theta}{\phi} \right) h(\theta,\phi) + \int_0^\theta g(x,\theta,\phi)\,dx$$

$$h(x,\phi) = \sqrt{\frac{Pe}{\pi\phi x}} \exp\left[-\frac{Pe(x-\phi)^2}{4\phi x} \right] - \frac{Pe}{2\phi} \exp(Pe)\ \mathrm{erfc}\left[\sqrt{\frac{Pe}{\phi x}} \frac{x+\phi}{2} \right] \tag{6.15}$$

$$g(x,\theta,\phi) = \frac{N}{\phi} \sqrt{\frac{\phi x}{(1-\phi)(\theta-x)}} I_1\left(2N \sqrt{\frac{x(\theta-x)}{\phi(1-\phi)}} \right) \exp\left[-\frac{N(x-2\phi x+\phi\theta)}{\phi(1-\phi)} \right] h(x,\phi)$$

where I_1 is the first-order modified Bessel function of the first kind.

The DPFS model is characterised by three parameters: Pe (Péclet number), ϕ (fraction of fluid in plug flow) and N (number of mass transfer units between plug flow and stagnant regions). This makes the DPFS model very flexible for data fitting, although the mathematical expression of the E(θ) curve is very complex and required implementation in Mathcad.

The DPFS model provided a very good fit in all cases, whereas the DPF_{oo} did not fit many of the experimental curves satisfactorily. An example of data fitting with both models is shown in Figure 6.16.

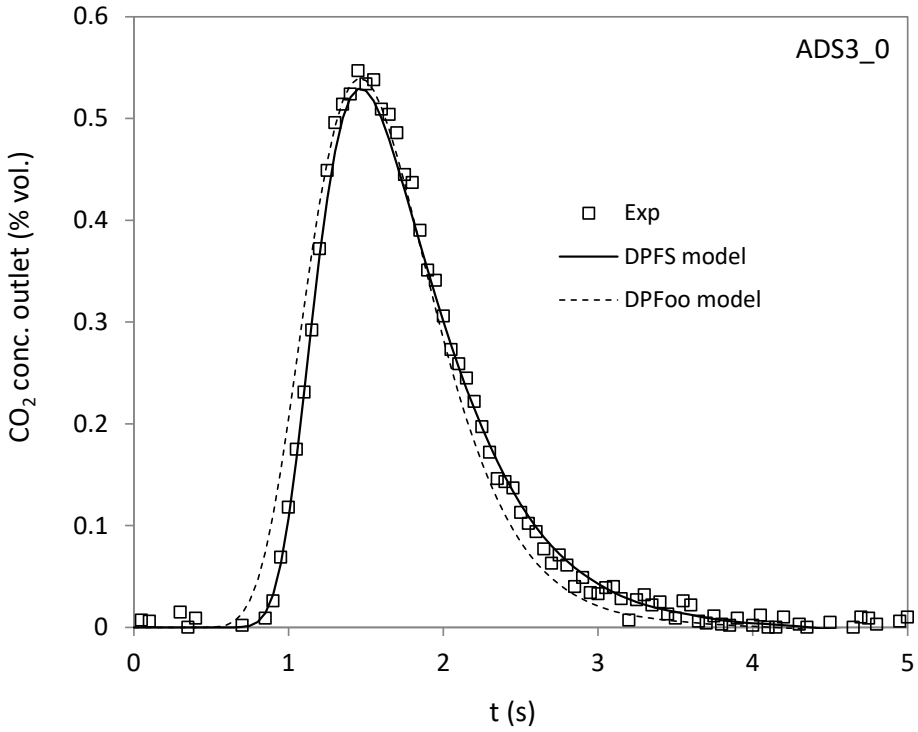

Figure 6.16. Data fitting comparison between the axially-dispersed plug flow with open-open boundaries (DPF_{oo}) and axially-dispersed plug flow with stagnant region (DPFS) models

Figures 6.17 to 6.27 show examples of experimental CO_2 concentration curves for the different CFB sections analysed and the corresponding calculated E(t) curves. The fit of the calculated outlet CO_2 concentration curve to the experimental data is very good in all cases. The gas residence time distributions for each experiment are presented in Tables 6.1 to 6.4 in form of values of the DPFS model parameters.

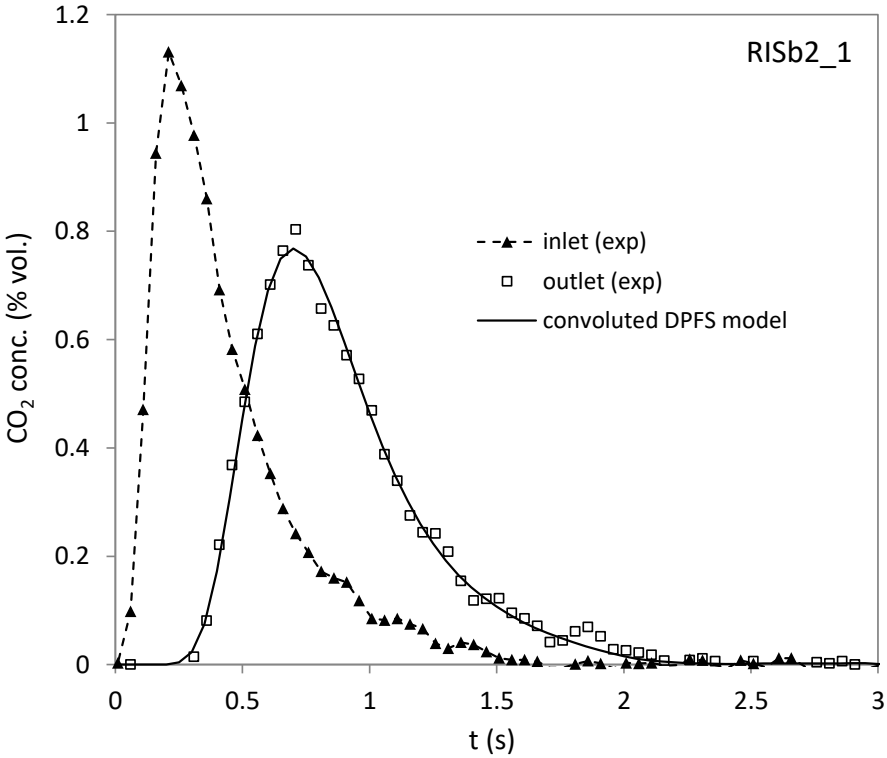

Figure 6.17. Experimental and modelled CO_2 concentration-time curves. Benchmark CFB riser, experiment RISb2_1

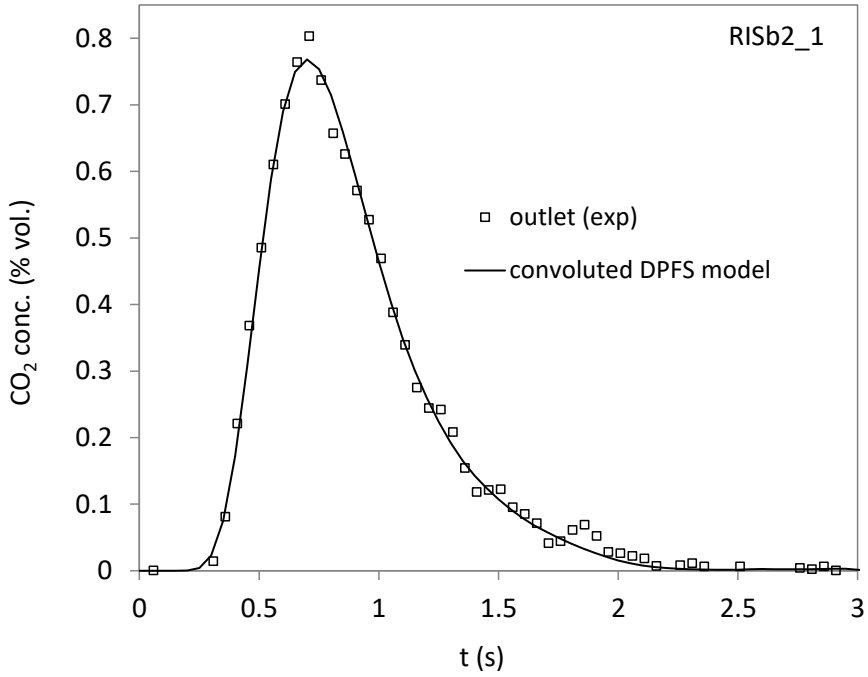

Figure 6.18. Experimental data fitting with convoluted DPFS model (zoomed from Figure 6.17). Benchmark CFB riser, experiment RISb2_1

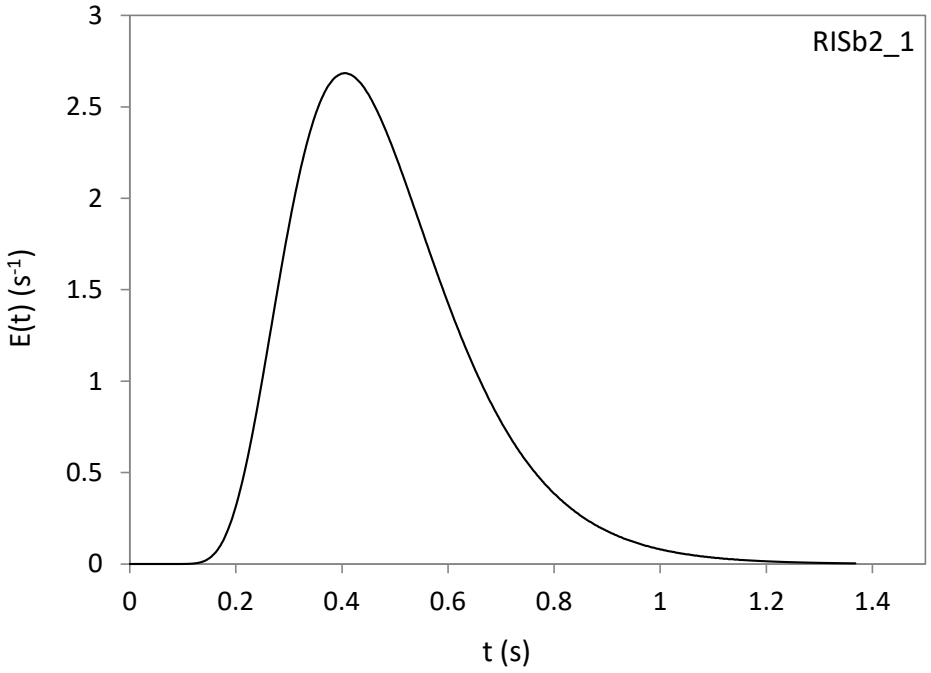

Figure 6.19. E(t) curve of the DPFS model before convolution. Benchmark CFB riser, experiment RISb2_1

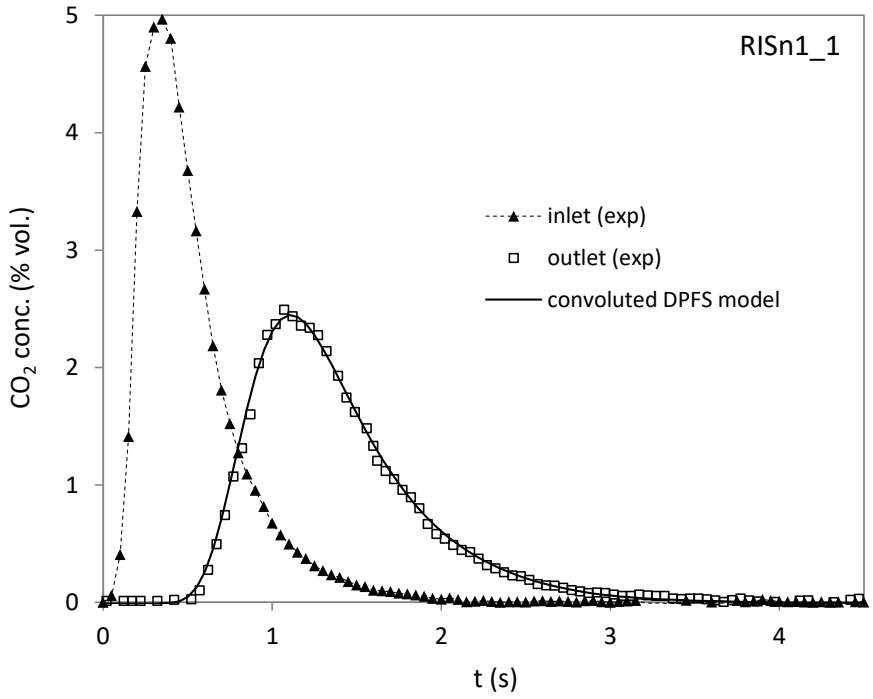

Figure 6.20. Experimental and modelled CO_2 concentration-time curves. Novel CFB riser, experiment RISn1_1

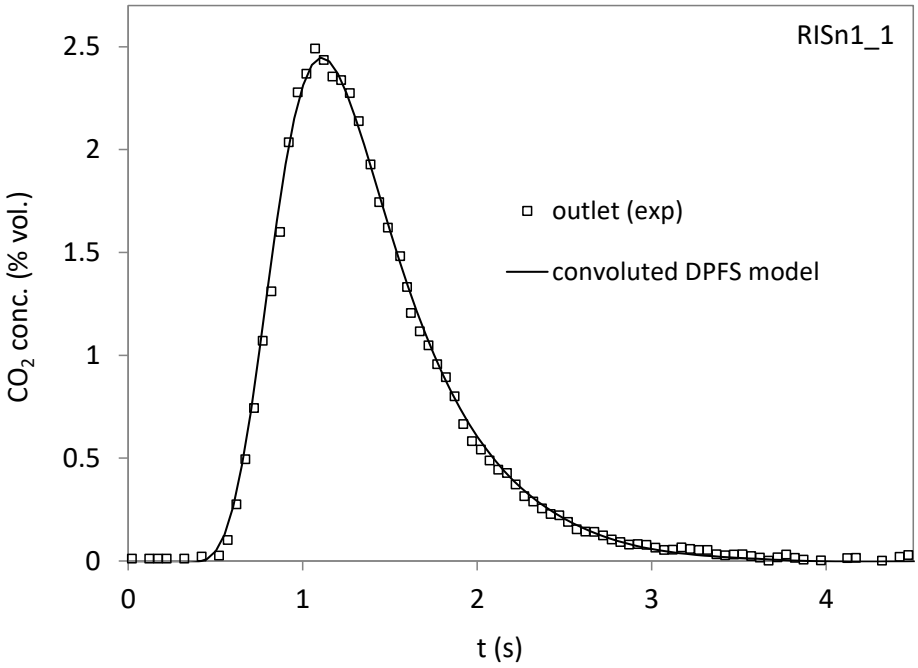

Figure 6.21. Experimental data fitting with convoluted DPFS model (zoomed from Figure 6.20). Novel CFB riser, experiment RISn1_1

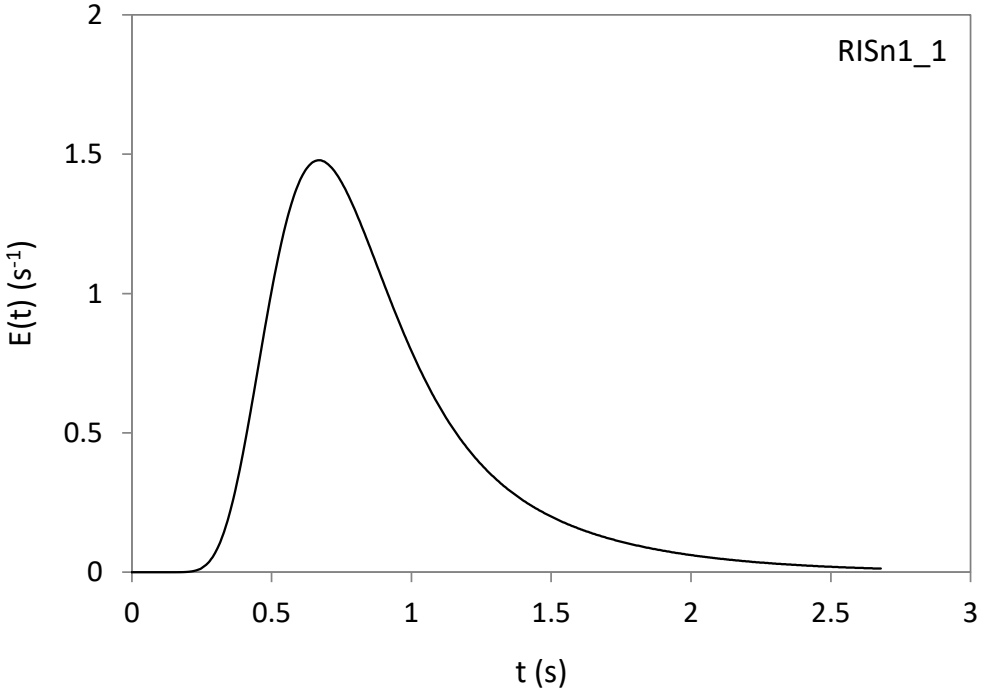

Figure 6.22. E(t) curve of the DPFS model before convolution. Novel CFB riser, experiment RISn1_1

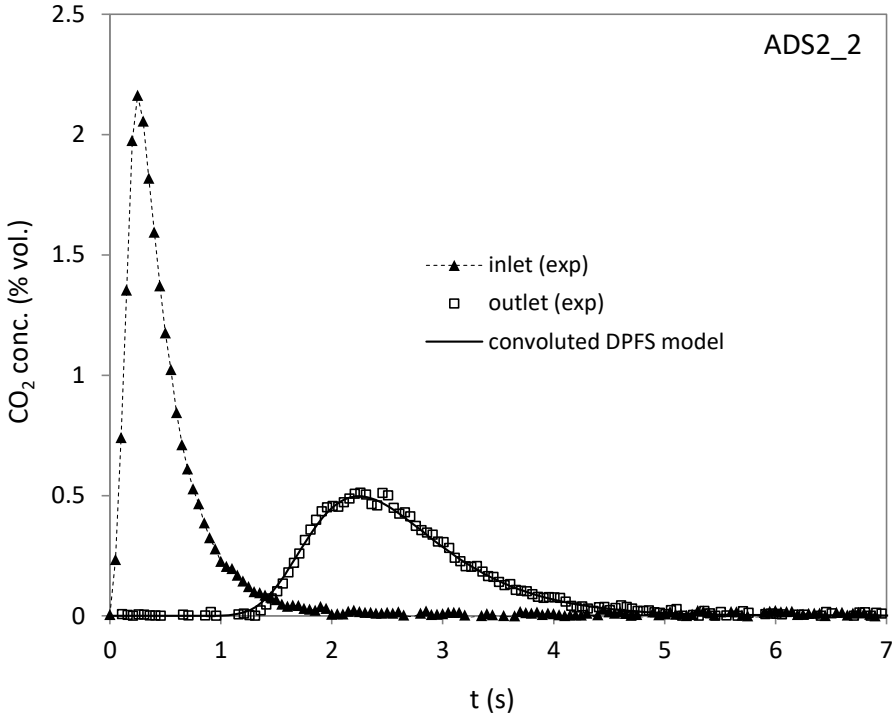

Figure 6.23. Experimental and modelled CO_2 concentration-time curves. Novel CFB adsorber, experiment ADS2_2

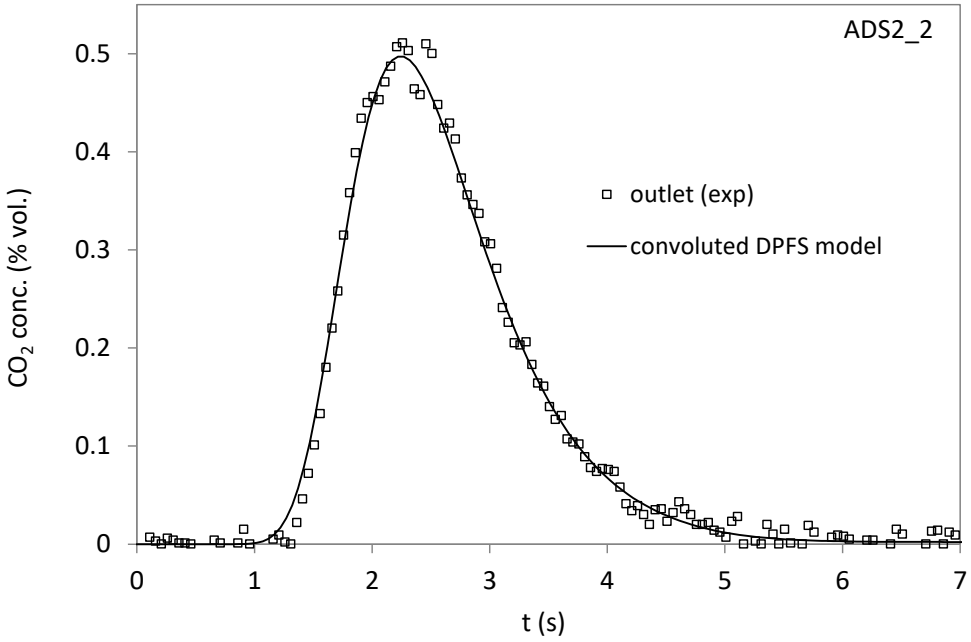

Figure 6.24. Experimental data fitting with convoluted DPFS model (zoomed from Figure 6.23). Novel CFB adsorber, experiment ADS2_2

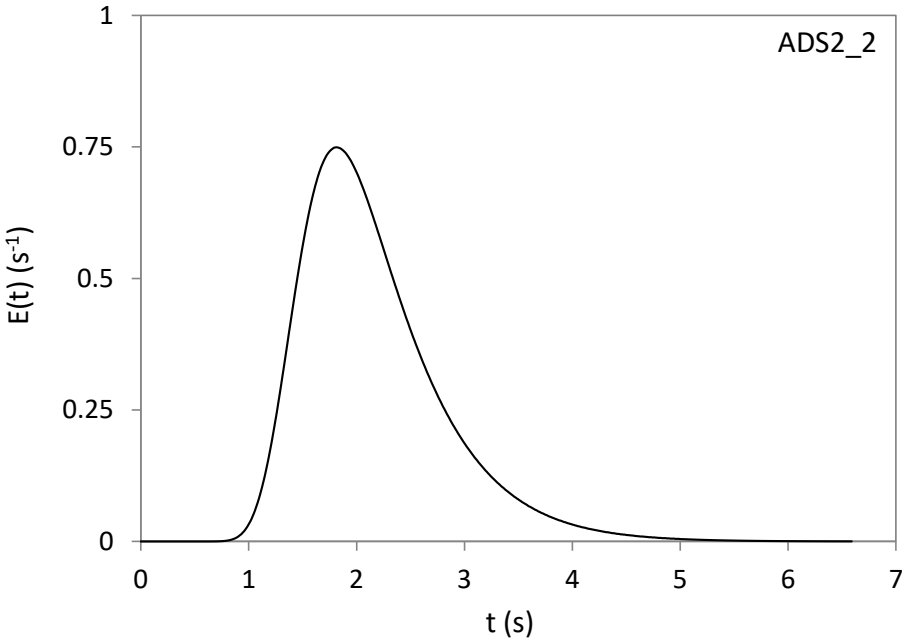

Figure 6.25. E(t) curve of the DPFS model before convolution. Novel CFB adsorber, experiment ADS2_2

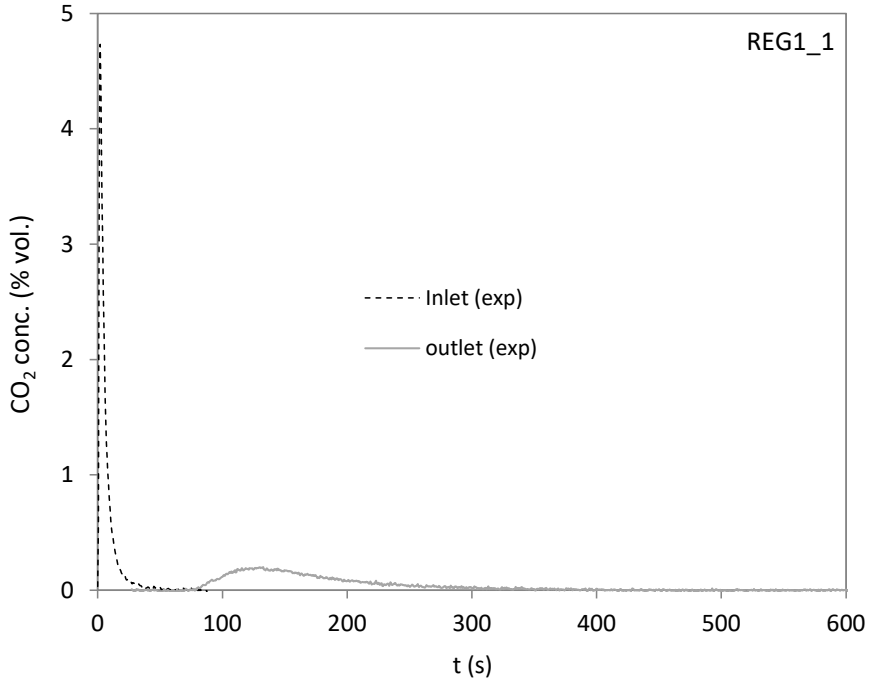

Figure 6.26. Experimental CO_2 concentration-time curves. Regenerator (integrated in novel CFB), experiment REG1_1

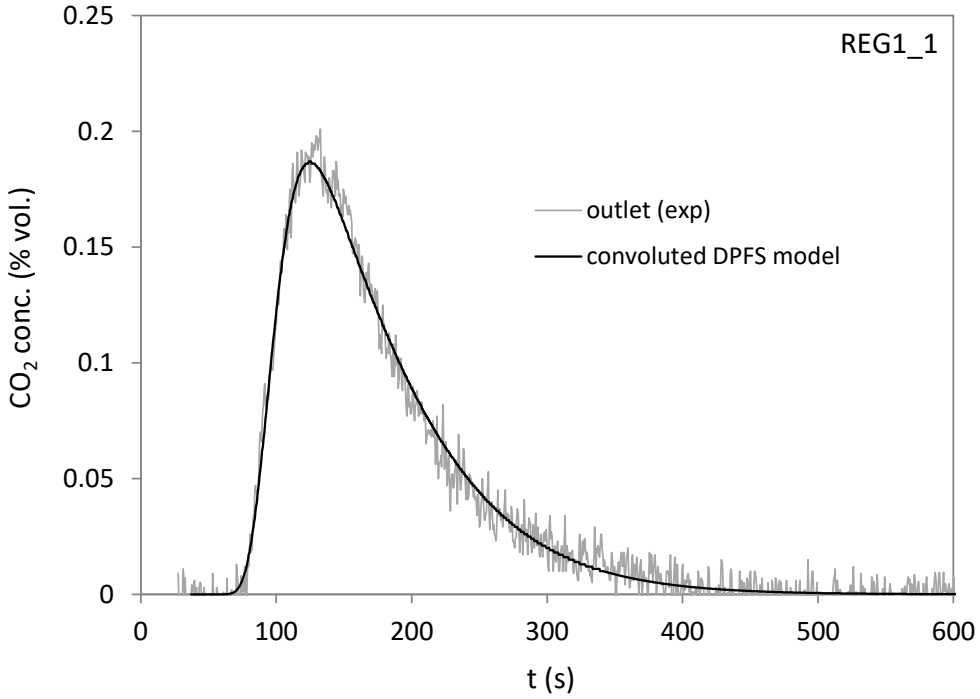

Figure 6.27. Experimental and modelled outlet CO_2 concentration-time curves. Regenerator (integrated in novel CFB), experiment REG1_1

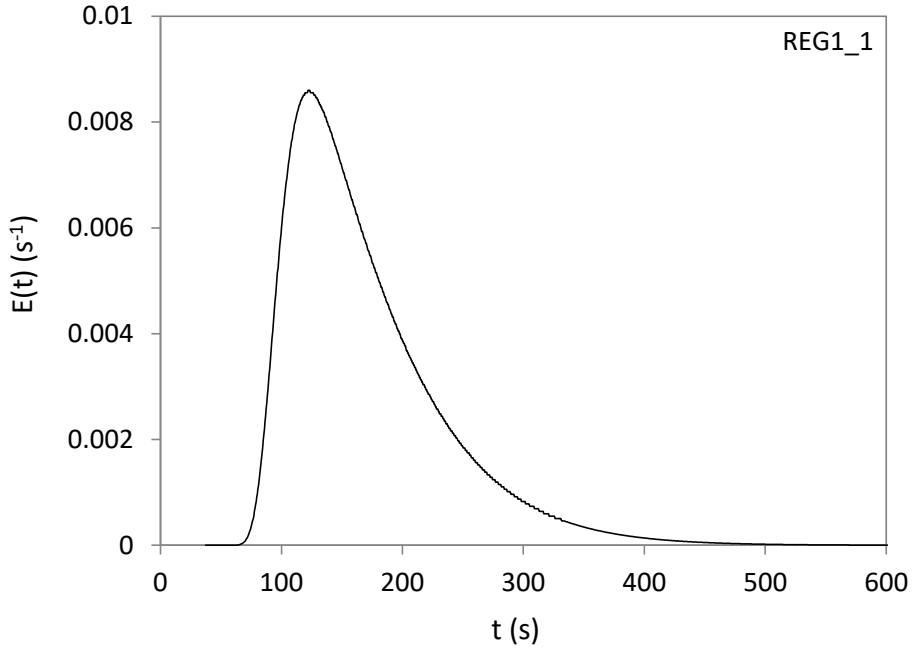

Figure 6.28. E(t) curve of the DPFS model before convolution. Regenerator (integrated in novel CFB), experiment REG1_1

6.5 Results and discussion

Buffham and Mason (1993) recommend the use of normalised moments of the residence time distribution (in particular the normalised variance) to define dispersion since "this would allow experimentalists to record and report dispersion results independently of models or theories". Following this recommendation, the variance of the reduced-time residence time distributions E(θ) is considered here as the main indicator of gas dispersion in the different CFB elements studied. The values of variance are shown in graphs against operating conditions. Values of skewness and graphs of the E(θ) curves themselves are presented afterwards for completeness and to further characterise gas residence time distribution.

All values of mean residence time, variance and skewness presented graphically in the following sections can be found in Tables 6.1 to 6.4.

6.5.1 Mean residence time

E(θ) curves are obtained from the exit age distributions E(t) and the mean residence time τ using eq. (6.7). Prior to that, an analysis of the value of the mean residence time is carried out to ensure the experimental data is meaningful. In this analysis, the experimental values of mean residence time are compared to the expected ones (based on the mass balance) in parity plots.

As explained in Section 6.2.3, the mass balance in a system of constant density dictates that $\tau = V/Q$, where τ is the mean residence time, V is the total volume and Q the volumetric flow rate. The CFB elements studied feature more than one gas inlet and/or outlet, so they are treated as a series of single-inlet, single-outlet sub-elements. The total calculated (or expected) mean residence time τ_{calc} for a given CFB element is:

$$\tau_{calc} = \tau_{calc,1} + \tau_{calc,2} + ... = V_1 / Q_1 + V_2 / Q_2 + ... \qquad (6.16)$$

where 1,2,… are the sub-elements in which a particular CFB element is divided. Figures 6.29 to 6.32 show a schematic representation of the CFB elements studied and how these are divided in sub-elements, together with the corresponding values of

geometrically-calculated volumes and gas streams. All gas flow rates are considered to be at 0 barg. Solid fractions are assumed to be zero except for the solids bed in the regenerator, where the value of ε_s is assumed to be 0.58, the average value between compact and loose bed.

Experimental values of mean residence time τ_{exp} can be obtained in two different ways: directly from the first moment of the E(t) curves:

$$\tau_{exp} = \frac{\int_0^\infty tE(t)dt}{\int_0^\infty E(t)dt} = \int_0^\infty tE(t)dt \tag{6.17}$$

or as the difference of first moments between the outlet and inlet concentration-time curves:

$$\tau_{exp} = \tau_{out,exp} - \tau_{in,exp} = \frac{\int_0^\infty tC_{out}(t)dt}{\int_0^\infty C_{out}(t)dt} - \frac{\int_0^\infty tC_{in}(t)dt}{\int_0^\infty C_{in}(t)dt} \tag{6.18}$$

It can be argued that equation (6.18) is the one to use to obtain the "truly" experimental value of mean residence time. However, the limits of integration need necessary to be changed to arbitrary "truncated" values if the noise signal before and after the tracer pulse is to be excluded from the integral. Once arbitrariness is accepted in the calculation, the use of equation (6.17) is justified since the E(t) curves were obtained from the tracer concentration curves by data fitting. The values of τ_{exp} presented in this work were obtained by using (6.17).

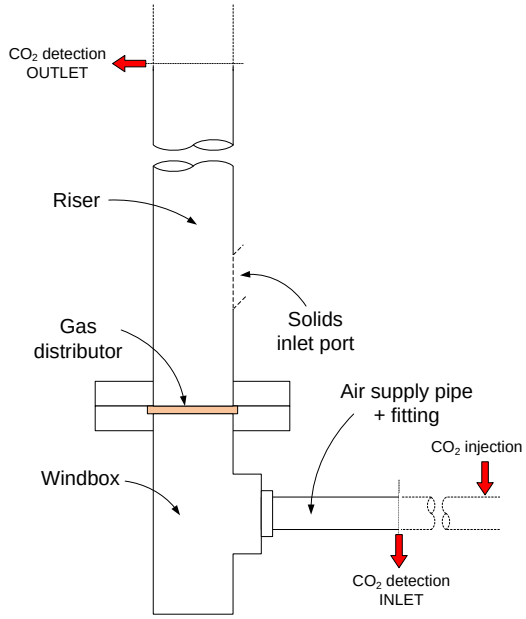

BENCHMARK CFB RISER		
	Volume (l)	Gas flow rate
Air supply pipe (from CO_2 inlet detection point) + fitting	0.04	$Q_{ris,in}$
Windbox	0.18	
Riser (from gas distributor to solids inlet port)	0.2	
Riser (from solids inlet port to CO_2 outlet detection point)	5.0	Q_{ris}
Total volume	**5.42**	

Figure 6.29. Volumes from tracer injection to detection planes. Benchmark CFB riser

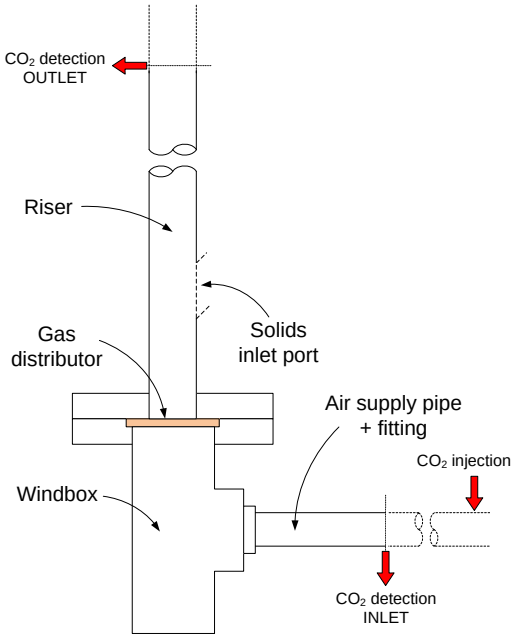

NOVEL CFB RISER		
	Volume (l)	Gas flow rate
Air supply pipe (from CO_2 inlet detection point) + fitting	0.04	$Q_{ris,in}$
Windbox	0.18	
Riser (from gas distributor to solids inlet port)	0.06	
Riser (from solids inlet port to CO_2 outlet detection point)	0.78	Q_{ris}
Total volume	**1.06**	

Figure 6.30. Volumes from tracer injection to detection planes. Novel CFB riser

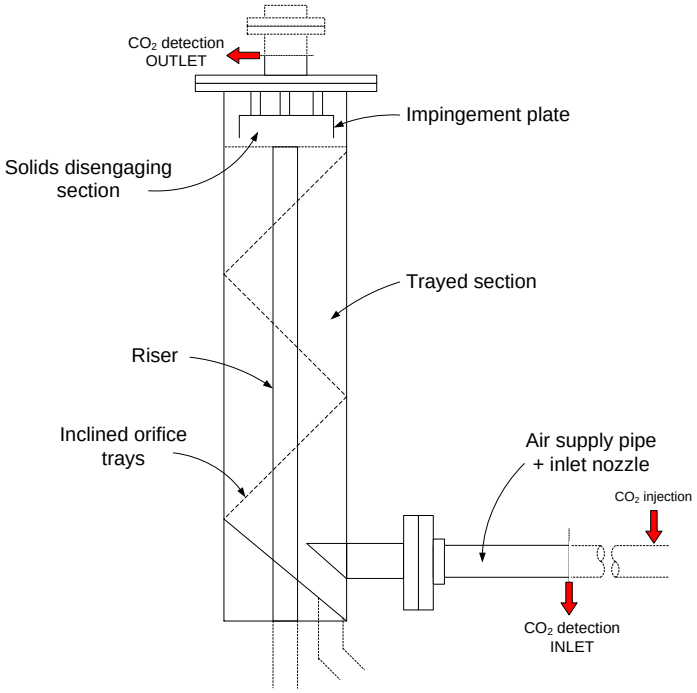

NOVEL CFB ADSORBER		
	Volume (l)	Gas flow rate
Air supply pipe (from CO_2 inlet detection point) + inlet nozzle	0.15	$Q_{ads,in}$
Trayed section	9.6	Q_{ads}
Inclined orifice trays (x3)	-0.25	
Riser	-0.29	
Solids disengaging section	1.1	Q_{top}
Impingement plate	-0.30	
Outlet pipe (to CO_2 outlet detection point)	0.04	
Total volume	**10.05**	

Figure 6.31. Volumes from tracer injection to detection planes. Novel CFB adsorber

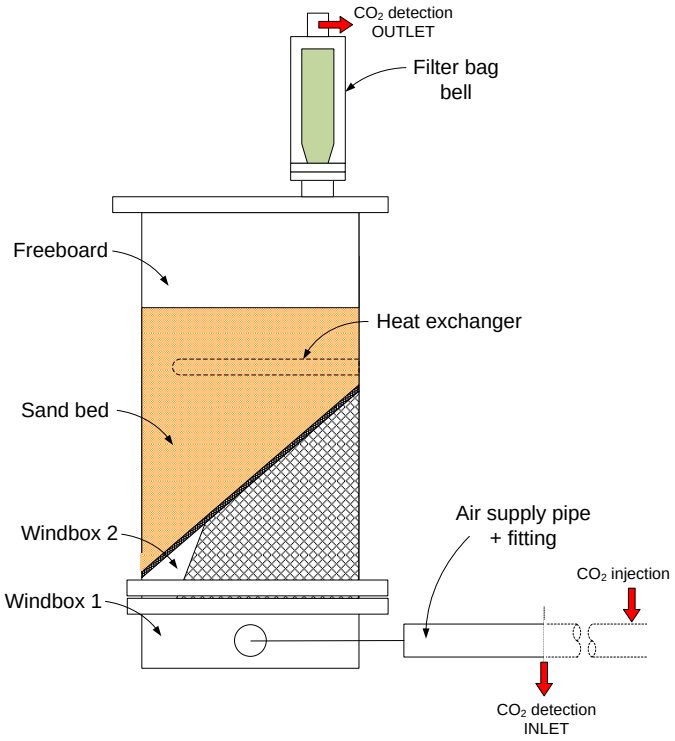

REGENERATOR		
	Volume (l)	Gas flow rate
Air supply pipe (from CO_2 inlet detection point) + fitting	0.04	$Q_{reg,in}$
Windbox 1+2	11.5	
Sand bed (interstitial volume, ε_s = 0.58)	6.3	Q_{reg}
Heat exchanger	-0.37	
Freeboard	22.5	$Q_{reg} + Q_{dc}$
Filter bag bell + outlet gas nozzle	2.0	$Q_{reg,out}$
Total volume	**42.0**	

Figure 6.32. Volumes from tracer injection to detection planes. Regenerator

- *Risers:*

The values of experimental tracer mean residence time are overall distributed within ±55% of the calculated values with no particular trend with the operating conditions. The values of absolute error, however, are small and range between 0.2 s and 0.3 s. These values of absolute error may well be attributed to lack of perfect synchronisation between the experiment time zero and the trace pulse injection, which was done by manually opening the injector ball valve after a 10-second countdown. This problem would be eliminated if inlet and outlet tracer concentrations were recorded simultaneously with two tracer sensors, rather than sequentially using only one.

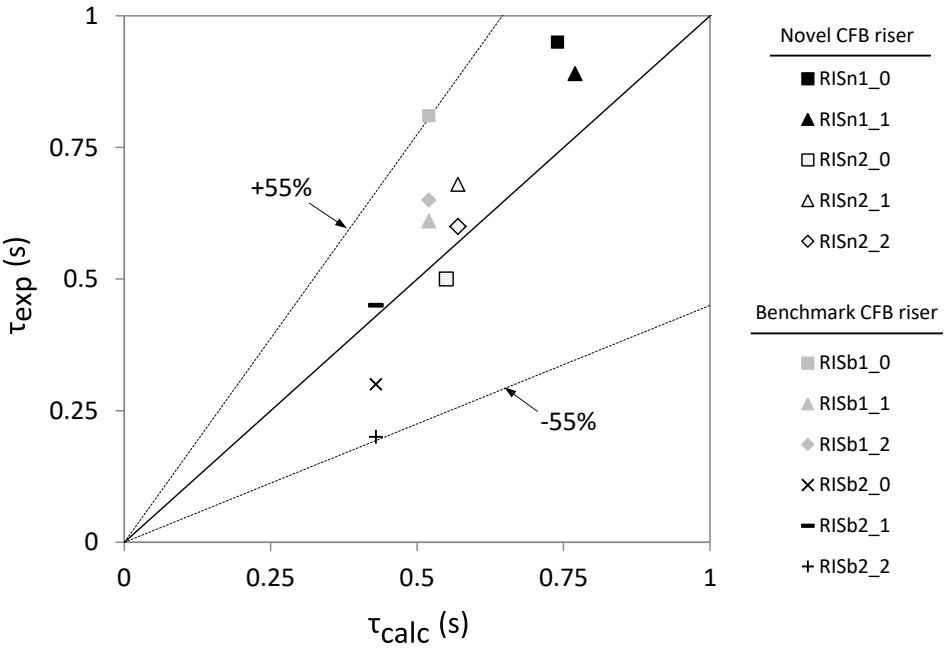

Figure 6.33. Parity plot of gas mean residence time. Benchmark and novel CFB risers

The high uncertainty in the values of mean residence time translates directly into high relative uncertainty in the shape of the corresponding E(θ) curves, by virtue of equation (6.7). Figure 6.34 shows how the shape of the curve and values of variance and skewness change with a shift of ±0.2 s in the E(t) curve. The data chosen to generate the graphs in Figure 6.34 correspond to the experiment with the shortest expected value of mean residence time (RISb2_1, $\tau_{calc} = 0.43$ s) and therefore the

impact of human response time is large. In this particular case, a shift of -0.2 s in the E(t) curve corresponds to a mean residence time reduced to a half, causing a threefold increase in the variance of the E(θ) curve. A shift of +0.2 s causes a lower impact since the relative change in mean residence time is lower. Given all the above, the expected values of mean residence time are used instead of the experimental to obtain the E(θ) curves for the riser experiments.

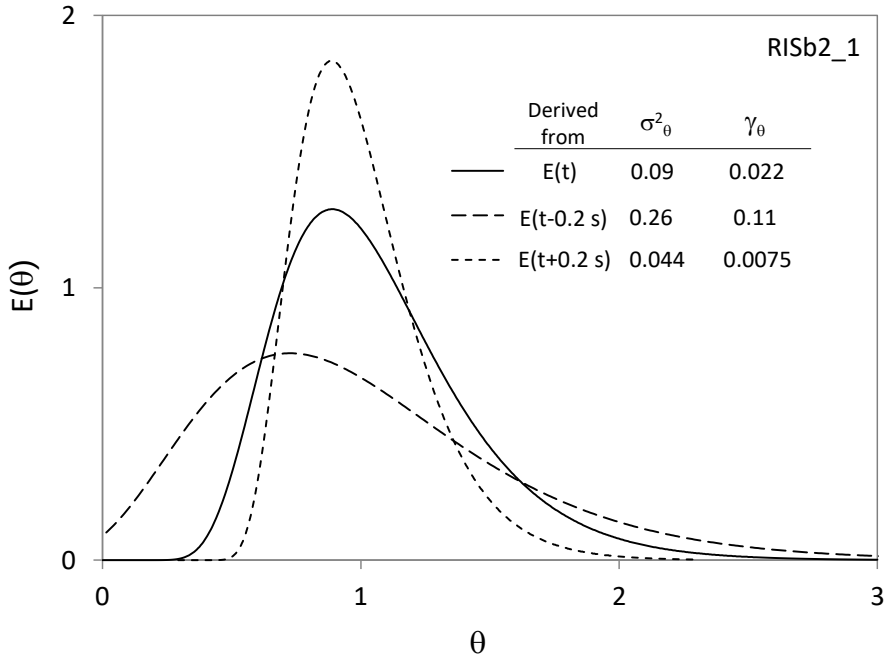

Figure 6.34. Impact of ±0.2 s shift in the E(t) curve on shape of the E(θ) curve and values of variance and skewness. Benchmark CFB riser, experiment RISb2_1

- *Novel CFB adsorber:*

Similarly to what is discussed above for the CFB risers, the experimental values of gas mean residence time in the novel CFB adsorber spread around the calculated, with values of absolute error between 0.2 s and 0.3 s and no discernible trend with operating conditions. The relative error is lower than for the risers (+40-10%) due to the overall higher value of gas mean residence time in this CFB element (1-4 s, compared to 0.4-0.8 s in the risers). Similarly to what was done for the risers, the expected values of mean residence time are used to obtain the corresponding E(θ) curves.

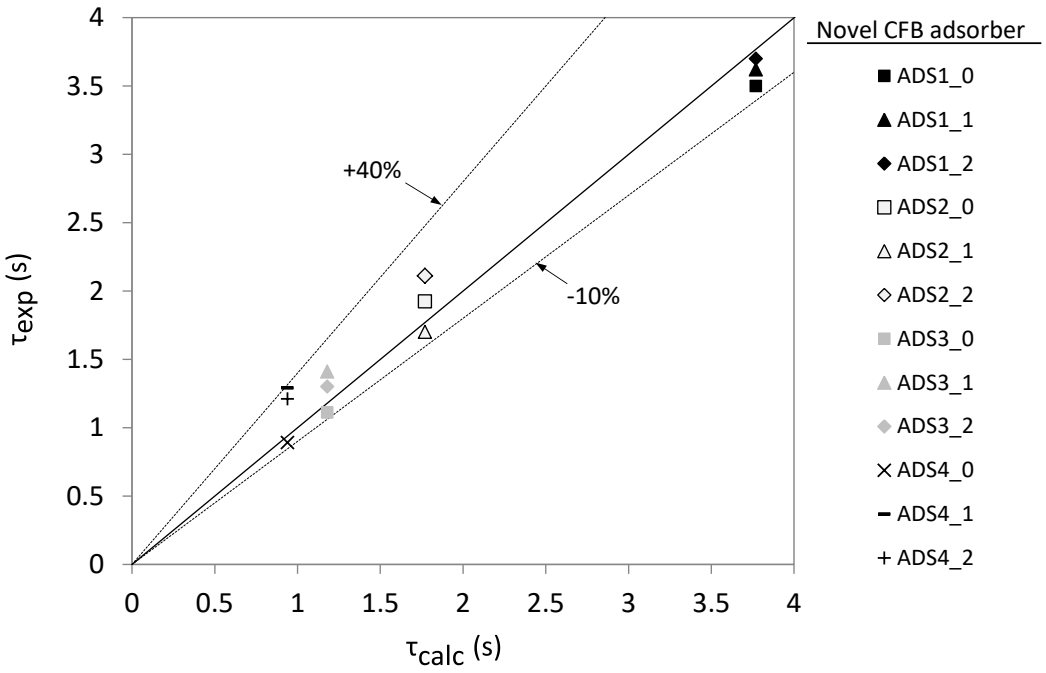

Figure 6.35. Parity plot of gas mean residence time. Novel CFB adsorber

- *Regenerator:*

The deviation between experimental and expected values of gas mean residence time in the regenerator is around 4%. The fact that all experimental values are lower than the theoretical could be caused by a systematic error in the gas flow rates or measured regenerator volume, but it could also be related to the system fluid dynamics. For example, the existence of stagnant regions in a flow system causes "tailing" in the tracer concentration curves that is often "truncated" or not properly detected, therefore shifting the mean residence time to lower values (Levenspiel, 1962; White, 1963). The experimental CO_2 concentration curves obtained here present a high noise-to-signal ratio in the tail region, making it difficult to accurately measure it.

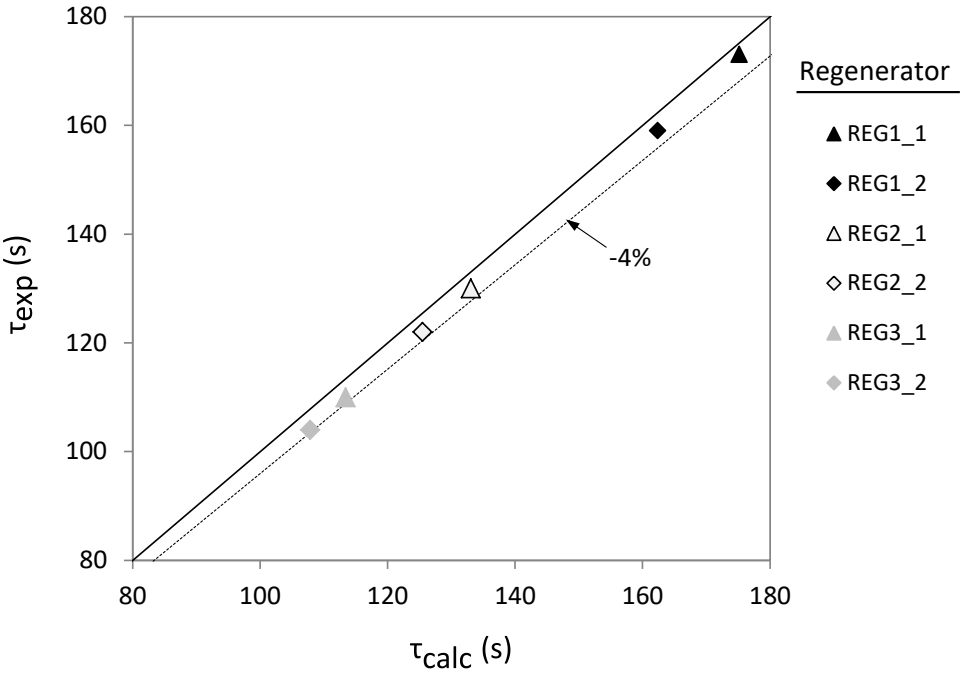

Figure 6.36. Parity plot of gas mean residence time. Regenerator (integrated in novel CFB)

6.5.2 Variance of reduced-time gas exit age distribution curves E(θ)

- *Risers:*

Figure 6.37 shows the values of variance of the E(θ) curves obtained for both CFB risers as a function of the solid flux and two different values of gas velocity. Variance increases with solids flux and decrease with gas velocity in both cases. These results are in agreement with most published works on gas axial dispersion in CFB risers for the ranges of U_g and G_s used here, see for example Li and Wu (1991), Bai et al. (1992) and Brereton et al. (1998).

The risers of the CFB rigs studied here are operated at conditions of gas velocity and solids flux around the transition between lean transport and fast fluidisation (see Chapter 5). In this region of the U_g - G_s diagram, any change in operating conditions leading to an increase in solids concentration is usually accompanied by a rapid increase in the relative velocity between phases (this will become evident from the results of the particle tracking experiments, Chapter 7) and the formation of larger structures than the single particle. The associated increase in dispersion of the gas phase can be attributed to the dragging effect of such structures upon the gas in the periphery or in the interstitial volume. At even higher gas velocities and solid fluxes, the effect of both operating variables on gas dispersion is less clear, but results suggest that gas dispersion decreases as the so-called dense upflow regime is approached (Dry and White, 1989; Contractor et al., 2000).

The geometry-induced contribution to the values of variance (given by the blank experiments) is at least of the same magnitude of that caused by the presence of solids for the ranges of U_g and G_s studied. Grace et al. (2003) stressed the strong effect of geometry on gas dispersion in CFBs, including riser entrance, exit, length and diameter.

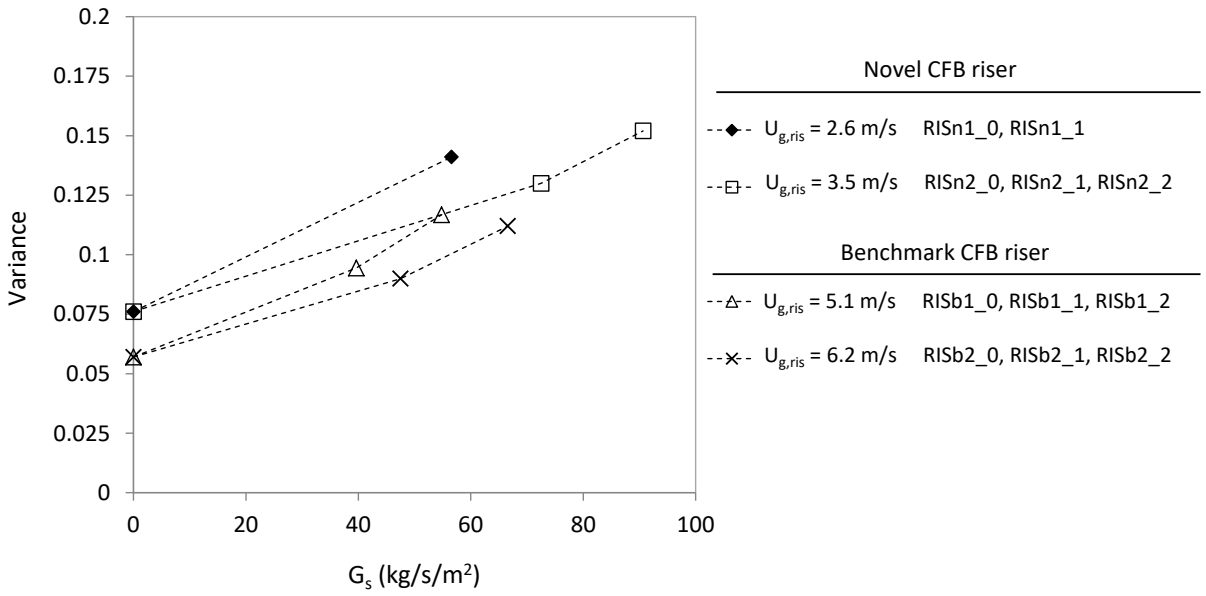

Figure 6.37. Variance of E(θ) curves as a function of solids flux at two different gas superficial velocities. Benchmark and novel CFB risers

- *Novel CFB adsorber:*

Figure 6.38 shows the values of variance of the E(θ) curves obtained for the counter-current adsorber as a function of solids flux and four different values of gas velocity. The impact of solids flux on the values of variance is strongest at the lowest value of gas velocity. As the value of $U_{g,ads}$ increases, the values of variance become increasingly less sensitive to solids flow rate.

Similarly to what was observed for the risers, the contribution of the system geometry on the absolute values of variance is at least of the same order of that due to gas-solid interaction. The increase in variance of the blank experiments from 0.07 to 0.12 units (78% increase) when the gas superficial velocity is increased from 0.35 m/s to 0.52 m/s could not be explained.

The effect of solids flow in gas dispersion found here agrees with the findings of Roes and van Swaaij (1979b) in gas-solid trickle flow in a packed column. The authors studied gas and solids mixing using tracer techniques, and reported a dramatic drop in the gas Bodenstein number (equivalent to the Péclet number using the packing element diameter as the characteristic length) in experiments with solids

flow with respect to no solids flow, the drop being greater at lower gas velocities. The exact same observation was made by Noordergraaf et al. (1980) for a similar study in a gas-solid zig-zag contactor. In both studies the investigators attributed the gas dispersion to gas entrainment by the trickling stream of solids. Westerterp and Kuczynski (1987a) hypothesised a mechanism for gas recirculation in a gas-solid column packed with Raschig rings, in which portions of gas would be carried down a number of times the geometric diameter of the packing element by trickles of solids, and released by impingement on the packing (refer to the literature review, Section 2.2, for discussion).

For the geometry of the novel CFB adsorber, it can be hypothesised that gas dispersion caused by solids flow occurs mostly at the orifices of the inclined trays, as it is here where the solids concentrate in dense trickle streams similar to those observed in gas-solid packed bed contactors. In case of the experiments at the lowest gas superficial velocity (ADS1_0 to ADS1_2), where the impact of solids flow rate on the values of variance is the strongest, the gas velocity at the tray orifices is 0.48 m/s, or 48% of the terminal velocity of the solids (u_t = 1 m/s). In these conditions the solid trickles can develop and flow through the orifices, carrying down the gas. As the gas velocity through the orifices approaches the terminal velocity of the solids by increasing the air flow rate, the solids flow through the orifices is hindered and occurs instead close to the adsorber wall, from the lower edge of the inclined orifice trays, in a similar way to in a staged fluidised bed with downcomers (this is revealed in the particle tracking experiments, Section 7.6.2). Gas dispersion due to gas-solid contact therefore occurs at a much lower extent at high gas velocities.

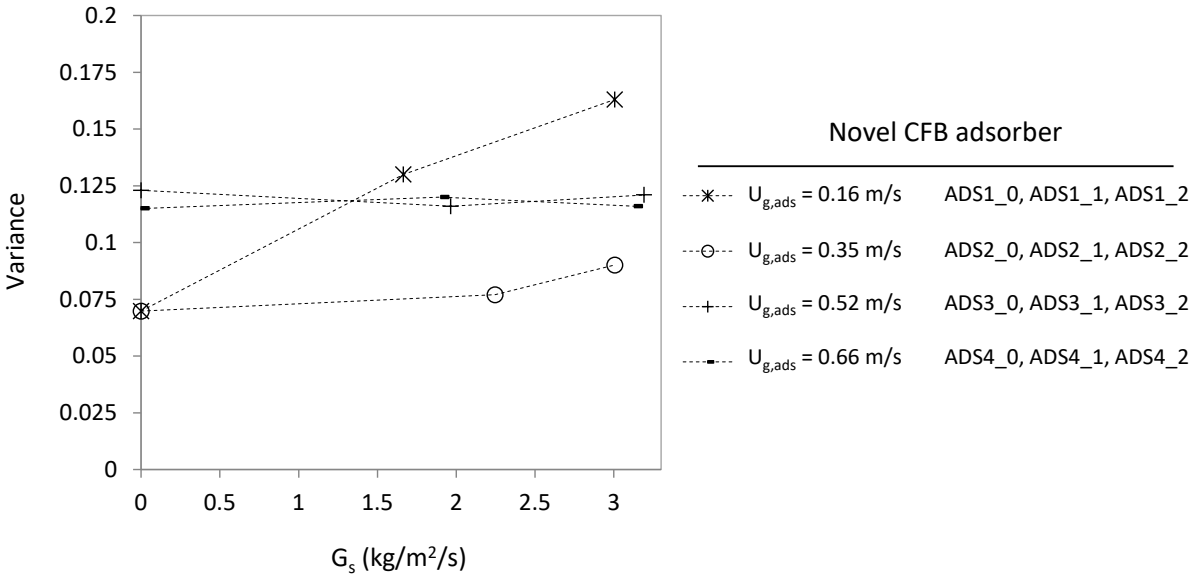

Figure 6.38. Variance of E(θ) curves as a function of solids flux at different gas superficial velocities. Novel CFB Adsorber

- *Regenerator:*

Figure 6.39 shows the values of variance of the E(θ) curves for the regenerator as a function of primary air flow rate $Q_{reg,in}$ and two different values of lube air flow rate (0 l/min and 10 l/min). Lube air was used to increase the solids flow rate at constant value of primary air flow rate.

Variance increases with primary air flow rate, especially at higher values of $Q_{reg,in}$. The impact of increasing the solids flow rate by using lube air is small, and a clear trend could not be found.

Increase in gas dispersion with gas flow rate in the regenerator is opposite to the trend expected for a fixed or moving bed, unless phenomena disturbing the structural and/or flow homogeneity of the bed is present (Wen and Fan, 1975; Westerterp et al., 1984; Levenspiel, 1999). The co-existence of a fixed and a moving bed (first observed visually and confirmed later by the PEPT technique, Chapter 7) may well cause radial differences in bed voidage and/or gas velocity that contribute to gas dispersion. Paterson et al. (2000) found that the shear force caused by rough walls on moving beds caused gas maldistribution that was not limited to the vicinity of the

wall but also extended into the bed. The particular asymmetric geometry and location of the regenerator gas distributor could be contributing to gas dispersion as well.

Nevertheless, it should be stressed that the bed of solids occupies only a fraction of the total regenerator volume (the interstitial volume of the bed of solids is just 15% of the total gas volume in the regenerator), and therefore its contribution to gas dispersion is masked mainly by that of the windbox and the freeboard, which are large empty volumes. Determination of gas RTD specific to the bed of solids in the regenerator would require dedicated experiments that were not carried out in this work.

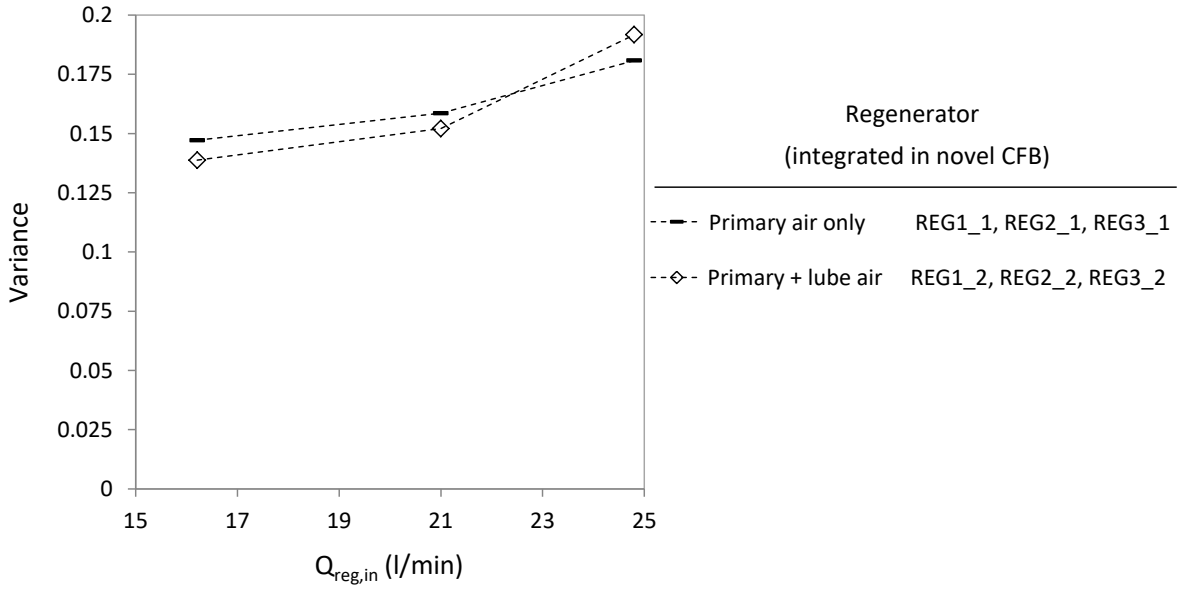

Figure 6.39. Variance of E(θ) curves as a function of air inlet flow rate at different lube air flow rates. Regenerator (integrated in novel CFB)

6.5.3 Skewness of E(θ) curves

Values of skewness of all E(θ) curves obtained are shown in Figure 6.40 as a function of variance. The curve skewness-variance of the DPFS model when $\phi = 1$ (no stagnant zone, and therefore equivalent to the axially-dispersed plug flow model with closed-open boundaries) is plotted in the same graph for reference as it represents the lower bound for the values of skewness.

The general trend in Figure 6.40 is an increasing level of "tailness" (increasing separation from the lower bound line) in gas RTDs with increasing gas dispersion. It can then be argued that the mechanisms causing gas axial dispersion in the CFB elements are also causing tailness in the gas RTDs in a higher extent than the predicted by the axially-dispersed plug flow model. The results for the risers and the novel CFB adsorber suggest that such mechanism could be the dragging effect of the solid particles on the gas phase, especially when forming aggregates.

It was commented previously that tailness is associated to fluid stagnancy (refer to the discussion related to the mean residence time in the regenerator, Figure 6.36). In can then be argued that gas stagnancy occurs in the CFB elements not in localised zones, but distributed around and within solid particles and particle aggregates.

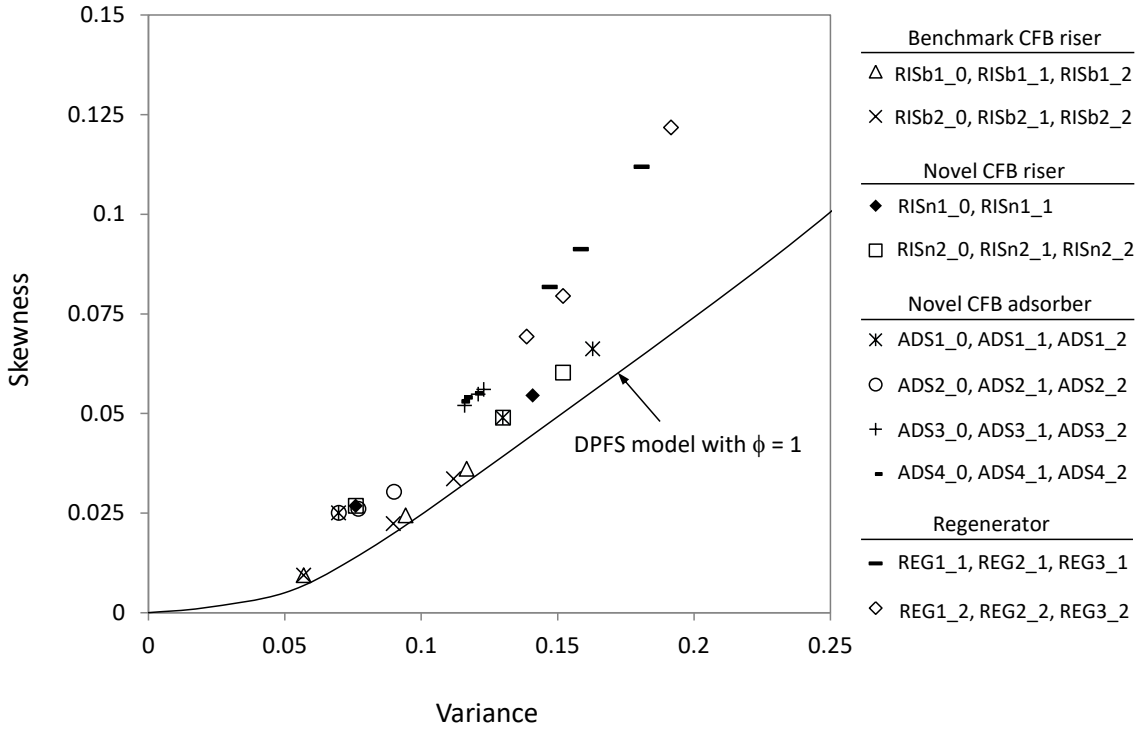

Figure 6.40. Skewness of E(θ) curves as a function of variance for all gas RTD experiments

6.5.4 E(θ) curves graphs

- *Benchmark CFB riser:*

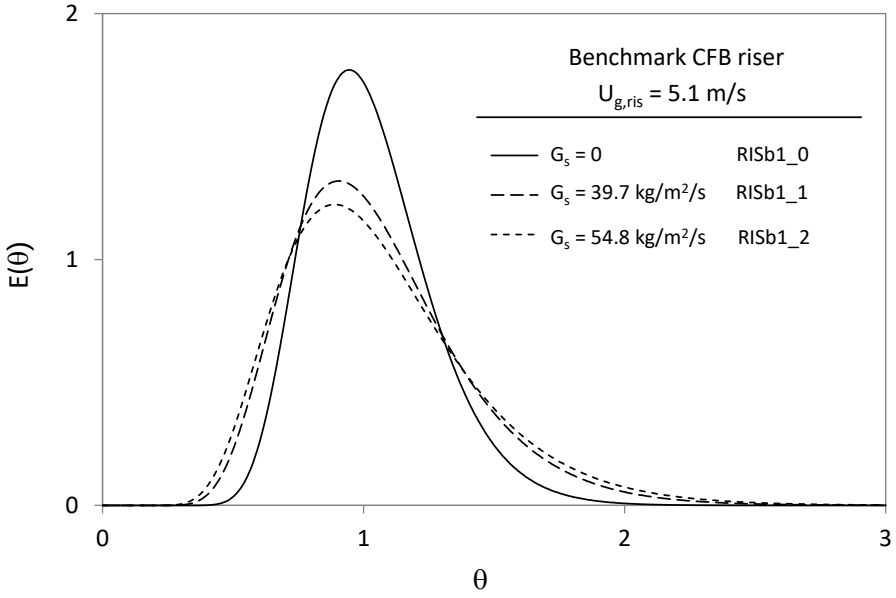

Figure 6.41. Reduced-time gas exit age distribution curves. Benchmark CFB riser, $U_{g,ris}$ = 5.1 m/s

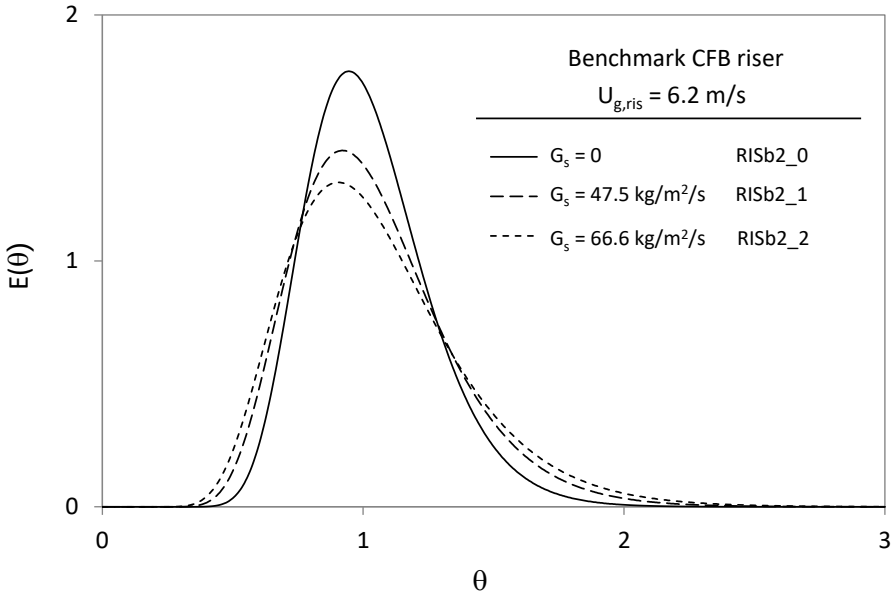

Figure 6.42. Reduced-time gas exit age distribution curves. Benchmark CFB riser, $U_{g,ris}$ = 6.2 m/s

- *Novel CFB riser:*

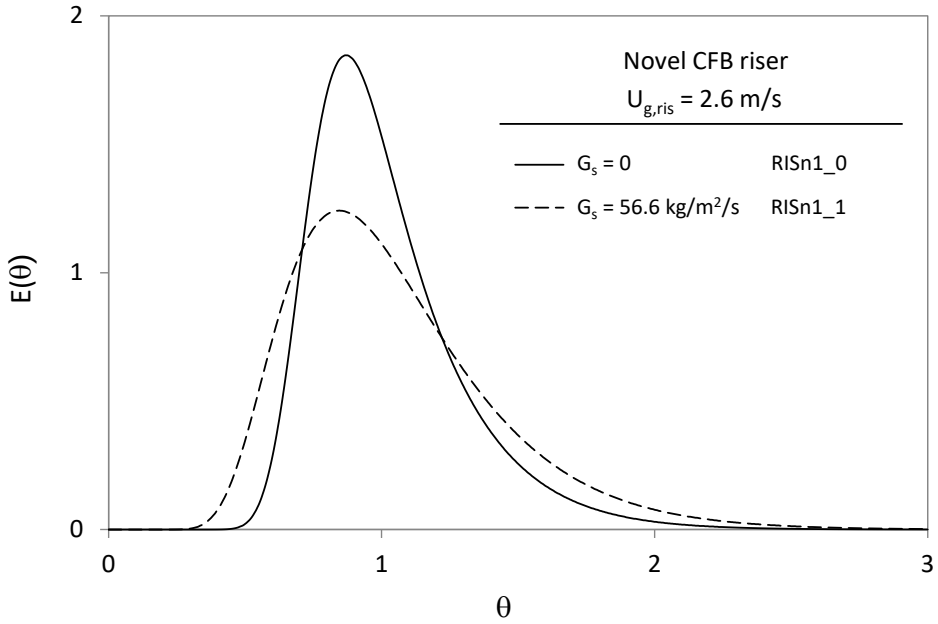

Figure 6.43. Reduced-time gas exit age distribution curves. Novel CFB riser, $U_{g,ris}$ = 2.6 m/s

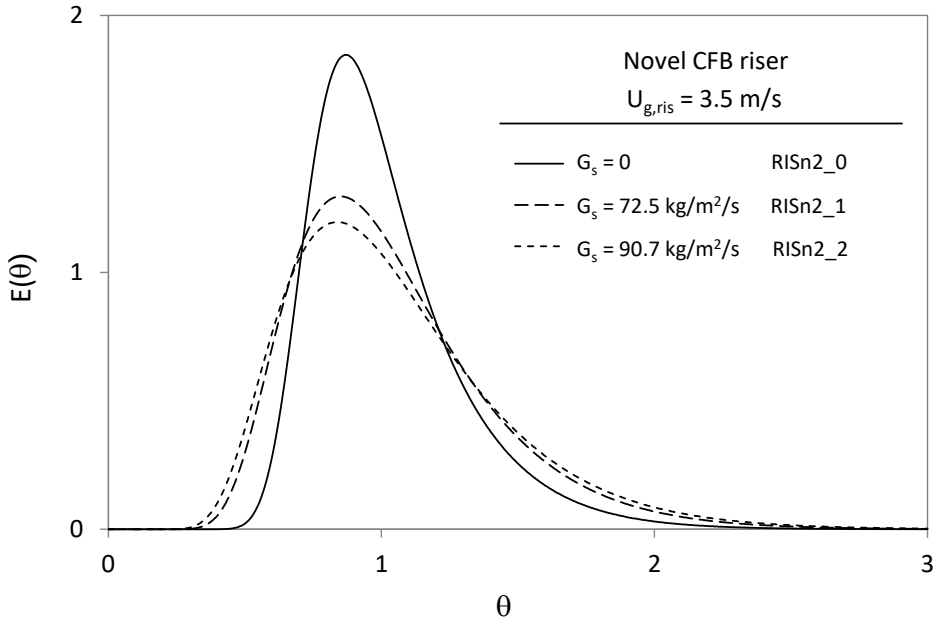

Figure 6.44. Reduced-time gas exit age distribution curves. Novel CFB riser, $U_{g,ris}$ = 3.5 m/s

- *Novel CFB adsorber:*

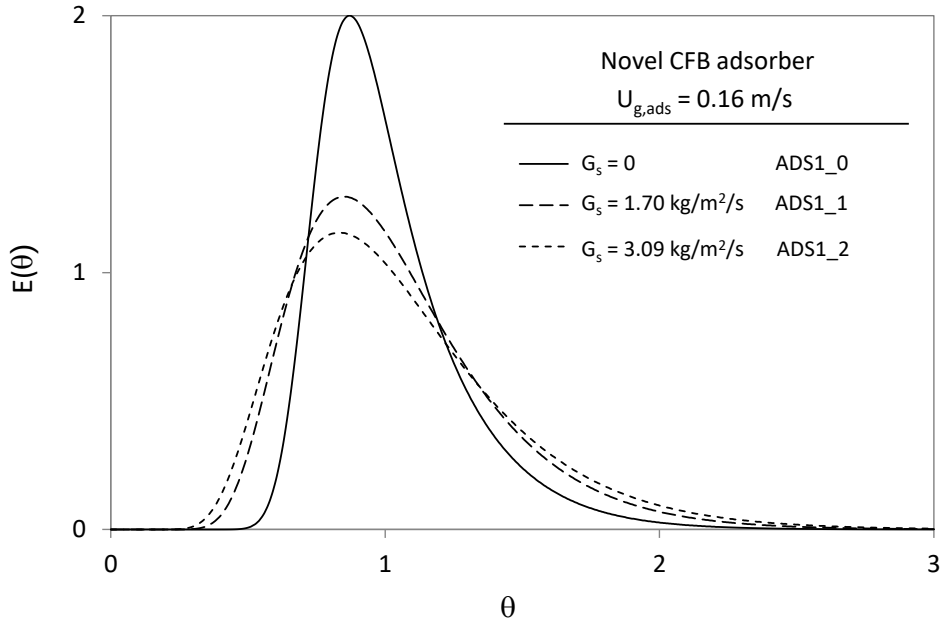

Figure 6.45. Reduced-time gas exit age distribution curves. Novel CFB adsorber, $U_{g,ads}$ = 0.16 m/s

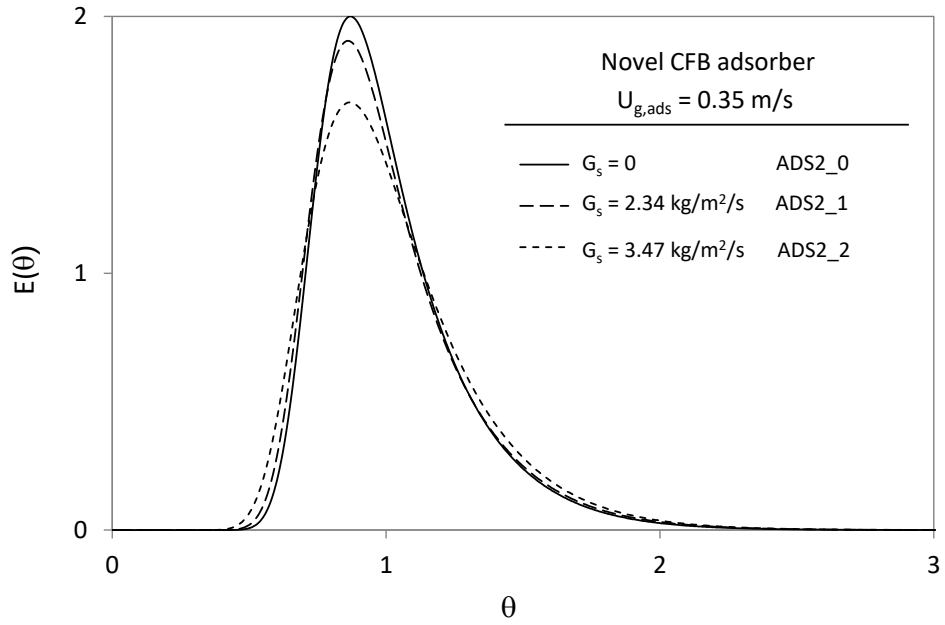

Figure 6.46. Reduced-time gas exit age distribution curves. Novel CFB adsorber, $U_{g,ads}$ = 0.35 m/s

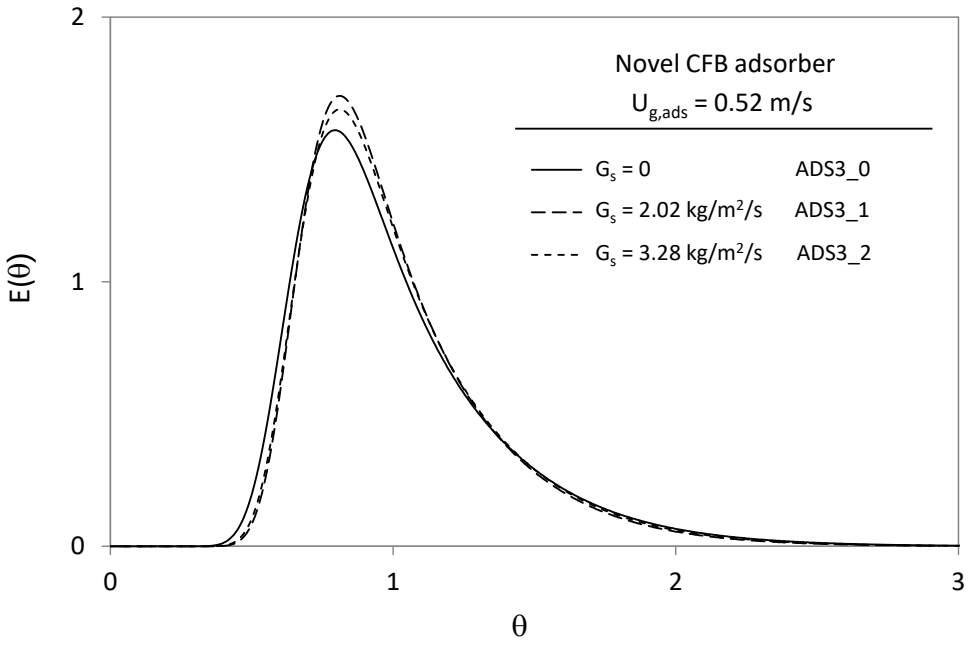

Figure 6.47. Reduced-time gas exit age distribution curves. Novel CFB adsorber, $U_{g,ads}$ = 0.52 m/s

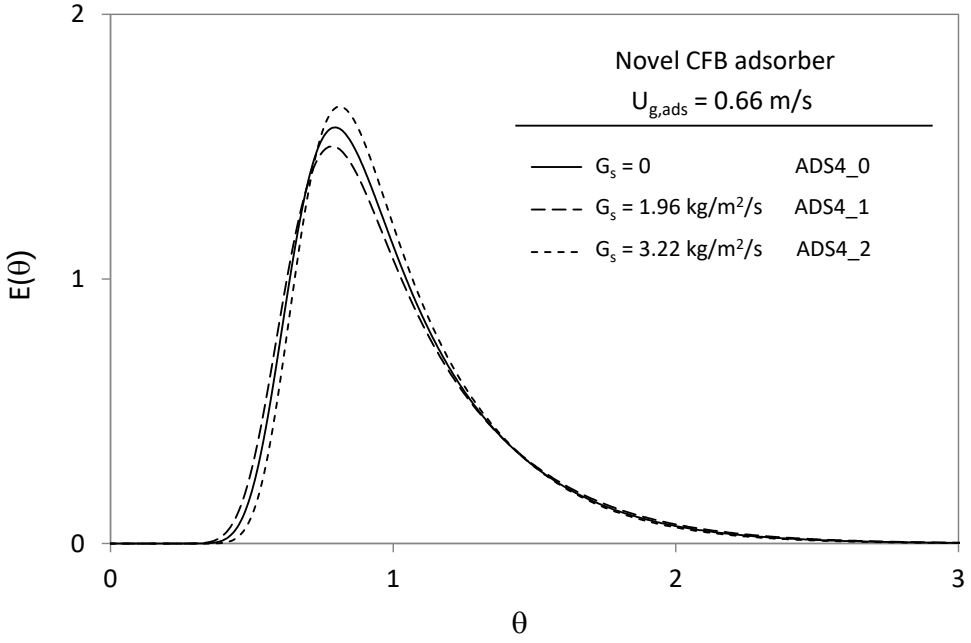

Figure 6.48. Reduced-time gas exit age distribution curves. Novel CFB adsorber, $U_{g,ads}$ = 0.66 m/s

- Regenerator (integrated in novel CFB):

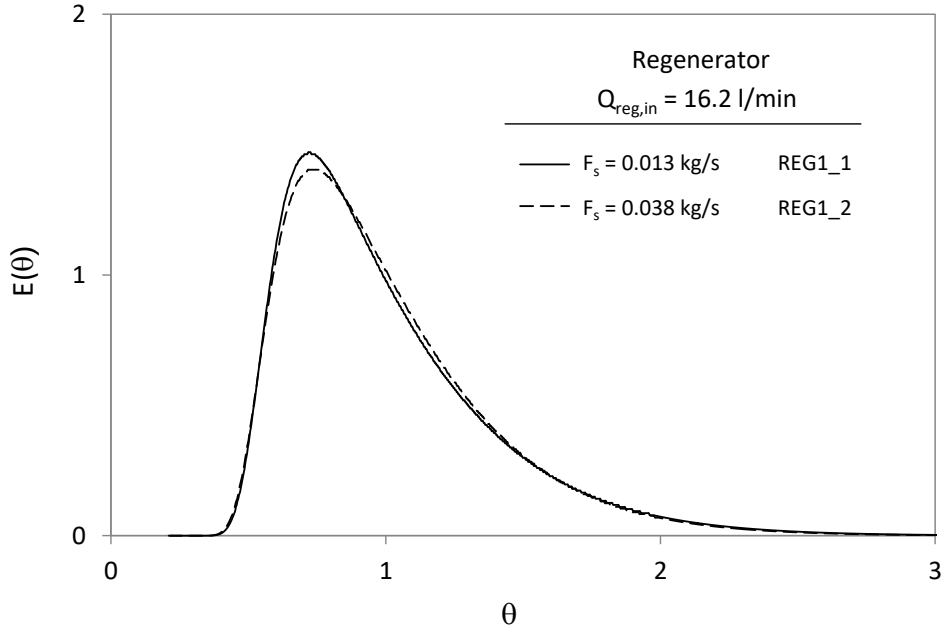

Figure 6.49. Reduced-time gas exit age distribution curves. Regenerator (integrated in novel CFB), $Q_{reg,in}$ = 16.2 l/min

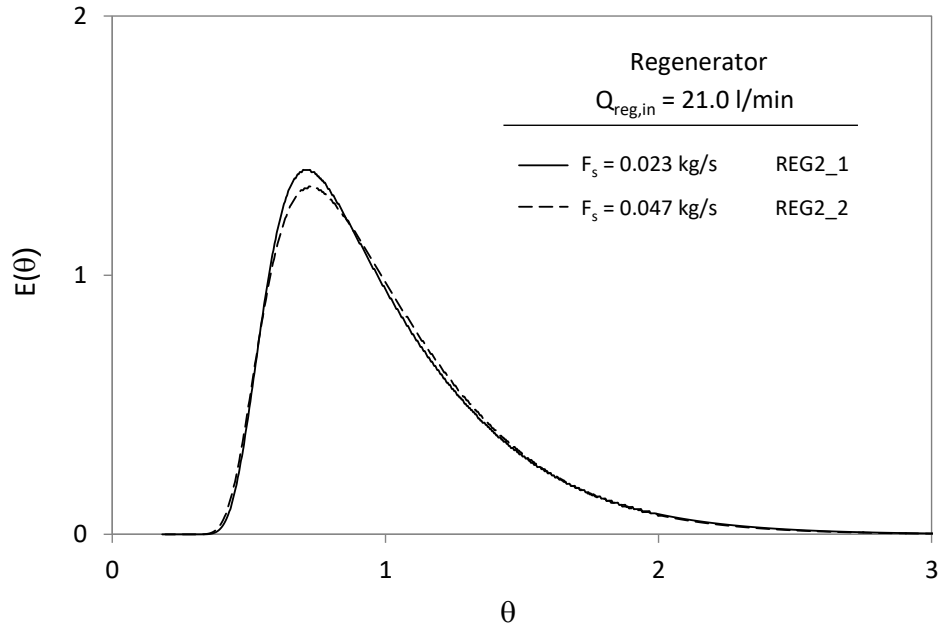

Figure 6.50. Reduced-time gas exit age distribution. Regenerator (integrated in novel CFB), $Q_{reg,in}$ = 21.0 l/min

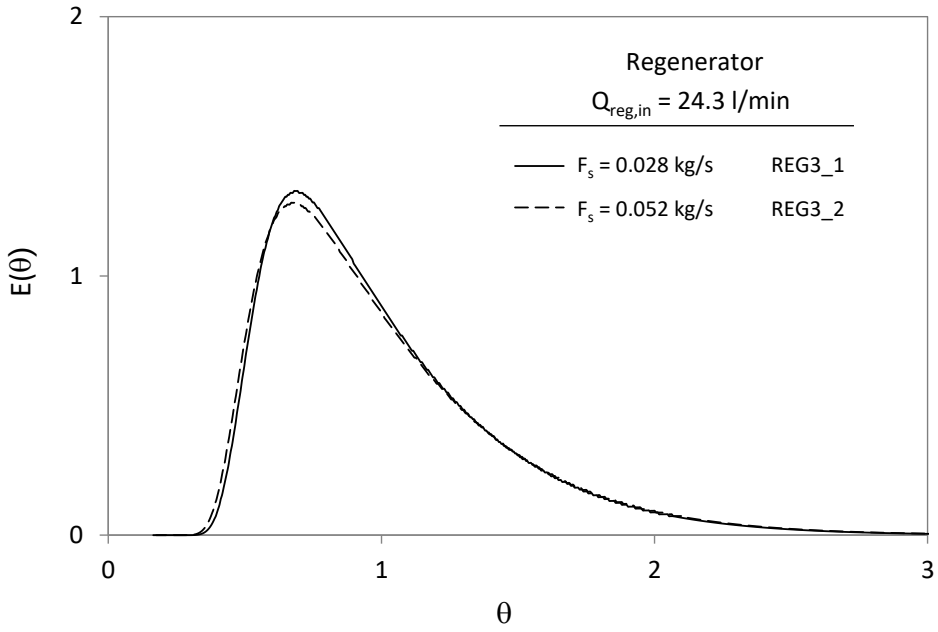

Figure 6.51. Reduced-time gas exit age distribution curves. Regenerator (integrated in novel CFB), $Q_{reg,in}$ = 24.3 l/min

6.5.5 Comparison with literature data

The values of variance presented in Section 6.5.2 can be converted to values of the Péclet number for the axially-dispersed plug flow model using equations (6.19) and (6.20) (Levenspiel, 1999). This allows: 1) comparison of the gas dispersion data obtained here with previous works, 2) estimation of the performance of the cold model CFB rigs as CO_2 capture processes by feeding the values of Pe (or rather the corresponding axial dispersion coefficients) into the adsorber model in Chapter 3.

$$\sigma^2{}_\theta\,(\mathrm{DPF}) = \frac{2}{\mathrm{Pe}} + \frac{8}{\mathrm{Pe}^2} \quad \text{(open-open boundaries)} \tag{6.19}$$

$$\sigma^2{}_\theta\,(\mathrm{DPF}) = \frac{2}{\mathrm{Pe}} - \frac{2}{\mathrm{Pe}^2}\left(1 - \mathrm{e}^{-\mathrm{Pe}}\right) \quad \text{(closed-closed boundaries)} \tag{6.20}$$

Figure 6.52 shows values of the gas axial Péclet number (Pe_g) as a function of the solids flux, comparing the data obtained in this work with those of the literature. Details of the systems used in previous gas axial dispersion studies are given in Table 6.5.

The overall trend in CFB risers and solid trickle flow contactors is towards lower values of Pe_g as solids flux increases. As discussed in Section 6.5.2, this is attributed to the capacity of solid particles (especially in aggregate forms) to "hold back" a fraction of the gas flow, contributing to gas dispersion. In case of CFB risers, the results obtained here are overall in agreement with those of previous works. Notably lower values of Pe_g were obtained for the counter-current adsorber compared with those reported for solid trickle flow in packed columns. The discrepancy could be due to the different geometry of the column internals or entry/exit effects, which in the case of the novel CFB adsorber already causes high gas dispersion even at zero solids flow rate.

The CFB regenerator has been excluded from this comparison exercise since the gas dispersion data obtained for this element, due to its design, corresponds to a combination of sub-elements, namely two tanks in series (windbox and freeboard)

and a moving bed. Suggestions will be given in the final chapter of this thesis for the study of gas dispersion specifically in the bed of solids.

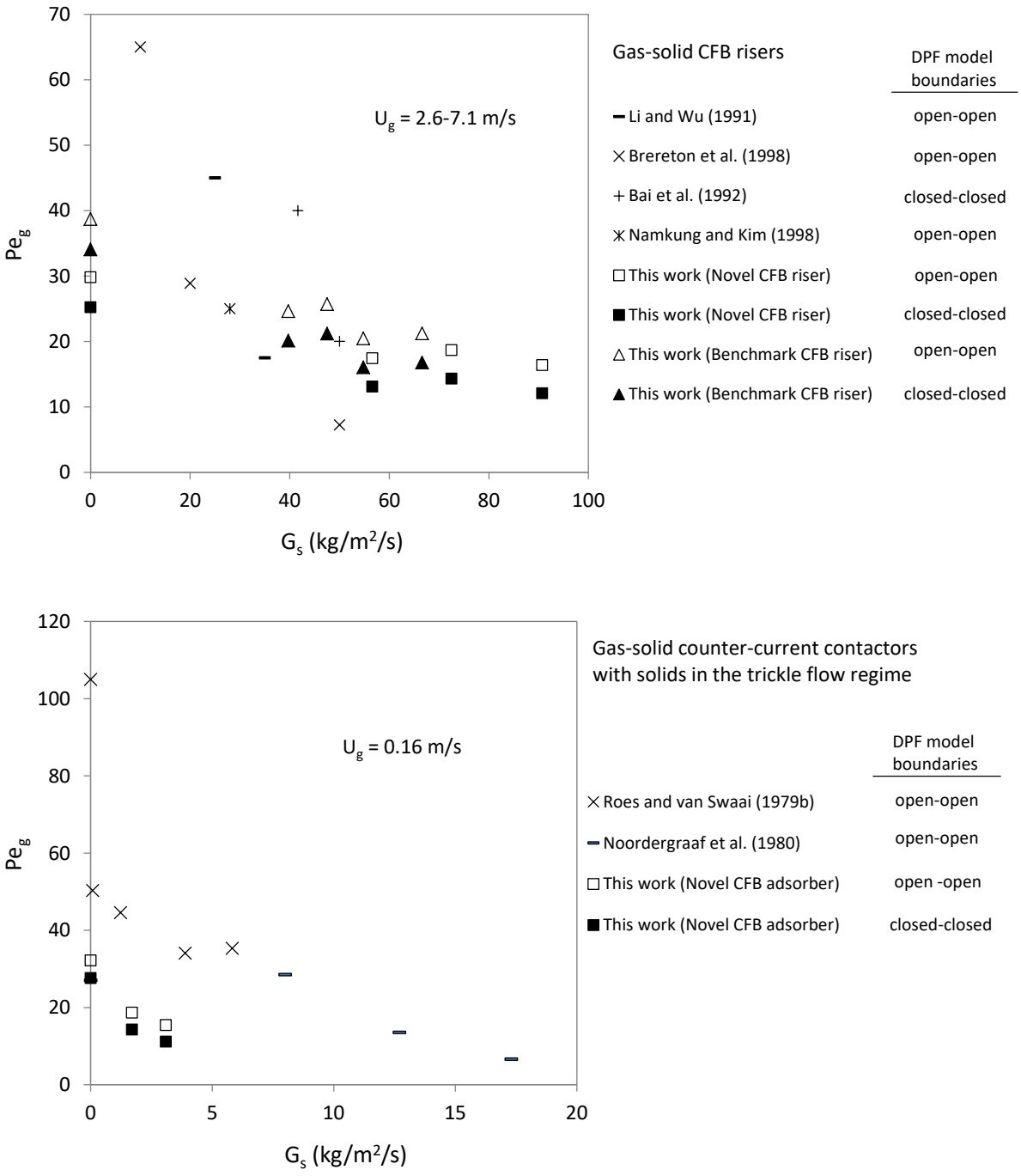

Figure 6.52. Gas axial Péclet number as a function of solids flux for different works in gas-solid systems (see Table 6.5 for details)

Table 6.5. Works in gas axial dispersion in gas-solid systems using tracer injection-detection techniques

Author	System	Operating conditions	Technique	Tracer	Results
Brereton et al. (1988)	CFB riser (ID = 152 mm, L = 9.3 m), abrupt and smooth exits Solids: sand (148 μm, 2650 kg/m^3)	U_g = 7.1 m/s G_s = 0-65 kg/m^2/s	Step tracer injection in windbox Detection (thermal conductivity cell) in riser-cyclone horizontal section	He	$Pe_{g,oo}$ = 10-100
Dry and White (1989)	CFB riser (ID = 90 mm, L = 7.2 m), 90°elbow exit with diameter reduction Solids: FCC catalyst (71 μm, 1370 kg/m^3)	U_g = 2-8 m/s G_s = 36-232 kg/m^2/s	Imperfect pulse injection in air supply line Detection (mass spectrometer) at air supply line and riser exit	Ar	D_g = 1-3.6 m^2/s for U_g = 2-5 m/s and G_s = 200 kg/m^2/s D_g = 1.2-5 m^2/s for U_g = 5-8 m/s and G_s = 200 kg/m^2/s
Li and Weinstein (1989)	CFB riser (ID = 152 mm, L = 8 m), abrupt exit Solids: FCC catalyst (59 μm, 1450 kg/m^3)	U_g = 3-5 m/s G_s = 153-271 kg/m^2/s	Step tracer injection at 4.5 m above distributor Detection (thermal conductivity analyser) 13 cm, 25 cm and 58 cm upstream injection plane	He	Dilute region: $D_{g,oo}$ = 0.2-0.35 m^2/s for U_g = 3-5 m/s and G_s = 153-271 kg/m^2/s Dense region: $D_{g,oo}$ = 0.76-0.78 m^2/s for U_g = 3-4 m/s and G_s = 153-271 kg/m^2/s

Table 6.5 (cont.)

Author	System	Operating conditions	Technique	Tracer	Results
Li and Wu (1991)	CFB riser (ID = 90 mm, L = 8 m), abrupt exit Solids: FCC catalyst (58 μm, 1575 kg/m^3)	U_g = 1.25-2.8 m/s G_s = 10-50 kg/m^2/s	Imperfect pulse injection in riser bottom 2×detection (thermal conductivity cells) downstream the injection point	H_2	$Pe_{g,oo}$ = 14-35
Bai et al. (1992)	CFB riser (ID = 141 mm, L = 10 m), abrupt exit Solids: silica gel (100 μm, 710 kg/m^3)	U_g = 2-10 m/s G_s = 10-100 kg/m^2/s	Perfect pulse injection in windbox Detection (chromatograph) in riser-cyclone horizontal section	Organic	$D_{g,cc}$ = 0.05-0.3 m^2/s for U_g = 3-9 m/s and G_s = 20-40 kg/m^2/s
Namkung and Kim (1998)	CFB riser (ID = 100 mm, L = 5.3 m), abrupt exit Solids: FCC catalyst (65 μm, 1720 kg/m^3)	U_g = 1.5-4.5 m/s G_s = 14-62 kg/m^2/s	Step tracer injection at 3 m and 1.85 m above distributor Detection (chromatograph) 0.55 m below injection plane	He and CO_2	$D_{g,oo}$ = 0.55-0.4 m^2/s for U_g = 2-4 m/s and G_s = 24-28 kg/m^2/s

Table 6.5 (cont.)

Author	System	Operating conditions	Technique	Tracer	Results
Contractor et al.(2000)	2×CFB risers (ID = 15.8 mm, L = 7.2 m and ID = 254 mm, L = 10.5 m), 90°elbow exit with diameter reduction Solids: FCC catalyst (68 μm, 1375 kg/m^3)	U_g = 2-8 m/s G_s = 83-386 kg/m^2/s	Imperfect pulse injection in air supply line Detection (mass spectrometer) at air supply line and riser exit	Ar	D_g = 0.1-1.3 m^2/s for ID = 254 mm D_g = 1-7 m^2/s for ID = 254 mm
Mahmoudi et al. (2010)	CFB riser (ID = 100 mm, L = 6.5 m), abrupt exit Solids: sand (90 μm, 2600 kg/m^3)	U_g = 5.5-8.3 m/s G_s = 40-170 kg/m^2/s	Perfect pulse injection in windbox Detection (chromatograph) in riser-cyclone horizontal section	C_3H_8	Given as RTD curves
Roes and van Swaaij (1979a, 1979b)	Packed bed (dumped Pall rings 1.5×1.5 cm), ID = 75.5 mm, L = 1 m Solids: FCC catalyst (70 μm, 813 kg/m^3)	U_g = 0-0.16 m/s G_s = 0-6 kg/m^2/s	Imperfect pulse injection below packing section Detection (thermal conductivity analyser) at bottom and top of packing section	He	$Bo_{g,oo}$ = 0.1-1.2 for U_g = 0-0.16 m/s and G_s = 0.081-5.83 kg/m^2/s

Table 6.5 (cont.)

Author	System	Operating conditions	Technique	Tracer	Results
Noordergraaf et al. (1980)	Zig-zag contactor (19 mm×40 mm×600 mm), 45° baffles, interval 40 mm) Solids: FCC catalyst (70 μm, 813 kg/m^3)	U_g = 0-0.2 m/s G_s = 0-21 kg/m^2/s	Imperfect pulse injection below zig-zag section Detection (thermal conductivity analyser) at bottom and top of zig-zag section	He	$Bo_{g,oo}$ = 0.1-2 for U_g = 0.03-0.2 m/s and G_s = 0-21 kg/m^2/s
This work	CFB risers (ID = 26.5 mm, L = 1.5 m and ID = 51 mm, L = 2.5 m), smooth exit Solids: sand (152 μm, 2650 kg/m^3)	U_g = 2.6-6.2 m/s G_s = 16-97 kg/m^2/s	Imperfect pulse injection in air supply line Detection (infrared absorption detector) at air supply line and riser top	CO_2	$Pe_{g,cc}$ = 12-39 m^2/s for U_g = 2.6-6.2 m/s and G_s = 0-97 kg/m^2/s
This work	Counter-current contactor (hydraulic ID = 142 mm, L = 0.65 m), 3×45° orifice trays Solids: sand (152 μm, 2650 kg/m^3)	U_g = 0-0.66 m/s G_s = 0-3.3 kg/m^2/s	Imperfect pulse injection in air supply line Detection (infrared absorption detector) at air supply line and above trayed section	CO_2	$Pe_{g,cc}$ = 11-32 m^2/s for U_g = 0-0.66 m/s and G_s = 0-3.3 kg/m^2/s

6.6 Conclusions

Gas residence time distribution and axial dispersion in the most important elements of the CFB cold model rigs have been experimentally studied using the imperfect tracer pulse technique. In such technique, a pulse of CO_2 (used as the gas tracer) is injected upstream the air inlet line of the CFB element studied, and the concentration of CO_2 measured with time at the element inlet and outlet. The gas RTDs of the CFB element at different operating conditions are obtained from the experimental CO_2 concentration-time curves using a convolute-and-fit approach using a flexible flow model, the axially-dispersed plug flow with stagnant section (DPFS). The DPFS model provided an excellent fit to the experimental data. These RTD curves are then normalised with respect to the gas mean residence time to 1) determine the impact of operating conditions on gas axial dispersion, 2) get insight into the fluid dynamics of the systems, and 3) comparing results between the different CFB elements and previous studies.

In the CFB risers, gas dispersion was found to increase with the solids flux but decrease with gas velocity. This is attributed to the formation of structures in the solid phase larger and slower than the single particle, which can trap gas in their interstitial volume or their periphery and keep it for longer time in the system. A similar mechanism for gas dispersion applies in the counter-current adsorber; in this case, gas dispersion is highest when gas velocity is low and solids can flow through the holes of the inclined trays in dense trickles. As gas velocity increases, the formation of trickles is impeded and gas dispersion decreases (Dry and White, 1989; Contractor et al., 2000). In both risers and the counter-current adsorber, the geometry-induced contribution to gas dispersion is deemed to be at least of the same magnitude of that caused by gas-solids interaction for the ranges of solids flux and gas velocity studied.

Gas dispersion in the regenerator increased with gas velocity but seemed to be little sensitive to the solids flow rate. Unfortunately, the contribution of the different regenerator sub-elements to gas dispersion, in particular that of the solids bed, could not be determined due to the geometry of the system.

7 Determination of solids residence time distributions

7.1 Introduction

The sensitivity analysis performed in the evaluation of CFB adsorbers for TSA carbon capture (Chapter 3) revealed that the impact of solids axial dispersion on CO_2 recovery can be more or less severe depending on the CFB configuration (refer to Figure 3.24). In the benchmark CFB, for example, complete back-mixing of solids implies an estimated drop in CO_2 recovery of only 0.8 percentage points with respect to the value at plug flow. This is directly related to the high solids-to-gas ratio needed to overcome the equilibrium limitations inherent to co-current contact between phases. The same argument applies to the riser of the novel CFB; in this case, the drop in overall CO_2 recovery with axial mixing of solids is deemed negligible.

In the counter-current adsorber of the novel CFB, on the other hand, solids-to-gas ratios are much lower in virtue of the more efficient contact mode, and therefore the impact of solids dispersion on overall CO_2 recovery is much more noticeable: a drop of 18 percentage points (from 90% to 72%) in overall CO_2 recovery was estimated for full back-mixing of solids. This loss in process performance may be significant enough to justify efforts in experimental determination of solids axial dispersion and the mechanisms that cause it in CO_2 capture equipment.

This chapter concerns the measurement of axial solids dispersion in the different CFB elements using positron emission particle tracking (PEPT). PEPT is a non-intrusive technique in which the trajectory of a single radioactive particle is tracked in real-time (particle location recorded every few milliseconds), therefore revealing detailed information about dynamic flow behaviour. A general introduction to the PEPT technique is given in Section 7.2. The PEPT facilities are described in Section 7.3, and details about the experimental procedure and processing of PEPT raw data are given in Sections 7.4 and 7.5 respectively. Results derived from PEPT depurated data are presented and discussed in Section 7.6, including comparison with previous works.

7.2 The positron emission particle tracking (PEPT) technique

7.2.1 Basic principle

The basic principle of the PEPT technique is the location of a radioactive particle in the 3-dimensional space by triangulation (Figure 7.1). The radioactive isotope contained in the particle decays emitting a positron, which in turn quickly annihilates with an electron. As a result of conservation of mass/energy and momentum, two gamma-rays are emitted in opposite directions to within ~0.5°. These gamma-rays can be detected using face-to-face detectors placed at both sides of the positron-emitting particle, forming a line of response (LoR) (Parker et al., 1994; Parker and Fan, 2008; Leadbeater et al., 2012).

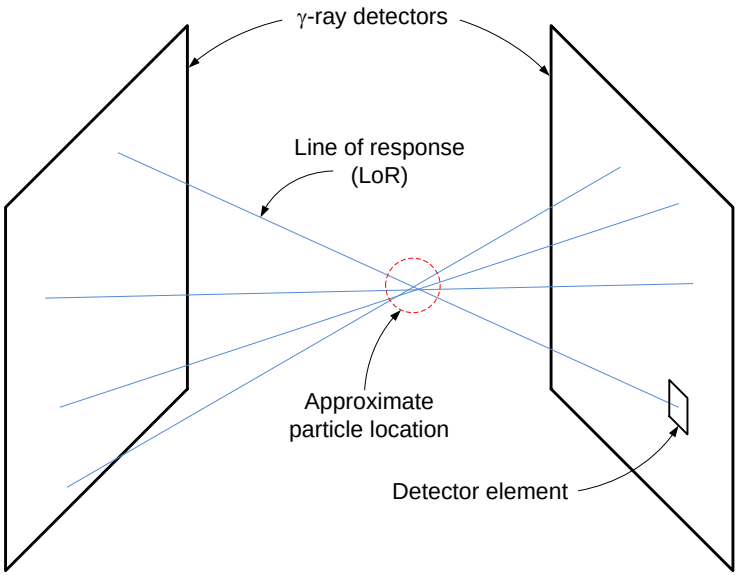

Figure 7.1. Basic principle for particle location using PEPT

7.2.2 Particle location (stationary particle)

Ideally, the intersection of only two LoR would suffice to measure the location of the particle. In practice however many LoR do not correspond to actual gamma-ray trajectories due to scattering or random association of pairs in gamma-ray detection (Parker et al., 1994; Parker and Fan, 2008). The following algorithm is used to eliminate corrupted LoR and quantify the error in particle location (Parker and Fan, 2008):

Step 1: Given an initial set S containing a number N of LoR, calculate the location (x,y,z) that minimizes the sum of distances between such location and the LoR in S.

Step 2: Let d_S be the mean distance between (x,y,z) and the LoR in S. Discard the LoR in S for which the distance between (x,y,z) and such LoR is greater that kd_S, where k is a parameter (normally k = 1-1.5).

Step 3: Let S_1 be the new set of LoR formed by the N_1 remaining LoR from Step 2. Repeat Steps 1 and 2 to generate S_2, S_3… S_n sets containing N_2, N_3… N_n number of LoR. Stop when $N_n = fN$. The value of the parameter f depends on factors like gamma-ray attenuation, scatter and camera geometry, and has a value typically between 0.05 and 0.4 (Leadbeater et al., 2012).

The result after application of the algorithm above is a particle location (x_n,y_n,z_n) with a precision given by d_{Sn} (mean distance to the LoR in the final set S_n). The value of d_{Sn} is proportional to $(fN)^{-1/2}$ (Leadbeater et al., 2012); a very high precision in the particle location can then be achieved by having a large number of LoR in the initial set S.

7.2.3 Particle location (moving particle)

For a moving particle, the total number of LoR generated after an experiment is divided in sets, each with an N number of LoR and processed as explained above to obtain a single particle position. The number N of LoR in each set S must be small enough so they are associated to a single position (within a certain accuracy range), but large enough to be statistically meaningful (Leadbeater et al., 2012). This implies that slow particles can be tracked with higher accuracy than fast ones for a given LoR acquisition rate, which in turn depends on camera resolution and particle radioactivity.

7.2.4 Tracers

PEPT tracers are created by labelling a particle from the bulk material (or a substitute with properties as close as possible to the bulk) with a radioisotope, typically ^{18}F, ^{22}Na, ^{61}Cu and ^{66}Ga.^{18}F is the most commonly used radioisotope (Parker and Fan, 2008; Leadbeater et al., 2012). It has a half-life of 110 m, which is usually sufficient for most applications and prevents radioactivity from remaining in the system under study for long periods of time (Leadbeater et al., 2012). The radioisotopes can be directly created in the particle by irradiation in a cyclotron if conditions allow (particle equal or larger than 1 mm, resistance to high temperature, right chemical composition, etc.), or can be transferred onto the particle surface by ion exchange or impregnation with a solution rich in the radioisotope. In the latter method, surface activation can dramatically increase the surface concentration of the radioisotope, increasing the particle radioactivity (Parker and Fan, 2008). Typical tracer radioactivity lies within the range 300-2000 μCi (Parker and Fan, 2008; Leadbeater et al., 2012).

7.2.5 Applications

The potential of PEPT stems from the high rate and precision at which tracer locations are recorded, and the capability to be used in real process equipment and conditions (steel walls, high temperature and pressure, etc.) (Parker et al., 2008; Leadbeater et al., 2012). The first application of PEPT was in the study of lubricant flow in aero-engines in 1984 (Hawkesworth et al. 1984, referenced in Parker et al., 2008). Since then, the PEPT technique has been used to investigate dynamic flow behaviour and to verify mathematical models in systems of many different kinds and with very different geometries, including chemical reactors, phase contactors, mixers, dryers, rotating kilns, ball mills, fluidised beds, food processors, etc. (Parker and Fan, 2008). Liquid flow can be studied as well by using a neutrally-buoyant particle as tracer representing the bulk (Leadbeater et al., 2012). Table 7.1 presents some examples of PEPT applications.

Table 7.1. Flow studies using PEPT

Author	System	Studied phenomena or system characteristics
Circulating fluidised beds		
Van de Velden et al. (2007)	CFB riser	Solids flow pattern and solids velocity
Chan et al. (2009a)	CFB riser (bottom)	Solids flow pattern and solids velocity, acceleration zone
Chan et al. (2009b)	CFB standpipe	Solids velocity profile, solids fraction, drag coefficients
Chan et al. (2009c)	CFB L-valve	Solids velocity profile, solids fraction, operating characteristics
Chan et al. (2009d)	CFB cyclone	Particle trajectory, tangential velocities, residence time
Chan et al. (2010a)	CFB exit	Particle trajectory and velocity, residence time, penetration depth in riser
Chan et al. (2010b)	CFB riser	Solids RTD
Mahmoudi et al. (2012)	CFB riser	Solids flow pattern and solids velocity
This work	CFB riser CFB counter-current adsorber CFB regenerator	Solids flow pattern, solids RTD

Table 7.1 (cont.)

Author	System	Studied phenomenon or system characteristic
Packed beds		
Ding et al. (2005)	Gas-solid co-current upflow in packed bed of solids spheres	Solids velocity and residence time distributions, solids velocity map, packing tortuosity
Ilankoon et al. (2013)	Liquid draining through packed bed of solids spheres	Liquid axial and radial dispersion using a neutrally-buoyant tracer
Other systems (examples)		
Li et al. (2015)	Wurster fluid bed	Solids RTD, cycle time, overall particle trajectories
García Triñanes et al. (2016)	Solar receivers	Solids radial profile of vertical velocities, solids axial dispersion
Morrison et al. (2016)	Rotating drum	Particle RTD
Chan Seem et al. (2016)	Twin screw granulator	Flow pattern, asymmetric transverse distribution
Griffiths et al. (2012)	Inclusions in alloy castings	Particle trajectory
Boucher et al. (2016)	Spiral concentrator	Solids velocity and trajectory
Radman et al. (2014)	Hydrocyclone	Solids trajectory
Yang et al. (2014)	Food cans	Solids rotational and translational motion
Rafiee et al. (2013)	Kenics static mixer	Axial velocity maps
Middha et al. (2013)	Pneumatic conveyors	Solids trajectory
Laurent and Cleary (2012)	Ploughshare mixer	Validation of a DEM model
Mac Namara et al. (2012)	Front-loading domestic washing machine	Occupancy and axial displacements distributions

Table 7.1 (cont.)

Author	System	Studied phenomenon or system characteristic
Simmons et al. (2012)	"SurePure turbulator" wirl-tube reactor	Hydrodynamic performance
Govender et al. (2011)	Laboratory tumbling mill	Velocity map
Jayasundara et al. (2011)	"IsaMill" high speed stirred mill	Validation of a CFD-DEM model

7.2.6 Use of PEPT in circulating fluidised beds

PEPT has been used previously to study particle flow characteristics in CFBs in a number of works, the most complete (in terms of number of different CFB elements studied) being that by Chan et al. (2009a, 2009b, 2009c, 2009d, 2010a, 2010b). The authors studied the bottom, main body and exit sections of the CFB riser, the solids feeding system (standpipe and L-valve) and the cyclone. Other investigators focused mainly on the main body of the CFB riser (Van de Velden et al., 2007; Mahmoudi et al., 2012).

In this work, solids flow in a portion of the CFB risers was studied using PEPT to investigate solids flow regimes and velocity distributions, similarly to Van de Velden et al. (2007), Chan et al. (2010b) and Mahmoudi et al. (2012), and solids residence time distributions, similarly to Chan et al. (2010b).

There appear to be no PEPT studies carried out in gas-solids counter-current systems with the geometry of the novel CFB adsorber and regenerator considered here. In case of the counter-current adsorber, the most similar systems studied with PEPT are those of Ding et al. (2005) and Ilankoon et al. (2013); in none of these systems the combination of gas-solid system and counter-current contact was present. Regarding the CFB regenerator, solids downflow in a dense form (moving bed) was already studied using PEPT by Chan et al. (2009b) in a CFB standpipe. However, the geometry of the regenerator is significantly different from that of a standpipe (as already observed visually, see Section 5.3), justifying a separate PEPT study of the former system.

7.3 PEPT facilities

PEPT experiments were carried out at the facilities of the University of Birmingham Positron Imaging Centre. The Centre provided two PEPT cameras (denominated "ADAC" and "modular") to accommodate for the large dimensions of the CFB rigs, radioactive tracers in the quantity needed, and auxiliaries (compressed air, water). A brief description of the PEPT cameras and their spatial arrangement with the CFB rigs are given next.

7.3.1 The ADAC camera

The ADAC Forte camera (referred simply as "ADAC") (Figure 7.2) consists of two planar face-to-face detectors, each one having an effective detection area of 50 cm×40 cm (height×width) and a maximum separation between them of 80 cm. The position of the detectors when oriented vertically (as in Figure 7.2) is constricted to approx. 88 cm from ground level to the detector lower edge. This makes the ADAC camera unsuitable for heights (with respect to ground) above 88 cm + 50 cm = 138 cm. Lower heights than 88 cm can be achieved by raising the system under study from ground level. In this work, the ADAC camera is used to study a portion of the CFB risers and the regenerator (see Figure 7.4 and Figure 7.6).

The ADAC camera represents a step improvement in the capabilities of the Positron Imaging Centre with respect to their previous PEPT camera. In optimal conditions, the ADAC camera is able to track a particle moving at 5 m/s every millisecond with an accuracy of less than 2 mm (Parker et al., 2008). A detailed description of the characteristics of the ADAC camera as a nuclear instrument can be found in Parker et al. (2002).

Figure 7.2. The ADAC Forte camera in the University of Birmingham Positron Imaging Centre (image borrowed from the Centre's website, with permission)

7.3.2 The modular camera

The PEPT modular camera is made up of physically independent blocks denominated "buckets" (Figure 7.3). A number of these buckets can be arranged in different geometries around the system studied, facing each other directly (similarly to the ADAC camera) or in a ring configuration. In this work, the modular camera was assembled to study the novel counter-current adsorber, which lies at a height not suitable for the ADAC camera (see Figure 7.4).

The portability and geometrical flexibility of the modular camera makes it very convenient for in-situ industrial applications. In 2007 the modular camera was used in BP's site in Hull to study the solids flow in a pilot-scale fluidised bed with a central vertical baffle (Ingram et al., 2007).

Compared to the ADAC, the modular camera has a superior performance thanks to a higher data acquisition rate. In theory, a particle moving at 10 m/s could be detected every 0.2 milliseconds with a precision of 0.9 mm in 3D (Leadbeater et al., 2011). However, the sensitivity of the camera is not constant throughout its detection area, being the highest in the area directly faced by the buckets, and the lowest in the gaps between buckets. Details about the characterisation of the Birmingham modular

camera are given in Parker et al. (2008), Leadbeater and Parker (2011) and Leadbeater et al. (2011).

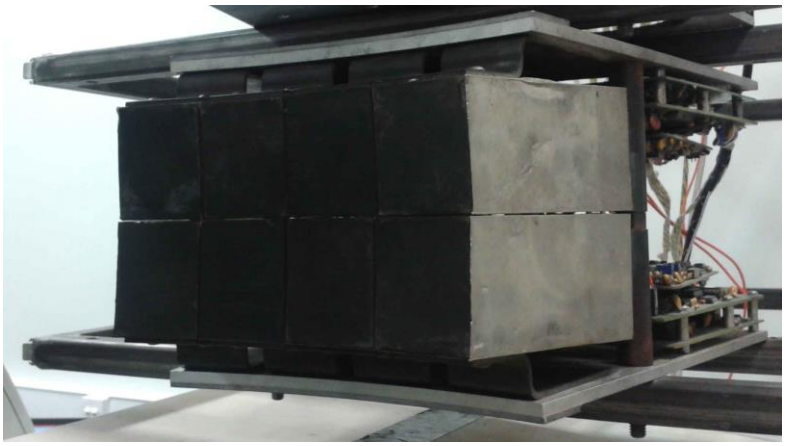

Figure 7.3. A detector bucket of the PEPT modular camera

7.3.3 PEPT camera-CFB spatial arrangement

The controlling factor in the mutual spatial arrangement between the PEPT cameras and the CFB rigs was the geometry of the ADAC camera. The values of detector height, width and maximum separation were known prior to the construction of the CFB rigs, and used to size their support frames accordingly. As it can be seen in Figure 7.4, the novel CFB rig fits with enough clearance in between the detectors of the ADAC camera. The same is true for the benchmark CFB, as they have the same frame horizontal dimensions.

The modular camera was made up of eight detector buckets, distributed in two face-to-face columns of four buckets each, as seen in Figure 7.4. The buckets were installed directly above the ADAC camera detectors on a bespoke support frame built by the Technical Services of the University of Birmingham. Unfortunately the height of this frame was limited by the PEPT laboratory door, making the overall position of the modular camera lower than the counter-current adsorber by approximately one adsorber module. As a consequence, the adsorber head and the upper-most module lied out of the modular camera detection window.

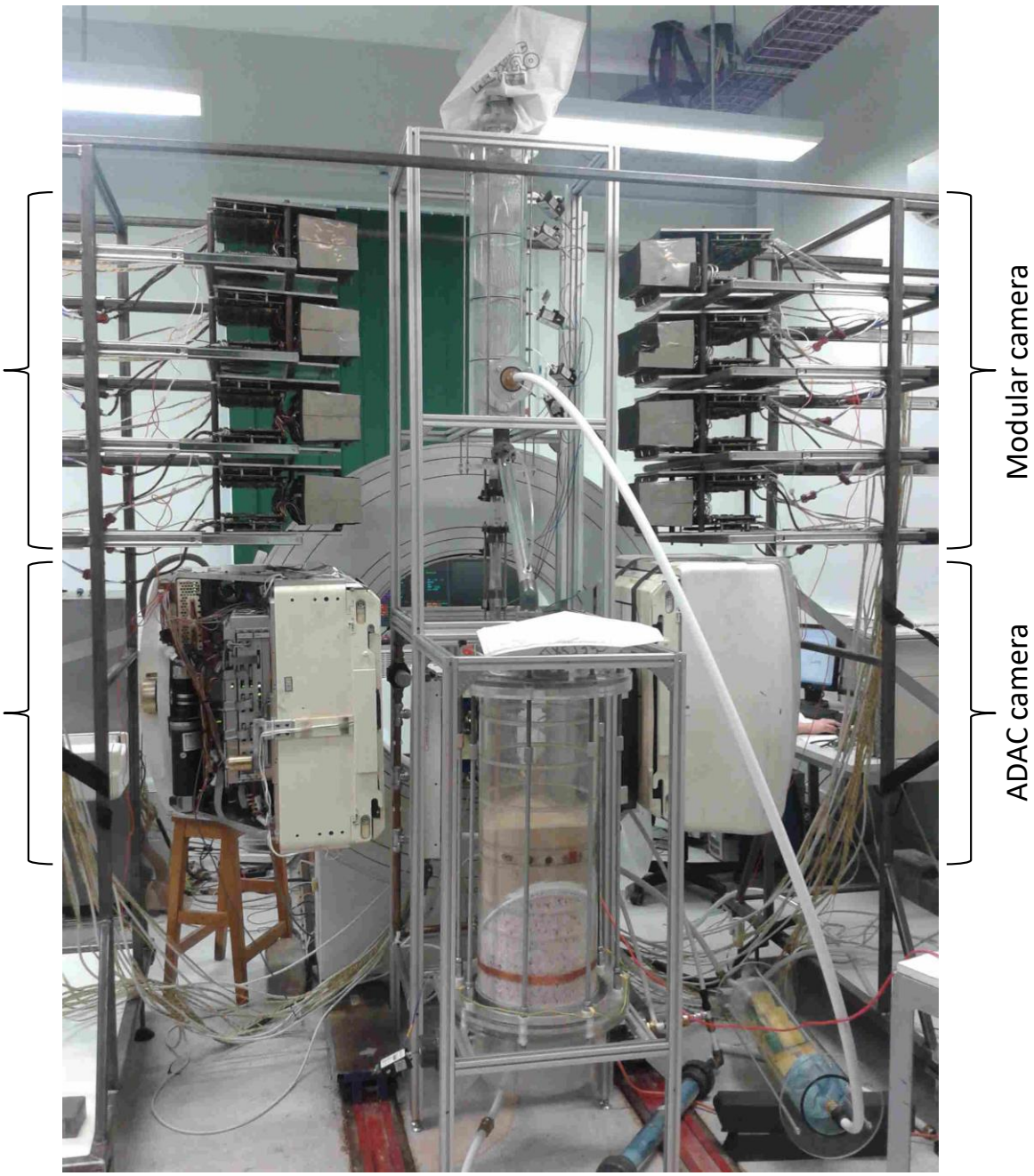

Figure 7.4. Novel CFB under PEPT study

7.4 Experimental procedure

7.4.1 Background

PEPT experiments were carried out in two separate visits to the University of Birmingham. The first visit (9^{th} to 12^{th} September 2013) was meant to provide experience with the PEPT technique using the ADAC camera and the novel CFB, in preparation for future visits and, if possible, obtaining some preliminary results. The only meaningful data generated were those of the experiments performed in the regenerator, for which the novel CFB was lifted on a pneumatic trolley to bring the regenerator into the detector area of the ADAC camera.

On a second visit (14^{th} to 17^{th} July 2014), both the ADAC and modular cameras were available, and both CFB configurations were brought. Lessons learned in the first batch of experiments were put to good use, and study of both CFB rigs was carried out. Unfortunately, during processing of the raw data it was realised that the modular camera had been malfunctioning, corrupting the data in some experiments. *The data affected by malfunction of the modular camera were all three xyz coordinates for the benchmark CFB riser and the z-coordinate for the counter-current adsorber*. Experiments in the counter-current adsorber are therefore analysed in terms of particle tracking in the xy-plane only. Fortunately, the xy-plane is the one containing the zig-zag pattern of the adsorber, allowing still valid qualitative and quantitative results to be obtained (see Section 7.6.2).

7.4.2 Tracer characteristics and interaction with PEPT experiments

All tracers used were particles of porous alumina with a size and apparent density similar to that of the bulk particles (d_p = 152 mm, ρ_s = 2650 kg/m^3), impregnated with a solution of ^{18}F (half-life 110 min). The radioisotope was generated in an in-house cyclotron by irradiation of purified water. The initial radioactivity of the tracers was in the range of 400-600 μCi.

In most applications, PEPT experiments run with a single tracer since location is based on triangulation of trajectories converging to a single point (multiple-tracer experiments are possible though using a modified algorithm and tailored tracer

activities, see Yang et al., 2006 and Parker et al., 2008). The use of a single tracer when studying both CFB risers and the novel CFB adsorber, however, required long periods of time (longer than 2 hours) to get enough data given the long residence time of the tracer in the regenerator. It was therefore decided to use 4-5 tracers when studying these CFB elements since the probability to encounter more than one in the detection window of the cameras (especially in the CFB risers) was very low. This approach turned out to be successful for the CFB risers given the very short residence time and the absence of static holdup in these elements where the particles could get stuck. Unfortunately, this was not the case for the counter-current adsorber: in many occasions two or more tracers were simultaneously detected by the modular camera, affecting the quality of PEPT data. A detailed discussion regarding raw data processing is presented in Section 7.5.

7.4.3 Description of a typical experiment

The common procedure for all PEPT experiments is as follows:

Step 1. Recharge the humidifiers.

Step 2. Run the rig at the desired operating conditions for a few minutes. This is meant to allow the solids and air flow rates to stabilise, and the solids static holdup to form. It also fills the "nooks and crannies" of the system where the tracer particle can get stuck.

Step 3. Introduce the tracer(s) (see procedure below).

Step 4. Set the PEPT camera(s) in data acquisition mode.

Step 5. Run the experiment for the desired time or until experiment conditions are unfavourable (departure from initial operating conditions, stuck tracer(s), excessive accumulation of static electricity). Ideally, a high number of tracer passages or "visits" is desirable to generate an adequate statistical representation of the bulk flow (over 100 for "once through" systems, according to Leadbeater et al., 2012).

Step 6. Set the PEPT camera(s) in idle mode.

Additionally to Steps 1 to 6, most experiments required constant "manual tracking" using a portable Geiger counter, especially when using multiple tracers, to make sure

the tracers were flowing. Very frequently the tracers would get stuck in the stagnant zone of the regenerator and sand pockets in the counter-current adsorber, and re-routing them into the solids bulk flow was a laborious task, if at all possible.

Tracers were introduced in the CFBs via the regenerator as illustrated in Figure 7.5. A piece of Perspex pipe with a funnel on top was inserted into the regenerator moving bed zone through the regenerator filling port. The tracer, which was previously mixed with a small amount of sand in the vial where it was supplied, is then poured into the funnel.

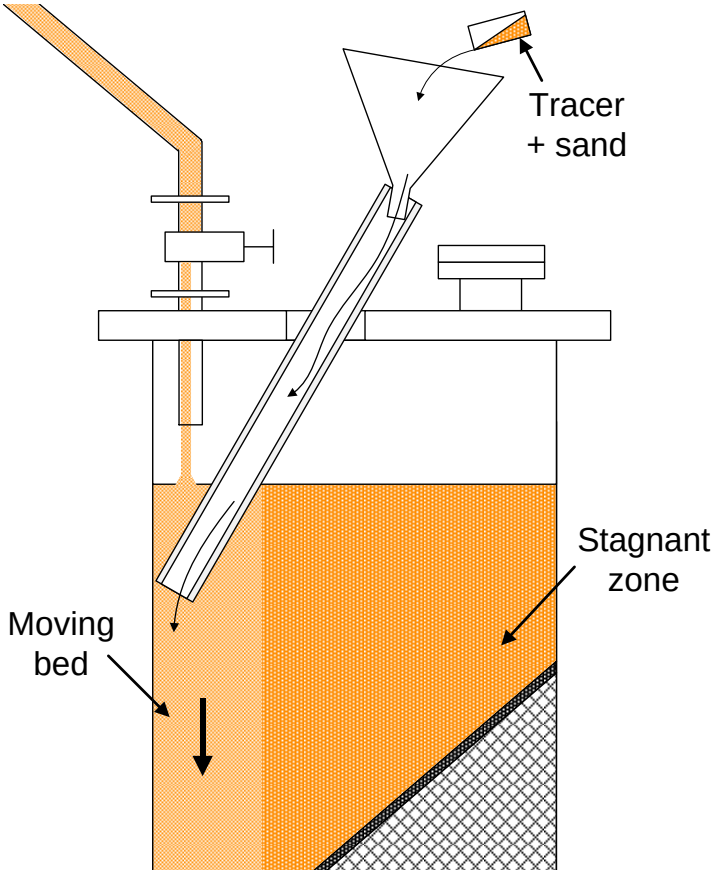

Figure 7.5. Introduction of a solid tracer in the CFB rig

7.4.4 Experiments

Four sets of PEPT experiments were carried out, and labelled according to the corresponding CFB element under study (see Figure 7.6 for reference):

- RISbx (where x = 1 to 4): Benchmark CFB riser (ADAC camera).
- RISnx (where x = 1 to 5): Novel CFB riser (ADAC camera).
- ADSx (where x = 1 to 4): Novel CFB adsorber (modular camera).
- REGx (where x = 1 to 4): Regenerator (modular camera).

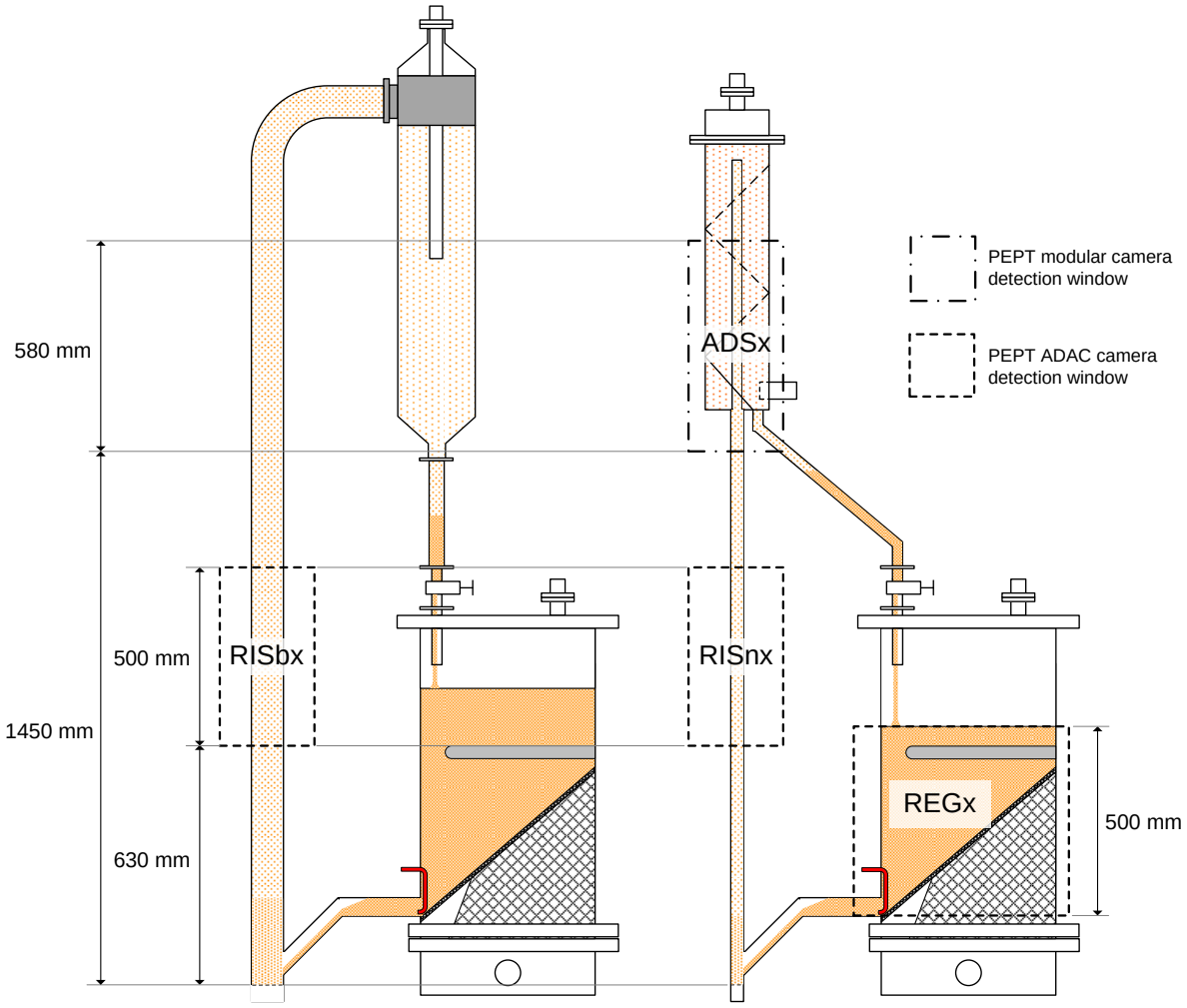

Figure 7.6. Size and position of PEPT cameras detection windows corresponding to the PEPT experiments

The operating conditions of the CFB rigs for the experiments carried out, along with the results obtained (Section 7.6) are presented in Tables 7.2 to 7.5.

Table 7.2. PEPT experimental data and results. Benchmark CFB riser

Exp. Ref.	CFB operating conditions				Histograms			RTD			
	Q_{ris} (l/min)	F_s (kg/s)	$U_{g,ris}$ (m/s)	G_s (kg/m^2/s)	No. passages	$u_{s,av}$ (m/s)	τ (s)	σ^2_θ	γ_θ	Pe_{oo}	Pe_{cc}
RISb1	760	0.032	6.2	16	101	4.9	0.10	0.014	0.0008	149	144
RISb2	760	0.098	6.2	48	95	4.6	0.11	0.081	0.069	28	24
RISb3	760	0.17	6.2	83	131	4.4	0.12	0.19	0.34	14	10
RISb4	625	0.090	5.1	44	86	3.8	0.15	0.23	0.34	12	7

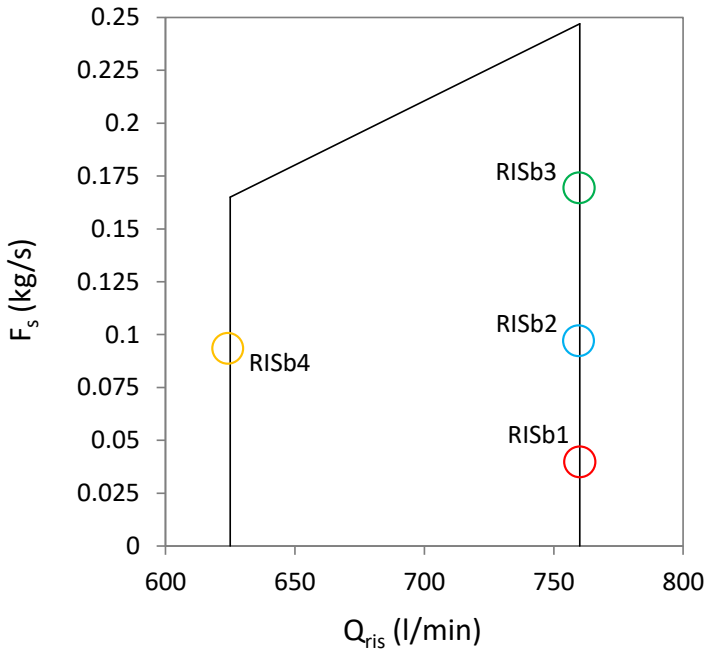

Figure 7.7. CFB operating conditions for PEPT experiments. Benchmark CFB riser

Table 7.3. PEPT experimental data and results. Novel CFB riser

Exp. Ref.	CFB operating conditions				Histograms			RTD			
	Q_{ris} (l/min)	F_s (kg/s)	$U_{g,ris}$ (m/s)	G_s (kg/m^2/s)	No. passages	$u_{s,av}$ (m/s)	τ (s)	σ^2_θ	γ_θ	Pe_{oo}	Pe_{cc}
RISn1	86	0.033	2.6	59	80	0.85	2.2	1.15	1.4	4	0
RISn2	99	0.032	3.0	59	39	1.28	0.76	0.66	0.68	5	1
RISn3	115	0.032	3.5	59	31	2.24	0.23	0.026	0.006	81	76
RISn4	115	0.040	3.5	72	26	2.0	0.28	0.19	0.19	14	10
RISn5	115	0.053	3.5	97	142	1.7	0.61	1.65	5.4	3	0

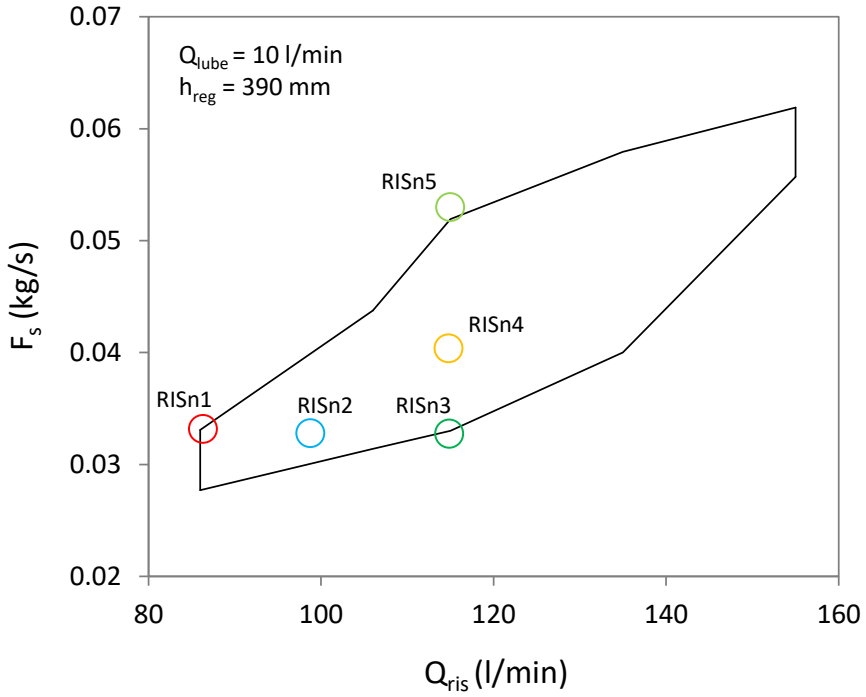

Figure 7.8. CFB operating conditions for PEPT experiments. Novel CFB riser

Table 7.4. PEPT experimental data and results. Novel CFB adsorber

Exp. Ref.	CFB operating conditions						Histograms			RTD			
	U_{ris} (m/s)	$Q_{ads,in}$ (l/min)	$U_{g,ads}$ (m/s)	$U_{g,tray}$ (m/s)	F_s (kg/s)	G_s (kg/m^2/s)	No. passages	$u_{s,av}$ (m/s)	τ (s)	σ^2_θ	γ_θ	Pe_{oo}	Pe_{cc}
ADS1	3.5	0	0	0	0.048	3.0	38	0.35	1.3	0.079	0.017	29	24
ADS2	3.5	340	0.35	1.01	0.052	3.3	29	0.22	2.3	0.19	0.076	14	9
ADS3	3.5	510	0.52	1.52	0.051	3.2	24	0.096	6.0	0.32	0.086	9	5
ADS3 with cut-off time*								0.13	3.4	0.058	0.0011	38	34
ADS4	3.5	0	0	0	0.047	3.0	35	0.2	4.3	0.76	0.57	5	0.9
ADS4 with cut-off time*								0.27	1.8	0.16	0.063	15	11

*Refer to Section 7.6.2 for definition and discussion of the "cut-off time" concept.

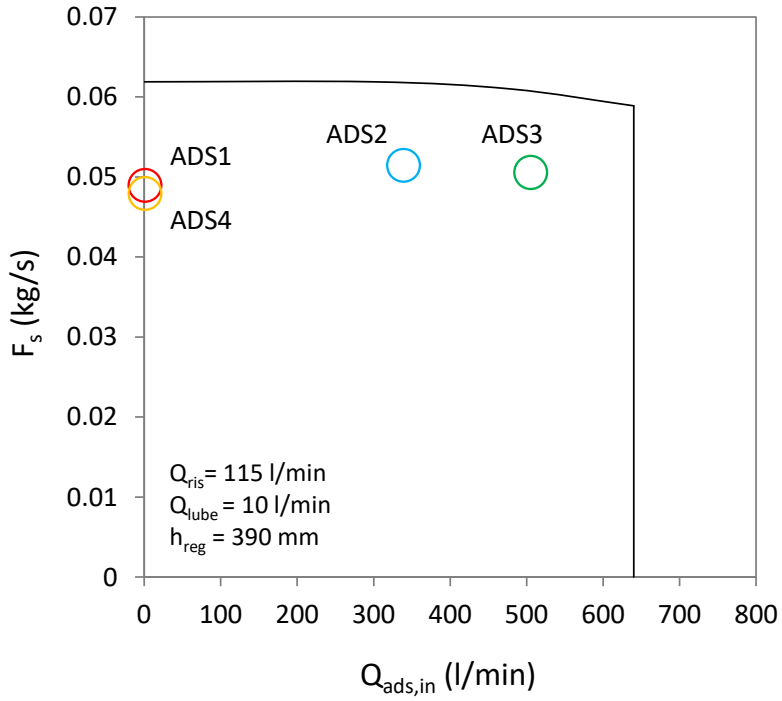

Figure 7.9. CFB operating conditions for PEPT experiments. Novel CFB adsorber

Table 7.5. PEPT experimental data and results. Regenerator (integrated in novel CFB)

Exp. Ref.	CFB operating conditions				Histograms			RTD			
	Q_{ris} (l/min)	F_s (kg/s)	$Q_{reg,in}$ (l/min)	h_{reg} (mm)	No. passages	$u_{s,av}$ (mm/s)	τ (s)	σ^2_θ	γ_θ	Pe_{oo}	Pe_{cc}
REG1	115	0.040	17.3	430	67	5.8	83	0.60	1.7	6	2
REG2	115	0.052	23.7	430	28	5.2	90	0.29	0.27	10	6
REG3	115	0.052	24.0	390	88	5.1	95	0.33	0.38	9	5
REG4	115	0.040	17.4	410	31	5.1	97	0.44	0.74	7	3

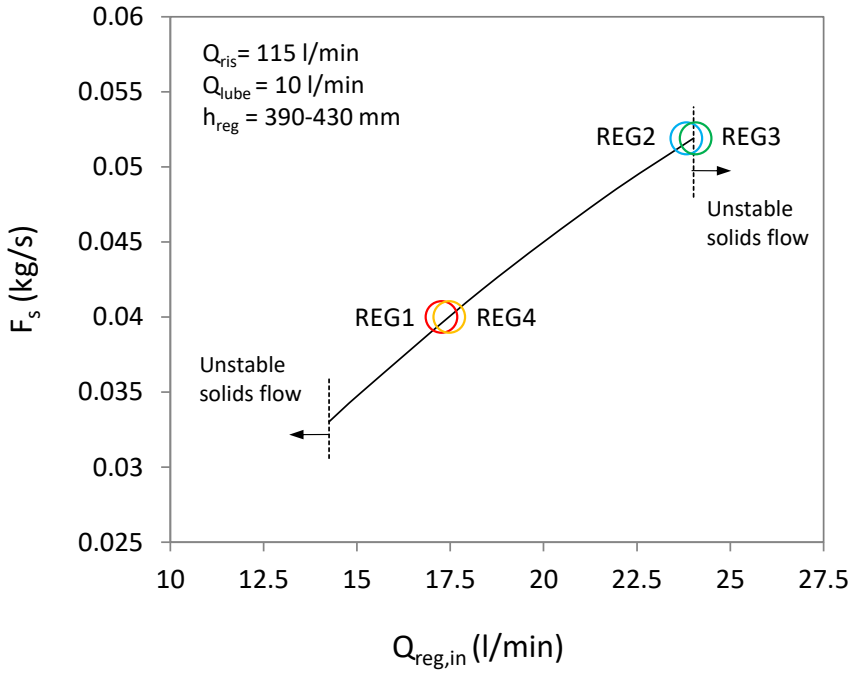

Figure 7.10. CFB operating conditions for PEPT experiments. Regenerator (integrated in novel CFB)

7.5 Raw data processing

The raw data of a PEPT experiment are the coordinates of the whole set of gamma-ray coincidences forming lines of response or LoR (that supposedly contain the location of the tracer at a given time) recorded by the camera. These raw data are then depurated from corrupted LoR and converted into a set of tracer locations (time,x,y,z) using the algorithm presented in Section 7.2 with adequate values of the algorithm parameters N and f. The value of f is related to the level of gamma-ray attenuation and scatter, and camera geometry; it was found that f = 0.15 was appropriate for all experiments (X. Fan, personal communication, September 2013).

The value of N depended on particle velocity since it defines the number of initial LoR that the algorithm processes per tracer location; for experiments in the risers, where the tracer is moving at high velocity, the value of N is lower than for the regenerator (where particles move more slowly) for the same accuracy in particle location. It was found that N = 150 was appropriate for experiments in both risers (RISbx and RISnx), and N = 500 for experiments in the regenerator (REGx). The particle location accuracy of experiments RISbx and RISnx was estimated in ±2 mm, ±2 mm and ±2 mm in the x-, y- and z-coordinate respectively. For experiments REGx, the values were ±1 mm, ±1 mm and ±1 mm in the x-, y- and z-coordinate respectively (X. Fan, personal communication, July 2014).

Raw data processing for the experiments in the counter-current adsorber (ADSx) was a much more tedious task. The reason is related to the simultaneous use of multiple tracers (see Section 7.4.2): in some occasions one of the tracers would get stuck within the detection area of the modular camera, making the data acquisition rate increase dramatically. Processing such large amount of raw data by the PEPT algorithm was very time consuming, especially when different combinations of values for the parameters f and N were investigated. Low values of f and N needed to be used to keep the number of data points for particle trajectory analysis to a reasonable level. The accuracy of the particle location suffered as a consequence, and was estimated in ±5 mm and ±5 mm for the x- and y-coordinates, or ten times larger than in normal conditions. These values are reasonably low given the dimensions of the counter-current adsorber, yielding reasonably well traced particle trajectories in the xy-plane (see Figure 7.20 and Figure 7.21). Note that the z-coordinate for experiments ADSx was not available due to malfunction of the modular camera, as commented previously in Section 7.4.1.

7.6 Results and discussion

7.6.1 CFB risers

- Particle average vertical velocity distributions:

An example of the evolution of one tracer passage through the risers in the vertical direction is shown in Figure 7.11. In this particular example the particle experiences

alternating up and down flow until it definitely leaves the PEPT camera detection window. The average vertical velocity of the particle was calculated as the vertical distance between it was first seen in the camera and it definitely leaves divided by the total time elapsed.

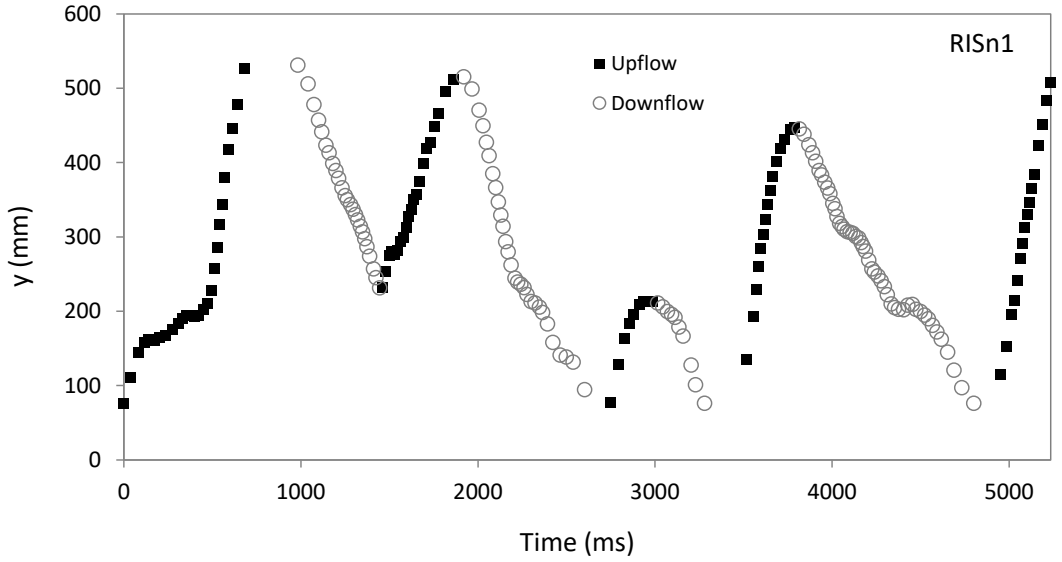

Figure 7.11. Example of evolution of one tracer passage in the vertical direction. Novel CFB riser, experiment RISn1

Figure 7.12 and Figure 7.13 show the tracer distribution in the cross section of the benchmark and novel CFB risers, respectively, according to its vertical velocity. It can be seen how location accuracy is lower in the z-coordinate than it is in the x-coordinate, which was an unexpected result.

The proportion of locations with negative vertical velocities (i.e. flowing downwards) increases for both CFB risers with increasing solids flux and/or decreasing gas velocity. The downflowing particles tend to locate near the wall, whereas the upflowing ones are more evenly spread in the cross section or tend to accumulate around the riser axis. Figure 7.14 shows how the relative magnitude of solids downflow distribute in the G_s-$U_{g,ris}$ diagram. Van de Velden et al. (2007) obtained similar results for 120 μm sand in the same range of operating conditions, using the PEPT technique in a steel CFB riser 46 mm ID, 2 m length – experiment conditions very similar to the ones in this work.

The distributions of tracer average vertical velocity are shown as frequency histograms in Figure 7.15 and Figure 7.16. The data clearly shows how the distribution of particle velocities spread towards lower values when increasing solids flux and/or decreasing gas velocity.

The values of tracer vertical velocity averaged over all passages within each experiment are presented as a function of the gas superficial velocity in Figure 7.17; the line corresponding to a slip velocity equal to the terminal velocity of the solid particles is drawn in the same graph for reference. All mean tracer velocities lie below such line, indicating that the slip velocity is greater than the solids terminal velocity. The data also reveal that, in general, the slip velocity increases with increasing solids flux and/or decreasing gas velocity for the ranges of G_s and U_g studied. This is consistent with the overall literature in CFB riser fluid dynamics, and it is generally attributed to the greater terminal velocity of solid aggregates (whether they are clusters, streaks, annulus, etc.) formed as the flow regime moves from lean transport to fast fluidisation (Yerushalmi and Cankurt, 1979; Patience et al., 1992; Berruti et al., 1995). The effect of riser diameter on solids agglomeration is not well understood, as pointed out by Berruti et al. (1995); Figure 7.14 suggests that solids downflow can be found in the benchmark CFB riser at values of G_s and U_g were it would not be expected in the narrower novel CFB riser, but the data is not conclusive.

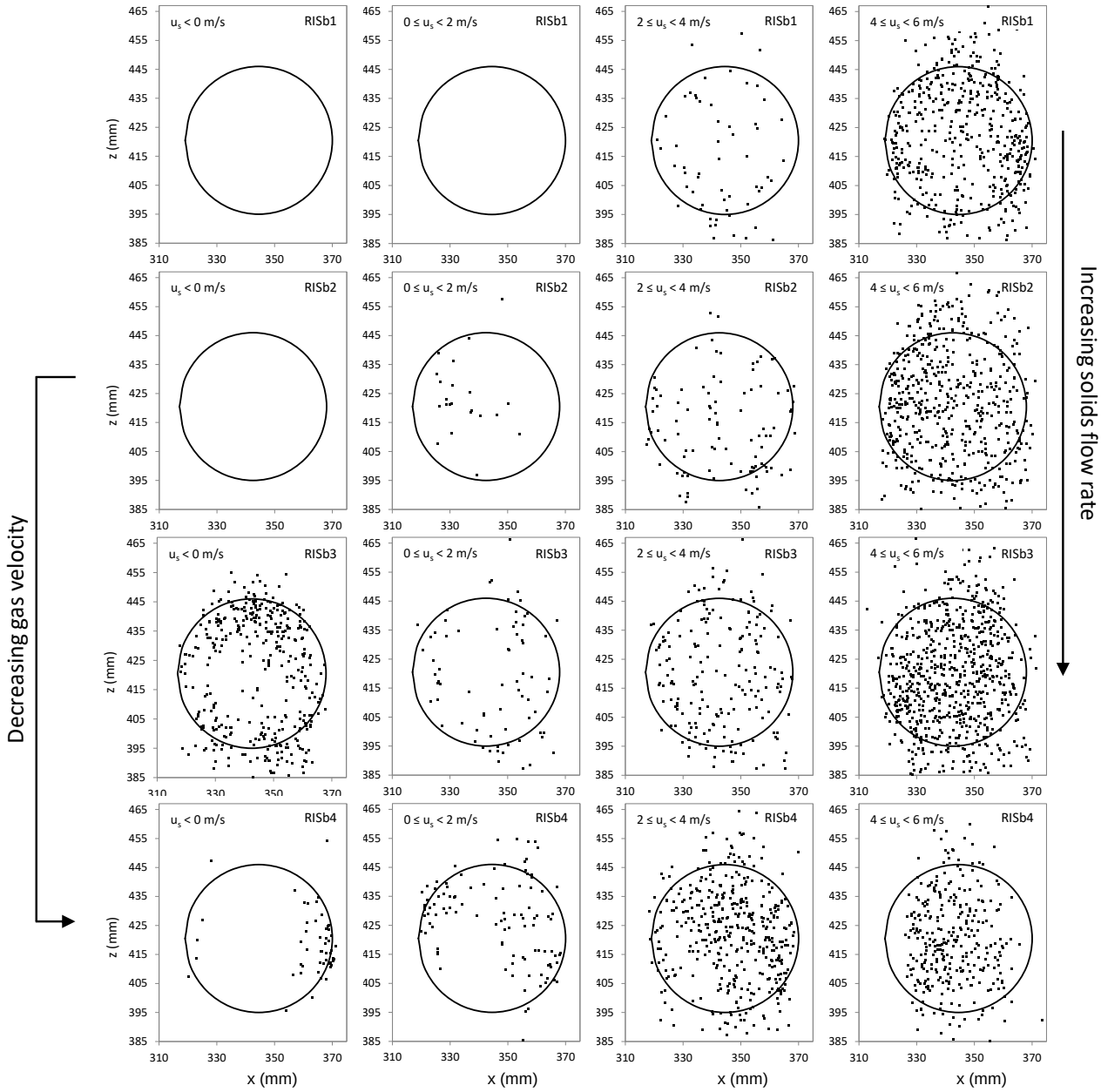

Figure 7.12. Tracer spatial distribution in riser cross section according to tracer vertical velocity. Benchmark CFB

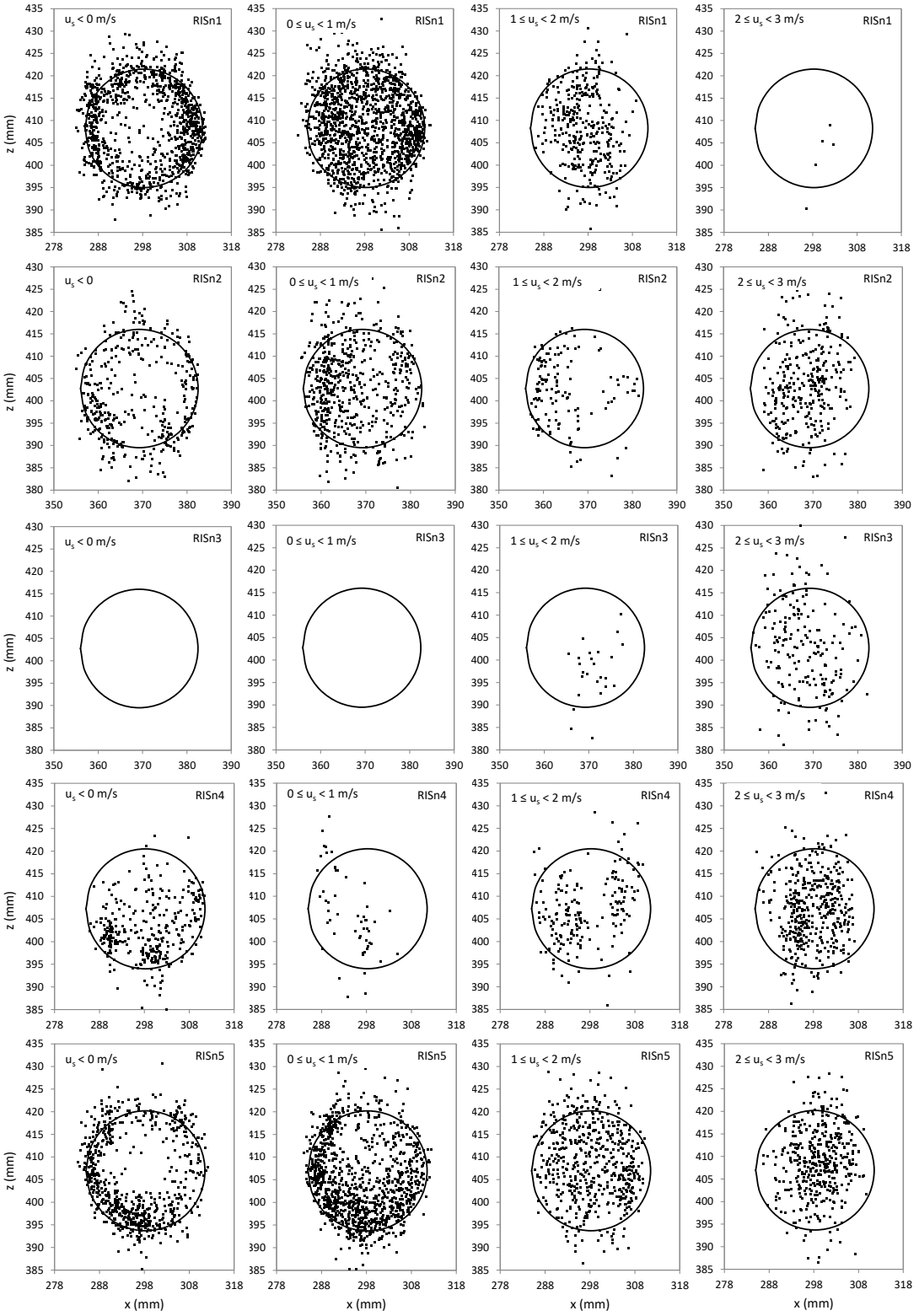

Figure 7.13. Tracer spatial distribution in riser cross section according to tracer vertical velocity. Novel CFB

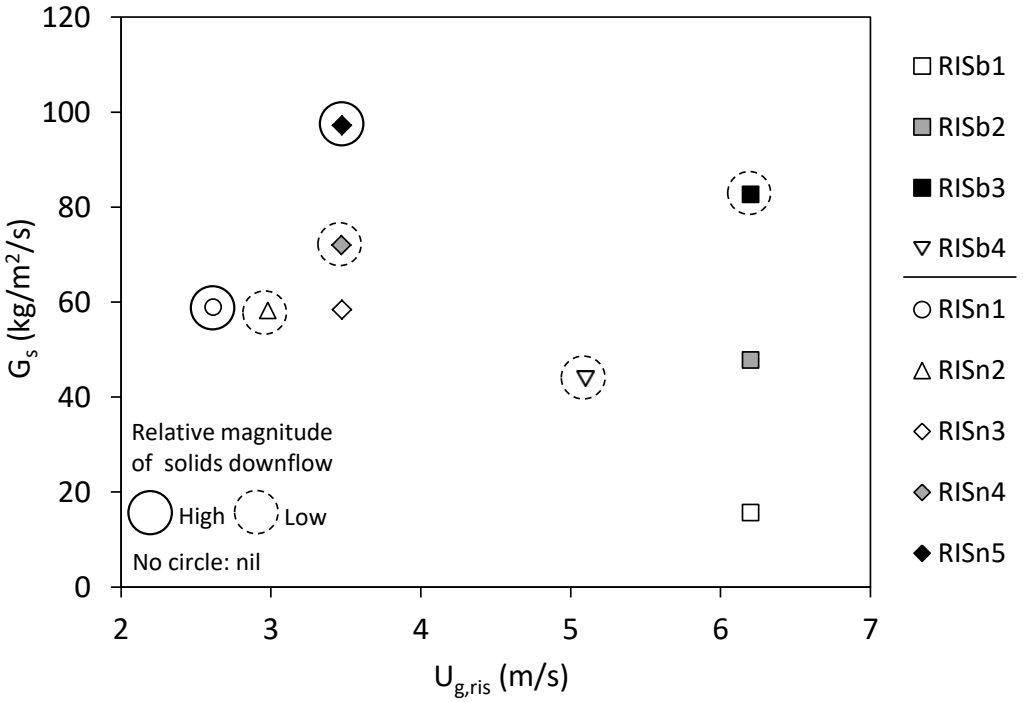

Figure 7.14. Position of PEPT experiments in the G_s-$U_{g,ris}$ diagram. Benchmark and novel CFB risers

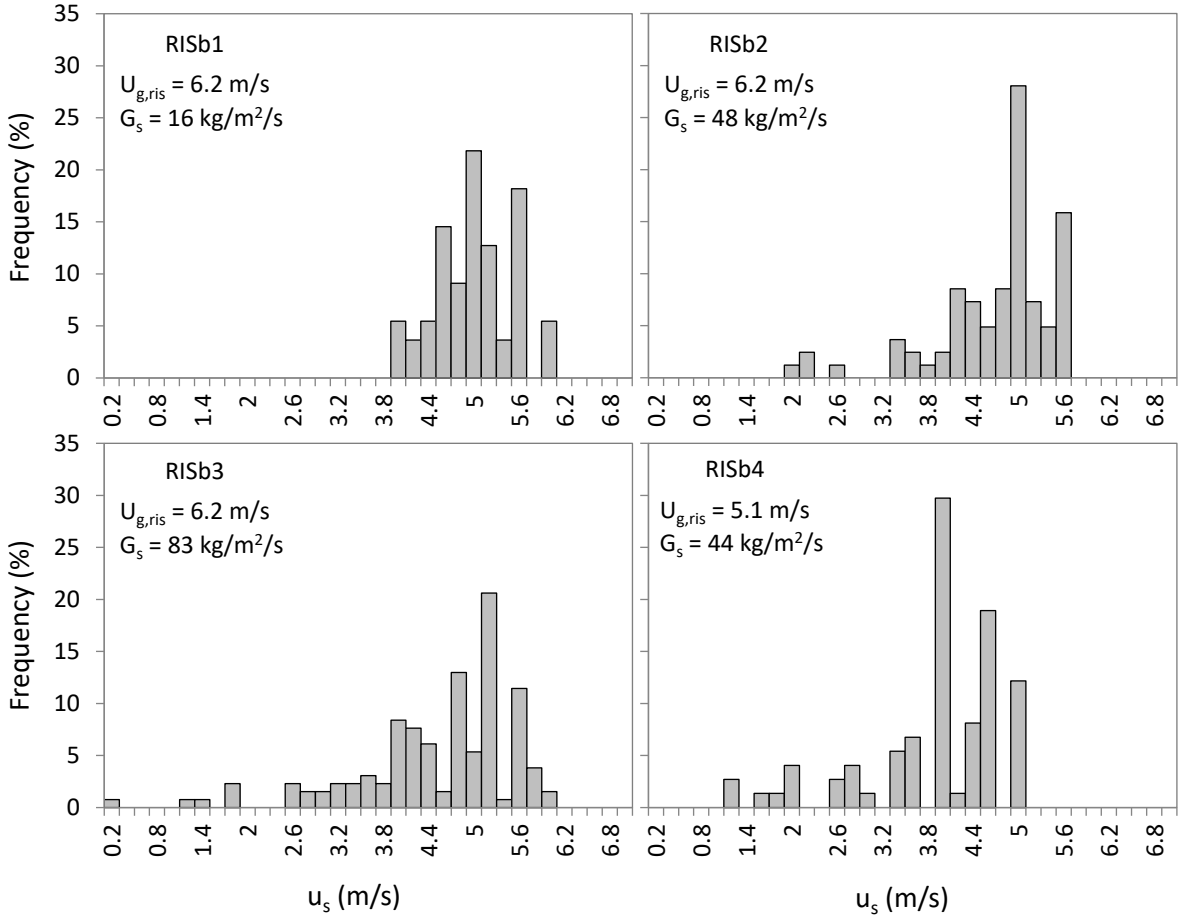

Figure 7.15. Average vertical velocity distributions of individual tracer passages. Benchmark CFB riser

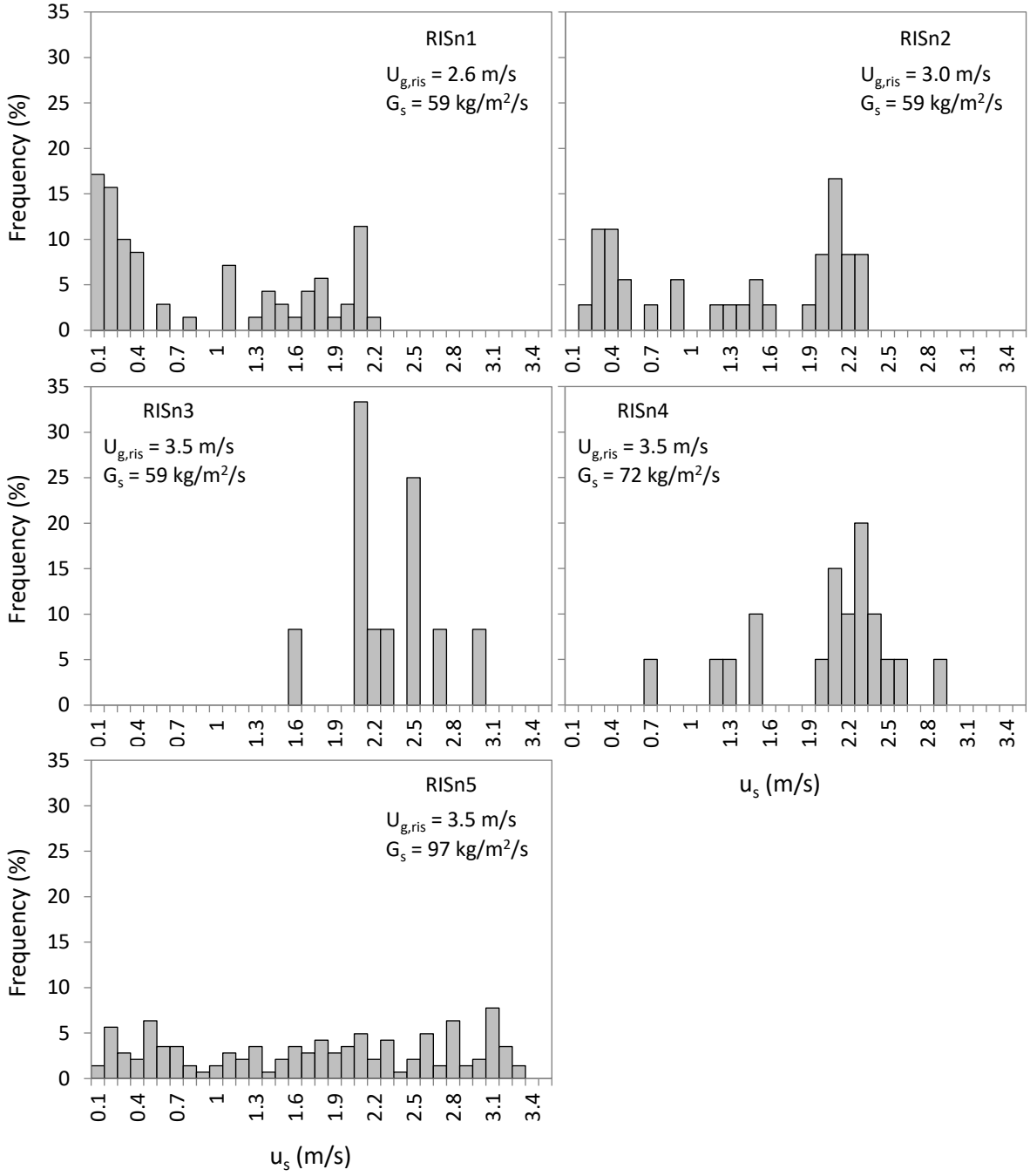

Figure 7.16. Average vertical velocity distributions of individual tracer passages. Novel CFB riser

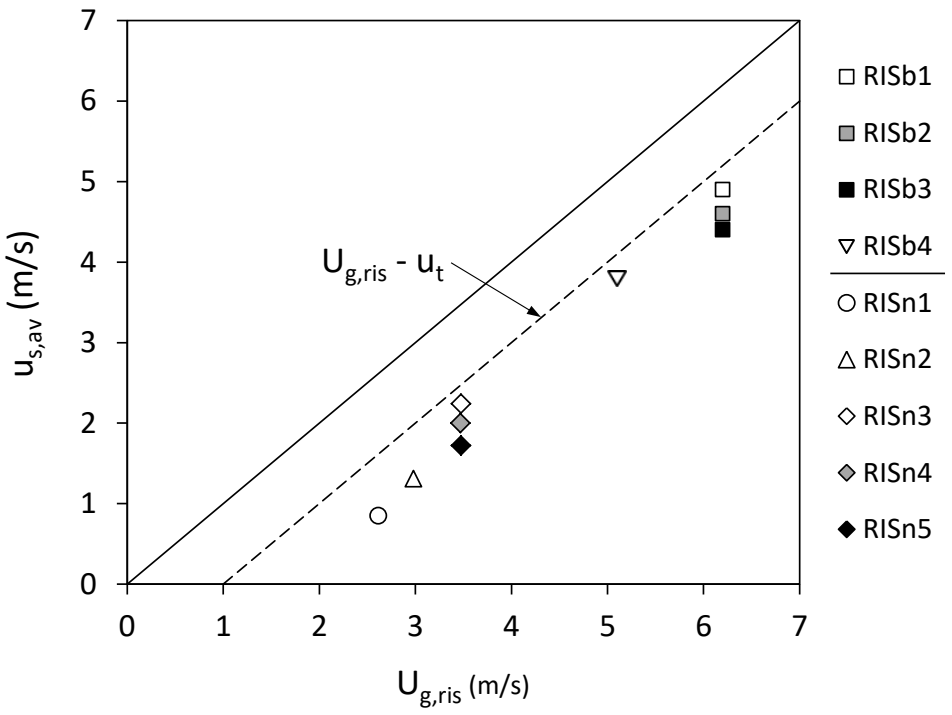

Figure 7.17. Mean tracer vertical velocity (averaged over all passages) as a function of air superficial velocity. Benchmark and novel CFB risers

- *Solids residence time distributions:*

Figure 7.18 and Figure 7.19 show the reduced-time residence time distributions E(θ) of the particle tracer for both CFB risers in form of column charts. These charts were generated from individual tracer passages according to the following 3-step procedure:

Step 1: Calculate the residence time of the solid tracer for each passage through the PEPT camera detection window (referred as the "system"), t_{res}:

$$t_{res} = t_{out} - t_{in} - \Delta t_{ex} \tag{7.1}$$

where t_{out} is the time stamp for the tracer when it leaves the system never to return, t_{in} is time stamp for the tracer when it first entered the system, and Δt_{ex} is the amount of time the tracer spent out of the system boundaries between t_{in} and t_{out}. This definition of residence time is consistent with the one given by Nauman (1981), see discussion in Section 6.2.4.

Step 2: Generate histograms H(t) from the values of t_{res} obtained in Step 1. Normalise to obtain the residence time distributions E(t) and the mean residence time τ:

$$E(t) = \frac{H(t)}{\sum_i H(t_i)\Delta t_i} \tag{7.2}$$

$$\tau = \frac{\sum_i t_i H(t_i)\Delta t_i}{\sum_i H(t_i)\Delta t_i} \tag{7.3}$$

where i refers to the i-th box in the histograms, each having an average time value of t_i and a width of Δt_i.

Step 3: Generate E(θ) charts from E(t) and the definition of reduced-time θ:

$$\theta = t / \tau \tag{7.4}$$

$$E(\theta) = \tau E(t) \tag{7.5}$$

The procedure above is analogous to the one used in Chapter 6 to generate E(θ) curves for the gas phase. The calculated values of τ are presented in Tables 7.2 to 7.5.

The solids RTDs shown in Figure 7.18 and Figure 7.19 are skewed towards high values of residence time, the skewness increasing with increasing solids flow rate and decreasing gas velocity. This evidences the increasing degree of solids back-mixing as operating conditions shift from dilute to denser solids flow, and is in overall agreement with previous works (Ambler at al., 1990; Patience et al., 1991; Bai et al., 1992; Wei and Zhu, 1996; Smolders and Baeyens, 2000; Harris et al., 2003).

An incipient second peak at values of θ between 1 and 4 can be seen for some cases in Figure 7.18 and Figure 7.19. Ambler et al. (1990) and Smolders and Baeyens (2000) modelled bimodal solids RTD by obtaining the pulse response function of the core-annulus model from Berruti and Kalogerakis (1989). This was done previously for gas-liquid systems by Jagota et al. (1973). The different shapes of the solids RTD

are obtained with such models by modifying the value of the solids transfer coefficient between core and annulus. Wei and Zhu (1996) postulated clustering of solid particles rather than formation of an annulus, and approached the modelling of solids RTD in CFB risers and downers by coupling the axially-dispersed plug flow model for both cluster and lean phases.

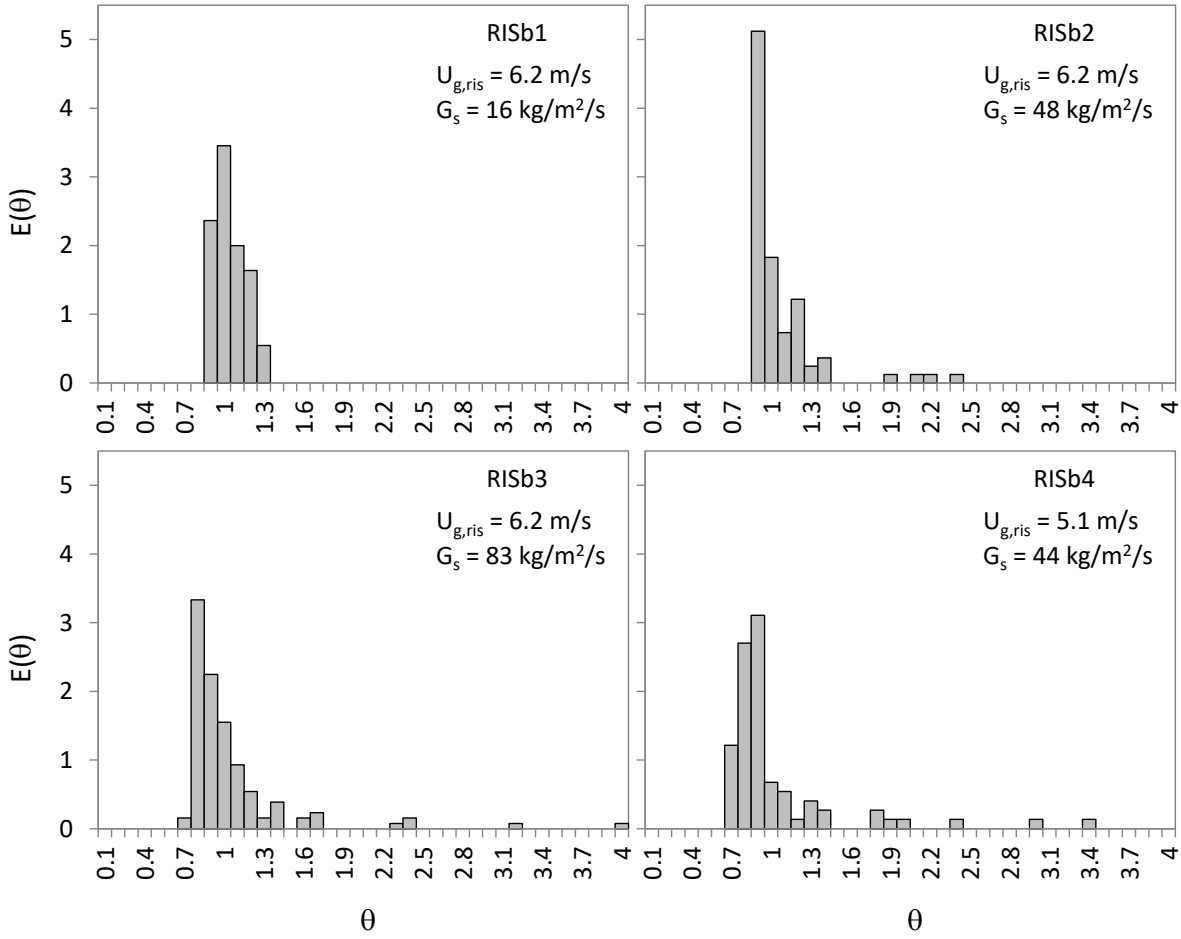

Figure 7.18. Reduced-time solids residence time distributions. Benchmark CFB riser

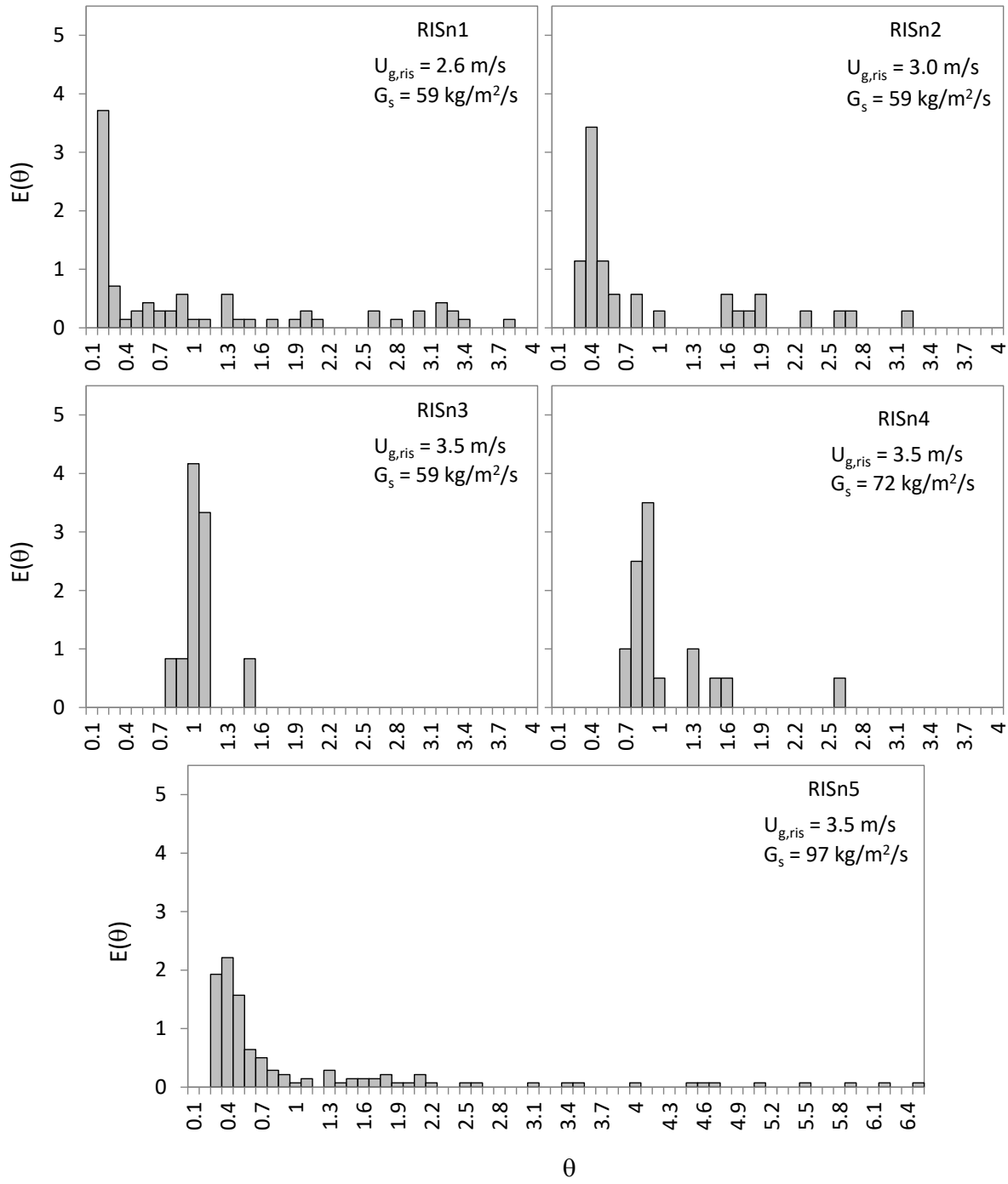

Figure 7.19. Reduced-time solids residence time distributions. Novel CFB riser

7.6.2 Novel CFB adsorber

Analysis of the PEPT experiments results for the novel CFB adsorber is based on both qualitative and quantitative characterisation of the solid tracer trajectories.

- *Qualitative analysis of solid tracer trajectories:*

Figure 7.20 and Figure 7.21 show, in the projected xy-plane, the tracer trajectories in the novel CFB adsorber for two different values of air superficial velocity (0.35 m/s and 0.52 m/s, experiments ADS2 and ADS3 respectively) and no air flow (experiments ADS1 and ADS4). Note that the original trajectory lines in experiments ADS2 to ADS4 were smoothed using a spline algorithm as they were noisy and made their visualisation difficult. This high noise-to-signal ratio in the particle location may have resulted from an excessive level of radioactivity in the tracer for the modular camera. According to Leadbeater et al. (2011), this could lead to an increase in the random background of the detection signal.

Figure 7.20 reveals that there is a higher fraction of tracer trajectories in zig-zag for the experiments with air flow through the adsorber than for those with no air flow. It can also be observed that air superficial velocity has an impact on the tracer trajectory when travelling through the space in between trays, sometimes to the point of completely suspending the particle and carrying it upwards. It also seems that the higher the flow rate, the higher this phenomenon penetrates upwards in the adsorber.

The tracer trajectories for two experiments at the same operating conditions (no air flow, G_s = 3.0 kg/m^2/s) but very different level of static electricity accumulation are compared in Figure 7.21. Experiment ADS1 was carried out with minimal amount of electrostatics (freshly reassembled rig, 1 hour of operation), whereas the novel CFB seemed to be highly charged during experiment ADS4. The differences between the tracer trajectories are not remarkable at first glance, and perhaps only a “bump” that the tracer trajectories form in experiment ADS4 on the lower end of the discharge plate stands out. A quantitative analysis of the tracer trajectories is therefore necessary to discern the effect of static electricity on the results obtained from the PEPT technique.

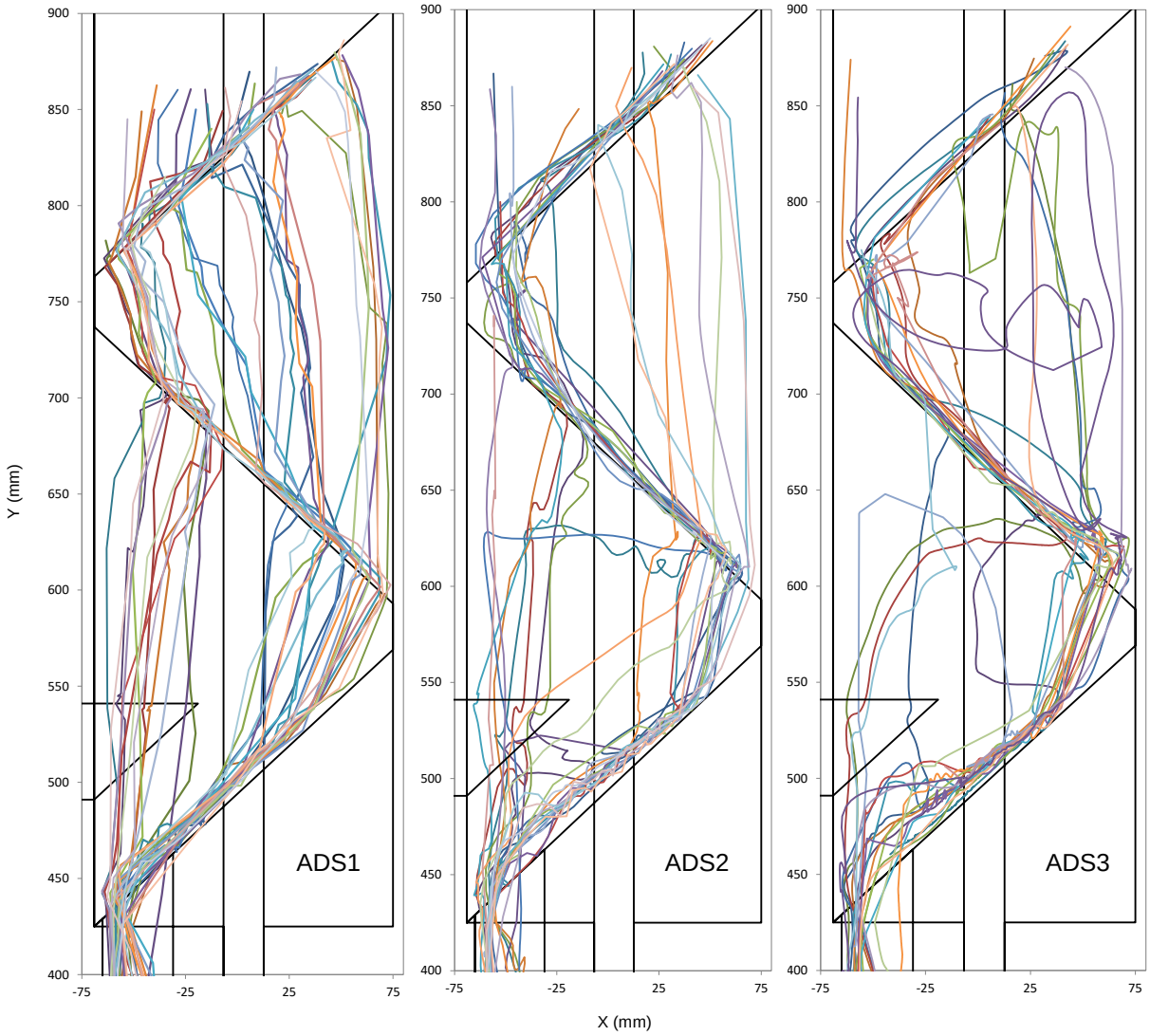

Figure 7.20. Tracer trajectories in the novel CFB adsorber xy-plane for three different air superficial velocities [zero (left), 0.35 m/s (centre) and 0.52 m/s (right)].

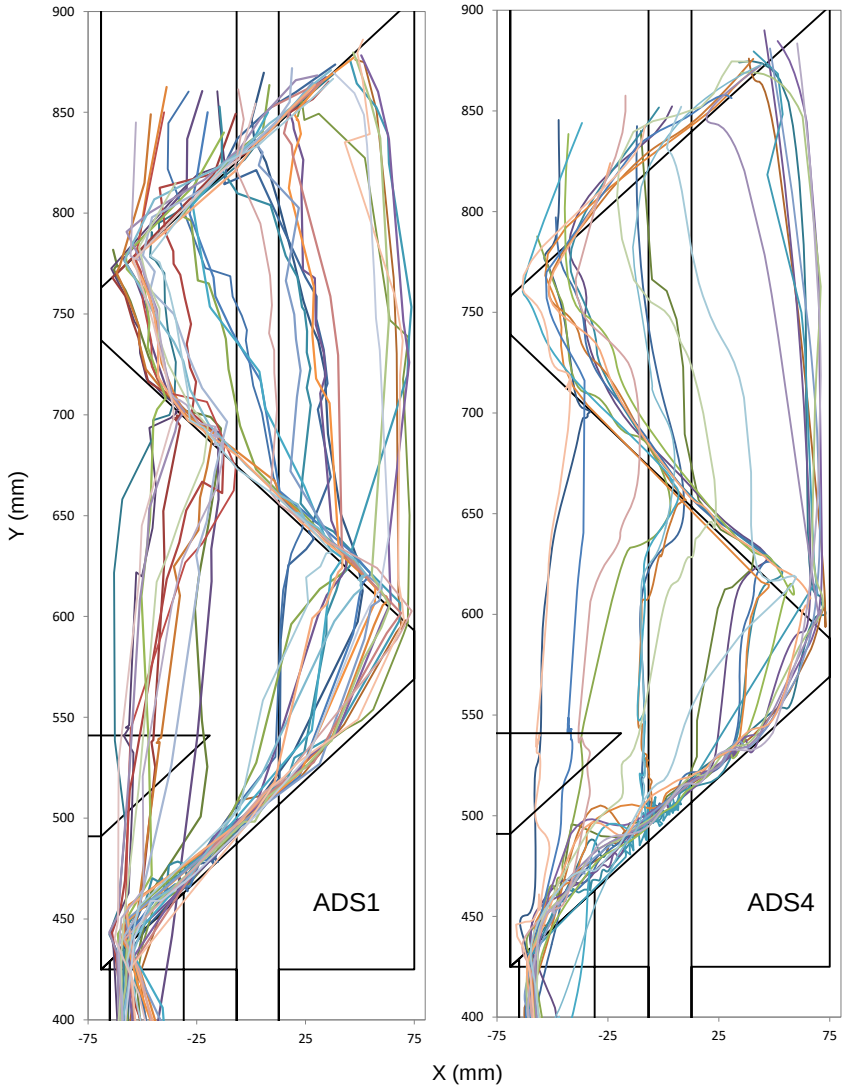

Figure 7.21. Tracer trajectories in the novel CFB adsorber xy-plane for experiments with no air flow. The effect of static electricity is compared between an experiment carried out with a clean, freshly reassembled CFB setup (ADS1, left) and another performed after 4 days of experiments and 4-5 hours of non-continuous operation (ADS4, right).

- *Quantitative analysis of solid tracer trajectories:*

To quantify the characteristics of solids flow in the novel CFB adsorber, the tracer trajectories in Figure 7.20 and Figure 7.21 are first divided in "segments" for which tracer average velocity and distance travelled along the trajectory line are calculated. These segments are labelled as follows (see Figure 7.22 for reference):

1) *Tray 1*: the tracer slides down on the top orifice tray.

2) *Tray 2*: the tracer slides down on the bottom orifice tray.

3) *Fall 1*: the tracer falls through a hole from the top orifice tray.

4) *Fall 2*: the tracer falls through a hole from the bottom orifice tray.

5) *Discharge plate*: the tracer slides down on the discharge plate.

6) *Airborne*: the particle is largely deviated from the free-fall trajectory.

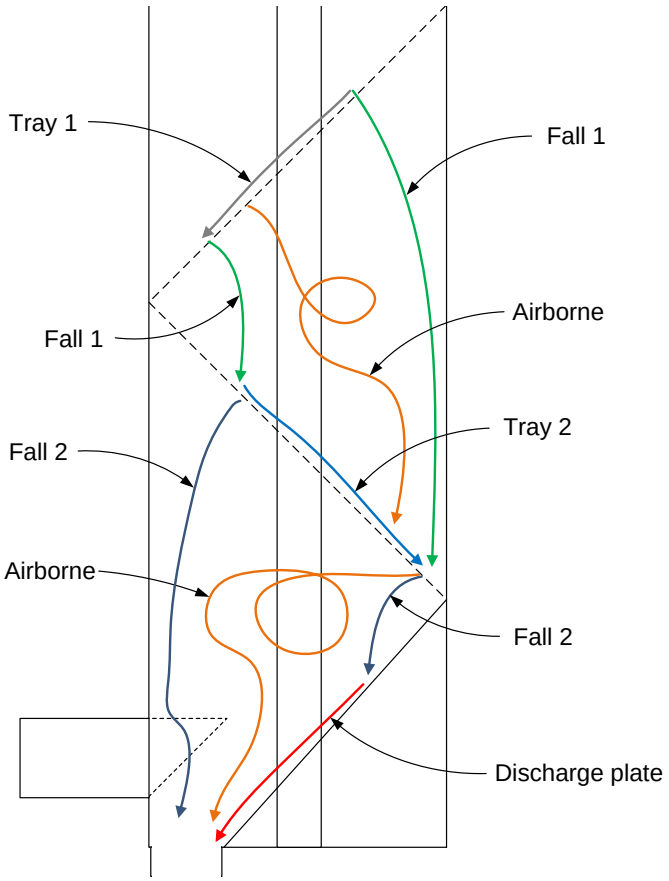

Figure 7.22. Sketch representing tracer trajectory segments in novel CFB adsorber

Figures 7.24 to 7.27 show the contributions of each tracer passage to the trajectory segments labelled as above, in terms of average velocity (in the xy-plane) versus distance travelled along its trajectory. Note that the actual tracer velocity (in the three-dimensional space) can be higher than the calculated value as the z-coordinate is not available due to problems with the modular camera (see discussion in Section 7.4.1).

• No air flow, no electrostatics (experiment ADS1, Figure 7.24):

The particles slide over 13-50% of the total length of both orifice trays. The average sliding velocities on the trays and the discharge plate are ~40 cm/s regardless of the distance travelled (Figure 7.24a, b and e). This might indicate that the sliding velocity is governed by friction between particles (whether single- or multi-layer) and the inclined Perspex surfaces. Looking at Figure 7.24c, the tracer average velocity falling from the top orifice tray increases with distance, which is expected as the particle is able to pick up speed and approach its terminal velocity. The same is seen for particles falling from the bottom orifice tray (Figure 7.24d), although in this case some of the particles are slowed down as they collide with the air inlet nozzle before reaching the bottom of the adsorber.

• $U_{g,ads}$ = 0.35 m/s (experiment ADS2, Figure 7.25):

The particles slide on the orifice trays for longer distances (50%-75% of the total length of the trays) and lower average velocities (~30 cm/s) with respect to the case of no air flow. It can be postulated that the air velocity through the tray holes, 1.01 m/s (just above the solids terminal velocity, 1 m/s) is high enough to hinder the particle fall through the holes, and therefore the distances travelled by the particles on the trays are longer. This is in line with the results reported by Kannan et al. (1994) in gas-solid trickle flow with horizontal orifice plates. The investigators found that gas velocities through the holes needed to be 0.9-1.1 times the particle terminal velocity to prevent solids from “dumping”, forming a layer on the plate surface.

Lower tracer velocity on the adsorber inclined trays with respect to the no air flow case could be due to particle “slaloming” around the different air jets. However, this

could not be confirmed since PEPT trajectory data in the z-coordinate is not available, as mentioned previously. Particles that do fall through tray holes present increasing average velocities as they fall from higher positions on the tray (Figure 7.25c), similarly to the case with no air flow.

The air inlet effect on the tracer trajectories is noticed only below the bottom orifice tray. Around 13% of the tracer passages get airborne here, and when they do so the time they remain suspended is less than 1 s. However, the impingement of the air inlet jet on the discharge plate causes another much more detrimental effect by pushing the solids to the sides as they slide down. This promotes the accumulation of solids in a large pocket at the lower edge of the discharge plate, as seen in Figure 7.23. The existence of such pocket is undesirable because the tracer particle can slow down (this is visible in Figure 7.25e as a shift of the tracer average velocity on the discharge plate towards lower values) or get stuck permanently.

Figure 7.23. Air inlet effect on the solids flow in the novel CFB adsorber. The air inlet jet pushes the particles to the sides, promoting the formation of a large solids pocket where the tracer particle can get stuck.

• $U_{g,ads}$ = 0.52 m/s (experiment ADS3, Figure 7.26):

If the air flow rate is increased further, but keeping the superficial gas velocity below the terminal velocity of the solid particles, the distances travelled by the tracer over the inclined trays increase (75%-100% of the total tray length). On the negative side, the air inlet effect penetrates further up in the adsorber, getting particles airborne above the bottom orifice tray, some of them being suspended for 2-3 seconds.

A notable fraction of tracer passages with very low average velocity (<5 cm/s) is detected in all zones within the adsorber. This strongly points to the accumulation of static electricity, as evidenced in experiment ADS4.

• No air flow, strong electrostatic effects (experiment ADS4, Figure 7.27):

Velocity-distance graphs for experiment ADS4 retain roughly the features of those for experiment ADS1. However, the presence of static electricity is evidenced by ~20% of tracer passages at a very low velocity in all zones within the adsorber. The tracer particle tends to cling to the inner surfaces, reducing its velocity dramatically. It can be seen in Figure 7.21 how particles falling from the centre of the bottom orifice tray deviate their trajectories in mid-air towards the riser, presumably caused by an attractive electrostatic force. This can also be seen in Figure 7.20 for experiment ADS3 but in less degree than for ADS4. Further evidence of the presence of electrostatics is the rapid growth of solid pockets throughout the system, especially at the lower edge of the orifice trays and discharge plate (see also Figure 4.36).

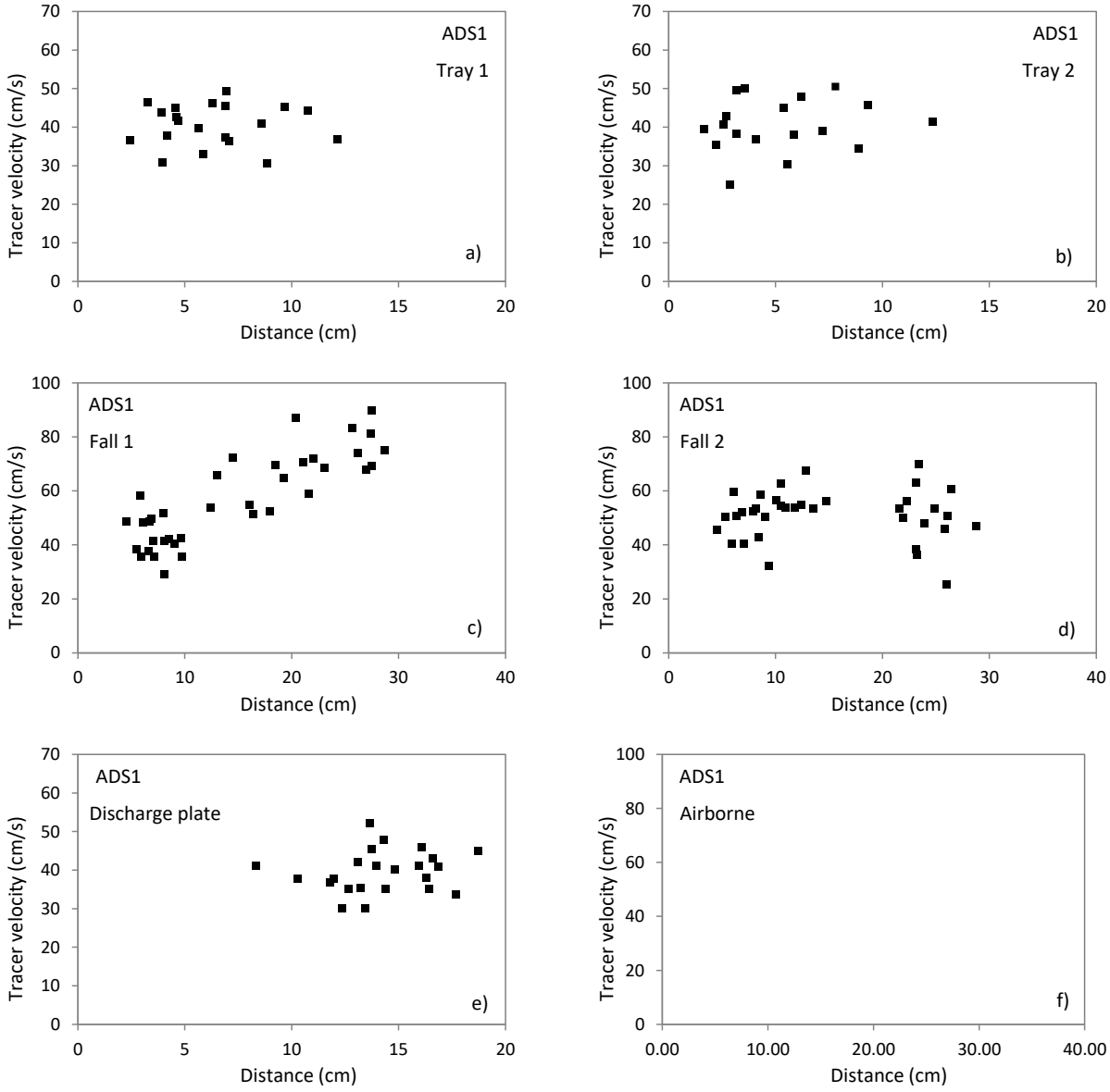

Figure 7.24. Tracer average velocity versus distance travelled along trajectory. Novel CFB adsorber, experiment ADS1 ($U_{g,ads}$ = 0, G_s = 3.0 kg/m^2/s).

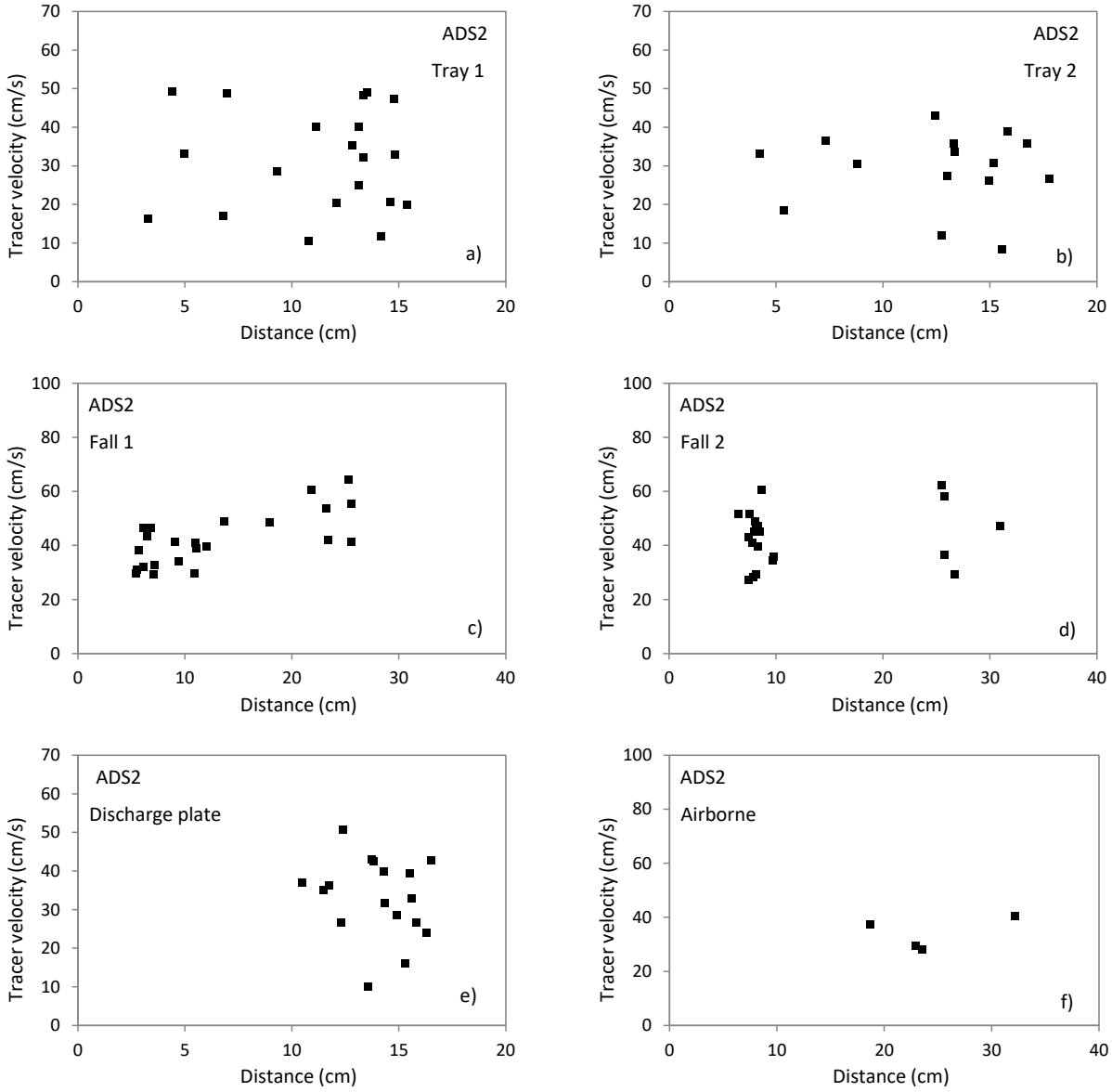

Figure 7.25. Tracer average velocity versus distance travelled along trajectory. Novel CFB adsorber, experiment ADS2 ($U_{g,ads}$ = 0.35 m/s, G_s = 3.3 kg/m^2/s).

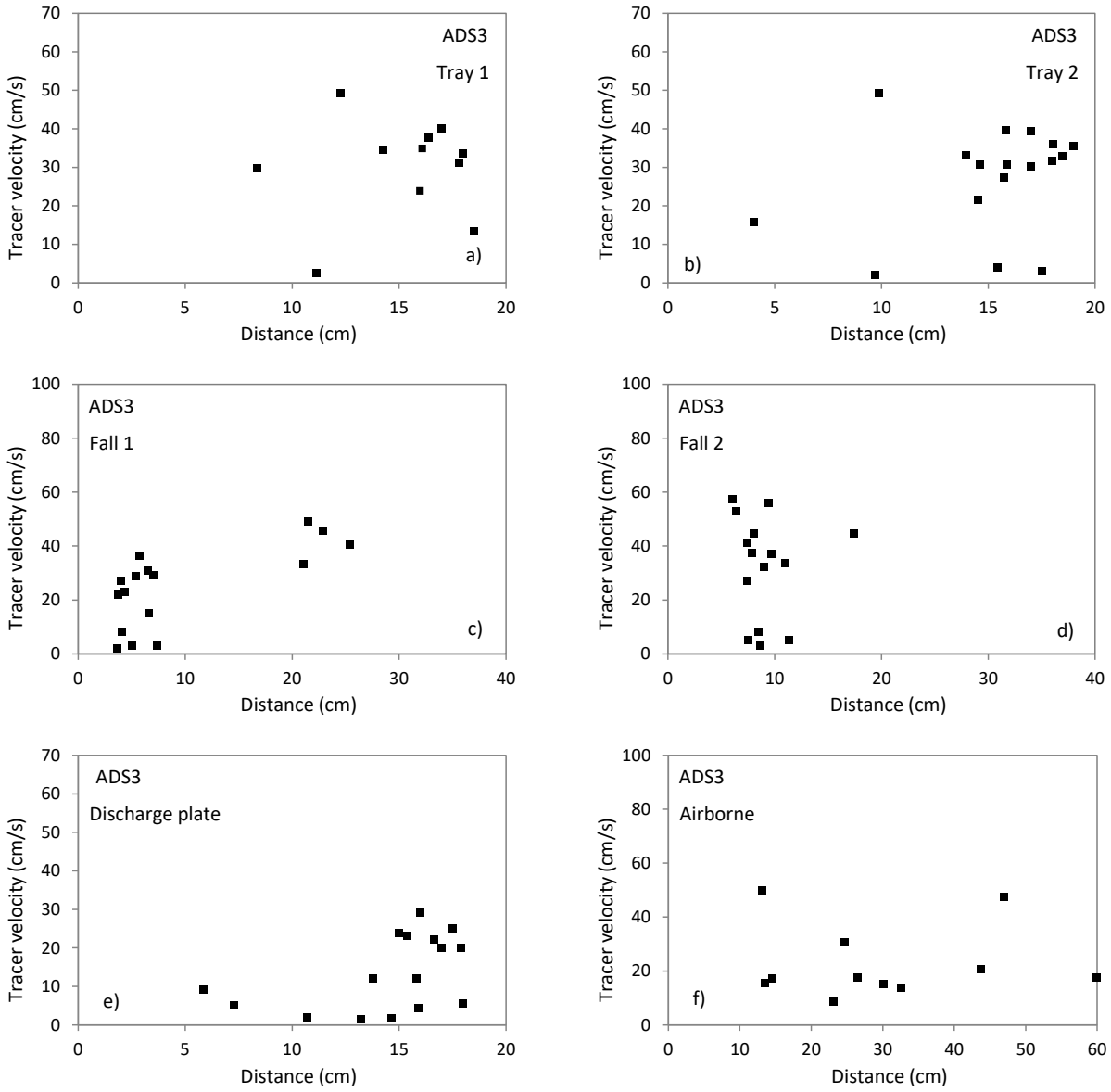

Figure 7.26. Tracer average velocity versus distance travelled along trajectory. Novel CFB adsorber, experiment ADS3 ($U_{g,ads}$ = 0.52 m/s, G_s = 3.2 kg/m^2/s).

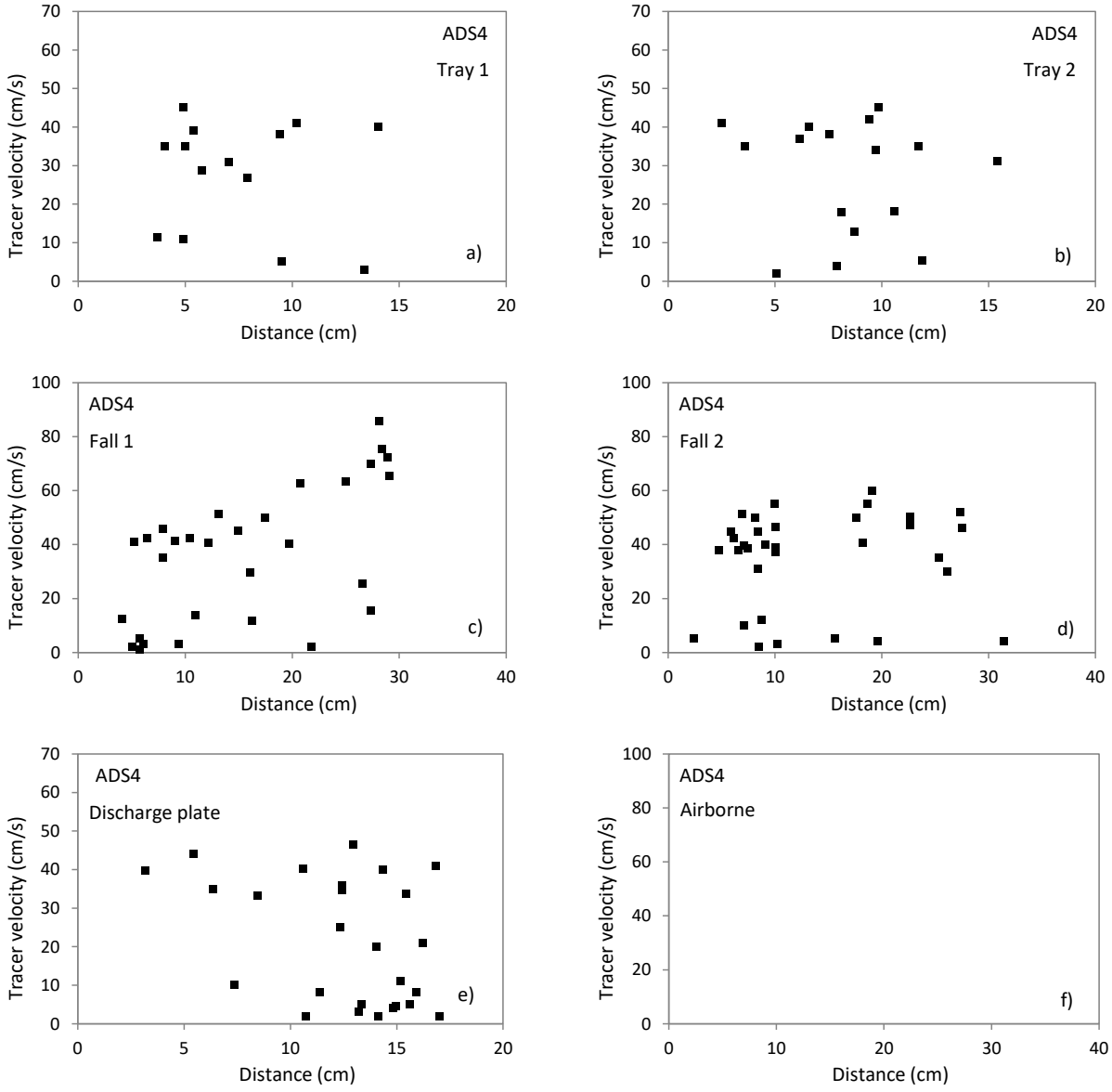

Figure 7.27. Tracer average velocity versus distance travelled along trajectory. Novel CFB adsorber, experiment ADS4 ($U_{g,ads}$ = 0, G_s = 3.0 kg/m^2/s).

- *Solids residence time distributions:*

The obtained solids residence time distributions in the portion of the adsorber visible by the PEPT modular camera are presented in the form of frequency histograms in Figure 7.28, and as E(θ) column charts in Figure 7.29. The residence time is taken as the time elapsed between the tracer first appears on top of the image ($y \approx 870$ mm) and the moment it leaves the adsorber, entering the top downcomer ($y \approx 440$ mm). An attempt to correct the effects of static electricity in the solids RTDs has been made by applying a "cut-off" value of residence time. This method obviously does not discern between phenomena causing tracer low velocities, introducing arbitrariness in the results. A clean cut can be obtained between the "main body" and the "tail" of the histograms by choosing a cut-off time of 5 s. Applying cut-off times to RTDs with the aim of discarding long tails is advocated by Levenspiel (1962) on the grounds of the little contribution of the RTD tail to process performance and large impact on the value of mean residence times. For the sake of completeness, results of both sub-cases (with and without cut-off time) are kept. The values of mean residence time for all cases are presented in Table 7.4.

The shape of the solids residence time distributions with cut-off time suggests that solids dispersion are the highest for gas velocities marking the transition between the two main flow modes in the adsorber, namely the "flow-through-holes" mode and zig-zag mode. This can be explained realising that in the transition region the residence times of the individual particles are necessarily spread in between the mean values of each flow mode.

- *Solids average vertical velocity distributions:*

Figure 7.30 shows the distributions of the tracer average vertical velocity in form of frequency histograms. For each individual tracer passage, the value of average vertical velocity was calculated dividing the height of the portion of the adsorber visible by the PEPT modular camera (0.43 m) over the corresponding residence time. The values obtained are presented in Table 7.4.

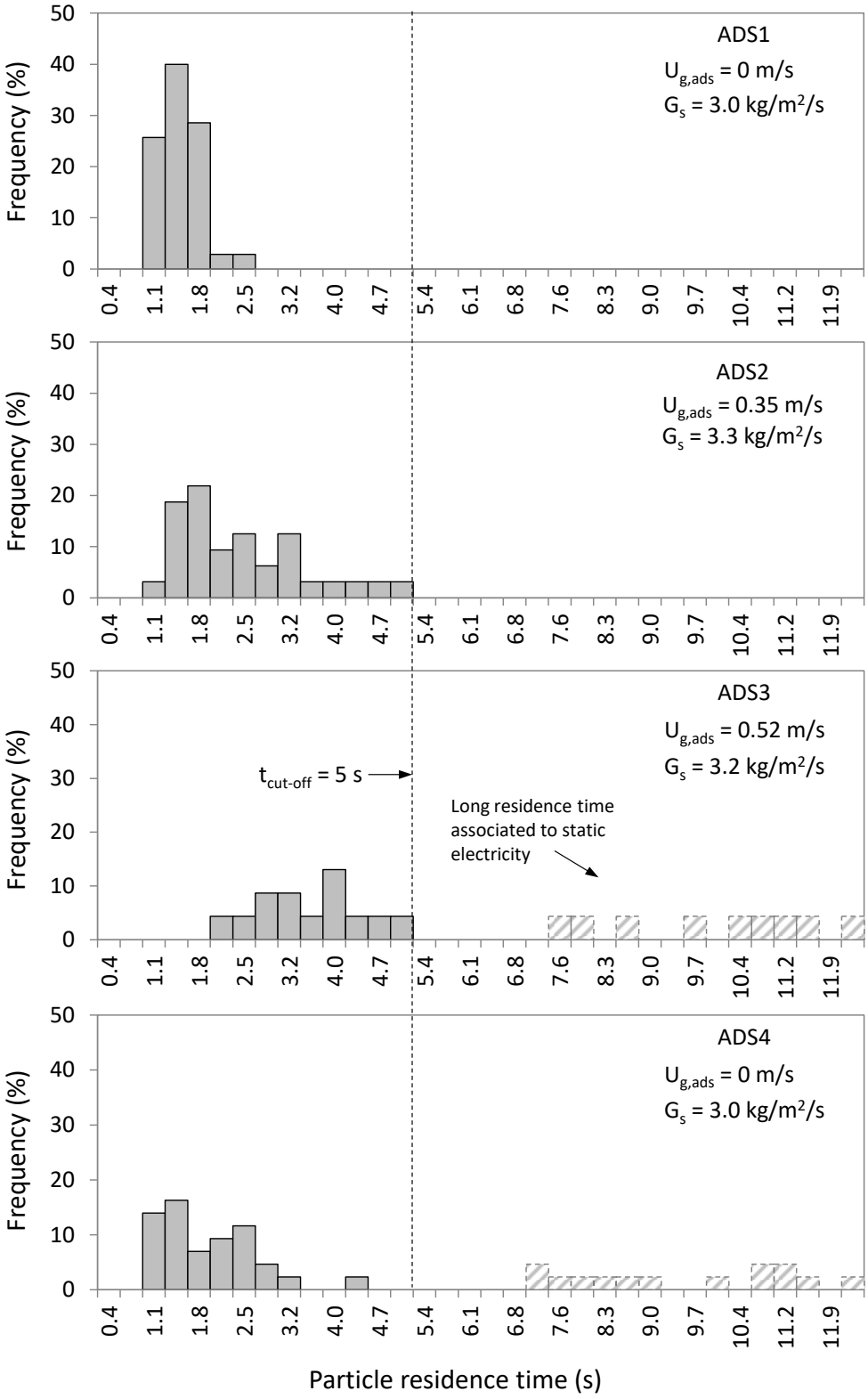

Figure 7.28. Solids RTD histograms. Novel CFB adsorber

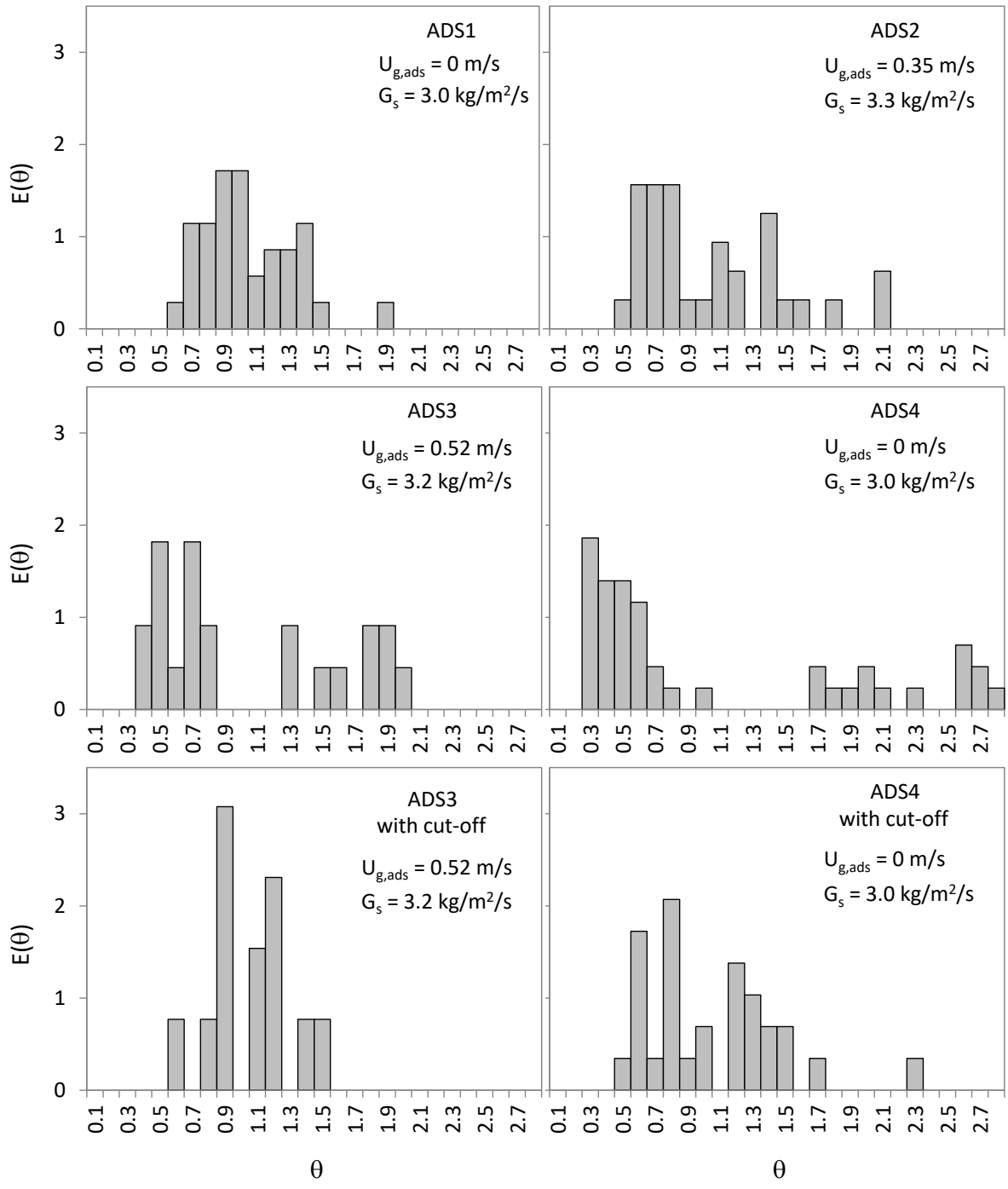

Figure 7.29. Reduced-time solids residence time distributions. Novel CFB adsorber

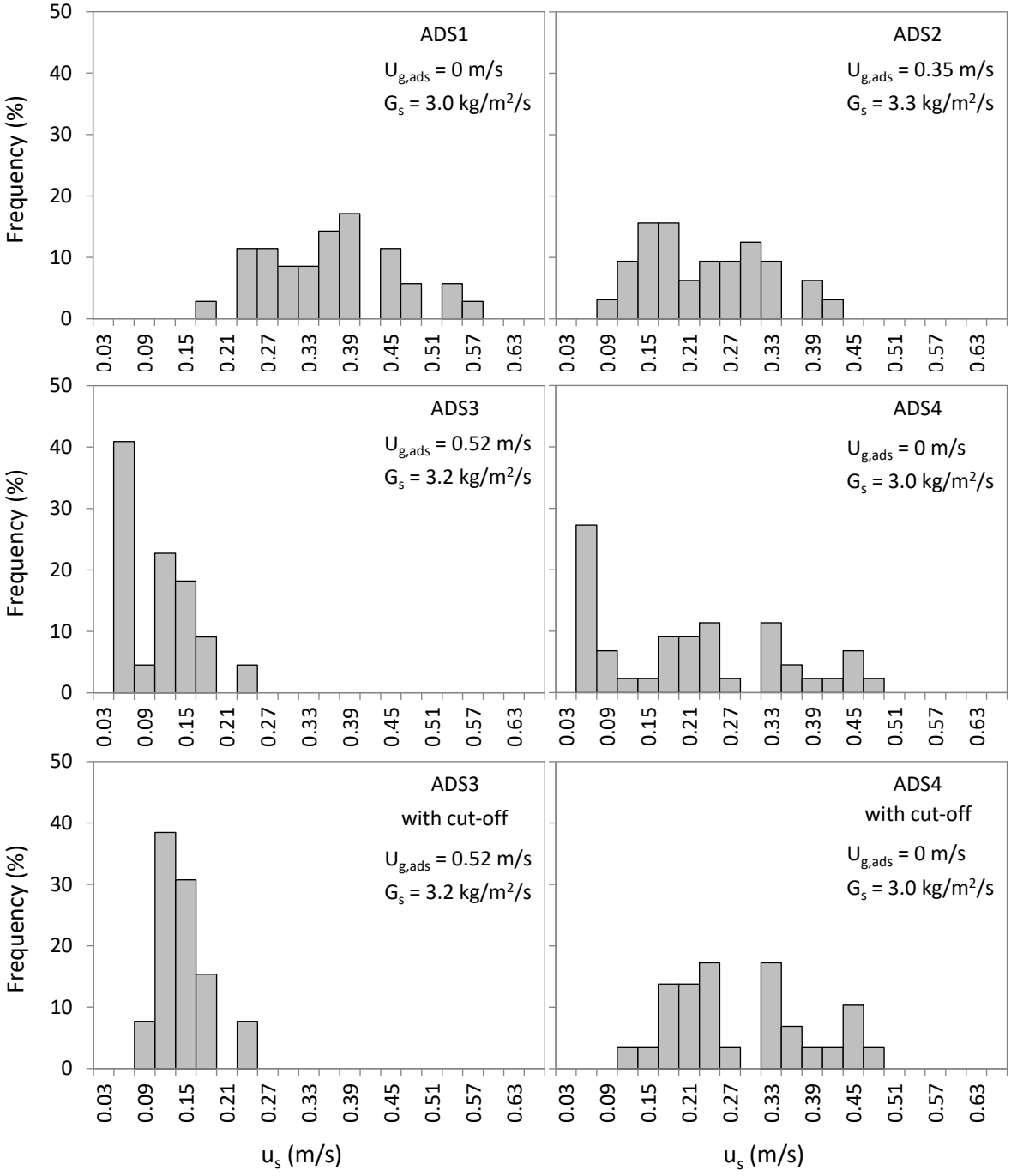

Figure 7.30. Solid tracer average vertical velocity distributions. Novel CFB adsorber

7.6.3 Regenerator

Figure 7.31 shows tracer trajectories in the xy-, zy- and xz-planes for the four PEPT experiments carried out in the regenerator (integrated in the novel CFB), see Table 7.5 for details on the operating conditions used.

The images in Figure 7.31 are overall similar to those generated by means of other visualisation techniques in eccentric discharge of silos (Sielamowicz et al., 2004; Wu et al., 2008). The particle tracer moves in overall convergent trajectories towards the solids outlet pipe at the regenerator bottom, although for the experiments with higher flow rates of both gas and solids (REG2 and REG3) the particle trajectories in the zy-plane are slightly divergent at the top two thirds of the solids bed, to then sharply converge at the bottom third. The tracer trajectories for the experiments REG1 and REG4, on the other hand, are convergent throughout the entire height of the solids bed.

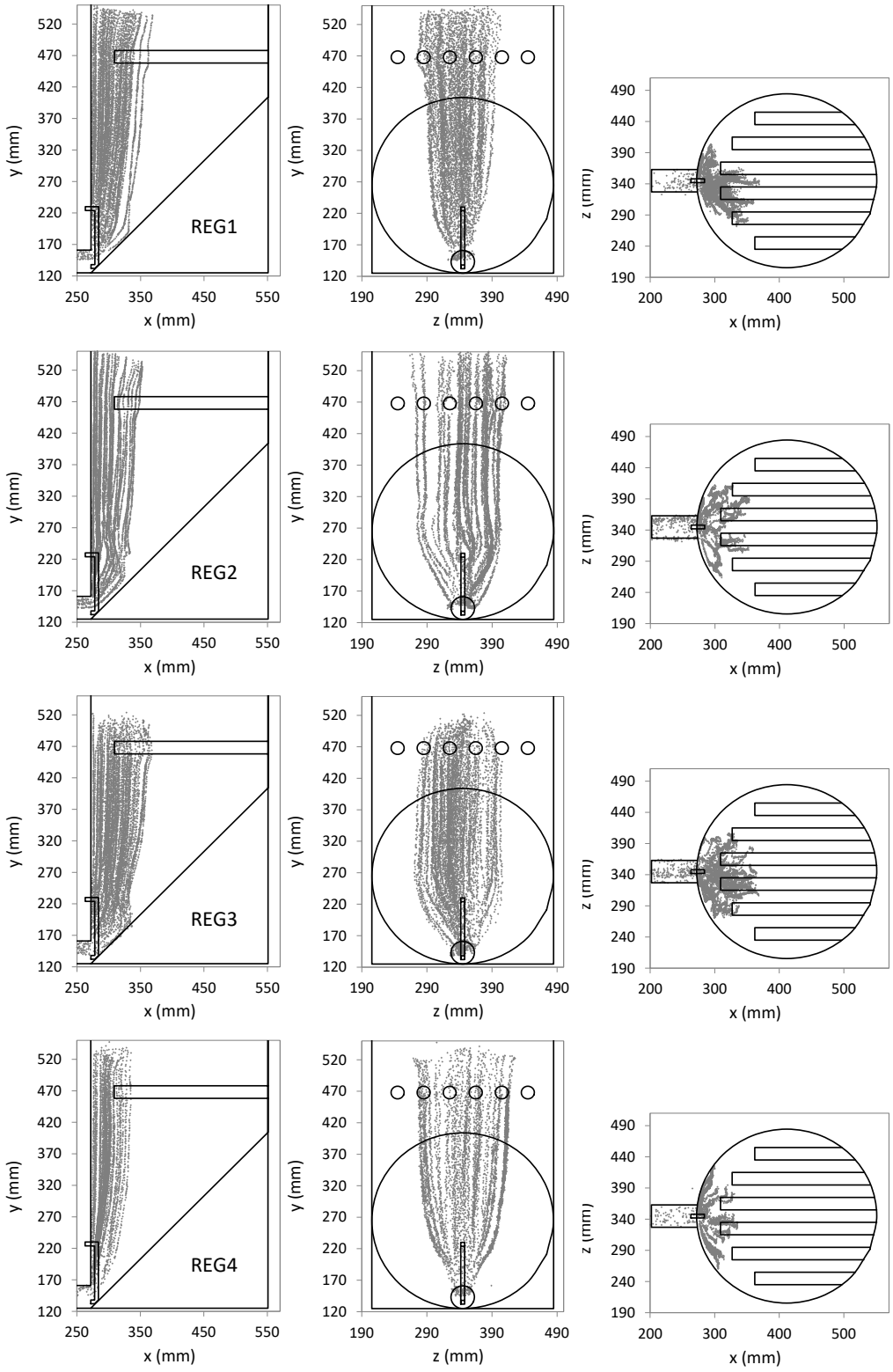

Figure 7.31. Solid tracer trajectories in the regenerator (integrated in novel CFB)

- *Estimation of the extension of the moving bed region:*

The initial horizontal position of the tracer was not freely chosen as it was discharged into the regenerator from the top downcomer, and therefore the envelope of tracer trajectories in Figure 7.31 should not be taken as a complete picture of the regenerator moving bed. The extension of the moving bed into the regenerator can be estimated however as the distance from the solids outlet pipe at which the tracer vertical velocities are zero, as illustrated in Figure 7.32.

Figure 7.33 shows the tracer vertical velocities in the plane y = 345 mm of the regenerator, roughly corresponding to half height of the solids bed. The tracer velocities were calculated as the average between planes y = 340 mm and 350 mm. It is estimated from extrapolation of the data to values of zero vertical velocity that, in such plane, the moving bed extends 10 cm into the bed of solids from the wall, the rest being stagnant.

- *Solids average vertical velocity distributions:*

Figure 7.34 shows the distributions of solids average vertical velocities in form of frequency histograms for the different experiments. The distributions are quite wide overall, with slightly more accentuated skewness towards low values of velocity for the experiments at low flow of gas and solids (REG1 and REG4). The mean values of velocity (presented in Table 7.5) are very similar, ranging from 5.1 m/s to 5.8 m/s, with no particular trend with the operating conditions or solids inventory.

- *Solids residence time distributions:*

Regenerator E(θ) charts are presented in Figure 7.35. The values of mean residence time and variance are presented in Table 7.5. The residence times were calculated as the time elapsed between the tracer is found at y = 515 mm (corresponding to h_{reg} = 390 mm) and the moment it enters the solids outlet pipe. A spread of residence time towards high values is evident in all cases, suggesting a strong “shearing” effect of the stagnant region on the moving bed.

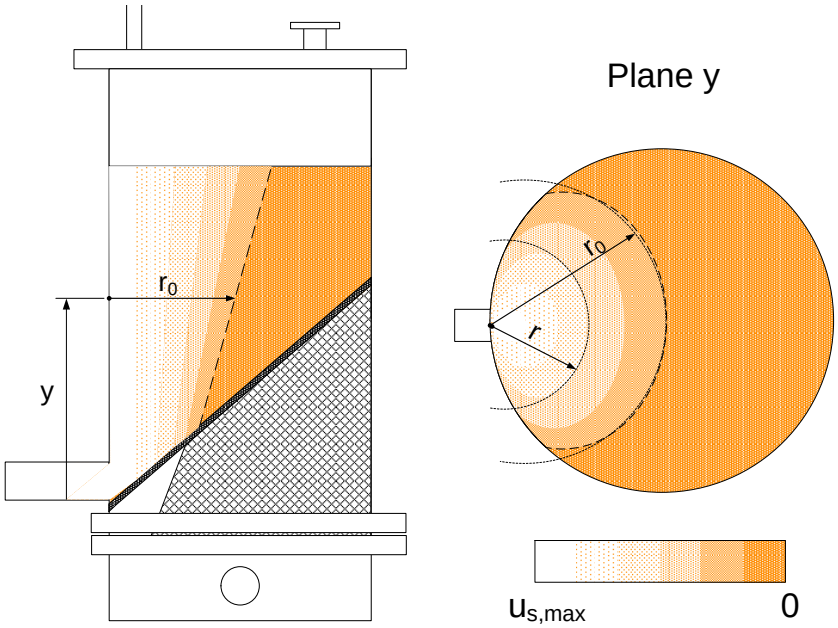

Figure 7.32. Estimation of the moving bed radius from radial profile of tracer vertical velocities

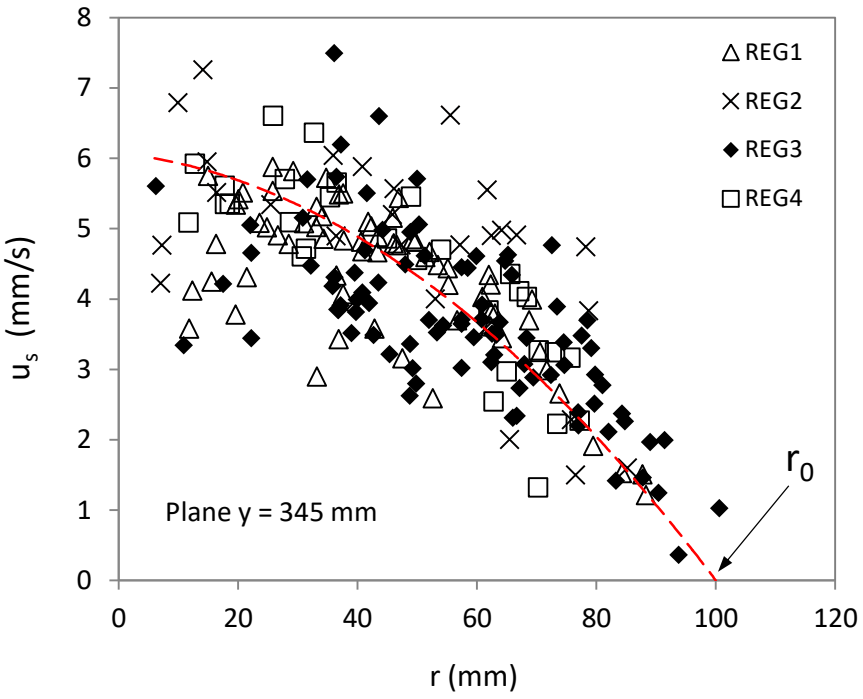

Figure 7.33. Solid tracer vertical velocity versus horizontal distance to the regenerator solids outlet pipe in the plane y = 345 mm.

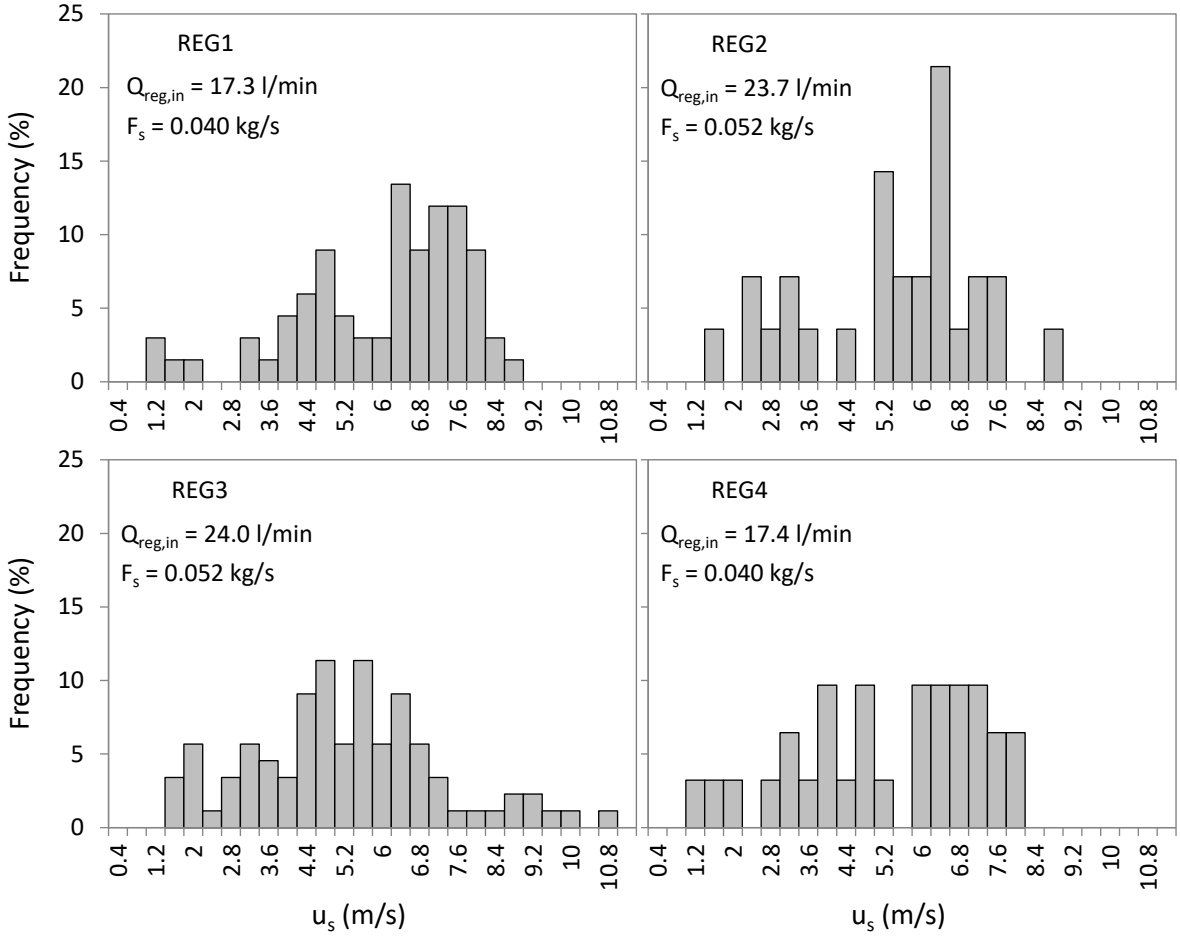

Figure 7.34. Solids average vertical velocity distributions. Regenerator (integrated in novel CFB)

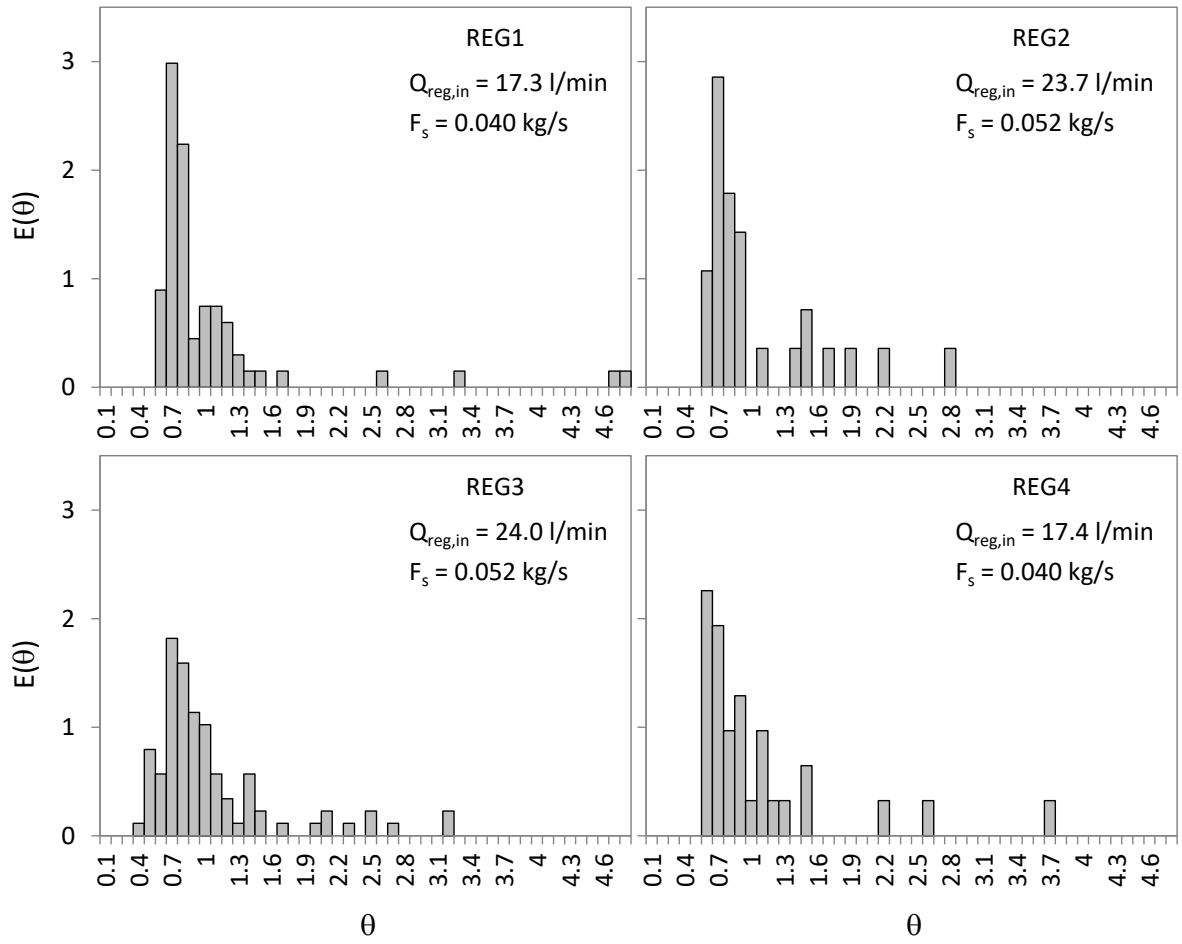

Figure 7.35. Reduced-time solids residence time distributions. Regenerator (integrated in novel CFB)

7.6.4 Comparison with literature data

Values of the solid-phase axial Péclet number (Pe_s) for the CFB risers and counter-current adsorber were obtained using the values of variance of the E(θ) charts in equations (6.19) and (6.20), analogously to how it was done for the gas phase. These values can be then compared with those of previous works and used in the adsorber model to estimate the performance of the CFB configurations studied in this work as CO_2 capture processes. The CFB regenerator is excluded from this comparison exercise since, as for the knowledge of the author at the time of writing, no works on solids axial dispersion with the geometry and operating conditions of the regenerator are published.

- *CFB risers:*

Figure 7.36 shows values of Pe_s for CFB risers as a function of the solids flux. The values of Pe_s from previous works are very low, in the range 0-15, for the whole range of solids flux. For the CFB risers studied here, the values of Pe_s are much higher (>80) at low solid fluxes but rapidly decrease to 0-30 as the solid flux is increased. A contributing factor in the discrepancy between values of Pe_s from previous works and this one may be the different solids used: most of previous works in riser fluid dynamics use Geldart type A solids (FCC catalyst being the most representative material), which have smaller particle diameters and lower densities than the sand used here (typical Geldart type B material). Therefore, solids fraction at given operating conditions must be higher for the former type of material, with the consequent higher interaction between particles and agglomeration effects. This, in turn, increases the solids back-mixing due to the higher relative velocity between agglomerates and single particles. The differences in riser diameter might be another contributing factor in the discrepancies in the results; as commented in Section 7.6.1, the PEPT data suggest (but do not prove) that solids dispersion increases with riser diameter.

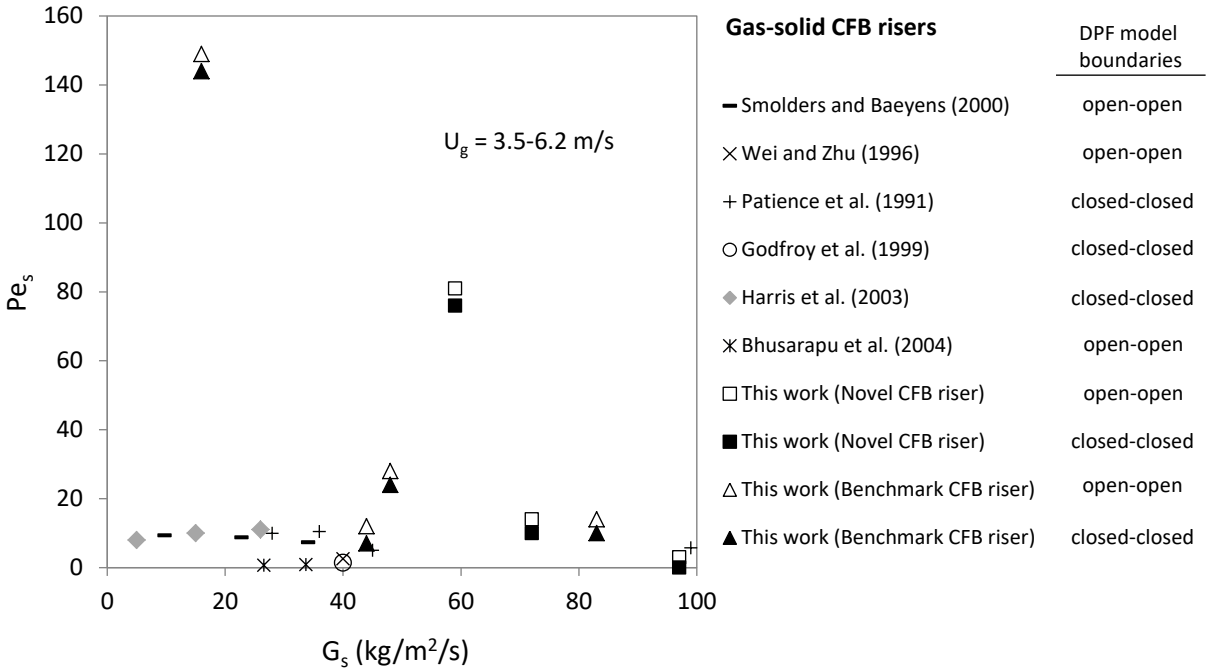

Figure 7.36. Solids axial Péclet number in function of solids flux for different works in CFB risers

- *Novel CFB adsorber:*

Figure 7.37 shows values of Pe_s for gas-solid counter-current contactors with solids in dilute flow, as a function of the gas superficial velocity relative to that of flooding, U_{fl} (in analogy with gas-liquid systems). In this work U_{fl} = 0.67 m/s, corresponding to the maximum value of gas flow rate without excessive carry-over of solids ($Q_{ads,in}$ = 640 l/min).

For the systems of Roes and van Swaai (1979b) and Noordergraaf et al. (1980), the values of Pe_s were found to be constant with gas velocity up to 0.6-0.8 times the flooding point and then decrease due to gross maldistribution of the solids flow. This indicates that the flow characteristics of the solid phase are not greatly affected by the upflowing gas for most of the operating range. In the novel CFB adsorber, on the other hand, the solids flow mode shifts from a relatively straight down path to zig-zag as the gas velocity is increased. The effect of such shift in flow mode on solids dispersion could not be properly determined with PEPT since the effects of static electricity on the particle tracer flow could not be rigorously subtracted. The "corrected" data after application of a cut-off value of solids residence time suggest

that solids dispersion goes through a local maximum (local minimum in the value of Pe_s) in the transition from straight-down to zig-zag flow. As discussed previously, this can be justified by taking into account that values of mean residence time of both flow regimes are different, and during the transition from one to the other the distribution of residence times is spread between the two.

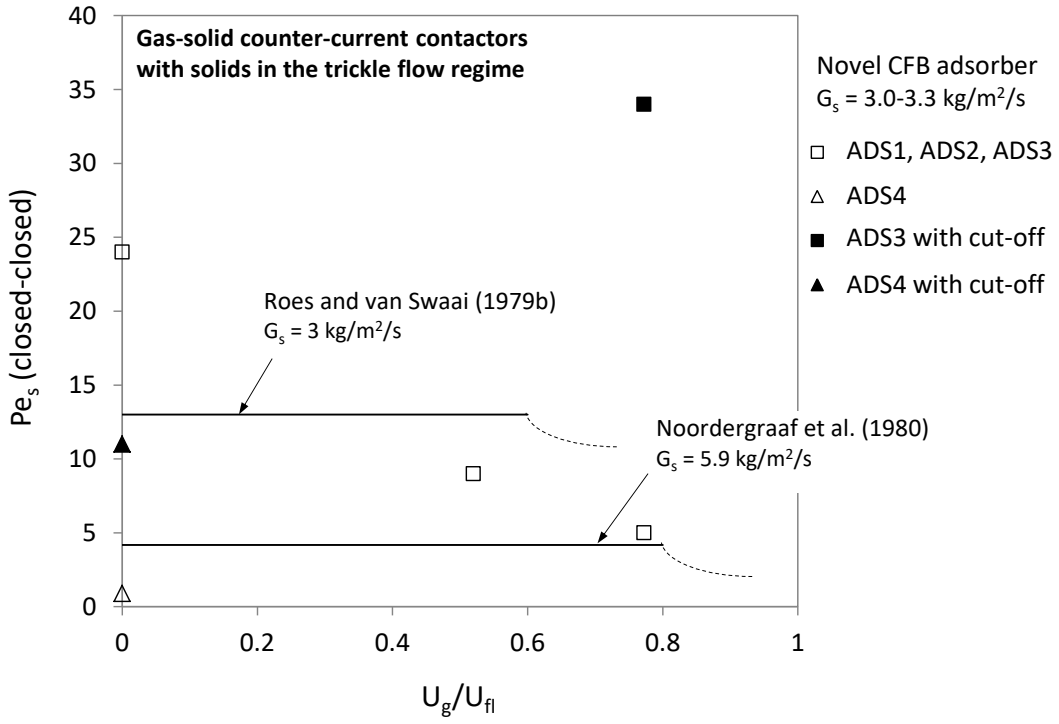

Figure 7.37. Solids axial Péclet number as a function of gas superficial velocity relative to flooding velocity for different works in gas-solid counter-current contactors in the trickle flow regime

Figure 7.38 presents the values of average vertical velocity for several gas-solid counter-current contactors with solids in dilute flow, as a function of gas superficial velocity. Despite the differences in geometry, the values and trends are very similar for the different systems. This suggests that the mechanisms or factors governing the velocities of solids in these systems are similar, for example the geometry and material of the contactor internals. It was hypothesised in Section 7.6.2 that the velocity of the solid tracer on the inclined plates was governed by particle-tray friction forces.

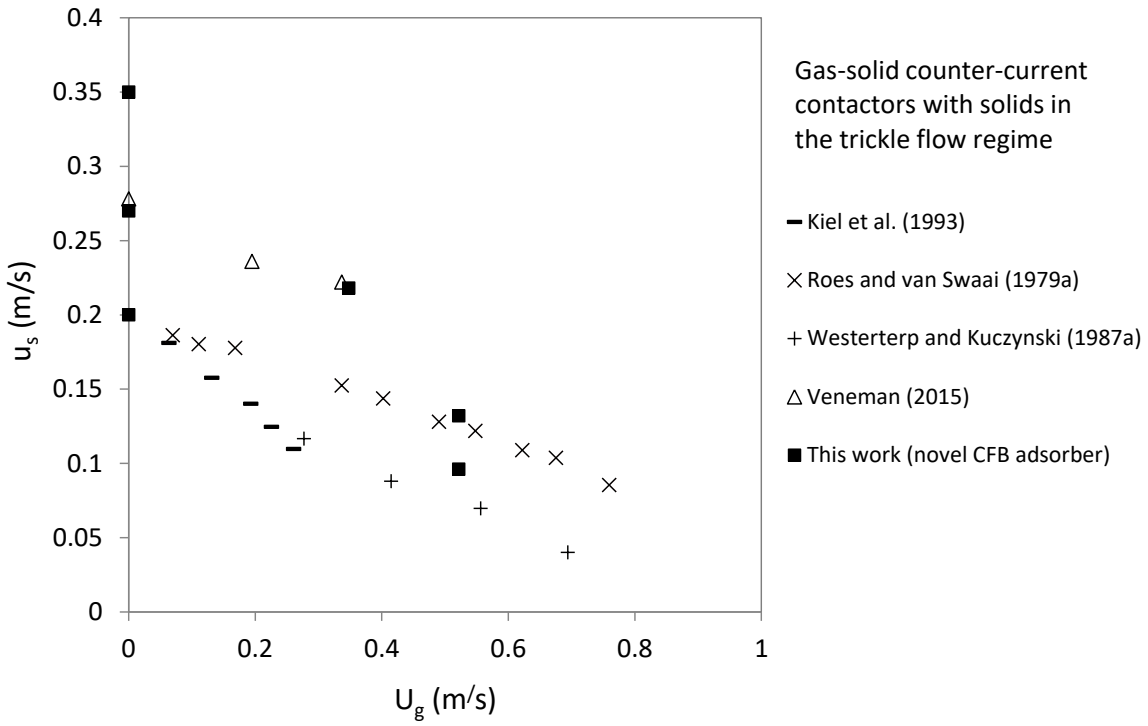

Figure 7.38. Solids average vertical velocity as a function of gas superficial velocity for different works in gas-solid counter-current contactors in the trickle flow regime. Data borrowed from Veneman (2015), with permission.

Table 7.6. Works in solids axial dispersion in gas-solid systems

Author	System	Operating conditions	Technique	Tracer	Results
Ambler et al. (1990)	CFB riser (ID = 141 mm, L = 10 m), abrupt exit Solids: sand (106 μm)	U_g = 4.5-7.1 m/s G_s = 124-305 kg/m^2/s	Perfect pulse injection in the riser bottom Detection (NaI scintillation detector) in riser-cyclone horizontal section	Radioactive bulk particles	Given as RTD curves
Bai et al. (1992)	CFB riser (ID = 141 mm, L = 10 m), abrupt exit Solids: silica gel (100 μm, 710 kg/m^3)	U_g = 2-10 m/s G_s = 10-100 kg/m^2/s	Perfect pulse injection in riser bottom Detection (chromatograph) in riser-cyclone horizontal section	"Solid tracer detected in gas phase"	Given as RTD curves
Smolders and Baeyens (2000)	CFB riser (ID = 100 mm, L = 6.5 m), abrupt exit Solids: sand (90 μm, 2650 kg/m^3)	U_g = 3-5 m/s G_s = 4-34 kg/m^2/s	Imperfect pulse injection in the riser bottom Detection (conductivity) in riser-cyclone horizontal section by dissolving samples in water	NaCl (150 μm, 2200 kg/m^3)	$Pe_{s,oo}$ = 5-20
Patience et al. (1991)	CFB riser (ID = 83 mm, L = 5 m), abrupt exit Solids: sand (108 μm, 275 μm and 513 μm, 2650 kg/m^3)	U_g = 4-6 m/s G_s = 25-166 kg/m^2/s	Imperfect pulse injection in the riser bottom Detection (NaI scintillation detector) 4.72 m upstream injection plane	Radioactive bulk particles	$Pe_{s,cc}$ = 10-14 for U_g = 4-6 m/s and G_s = 25-36 kg/m^2/s $Pe_{s,cc}$ = 4.5-9 for U_g = 4-6 m/s and G_s = 42-166 kg/m^2/s

Table 7.6 (cont.)

Author	System	Operating conditions	Technique	Tracer	Results
Harris et al. (2003)	CFB riser (square section, hydraulic ID = 140 mm, L = 5.8 m), smooth and abrupt exits Solids: phosphorescent pigment (25 μm, 4060 kg/m^3)	U_g = 1.3-4.6 m/s G_s = 1-26.9 kg/m^2/s	Perfect pulse (activation by light) at riser bottom Detection (photomultiplier tube) in riser-cyclone horizontal section	Lit bulk particles	$Pe_{s,cc}$ = 8-25 for U_g = 2.2-4 m/s and G_s = 2-27 kg/m^2/s $Pe_{s,cc}$ = 33-55 for U_g = 1.3 m/s and G_s = 2-14 kg/m^2/s
Wei and Zhu (1996)	CFB riser (ID = 140 mm, L = 15 m), abrupt exit Solids: blend of phosphorescent particles and alumina powder (54 μm, 1710 kg/m^3)	U_g = 2.6-8 m/s G_s = 8-80 kg/m^2/s	Perfect pulse (activation by light) 4 m above riser bottom Detection (photomultiplier tube) 5 m downstream injection plane	Lit bulk solid particles	$Pe_{s,oo}$ = 2-4 for U_g = 3-8 m/s and G_s = 40 kg/m^2/s
Godfroy et al. (1999)	CFB riser (ID = 82 mm, L = 7 m), smooth exit Solids: sand (150 μm, 2600 kg/m^3)	U_g = 4 m/s G_s = 23-75 kg/m^2/s	Radioactive Particle tracking (RPT) using multiple NaI scintillation detectors along 1 m riser section	Single radioactive particle (500 μm, 2600 kg/m^3)	$Pe_{s,cc}$ = 1.7-3 for U_g = 4 m/s and G_s = 23-75 kg/m^2/s

Table 7.6 (cont.)

Author	System	Operating conditions	Technique	Tracer	Results
Bhusarapu et al. (2004)	CFB riser (ID = 152 mm, L = 7.9 m), disengagement section as exit Solids: sand (150 μm, 2550 kg/m^3)	U_g = 3.2-4.5 m/s G_s = 27-37 kg/m^2/s	Particle detection using NaI scintillation detectors at riser bottom and top	Single radioactive particle (same properties as bulk)	$Pe_{s,oo}$ = 0.6 for U_g = 3.2 m/s and G_s = 26.6 kg/m^2/s $Pe_{s,oo}$ = 0.8 for U_g = 3.9 m/s and G_s = 33.7 kg/m^2/s
Chan et al. (2010)	CFB risers (ID = 46 mm, 90 mm and 160 mm), abrupt exit Solids: sand (120 μm, 2260 kg/m^3)	U_g = 1-10 m/s G_s = 5-622 kg/m^2/s	Positron emission particle tracking (PEPT) in 0.6 m riser section	Single radioactive particle (same properties as bulk)	Given as RTD curves
Roes and van Swaaij (1979a, 1979b)	Packed bed (dumped Pall rings 1.5×1.5 cm), ID = 75.5 mm, L = 1 m Solids: FCC catalyst (70 μm, 813 kg/m^3)	U_g = 0-0.16 m/s G_s = 0-6 kg/m^2/s	Perfect pulse injection above packing section Detection (reflectometer) below packing section	Inked bulk particles	$Bo_{g,oo}$ = 0.06-0.24 for U_g = 0-0.033 m/s and G_s = 1-5.83 kg/m^2/s

Table 7.6 (cont.)

Author	System	Operating conditions	Technique	Tracer	Results
Noordergraaf et al. (1980)	Zig-zag contactor (19 mm×40 mm×600 mm), 45° baffles, interval 40 mm) Solids: FCC catalyst (70 μm, 813 kg/m^3)	U_g = 0-0.2 m/s G_s = 0-21 kg/m^2/s	Perfect pulse injection above zig-zag section Detection (reflectometer) below zig-zag packing section	Inked bulk particles	$Bo_{s,cc}$ = 0.7-1.9 for U_g = 0-0.15 m/s and G_s = 6-20 kg/m^2/s
This work	CFB risers (ID = 26.5 mm, L = 1.5 m and ID = 51 mm, L = 2.5 m), smooth exit Solids: sand (152 μm, 2650 kg/m^3)	U_g = 2.6-6.2 m/s G_s = 16-97 kg/m^2/s	Positron emission particle tracking (PEPT) in 0.5 m riser section	Multiple (×5) radioactive particles	$Pe_{g,cc}$ = 0-149 m^2/s for U_g = 2.6-6.2 m/s and G_s = 0-97 kg/m^2/s
This work	Counter-current contactor (hydraulic ID = 142 mm, L = 0.65 m), 3×45° orifice trays Solids: sand (152 μm, 2650 kg/m^3)	U_g = 0-0.66 m/s G_s = 0-3.3 kg/m^2/s	Positron emission particle tracking (PEPT) in 0.73 m contactor section	Multiple (×5) radioactive particles	$Pe_{g,cc}$ = 1-38 m^2/s for U_g = 0-0.52 m/s and G_s = 3-3.3 kg/m^2/s

7.7 Conclusions

Positron emission particle tracking (PEPT) is a powerful technique for the dynamic study of flow systems, in which the position of a single radioactive solid particle is tracked in real-time in the 3-D space using gamma-ray detectors. PEPT was used in this work to obtain residence time and velocity distributions of the solid phase in different elements of the two CFB rigs studied, namely the risers, the counter-current adsorber and the regenerator.

The PEPT data generated in the CFB risers show a transition from dilute upflow to core-annulus (downflowing particles near the wall) regime when increasing solid flux and decreasing air velocity. Solids axial dispersion increases under the same conditions, as indicated by the increase in variance and tailness of the solids residence time distributions. Although not conclusively, the data suggest that the transition between dilute upflow and core-annulus occurs at lower values of solids flux and higher values of gas velocity in the riser with the larger diameter (benchmark CFB). These results are consistent with previous works in riser gas-solid fluid dynamics, indicating that PEPT is a reliable technique in the characterisation of solid flow.

Characterisation of the solids flow in the counter-current adsorber was achieved to an extent limited by problems with the PEPT camera (tracer trajectories were not recorded in the 3-D space but only on the plane containing the zig-zag pattern of the adsorber) and the presence of static electricity in the system. Two solids flow modes were identified: at low gas superficial velocity, particles tend to fall through the tray holes in a relative straight down trajectory. As the gas velocity is increased, the particles slide on the trays for longer distances, so the overall solids flow is in zig-zag. This could be quantified in form of residence time distributions. Unfortunately, the presence of electrostatics interfered on the shape of the RTDs, which presented much longer values of mean residence time, variance and tailness than what it could be attributed visually for the bulk flow. The “corrected” data applying a cut-off value of mean residence time suggest that solids dispersion is highest at the transition between the two solids flow modes described above. Despite the problems encountered (which are likely to be solved or at least minimised), PEPT has proven

to be able to provide a deep insight into the fluid dynamics of the counter-current adsorber both qualitatively and quantitatively. Overall results regarding axial dispersion of both phases and pressure drop are deemed promising enough to justify future work in the development of the proposed design, which PEPT could greatly accelerate by pinpointing the aspects to improve or focus on.

The visualization of individual particles trajectories in the regenerator revealed that solids flow lines and shape of the moving bed region resemble those of a discharging eccentric silo. Estimation of the extent of the moving bed into the regenerator cross section was possible from the solids average vertical velocity profiles and, for example, the data show that the moving bed penetrates a 35% of the regenerator inner diameter at half height of the solids bed. Solids axial dispersion in the regenerator (quantified by solids residence time distributions) was found to be high probably due to the strong “shearing” effect of the stagnant region on the moving bed. Both the existence of stagnant regions and high solids dispersion are detrimental for the actual carbon capture process since it would incur higher regenerator volumes, with the subsequent higher energy consumption.

8 Compartment models of CFB elements

Confident prediction of process performance using flow models requires that such models not only fit experimental residence time distribution data but also physically represent the system (Wen and Chung, 1965; Paris et al., 1971; Levenspiel, 1999; Fogler, 2006). The two flow models used here, namely the axially-dispersed plug flow (DPF) and the axially-dispersed plug flow with stagnant zone (DPFS), proved to be helpful for estimation of performance in idealised adsorbers (Chapter 3) and in the determination of gas RTDs using the imperfect pulse technique (Chapter 6). However, it is hardly justifiable that either model could, on its own, represent the complexity of the gas-solid flow in any of the CFB elements studied.

A more physically representative model of a flow system that also relate gas and solids RTDs can be obtained by division of such system in compartments in which an idealised flow pattern is assumed to take place (Wen and Chung, 1965; Levenspiel, 1999). Such compartment model is useful in qualitatively (by visualisation of the different compartments and their connections) and quantitatively (by determination of the values of the different parameters) relating residence time distributions of the different flowing phases, as well as in making predictions about process performance by estimating contact times (Raghuraman and Varma, 1974). In this chapter, suggestions are given on the compartmentalisation of the different CFB elements studied based on the results and findings in gas and solids residence time distributions obtained experimentally. The aim is to provide a starting point for future work in finding a holistic model for prediction of CFB performance as a TSA carbon capture process.

- *CFB risers:*

Radial inhomogeneities in CFB risers in the fast fluidisation regime are usually modelled as two compartments representing the dilute (bulk gas with single particles flowing at the terminal velocity) and the dense (solid aggregates, retaining gas in the interstitial volume) phases (Berruti et al., 1995; Bi, 2002; Grace et al., 2003). As discussed in Chapter 7, the typical approaches in the literature for the dense phase consider either an annulus of downflowing solids at the riser wall or clusters

distributed across the riser diameter (Berruti et al., 1995; Bi, 2002). More sophisticated models combine both approaches by taking into account radial variations of solids concentrations and aggregate vertical velocity (Bi, 2002). The different average vertical velocity of each phase and material exchange between them are responsible of skewed and/or bimodal RTDs of both gas and solids.

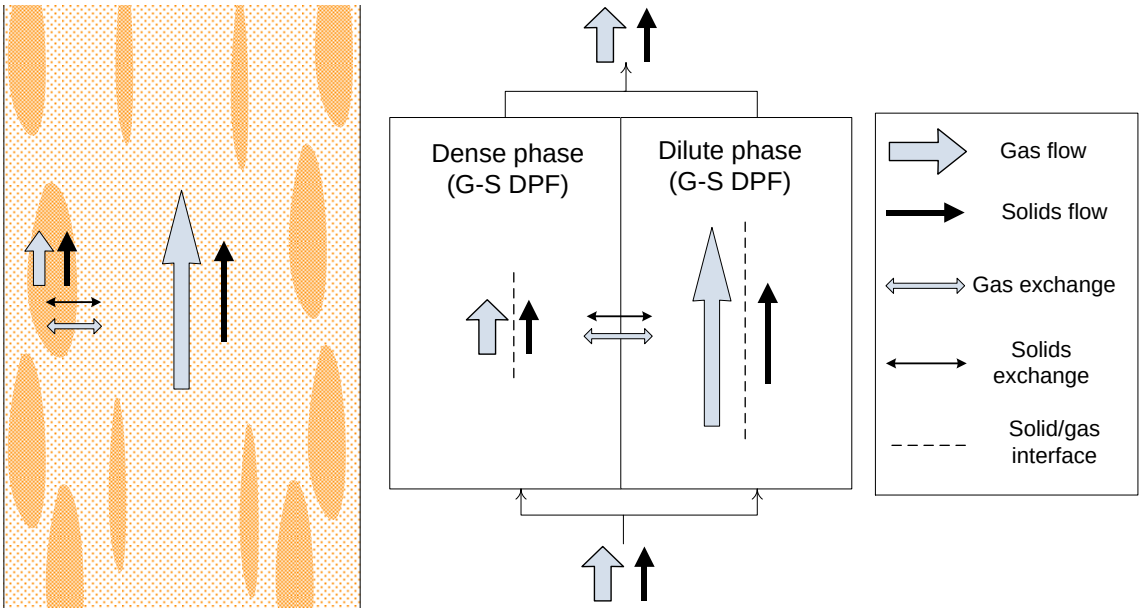

Figure 8.1. Compartment model suggested for the CFB risers (drawing on the left-hand side adapted from Bi, 2002)

- *Novel CFB adsorber:*

RTD experiments in the counter-current adsorber revealed that two distinctive flow regimes exist depending on the gas velocity. At low gas velocities, solids tend to flow through the holes of the inclined trays. Whereas this does not seem to cause high solids axial dispersion, axial dispersion of the gas phase was found to be high especially at high solids flow rates. On the other hand, high gas velocities cause the particles to zig-zag in the adsorber as they stay longer on the tray surface. In the latter case the adsorber shows a resemblance to a multi-stage fluidised bed with downcomers, and the gas dispersion due to gas-solid interaction is low.

The above gas-solid behaviour could be modelled at the individual adsorber tray level as illustrated in Figure 8.2. The stream of solids falling onto the tray is divided in two, one flowing through the holes and the other flowing in zig-zag. This can be

quantified by PEPT in function of the operating conditions. The stream of particles falling through the holes flow in dense trickles that drag a portion of gas downwards, until the trickle breaks into a more dilute downflow of solids and the gas is redirected upwards. This creates gas recirculation (Roes and van Swaaij, 1979b; Noordergraaf et al., 1980; Westerterp and Kuczynski; 1987a). When the flow regime is zig-zag, the gas-solid contact is in cross-flow, which has been modelled previously in units like multi-stage fluidised beds (Raghuraman and Varma, 1973, 1974), dryers (Qi and Krishnan, 1996) and distillation columns (Müller and Segura, 2000).

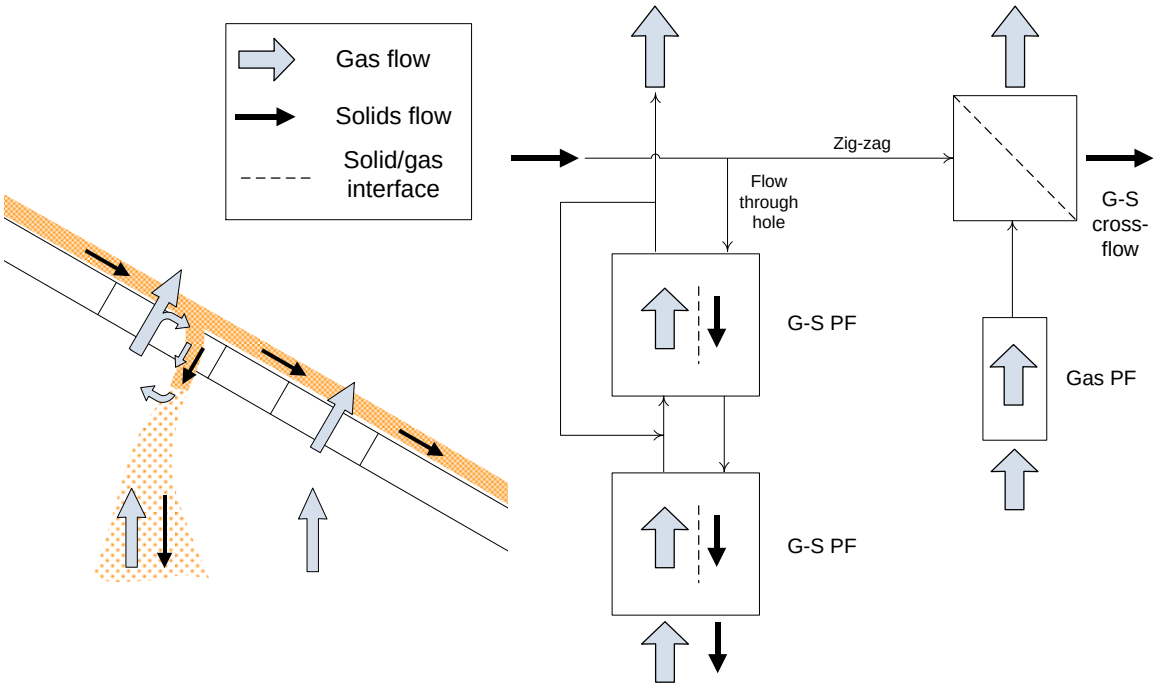

Figure 8.2. Compartment model suggested for an inclined plate of the novel CFB adsorber

- *Regenerator:*

The flow regime in the CFB regenerator is characterized by the co-existence of a moving bed and a stagnant region. PEPT experiments showed that the solids residence time is wide and skewed, which was attributed to the "shearing effect" of the stagnant region on the moving bed. This could be modelled using the scheme in Figure 8.3. The moving bed is divided in (at least) two parallel compartments to account for the radial variation in particle vertical velocity causing high solids axial

dispersion and RTD skewness. On the other hand, distribution of the gas phase across the different regions causes a similar effect on the gas RTD.

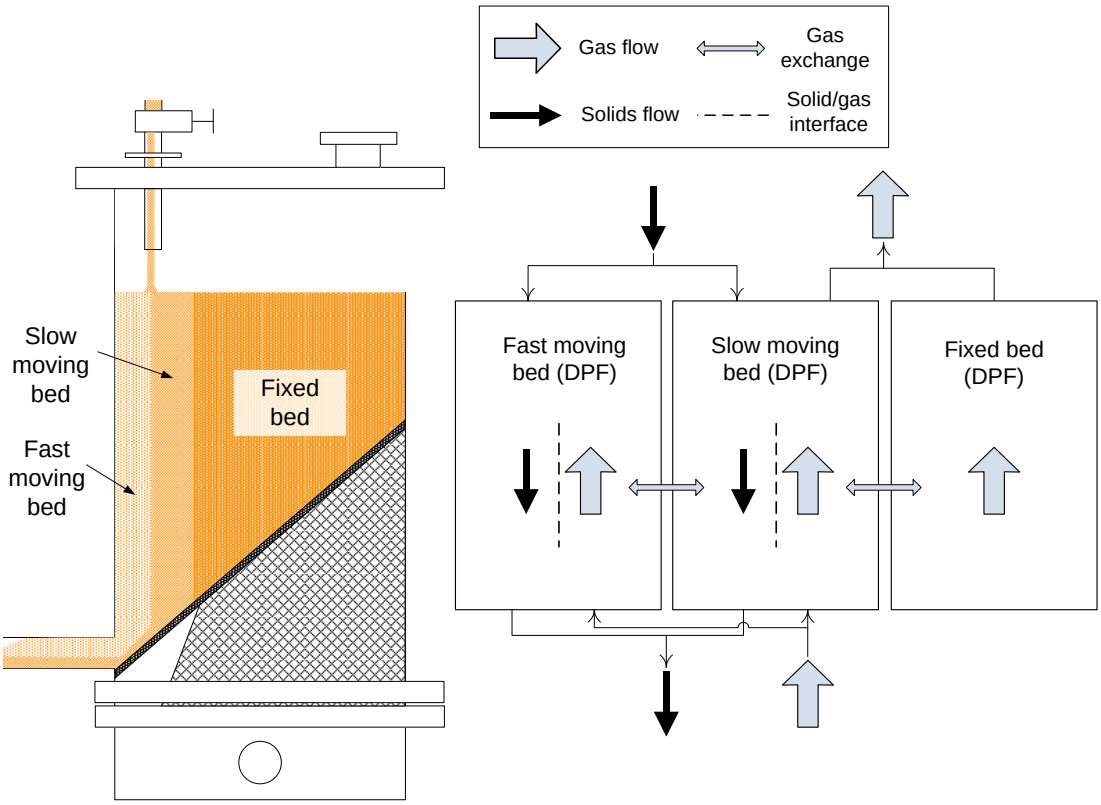

Figure 8.3. Compartment model suggested for the solids bed in the CFB regenerator

9 Conclusions, recommendations and future work

- *Overall conclusions:*

A methodology for the thermodynamic-kinetic evaluation of circulating systems as TSA carbon capture processes is developed and used in the assessment of a novel CFB configuration against a benchmark (co-current riser). The novel CFB features a counter-current adsorber, a counter-current regenerator and a riser, the latter element playing a double role of solids conveyer and co-current adsorber. The advantages sought by using a counter-current adsorber are not only the more efficient gas-solid contact mode with respect co-current, but also a low pressure drop derived from operation at lower gas velocities and hydrostatic head partially supported on the contactor internals.

As a first step, the adsorption equilibrium of the sorbent material and flue gas characteristics are used to determine the minimum solids circulation rate that a particular circulation system would require for a desired separation (CO_2 recovery). Knowledge of the minimum solids circulation rate is sufficient to realise the superior performance of counter-current configurations compared to co-current (or well-mixed) units. The latter systems, due to adsorption equilibrium limitations, incur high energy demands in the regeneration step as they require either high solids circulation rates (with the consequent high sensible heat duty needed to perform the temperature swing) or sorbents with high adsorption capacity at very low CO_2 partial pressure (high desorption energy required) (Berger and Bhown, 2011). Therefore, research efforts in TSA carbon capture using such systems are only justified in the context of sorbent development.

A more quantitative insight into the CFB configurations studied was obtained via a sensitivity analysis using a simplified 1-D adsorber model. In the approach followed here, data from cold model CFB rigs were fed into the model to come up with a limited number of study cases that show the impact of key characteristics (operating conditions, equipment dimensions and fluid dynamics) on system performance. The results reveal that the proposed novel CFB configuration can be (using the characteristics of the cold model rigs as the base case) three times smaller in size and

require solids circulation rates 3-4 times lower than the benchmark at 90% CO_2 recovery. However, proper design of the counter-current adsorber is required since axial dispersion of both gas and solids can have a significant negative impact on CO_2 recovery. The adsorption performance of the novel CFB riser, on the other hand, is virtually insensitive to axial dispersion of either gas or solid phases.

Experimental study of cold models in parallel to theoretical assessment is justified from two standpoints: first, experimental data on system operation, dimensions and fluid dynamics can be fed into the mathematical model and by doing so providing a more realistic picture of the possibilities and limitations of the studied systems. For instance, solids concentration (ε_s) and solids vertical velocity (u_s) are two important variables that directly impact performance as they are related to solids residence time and surface available for mass transfer. The values of ε_s and u_s depend on operating conditions and system geometry and therefore are not to be used as free parameters. On the other hand, correlations to estimate the values of ε_s and u_s in the literature are highly system specific and generally only recommended for preliminary studies (Berruti et al., 1995). Second, the magnitude of other factors that are not readily predictable but might affect process performance can be estimated. For example, the operating window of the risers in both CFB configurations are narrowed by instabilities in the solids flow rate (novel CFB) and blockage of the horizontal section (benchmark CFB). In the case of the novel CFB, increasing the solids flow rate requires that a larger fraction of the flue gas stream needs to be diverted to the riser in order to keep operating conditions within the operating window. This is detrimental for process performance since less flue gas is fed to the more efficient counter-current adsorber. Pressure drop is another important variable to quantify experimentally in the systems studied since, for instance, a low value in the counter-current adsorber is sought as a main advantage of using such contactor. The results show low values of pressure drop in the novel CFB adsorber, around 25-30% of the hydrostatic head.

The effect of axial dispersion of both phases on CO_2 recovery is estimated assuming axially-dispersed plug flow in the adsorber model. As commented previously, the performance of the counter-current adsorber is found to be very sensitive to axial

dispersion; given the potential benefits of using such a contactor, a justification exists to 1) find out the amount of axial dispersion in the actual system geometry, and 2) understand the underlying phenomena in order to minimise it.

Axial gas dispersion in cold model CFB elements was quantified from residence time distributions obtained using the imperfect tracer pulse technique. Both CFB risers showed an increase in gas axial dispersion with increasing solids flux and decreasing gas velocity. This is in overall agreement with previous works in riser fluid dynamics, and is attributed to the formation of solid aggregates that flow at lower vertical velocities than the single particle and "hold back" part of the flowing gas by retaining it in the interstitial volume. Results for the counter-current adsorber showed that axial gas dispersion is highest when gas velocity through the inclined tray holes is lower than the terminal velocity of the particles; particles falling through the holes in form of dense trickles drag down the upflowing gas, in a similar mechanism to that in the risers. As the gas velocity is increased, fall of particles through the holes is hindered and gas axial dispersion due to gas-solid contact is reduced. As for the regenerator, gas dispersion in the system seemed to increase with gas velocity but to be insensitive to the solids flow rate. In all CFB elements studied, system geometry contributed considerably to overall gas dispersion: in the risers and the counter-current adsorber this contribution is at least of the same magnitude than that coming from gas-solid interaction. In case of the regenerator, the bed of solids occupies just 15% of the total gas volume and therefore results of axial dispersion are heavily masked by the rest of the system volume (mainly the windbox and the freeboard). Further uncertainty in gas RTD results was introduced by performing CO_2 pulse detection in a single location, alternating inlet and outlet, and combining results. The lack of perfect synchronisation between experiment time zero and manual pulse injection introduced an absolute error in the values of tracer mean residence time of at least 0.2 s, which was shown to influence heavily the shape of the normalized residence time curve (and consequently the values of the second moment) for experiments with very short residence time, i.e. highest air flow rates in risers and counter-current adsorber.

Solids residence time distributions experiments were carried out using positron emission particle tracking (PEPT). PEPT is a powerful technique that allowed the "visualization" and quantification of the solids flow pattern in CFB risers, counter-current adsorber and regenerator. An increasing magnitude of solids downflow near the riser wall was identified when solids flux was increased and gas velocity decreased, while solids RTD increases in variance and skewness, showing an incipient second peak. These results are consistent with previous works in gas-solid riser fluid dynamics and support the idea of formation of solid aggregates that was suggested from the gas RTDs. Application of PEPT in the regenerator revealed that solid particles flow in overall convergent trajectories towards the solids outlet resembling a discharging eccentric silo. The extent of the moving bed region into the regenerator cross section was estimated from the radial profile of particle vertical velocity: at half the height of the solids bed, the moving bed penetrates 35% of the regenerator inner diameter at the conditions studied. Solids RTD were found to be heavily skewed, evidencing the strong "shearing" effect of the stagnant region on the moving bed.

The PEPT technique was considered to be reliable in the characterisation of the counter-current adsorber as it was successfully applied in other CFB elements. However, in this case PEPT data were obtained only in the plane containing the zig-zag pattern of the adsorber rather than in 3D due to problems with the PEPT camera. The individual tracer trajectories showed that two solids flow modes were present: at low gas velocities, particles flow in a relatively straight down trajectory through the holes of the inclined trays. When gas velocity is increased, the particles tend to stay on the tray surface for longer distances/time, until most of the solid particles flow in zig-zag. Quantification of the solids RTD and particle velocity at different zones within the adsorber revealed that the tracer particle would get stuck or flow very slowly, skewing the RTD. This was associated to the accumulation of static electricity in the system that from visual observations did not seem to affect the bulk solids flow. An attempt to subtract the effect of static electricity from the RTDs was made by applying a "cut-off" value of mean residence time. After "correction", the data suggest that solids dispersion is highest at the transition between the two solids flow modes just described. Overall results regarding axial dispersion of both phases

and pressure drop are deemed promising enough to justify future work in the development of the proposed design, which PEPT could greatly accelerate by pinpointing the aspects to improve.

In view of the findings above, it can be concluded that the novel CFB configuration shows the potential to become an efficient system for TSA carbon capture that stem from the features of the counter-current adsorber: 1) counter-current gas-solid contact; 2) low pressure drop; 3) low axial dispersion (provided gas velocity is kept above a minimum).

- *Recommendations:*

Suggestions for improving the quality of the experimental work carried out in this study are the following:

- Redesign the solids feeding system of the CFB rigs so it is not coupled with operation of the regenerator. In the current design, investigation of solids fluidisation in the regenerator to simulate the desorbed CO_2 (see for example Christensen et al., 2008) is not possible as it interacts with control of the solids flow rate. Independent control of the solids circulation rate can be achieved by, for example, installing a loop seal (Basu, 2006) between regenerator and riser. This might also eliminate the instabilities in solids flow rate encountered in the novel CFB and widen its operational window.

- Redesign the riser top in the benchmark CFB to prevent blockage of the horizontal section. A riser-cyclone connection with an angle higher than the angle of repose of the solids could be used (Chalermsinsuwan et al. 2014; Bai et al., 1995), or an impingement system like the one used in the novel CFB (see also Kim et al., 2004).

- Increase the length of the risers and the counter-current adsorber to increase the residence time, so RTD (in particular for the gas phase) and pressure drop data can be obtained with higher accuracy and be more representative of the flow patterns of interest by minimising the impact of inlet and outlet effects. CFB risers in lab/bench-scale studies are usually longer (between 2 m and 13 m) than the ones

used here, even when lower gas velocities are used (see Table 6.5, Table 7.6 and the work of Xiao et al., 2012).

- Redesign the regenerator to eliminate the stagnant section in the bed of solids and narrow the solids RTD. A simple solution is to increase the aspect ratio. If regenerator and solids feeding system are decoupled (as recommended above), the design of the regenerator can be varied completely, becoming a separate subject of study. The quality of gas RTD data for the current regenerator geometry would greatly improve if the contribution of the different regenerator sub-elements to the overall RTD was known. The contribution of the bed of solids can be determined by removing the regenerator modules forming the freeboard. As for the windbox, it could be bypassed since it lost its function after installation of the inclined gas distributor.

- Redesign the counter-current adsorber to minimise the solids static holdup, which could be beneficial in decreasing solids axial dispersion and mitigate the effects of static electricity accumulation. This concerns especially the inclined orifice trays and the adsorber bottom. A slot could be opened at the lower edge of the trays to allow particles to fall rather than accumulate in pockets. The adsorber bottom should be redesigned to resemble a conical hopper with high-angle walls.

- *Future work:*

It has been suggested in this work (see Sections 6.5.5 and 7.6.4) that the residence time distributions obtained experimentally can be used for prediction of process performance by feeding the corresponding Péclet number into the adsorber model developed in Chapter 3. This is a greatly simplified approach since it not only reduces the complexity of the RTD shape to a single numerical value, but also assumes the validity of the axially-dispersed plug flow in the studied CFB elements. A more rigorous approach should use models (see Chapter 8) that not only can replicate the shape of the RTD curves but also reflect the physical phenomena. As originally proposed in the FOCUS project (see Section 1.4), CFD models should be constructed to validate the RTD data and get insight into the behaviour of the systems with conditions closer to the real carbon capture process.

Further investigation into the operating characteristics of the novel CFB configuration is recommended. If the design modifications proposed above are made, it is possible to reduce the fraction of flue gas fed to the riser, with the consequent increase in performance. Attention should then be paid to the possible flow regime transition from fast fluidisation to slug flow.

An interesting line of future work could be the application of the PEPT technique to the regenerator in real conditions for carbon capture, i.e. 100-120°C with real CO_2 sorbents. Yang and Hoffman (2009) postulated that "self-fluidisation" due to homogeneous release of CO_2 could bring benefits of improved heat transfer between particles and embedded heat exchange surfaces. Such regime could be identified and characterized with PEPT.

The next suggested steps in the development of the counter-current adsorber are: 1) exploration of alternative designs or variations of the inclined orifice trays to widen the operating window and reduce axial dispersion, and 2) mass and heat transfer experiments with actual CO_2 sorbent materials. CFD models could be useful in the design of such experiments and suggest improved geometries.

References

Abanades, J.C., B. Arias, A. Lyngfelt, T. Mattisson, D.E. Wiley, H. Li, M.T. Ho, E. Mangano and S. Brandani, 2015. Emerging CO_2 capture systems. International Journal of Greenhouse Gas Control 40 126-166

Abu-Zahra, M.R.M., L.H.J. Schneiders, J.P.M. Niederer, P.H.M. Feron and G.F. Versteeg, 2007. CO2 capture from power plants: Part I. A parametric study of the technical performance based on monoethanolamine. International Journal of Greenhouse Gas Control 1(1) 37-46

ADA, 2011. Evaluation of solid sorbents as a retrofit technology for CO_2 capture from coal-fired power plants. Final technical report. DOE NETL website. Accessed August 2016. https://www.netl.doe.gov/File%20Library/Research/Coal/ewr/co2/evaluation-of-solid-sorbents-nov2011.pdf

Ahn, H., M. Luberti, Z. Liu and S. Brandani, 2013. Process configurations studies on the amine capture process for coal-fired power plants. International Journal of Greenhouse Gas Control 16 29-40

Ambler, P.A., B.J. Milne, F. Berruti and D.S. Scott, 1990. Residence time distribution of solids in a circulating fluidized bed: Experimental and modelling studies. Chemical Engineering Science 45(8) 2179-2186

Bafrnec, M. and J. Beňa, 1972. Quantitative data on the lowering of electrostatic charge in a fluidized bed. Chemical Engineering Science 27(5) 1177-1181

Bai, D., E. Shibuya, Y. Masuda, K. Nishio, N. Nakagawa and K. Kato, 1995. Distinction between upward and downward flows in circulating fluidized beds. Powder Technology 84(1) 75-81

Bai, D., J. Yi, Y. Jin and Z. Yu, 1992. Residence time distributions of gas and solids in a circulating fluidized bed, in *Fluidization VII*, O.E. Potter and D.J. Nicklin (Ed.). Engineering Foundation, New York, pp. 195-202

Baron, T., C.L. Briens, P. Galtier and M.A. Bergougnou, 1992. A new technique for the measurement of the residence time distribution of an inert gas tracer in gas-solid fluidized beds, in *Fluidization VII*, O.E. Potter and D.J. Nicklin (Ed.). Engineering Foundation, New York, pp. 731-739

Basu, P. Combustion and Gasification in Fluidized Beds. Taylor & Francis, 2006

Beck, J., D. Friedrich, S. Brandani and E.S. Fraga, 2015. Multi-objective optimisation using surrogate models for the design of VPSA systems. Computers & Chemical Engineering 82 318-329

Berger, A.H. and A.S. Bhown, 2011. Comparing physisorption and chemisorption solid sorbents for use separating CO_2 from flue gas using temperature swing

adsorption. Energy Procedia 4 562-567

Berruti, F. and N. Kalogerakis, 1989. Modelling the internal flow structure of circulating fluidized beds. The Canadian Journal of Chemical Engineering 67(6) 1010-1014

Berruti, F., T.S. Pugsley, L. Godfroy, J. Chaouki and G.S. Patience, 1995. Hydrodynamics of circulating fluidized bed risers: A review. The Canadian Journal of Chemical Engineering 73(5) 579-602

Bhusarapu, S., M. Al-Dahhan and M.P. Dudukovic, 2004. Quantification of solids flow in a gas–solid riser: single radioactive particle tracking. Chemical Engineering Science 59(22–23) 5381-5386

Bi, H.T., J.R. Grace and J.X. Zhu, 1993. Types of choking in vertical pneumatic systems. International Journal of Multiphase Flow 19(6) 1077-1092

Bird, R.B., W.E. Steward and E.N. Lightfoot. Transport phenomena. John Wiley & Sons, 1960

Bischoff, K.B. and O. Levenspiel, 1962. Fluid dispersion-generalization and comparison of mathematical models – I generalization of models. Chemical Engineering Science 17(4) 245-255

Bischoff, K.B., 1963. The general use of imperfect pulse inputs to find characteristics of flow systems. The Canadian Journal of Chemical Engineering 41(3) 129-129

Boot-Handford, M.E., J.C. Abanades, E.J. Anthony, M.J. Blunt, S. Brandani, N. Mac Dowell, J.R. Fernandez, M.-C. Ferrari, R. Gross, J.P. Hallett, R.S. Haszeldine, P. Heptonstall, A. Lyngfelt, Z. Makuch, E. Mangano, R.T.J. Porter, M. Pourkashanian, G.T. Rochelle, N. Shah, J.G. Yao and P.S. Fennell, 2014. Carbon capture and storage update. Energy & Environmental Science 7(1) 130-189

Boucher, D., Z. Deng, T.W. Leadbeater, R. Langlois and K.E. Waters, 2016. Speed analysis of quartz and hematite particles in a spiral concentrator by PEPT. Minerals Engineering 91 86-91

Brandani, S. and K. Zhang, 2006. A new model for the prediction of the behaviour of fluidized beds. Powder Technology 163(1–2) 80-87

Brereton, C.M.H., J.R. Grace and J. Yu, 1988. Axial gas mixing in a circulating fluidised bed, in *Circulating Fluidized Bed Technology II*, P. Basu and J.F. Large (Ed.). Pergamon Press, pp. 307-314

Buffham, B.A. and G. Mason, 1993. Holdup and dispersion: tracer residence times, moments and inventory measurements. Chemical Engineering Science 48(23) 3879-3887

CCC, 2015. Power sector scenarios for the fifth carbon budget. Accessed December

2016

https://documents.theccc.org.uk/wp-content/uploads/2015/10/Power-sector-scenarios-for-the-fifth-carbon-budget.pdf

CCC, 2016a. Letter to Rt Hon Amber Rudd: A strategic approach to Carbon Capture and Storage. Accessed December 2016 https://www.theccc.org.uk/wp-content/uploads/2016/07/Letter-to-Rt-Hon-Amber-Rudd-CCS.pdf

CCC, 2016b. UK climate action following the Paris Agreement. Accessed December 2016 https://www.theccc.org.uk/wp-content/uploads/2016/10/UK-climate-action-following-the-Paris-Agreement-Committee-on-Climate-Change-October-2016.pdf

Chalermsinsuwan, B., T. Thummakul, D. Gidaspow and P. Piumsomboon, 2014. Characterization of fluidization regime in circulating fluidized bed reactor with high solid particle concentration using computational fluid dynamics. Korean Journal of Chemical Engineering 31(2) 350-363

Chan Seem, T., N.A. Rowson, I. Gabbott, M. de Matas, G.K. Reynolds and A. Ingram, 2016. Asymmetric distribution in twin screw granulation. European Journal of Pharmaceutics and Biopharmaceutics 106 50-58

Chan, C.W., A. Brems, S. Mahmoudi, J. Baeyens, J. Seville, D. Parker, T. Leadbeater and J. Gargiuli, 2010a. PEPT study of particle motion for different riser exit geometries. Particuology 8(6) 623-630

Chan, C.W., J. Seville, X. Fan and J. Baeyens, 2009b. Solid particle motion in a standpipe as observed by Positron Emission Particle Tracking. Powder Technology 194(1–2) 58-66

Chan, C.W., J. Seville, X. Fan and J. Baeyens, 2009c. Particle motion in L-valve as observed by positron emission particle tracking. Powder Technology 193(2) 137-149

Chan, C.W., J. Seville, Z. Yang and J. Baeyens, 2009a. Particle motion in the CFB riser with special emphasis on PEPT-imaging of the bottom section. Powder Technology 196(3) 318-325

Chan, C.W., J.P.K. Seville, D.J. Parker and J. Baeyens, 2010b. Particle velocities and their residence time distribution in the riser of a CFB. Powder Technology 203(2) 187-197

Chan, C.W., J.P.K. Seville, X. Fan and J. Baeyens, 2009d. Particle Motion in CFB Cyclones as Observed By Positron Emission Particle Tracking. Industrial & Engineering Chemistry Research 48(1) 253-261

Chang, H. and M. Louge, 1992. Fluid dynamic similarity of circulating fluidized beds. Powder Technology 70(3) 259-270

Christensen, D., J. Nijenhuis, J.R. van Ommen and M.O. Coppens, 2008. Influence of distributed secondary gas injection on the performance of a bubbling fluidized-bed

reactor. Industrial & Engineering Chemistry Research 47(10) 3601-3618

Claus, G., F. Vergnes and P.L. Goff, 1976. Hydrodynamic study of gas and solid flow through a screen-packing. The Canadian Journal of Chemical Engineering 54(3) 143-147

Contractor, R., R.J. Dry, C. White, Q.M. Mao, S. Konstantinidis and O.E. Potter, 2000. Circulating fluidized beds – diameter, solids hold-up, axial gas-mixing, and contact efficiency. Powder Technology 111(1–2) 132-144

Danckwerts, P.V., 1953. Continuous flow systems: Distribution of residence times. Chemical Engineering Science 2(1) 1-13

Dang, W., D. Friedrich and S. Brandani, 2013. Characterisation of an Automated Dual Piston Pressure Swing Adsorption (DP-PSA) System. Energy Procedia 37(57-64

Ding, Y., Z. Wang, D. Wen, M. Ghadiri, X. Fan and D. Parker, 2005. Solids behaviour in a gas–solid two-phase mixture flowing through a packed particle bed. Chemical Engineering Science 60(19) 5231-5239

DOE NETL, 2015. Cost and Performance Baseline for Fossil Energy Plants. Volume 1a: Bituminous Coal (PC) and Natural Gas to Electricity. Revision 3. Accessed October 2016 from the US Department of Energy National Energy Technology Laboratory's website (www.netl.doe.gov)

DOE NETL, 2016. Evaluation of Solid Sorbents as a Retrofit Technology for CO_2 Capture. Project closeout meeting presentation. Accessed December 2016. https://www.netl.doe.gov/File%20Library/Research/Coal/carbon%20capture/post-combustion/7013-Closeout-Final-0004343.pdf

Dry, R.J. and C.C. White, 1989. Gas residence-time characteristics in a high-velocity circulating fluidised bed of FCC catalyst. Powder Technology 58(1) 17-23

EDGAR, 2013. Emissions Database for Global Atmospheric Research. European Commission. Accessed December 2016. http://edgar.jrc.ec.europa.eu/overview.php?v=CO2ts1990-2015&sort=des9

ETI, 2015. Building the UK carbon capture and storage sector by 2030 – Scenarios and actions. An insights report by the Energy Technologies Institute. Accessed December 2016 from ETI's website (www.eti.co.uk)

ETI, 2016. Reducing the cost of CCS – Developments in Capture Plant technology. An insights report by the Energy Technologies Institute. Accessed December 2016 from ETI's website (www.eti.co.uk)

Fan, X., 2011. FOCUS – Fundamentals of Optimised Capture Using Solids. Presented at the UKCCS Community Network Meeting, 5th–6th April. Accessed May 2011. http://www.geos.ed.ac.uk/ccs/Meetings/cornwall-april2011/XFan.pdf

Fogler, H.S. Elements of Chemical Reaction Engineering. Fourth Edition. Prentice Hall, 2006

Friedrich, D., M.-C. Ferrari and S. Brandani, 2013. Efficient Simulation and Acceleration of Convergence for a Dual Piston Pressure Swing Adsorption System. Industrial & Engineering Chemistry Research 52(26) 8897-8905

García-Triñanes, P., J. Seville, B. Boissière, R. Ansart, T. Leadbeater and D. Parker, 2016. Hydrodynamics and particle motion in upward flowing dense particle suspensions: Application in solar receivers. Chemical Engineering Science 146 346-356

Geldart, D., 1973. Types of gas fluidization. Powder Technology 7(5) 285-292

Glass, D.H., D. Mignard and J. Skilling, 2009. Gas distribution and particle mobility in a model fluid-bed polymer recycling reactor. Powder Technology 189(3) 481-496

Glicksman, L.R., M. Hyre and K. Woloshun, 1993. Simplified scaling relationships for fluidized beds. Powder Technology 77(2) 177-199

Global CCS Institute, 2016a. The Global Status of CCS. Summary Report. Accessed November 2016.
http://hub.globalccsinstitute.com/sites/default/files/publications/201158/global-status-ccs-2016-summary-report.pdf

Global CCS Institute, 2016b. Boundary Dam Carbon Capture and Storage Project. Accessed November 2016.
https://www.globalccsinstitute.com/projects/boundary-dam-carbon-capture-and-storage-project

Global CCS Institute, 2016c. Introduction to Industrial Carbon Capture and Storage. Accessed July 2017.
http://hub.globalccsinstitute.com/sites/default/files/publications/199858/Introduction%20to%20Industrial%20CCS.pdf

Godfroy, L., J. Chaouki and F. Larachi, 1999. Position and velocity of a large particle in a gas/solid riser using the radioactive particle tracking technique. The Canadian Journal of Chemical Engineering 77(2) 253-261

Govender, I., N. Mangesana, A.N. Mainza and J.P. Franzidis, 2011. Measurement of shear rates in a laboratory tumbling mill. Minerals Engineering 24(3–4) 225-229

Grace, J.R., H. Bi and M. Golriz, 2003. Circulating Fluidized Beds, in *Handbook of Fluidization and Fluid-Particle Systems*, W.-C. Yang (Ed.). Marcel Dekker

Guo, Z.C. and M. Tokuda, 2002. Flow Behavior in Z-Path Fluidized-Moving Bed with Inclined Perforated Plate. Journal of Iron and Steel Research: International 9(1) 19-24

Hagyard, T. and A.M. Sacerdote, 1966. Viscosity of Suspensions of Gas-Fluidized

Spheres. Industrial & Engineering Chemistry Fundamentals 5(4) 500-508

Harris, A.T. PhD thesis. University of Cambridge, 2002

Harris, A.T., J.F. Davidson and R.B. Thorpe, 2003. Particle residence time distributions in circulating fluidised beds. Chemical Engineering Science 58(11) 2181-2202

Hornbostel, M., 2015. Pilot-Scale Evaluation of an Advanced Carbon Sorbent-Based Process for Post-Combustion Carbon Capture. Presented at the NETL CO_2 Capture Technology Meeting, Pittsburgh, PA, June 23–26. Accessed February 2016. https://www.netl.doe.gov/File%20Library/Events/2015/co2captureproceedings/M-Hornbostel-SRI-Pilot-Advanced-Sorbent-Process.pdf

Hu, X., S. Brandani, A.I. Benin and R.R. Willis, 2015. Development of a Semiautomated Zero Length Column Technique for Carbon Capture Applications: Rapid Capacity Ranking of Novel Adsorbents. Industrial & Engineering Chemistry Research 54(26) 6772-6780

IEA, 2015a. Energy and Climate Change. World Energy Outlook Special Briefing for COP21. Accessed December 2016. https://www.iea.org/media/news/WEO_INDC_Paper_Final_WEB.PDF

IEA, 2015b. CO_2 emissions from fuel combustion highlights. Accessed December 2016 https://www.iea.org/publications/freepublications/publication/CO2EmissionsFromFuelCombustionHighlights2015.pdf

IEA, 2016. Energy Technology Perspectives. Executive Summary. Accessed October 2016. http://www.iea.org/publications/freepublications/publication/EnergyTechnologyPerspectives2016_ExecutiveSummary_EnglishVersion.pdf

IEAGHG, 2001. Putting Carbon Back into the Ground. Accessed November 2016. http://www.ieaghg.org/docs/general_publications/putcback.pdf

Ilankoon, I.M.S.K., K.E. Cole and S.J. Neethling, 2013. Measuring hydrodynamic dispersion coefficients in unsaturated packed beds: Comparison of PEPT with conventional tracer tests. Chemical Engineering Science 89 152-157

Ingram, A., M.N. Hausard, X. Fan, D.J. Parker, J.P.K. Seville, N. Finn and M. Evans, 2007. Portable Positron Emission Particle Tracking (PEPT) for Industrial Use, in *Fluidization XII*, Engineering Conferences International

IPCC, 2005. Special Report on Carbon Dioxide Capture and Storage. Accessed October 2012. https://www.ipcc.ch/pdf/special-reports/srccs/srccs_wholereport.pdf

IPCC, 2013. Climate Change 2013: The Physical Science Basis. Contribution of Working Group I to the Fifth Assessment Report of the Intergovernmental Panel on

Climate. Summary for Policymakers. Accessed December 2016.

http://www.climatechange2013.org/images/report/WG1AR5_SPM_FINAL.pdf

Jagota, A.K., E. Rhodes and D.S. Scott, 1973. Measurement of residence times, and film and drop velocities in two phase annular flow. The Canadian Journal of Chemical Engineering 51(4) 393-400

Jansen, D., M. Gazzani, G. Manzolini, E.v. Dijk and M. Carbo, 2015. Pre-combustion CO2 capture. International Journal of Greenhouse Gas Control 40 167-187

Jayasundara, C.T., R.Y. Yang, B.Y. Guo, A.B. Yu, I. Govender, A. Mainza, A.V.D. Westhuizen and J. Rubenstein, 2011. CFD–DEM modelling of particle flow in IsaMills – Comparison between simulations and PEPT measurements. Minerals Engineering 24(3–4) 181-187

Kannan, C.S., S.S. Rao and Y.B.G. Varma, 1994. A study of stable range of operation in multistage fluidised beds. Powder Technology 78(3) 203-211

Kiel, J.H.A., W. Prins and W.P.M. van Swaaij, 1993. Mass transfer between gas and particles in a gas–solid trickle flow reactor. Chemical Engineering Science 48(1) 117-125

Kim, S.W., G. Kirbas, H. Bi, C. Jim Lim and J.R. Grace, 2004. Flow behavior and regime transition in a high-density circulating fluidized bed riser. Chemical Engineering Science 59(18) 3955-3963

Klinzing, J.E, 2003. Electrostatics in Pneumatic Conveying, in *Handbook of Fluidization and Fluid-Particle Systems*, W.-C. Yang (Ed.). Marcel Dekker

Knowlton, T.M. and I. Hirsan, 1978. L-valves characterized for solids flow. Hydrocarbon Processing 57(3) 149-156

Krutka, H., S. Sjostrom, T. Starns, M. Dillon and R. Silverman, 2013. Post-Combustion CO_2 Capture Using Solid Sorbents: 1 MWe Pilot Evaluation. Energy Procedia 37 73-88

Kunii, D. and O. Levenspiel. Fluidization Engineering. Second Edition. Butterworth-Heinemann, 1991

Large, J.F., M. Naud, P. Guigon and M.A. Bergougnou, 1981. Hydrodynamics of the raining packed-bed gas-solids heat exchanger. The Chemical Engineering Journal 22(2) 95-100

Laurent, B.F.C. and P.W. Cleary, 2012. Comparative study by PEPT and DEM for flow and mixing in a ploughshare mixer. Powder Technology 228 171-186

Leadbeater, T.W. and D.J. Parker, 2011. A modular positron camera for the study of industrial processes. Nuclear Instruments and Methods in Physics Research Section

A: Accelerators, Spectrometers, Detectors and Associated Equipment 652(1) 646-649

Leadbeater, T.W., D.J. Parker and J. Gargiuli, 2011. Characterization of the latest Birmingham modular positron camera. Measurement Science and Technology 22

Leadbeater, T.W., D.J. Parker and J. Gargiuli, 2012. Positron imaging systems for studying particulate, granular and multiphase flows. Particuology 10(2) 146-153

Levenspiel, O. and W.K. Smith, 1957. Notes on the diffusion-type model for the longitudinal mixing of fluids in flow. Chemical Engineering Science 6(4–5) 227-235

Levenspiel, O. Chemical Reactor Engineering. Third Edition. John Wiley & Sons, 1999

Levenspiel, O., 1962. Mixed models to represent flow of fluids through vessels. The Canadian Journal of Chemical Engineering 40(4) 135-138

Li, L., A. Rasmuson, A. Ingram, M. Johansson, J. Remmelgas, C. Corswant and S. Folestad, 2015. PEPT study of particle cycle and residence time distributions in a Wurster fluid bed. AIChE Journal 61(3) 756-768

Li, Y. and P. Wu, 1991. A study on axial gas mixing in a fast fluidized bed, in *Circulating Fluidized Bed Technology III*, P. Basu M. Horio and M. Hasatani (Ed.). Pergamon Press, pp. 581-586

Luyben, W.L. Process modeling, simulation and control for chemical engineers. Second edition. McGraw-Hill, 1990

Mac Namara, C., A. Gabriele, C. Amador and S. Bakalis, 2012. Dynamics of textile motion in a front-loading domestic washing machine. Chemical Engineering Science 75 14-27

Mahmoudi, S., C.W. Chan, A. Brems, J. Seville and J. Baeyens, 2012. Solids flow diagram of a CFB riser using Geldart B-type powders. Particuology 10(1) 51-61

Malek, M.A. and B.C.Y. Lu, 1965. Pressure Drop and Spoutable Bed Height in Spouted Beds. Industrial & Engineering Chemistry Process Design and Development 4(1) 123-128

Mangano, E., S. Brandani, M.C. Ferrari, H. Ahn, D. Friedrich, M.L. Lozinska, P.A. Wright, J. Kahr, R. Morris, M. Croad, N. McKeown, H. Shamsipour and P. Budd, 2013. Efficient and Rapid Screening of Novel Adsorbents for Carbon Capture in the UK IGSCC Project. Energy Procedia 37(40-47

McCabe, W. and J.L. Smith. Unit operations of chemical engineering. Third Edition. McGraw-Hill, 1976

Middha, P., B.V. Balakin, L. Leirvaag, A.C. Hoffmann and P. Kosinski, 2013. PEPT – A novel tool for investigation of pneumatic conveying. Powder Technology 237

87-96

Morrison, A.J., I. Govender, A.N. Mainza and D.J. Parker, 2016. The shape and behaviour of a granular bed in a rotating drum using Eulerian flow fields obtained from PEPT. Chemical Engineering Science 152 186-198

Moughrabiah, W.O., J.R. Grace and X.T. Bi, 2012. Electrostatics in gas–solid fluidized beds for different particle properties. Chemical Engineering Science 75 198-208

Müller, N.P. and H. Segura, 2000. An overall rate-based stage model for cross flow distillation columns. Chemical Engineering Science 55(13) 2515-2528

Nagata, K., K. Murase, H. Yamaguchi, K. Kanai, M. Nakamura and S. Toyama, 1994b. The Flow Properties of a Gas-solid Contactor with Inclined Baffle Plates. Journal of the Society of Powder Technology, Japan 31(12) 869-874

Nagata, K., M. Nakamura, N. Yamagishi, H. Yamaguchi, H. Mori, S. Toyama, Y. Hamada and S. Tamura, 1994a. The Flow Properties of a Gas-solid Contactor with Baffle Plates. Journal of the Society of Powder Technology, Japan 31(8) 556-560

Nagata, K., T. Tadama, H. Kobayashi, Y. Bando, M. Nakamura and S. Toyama, 1998. Flow Properties of Moving-Fluidized Bed with Inclined Baffle Plates. Journal of Chemical Engineering of Japan 31(6) 1020-1024

Nauman, E.B., 1981. Residence time distributions in systems governed by the dispersion equation. Chemical Engineering Science 36(6) 957-966

Nauman, E.B., 2008. Residence Time Theory. Industrial & Engineering Chemistry Research 47(10) 3752-3766

Noordergraaf, I.W., A.W.M. Roes and W.P.M. van Swaaij, 1980. Axial Mixing and Mass Transfer in a Zig-Zag Contactor, in *Fluidization*, J.R. Grace and J.M. Matsen (Ed.). Plenum Press, New York, pp. 341-348

Olazar, M., M.J. San José, A.T. Aguayo, J.M. Arandes and J. Bilbao, 1993. Pressure drop in conical spouted beds. The Chemical Engineering Journal 51(1) 53-60

Ozcan, D. Techno-Economic Study of the Calcium Looping Process for CO_2 Capture from Cement and Biomass Power Plants. PhD thesis. University of Edinburgh, 2014

Paris, J.R., P.N. Ross, S.P. Dastur and R.L. Morris, 1971. Modeling of the Air Flow Pattern in a Countercurrent Spray-Drying Tower. Industrial & Engineering Chemistry Process Design and Development 10(2) 157-164

Park, A.-H., H. Bi and J.R. Grace, 2002. Reduction of electrostatic charges in gas–solid fluidized beds. Chemical Engineering Science 57(1) 153-162

Parker, D.J., M.R. Hawkesworth, C.J. Broadbent, P. Fowles, T.D. Fryer and P.A. McNeil, 1994. Industrial positron-based imaging: Principles and applications.

Nuclear Instruments and Methods in Physics Research Section A: Accelerators, Spectrometers, Detectors and Associated Equipment 348(2–3) 583-592

Parker, D.J., R.N. Forster, P. Fowles and P.S. Takhar, 2002. Positron emission particle tracking using the new Birmingham positron camera. Nuclear Instruments and Methods in Physics Research Section A: Accelerators, Spectrometers, Detectors and Associated Equipment 477(1–3) 540-545

Parker, D.J., T.W. Leadbeater, X. Fan, M.N. Hausard, A. Ingram and Z. Yang, 2008. Positron imaging techniques for process engineering: recent developments at Birmingham. Measurement Science and Technology 19

Paterson, W.R., E.L. Berresford, D.L. Moppett, D.M. Scott, V.K. Simmons and R.B. Thorpe, 2000. Gas flow maldistribution in moving beds of monosized particles. Chemical Engineering Science 55(17) 3515-3527

Patience, G.S. and J. Chaouki, 1991. Solids circulation rate determined by pressure drop measurements, in *Circulating Fluidized Bed Technology III*, P. Basu M. Horio and M. Hasatani (Ed.). Pergamon Press, pp. 627-632

Patience, G.S., J. Chaouki, F. Berruti and R. Wong, 1992. Scaling considerations for circulating fluidized bed risers. Powder Technology 72 31-37

Perry, R.H., D.W. Green and J.O. Maloney (Ed.). Perry's Chemical Engineers' Handbook. Seventh Edition. McGraw-Hill, 1997

Pirngruber, G.D., F. Guillou, A. Gomez and M. Clausse, 2013. A theoretical analysis of the energy consumption of post-combustion CO2 capture processes by temperature swing adsorption using solid sorbents. International Journal of Greenhouse Gas Control 14 74-83

Pröll, T., G. Schöny, G. Sprachmann and H. Hofbauer, 2016. Introduction and evaluation of a double loop staged fluidized bed system for post-combustion CO_2 capture using solid sorbents in a continuous temperature swing adsorption process. Chemical Engineering Science 141 166-174

Qi, J.S. and C. Krishnan, 1996. Mathematical modeling of continuous cross-flow diffusion-controlled dryers. Chemical Engineering Science 51(21) 4769-4780

Radman, J.R., R. Langlois, T. Leadbeater, J. Finch, N. Rowson and K. Waters, 2014. Particle flow visualization in quartz slurry inside a hydrocyclone using the positron emission particle tracking technique. Minerals Engineering 62 142-145

Rafiee, M., M.J.H. Simmons, A. Ingram and E.H. Stitt, 2013. Development of positron emission particle tracking for studying laminar mixing in Kenics static mixer. Chemical Engineering Research and Design 91(11) 2106-2113

Raghuraman, J. and Y.B.G. Varma, 1973. A model for residence time distribution in multistage systems with cross-flow between active and dead regions. Chemical

Engineering Science 28(2) 585-591

Raghuraman, J. and Y.B.G. Varma, 1974. A stochastic model for residence time and contact time distributions of the gas in multistage fluidised beds. Chemical Engineering Science 29(3) 697-703

Roes, A.W.M. and W.P.M. van Swaaij, 1979a. Hydrodynamic behaviour of a gas – solid counter-current packed column at trickle flow. The Chemical Engineering Journal 17(2) 81-89

Roes, A.W.M. and W.P.M. van Swaaij, 1979b. Axial dispersion of gas and solid phases in a gas – solid packed column at trickle flow. The Chemical Engineering Journal 18(1) 13-28

Ruthven, D.M. and C.B. Ching, 1989. Counter-current and simulated counter-current adsorption separation processes. Chemical Engineering Science 44(5) 1011-1038

Ruthven, D.M. Principles of Adsorption and Adsorption Processes. John Wiley & Sons, 1984

Samanta, A., A. Zhao, G.K.H. Shimizu, P. Sarkar and R. Gupta, 2012. Post-Combustion CO2 Capture Using Solid Sorbents: A Review. Industrial & Engineering Chemistry Research 51(4) 1438-1463

Shi, Y.F., Y.S. Yu and L.T. Fan, 1984. Incipient fluidization condition for a tapered fluidized bed. Industrial & Engineering Chemistry Fundamentals 23(4) 484-489

Sielamowicz, I., T.A. Kowalewski and S. Blonski, 2004. Central and eccentric granular material flows in bins/hoppers registered by DPIV optical technique. Acta Agrophysica 4(2) 519-531

Simmons, M.J.H., F. Alberini, A.N. Tsoligkas, J. Gargiuli, D.J. Parker, P.J. Fryer and S. Robinson, 2012. Development of a hydrodynamic model for the UV-C treatment of turbid food fluids in a novel 'SurePure turbulator™' swirl-tube reactor. Innovative Food Science & Emerging Technologies 14 122-134

Sjostrom et al., 2011. Pilot Tests Results of Post-Combustion CO_2 Capture Using Solid Sorbents. Energy Procedia 4 1584-1592

Sjostrom, S. and H. Krutka, 2010. Evaluation of solid sorbents as a retrofit technology for CO_2 capture. Fuel 89(6) 1298-1306

Smolders, K. and J. Baeyens, 2000. Overall solids movement and solids residence time distribution in a CFB-riser. Chemical Engineering Science 55(19) 4101-4116

Stemerding, S., 1962. The pneumatic transport of cracking catalyst in vertical risers. Chemical Engineering Science 17(8) 599-608

Tarka, T.J., J.P. Ciferno, M.L. Gray and D. Fauth, 2006. CO_2 Capture Systems Using Amine Enhanced Solid Sorbents. Presented at the 5th Annual Conference on Carbon

Capture & Sequestration, Washington DC, USA

Tong, H., H. Li, X. Lu and Q. Zheng, 2003. Hydrodynamic modeling of the L-valve. Powder Technology 129(1–3) 8-14

UK Government, 2008. Climate Change Act 2008. Accessed December 2016. http://www.legislation.gov.uk/ukpga/2008/27/pdfs/ukpga_20080027_en.pdf

UK Government, 2013. UK carbon capture and storage: government funding and support. CCS Commercialisation competition. Accessed December 2016. https://www.gov.uk/guidance/uk-carbon-capture-and-storage-government-funding-and-support

UKCCSRC, 2016. National Audit Office on the cancellation of the CCS competition – Comment from UKCCSRC Director Jon Gibbins. Accessed December 2016. https://ukccsrc.ac.uk/news-events/news/national-audit-office-cancellation-ccs-competition-comment-ukccsrc-director-jon

UNFCCC, 2015. The Paris Agreement. Authentic text of the Paris Agreement (English). Accessed December 2016.

http://unfccc.int/files/essential_background/convention/application/pdf/english_paris_agreement.pdf

Van de Velden, M., J. Baeyens and K. Smolders, 2007. Solids mixing in the riser of a circulating fluidized bed. Chemical Engineering Science 62(8) 2139-2153

van Ommen, J.R., J.C. Schouten, M.L.M. vander Stappen and C.M. van den Bleek, 1999. Response characteristics of probe-transducer systems for pressure measurements in gas-solid fluidized beds: how to prevent pitfalls in dynamic pressure measurements. Powder Technology 106(3) 199-218

van Ommen, J.R., S. Sasic, J. van der Schaaf, S. Gheorghiu, F. Johnsson and M.-O. Coppens, 2011. Time-series analysis of pressure fluctuations in gas–solid fluidized beds – A review. International Journal of Multiphase Flow 37(5) 403-428

Veneman, R. PhD thesis. Twente University, 2015

Veneman, R., T. Hilbers, D.W.F. Brilman and S.R.A. Kersten, 2016. CO_2 capture in a continuous gas–solid trickle flow reactor. Chemical Engineering Journal 289 191-202

Veneman, R., Z.S. Li, J.A. Hogendoorn, S.R.A. Kersten and D.W.F. Brilman, 2012. Continuous CO_2 capture in a circulating fluidized bed using supported amine sorbents. Chemical Engineering Journal 207–208 18-26

Verver, A.B. and W.P.M. van Swaaij, 1986. The hydrodynamic behaviour of gas–solid trickle flow over a regularly stacked packing. Powder Technology 45(2) 119-132

Verver, A.B. and W.P.M. Van Swaaij, 1987. The gas--solid trickle-flow reactor for the catalytic oxidation of hydrogen sulphide: A trickle-phase model. Chemical Engineering Science 42(3) 435-445

Villermaux, J. and W.P.M. van Swaaij, 1969. Modèle représentatif de la distribution des temps de séjour dans un réacteur semi-infini à dispersion axiale avec zones stagnantes. Application à l'écoulement ruisselant dans des colonnes d'anneaux Raschig. Chemical Engineering Science 24(7) 1097-1111

Walters, D., 2004. The ins and outs of HEPA filters. Chemical Health and Safety 11(2) 33

Wang, F. PhD thesis. The University of Western Ontario, 1997

Webley, P.A., 2014. Adsorption technology for CO2 separation and capture: a perspective. Adsorption 20(2) 225-231

Wei, F. and J.-X. Zhu, 1996. Effect of flow direction on axial solid dispersion in gas–solids co-current upflow and downflow systems. The Chemical Engineering Journal and the Biochemical Engineering Journal 64(3) 345-352

Weinstein, H. and J. Li, 1989. An evaluation of the actual density in the acceleration section of vertical risers. Powder Technology 57(1) 77-79

Wen, C.Y. and L.T. Fan. Models for Flow Systems and Chemical Reactors. Marcel Dekker, 1975

Wen, C.Y. and S.F. Chung, 1965. Dynamic response equations for various reactor models. The Canadian Journal of Chemical Engineering 43(3) 101-109

Westerterp, K.R. and M. Kuczynski, 1987a. Gas-solid trickle flow hydrodynamics in a packed column. Chemical Engineering Science 42(7) 1539-1551

Westerterp, K.R. and M. Kuczynski, 1987b. A model for a countercurrent gas–solid–solid trickle flow reactor for equilibrium reactions. The methanol synthesis. Chemical Engineering Science 42(8) 1871-1885

Westerterp, K.R., W.P.M. van Swaaij and A.A.C.M. Beenackers. Chemical Reactor Design and Operation. John Wiley & Sons, 1984

White, E.T., 1963. On deadwater regions and stagnant zones in mixing. The Canadian Journal of Chemical Engineering 41(3) 131-132

Wilcox, J. Carbon Capture. Springer, 2012

Wu, J., J. Chen and Y. Yang, 2008. A modified kinematic model for particle flow in moving beds. Powder Technology 181(1) 74-82

Xiao, Y., S. Wang, S. Yang, K. Zhao, X. Zeng and X. Xu, 2012. Solids acceleration

length in a cold dense transport bed. Journal of Thermal Science 21(6) 533-538

Yang, W.-C. and J. Hoffman, 2009. Exploratory Design Study on Reactor Configurations for Carbon Dioxide Capture from Conventional Power Plants Employing Regenerable Solid Sorbents. Industrial & Engineering Chemistry Research 48(1) 341-351

Yang, Z., D.J. Parker, P.J. Fryer, S. Bakalis and X. Fan, 2006. Multiple-particle tracking – an improvement for positron particle tracking. Nuclear Instruments and Methods in Physics Research Section A: Accelerators, Spectrometers, Detectors and Associated Equipment 564(1) 332-338

Yang, Z., H. Fan, D.J. Parker, P.J. Fryer, S. Bakalis and X. Fan, 2014. Study on solids translational and rotational motions in rotating cans. LWT - Food Science and Technology 57(1) 383-392

Yao, J., Y. Zhang, C.-H. Wang and Y.C. Liang, 2006. On the electrostatic equilibrium of granular flow in pneumatic conveying systems. AIChE Journal 52(11) 3775-3793

Yerushalmi, J. and N.T. Cankurt, 1979. Further studies of the regimes of fluidization. Powder Technology 24(2) 187-205

Yousfi, Y. and G. Gau, 1974. Aerodynamique de l'ecoulement vertical de suspensions concentrees gaz-solides—I. Regimes d'ecoulement et stabilite aerodynamique. Chemical Engineering Science 29(9) 1939-1946

Zhang, J., P. Jiang and L.-S. Fan, 1998. Dynamic behavior in transients of solids flow rates in a circulating fluidized bed system, in *Fluidization IX*, L.S. Fan and T.M. Knowlton (Ed.). Engineering Foundation, New York, pp. 245-252

Zhang, Y.-F., Y. Yang and H. Arastoopour, 1996. Electrostatic effect on the flow behavior of a dilute gas/cohesive particle flow system. AIChE Journal 42(6) 1590-1599

Zhao, W., Z. Zhang, Z. Li and N. Cai, 2013. Investigation of Thermal Stability and Continuous CO_2 Capture from Flue Gases with Supported Amine Sorbent. Industrial & Engineering Chemistry Research 52(5) 2084-2093

Appendices

Appendix 1. CFB pressure, pressure drop and air flow labels and locations

- Pressure labels and locations in the benchmark CFB:

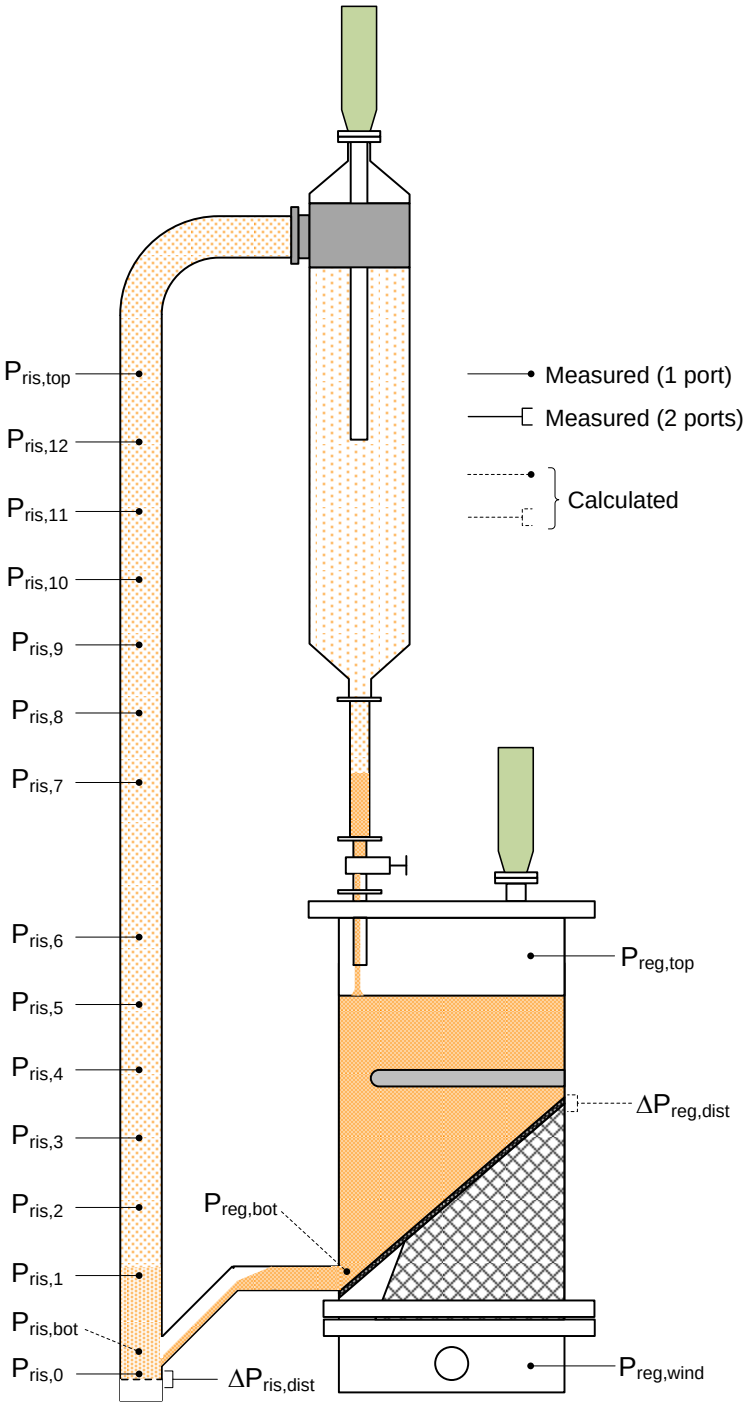

- Pressure drop labels and locations in the benchmark CFB:

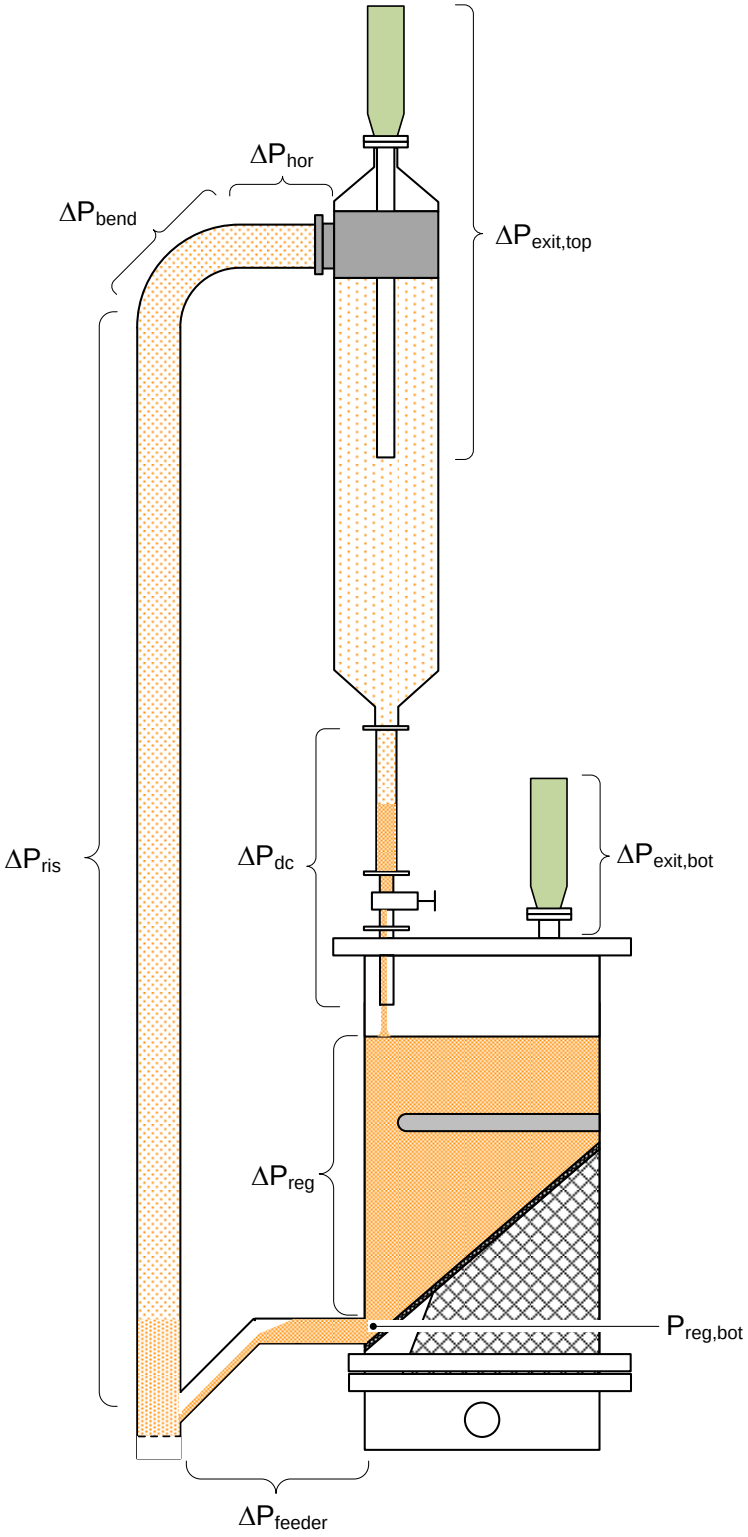

- Air flow labels and locations in the benchmark CFB:

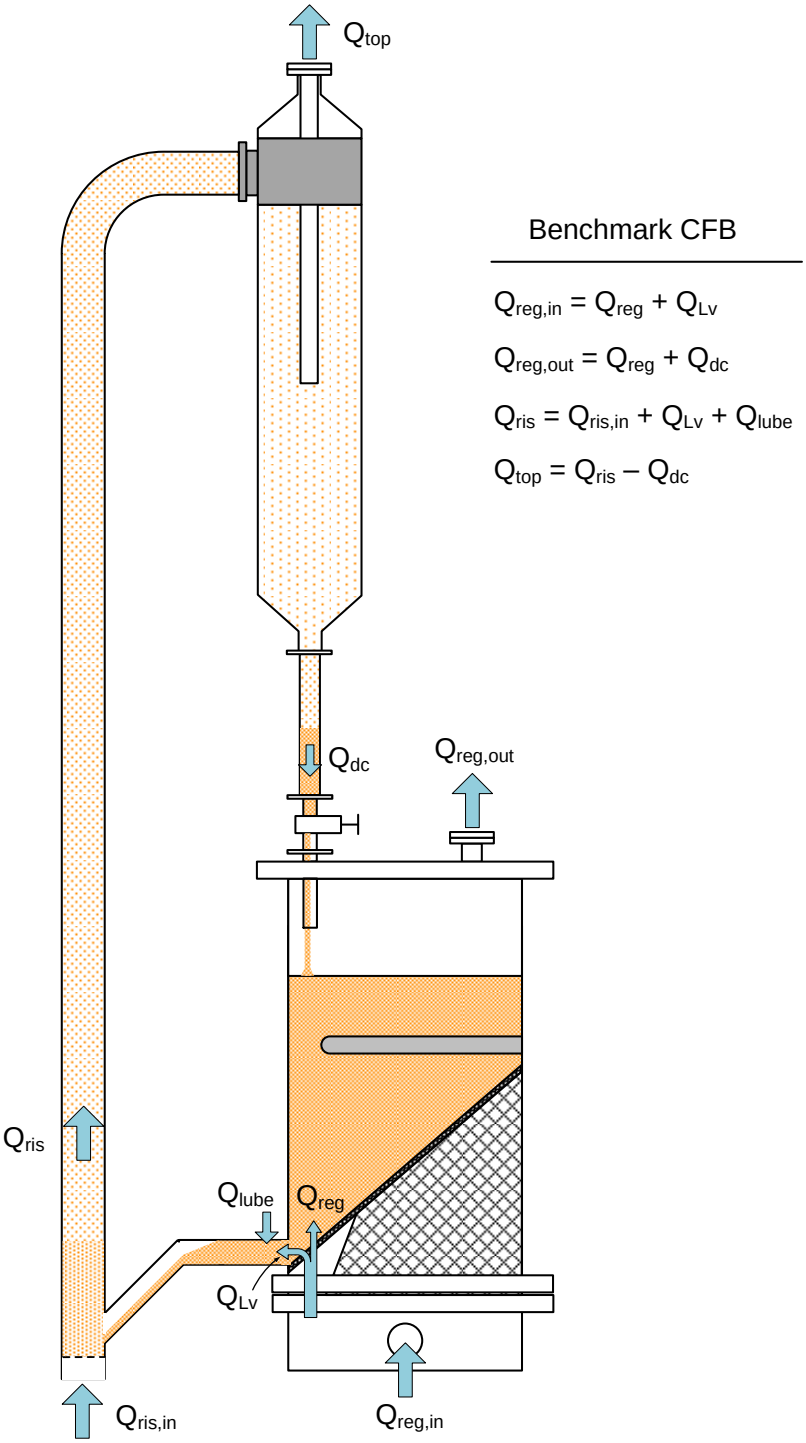

- *Pressure labels and locations in the novel CFB:*

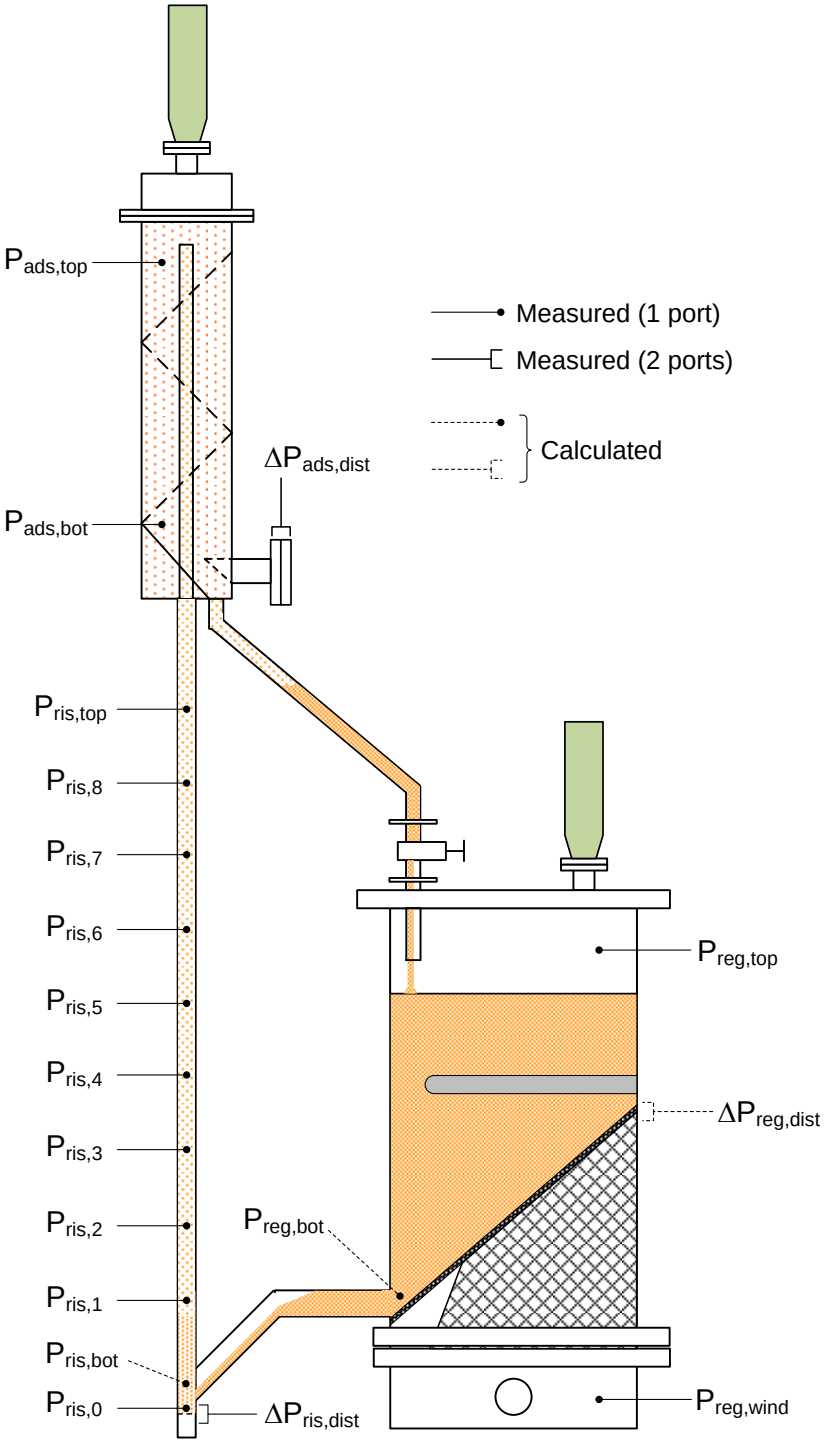

- *Pressure drop labels and locations in the novel CFB:*

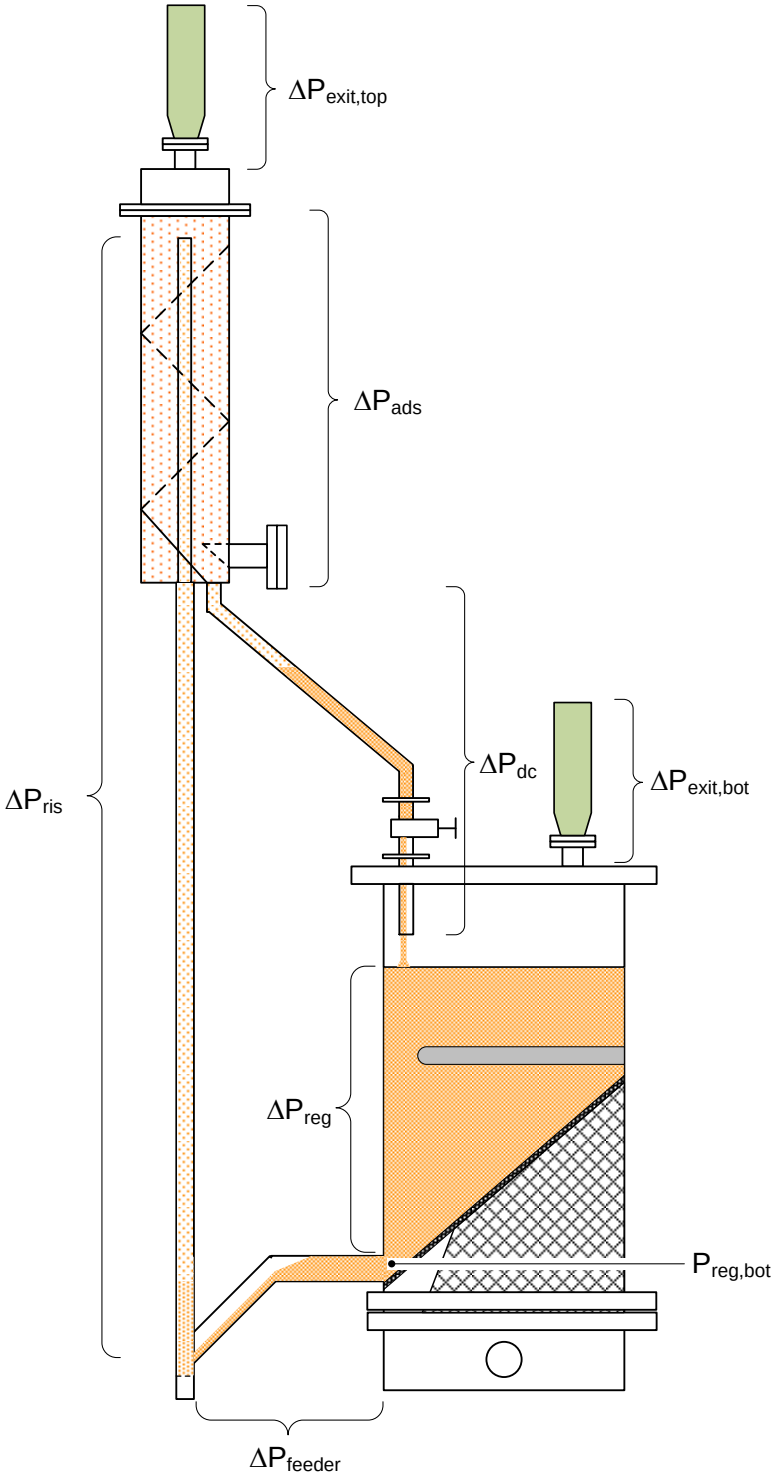

- Air flow labels and locations in the novel CFB:

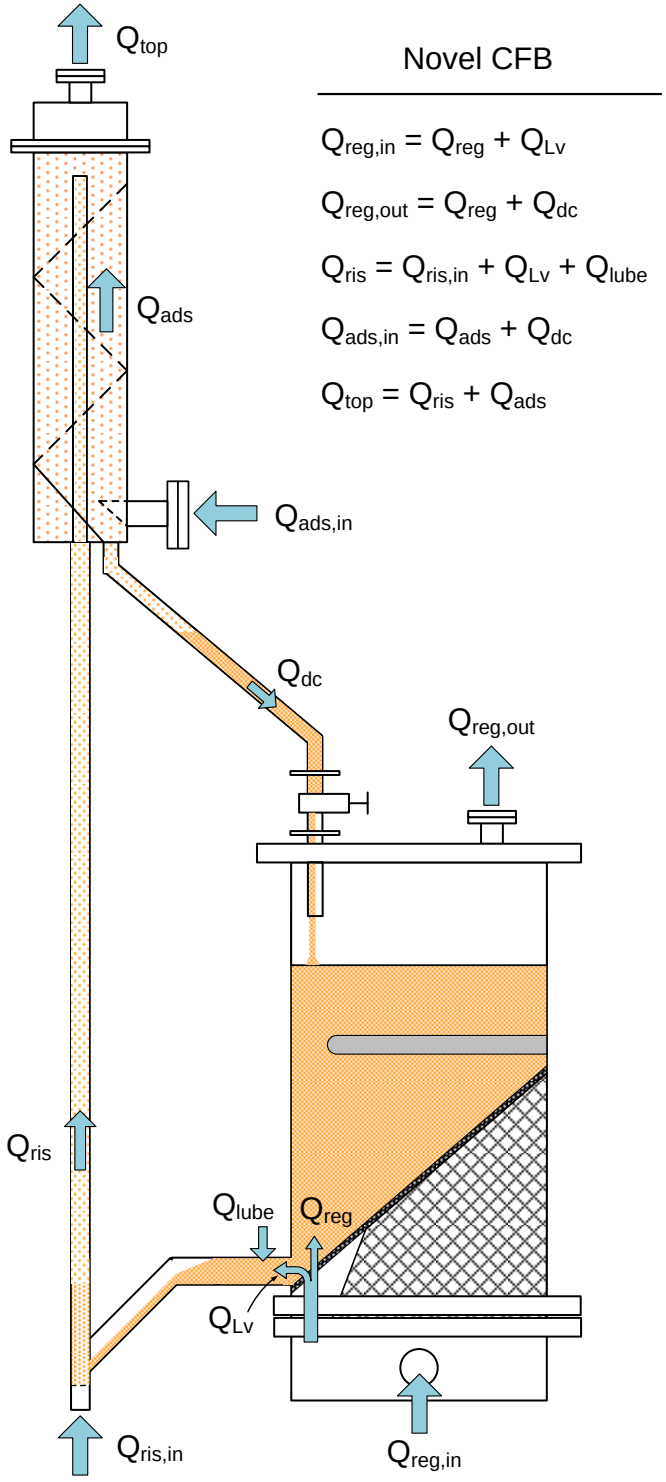

Appendix 2. Pressure drop curves

NOTE: Pressure drop in the empty novel CFB counter-current adsorber was found negligible for the air flow rates used and therefore no pressure drop curve is generated

- *Regenerator air distributor:*

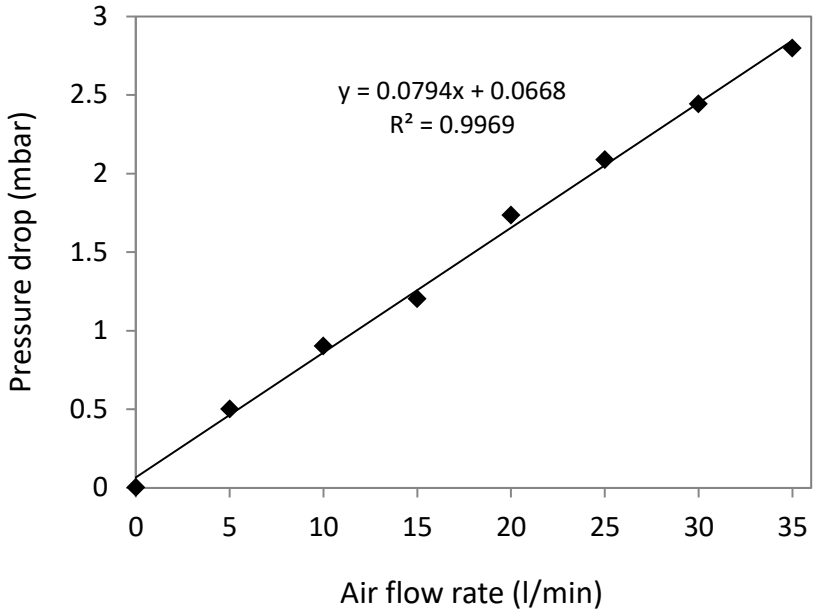

- *Novel CFB riser air distributor:*

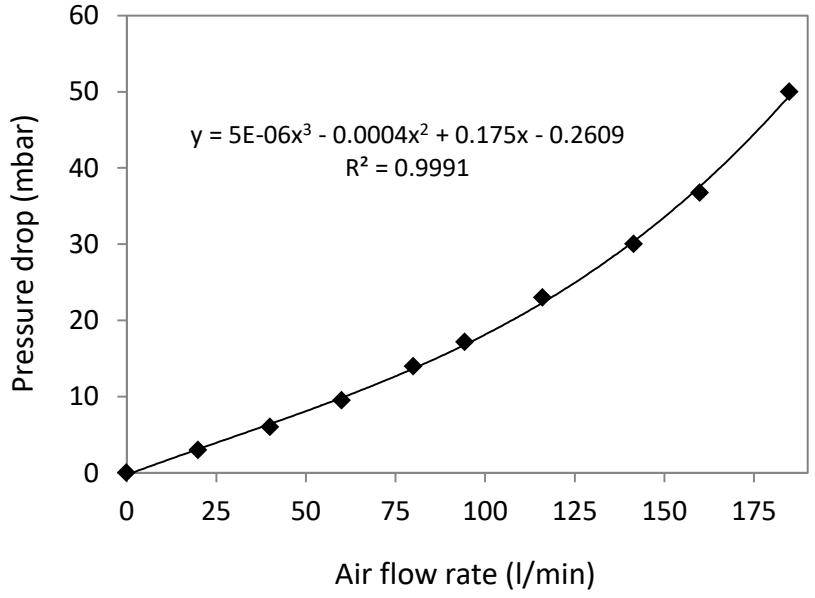

- *Benchmark CFB riser air distributor:*

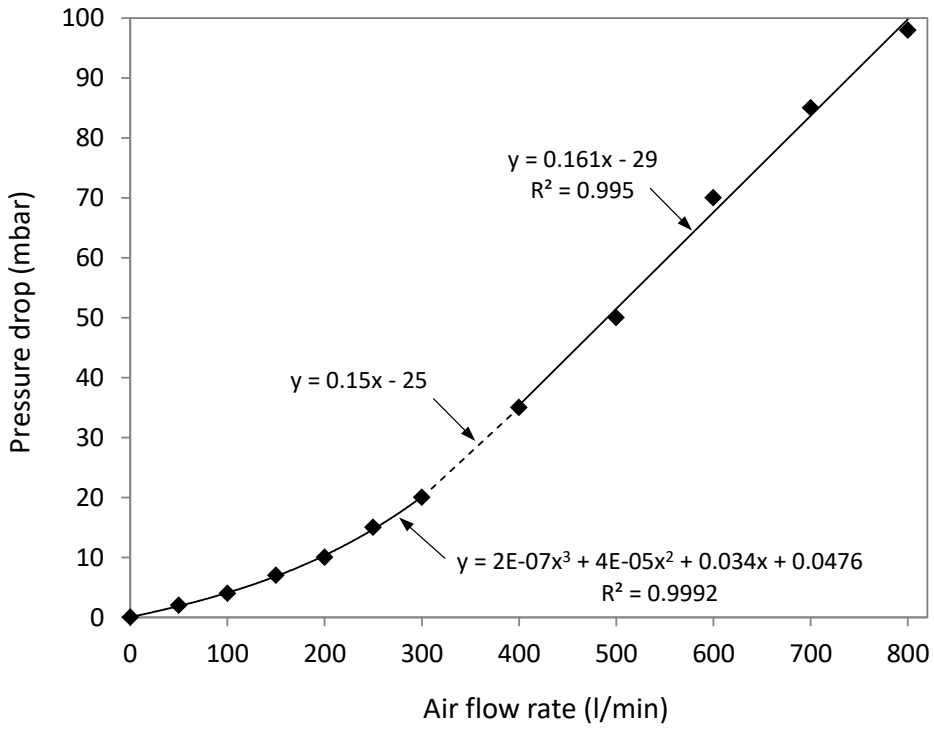

- *Porous disc in novel CFB adsorber air inlet nozzle (install only if needed as backup for air flow rate measurement):*

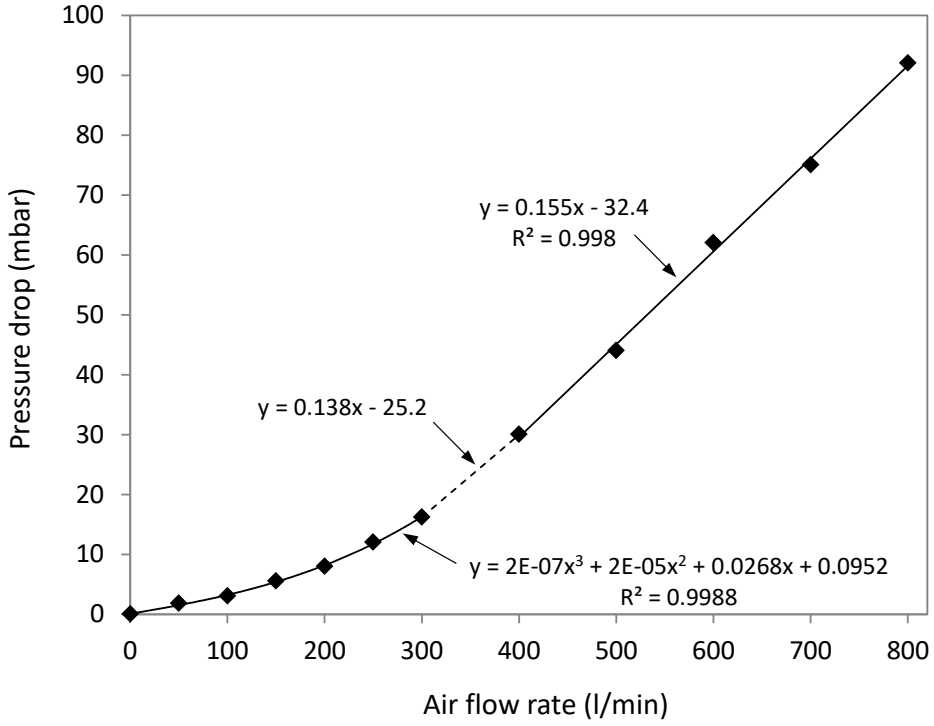

- *Novel CFB lower riser (empty):*

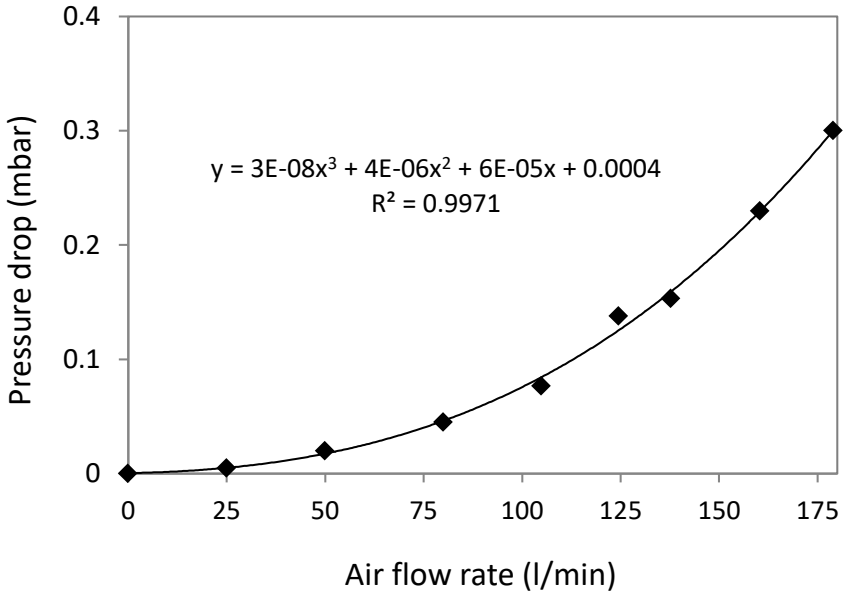

- *Novel CFB upper riser (empty):*

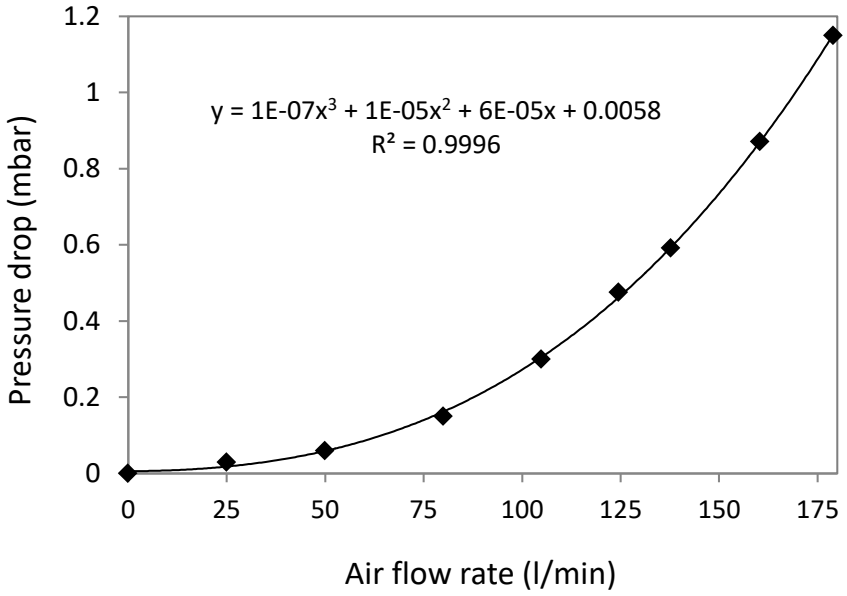

- *Benchmark CFB riser (empty):*

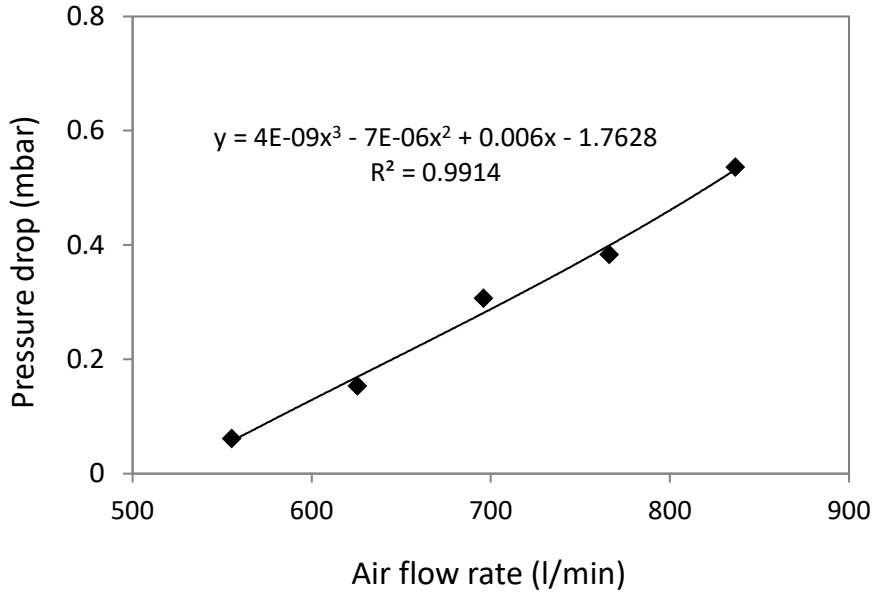

Appendix 3. Instrumentation calibration curves

- *Rotameter 1 (lube air):*

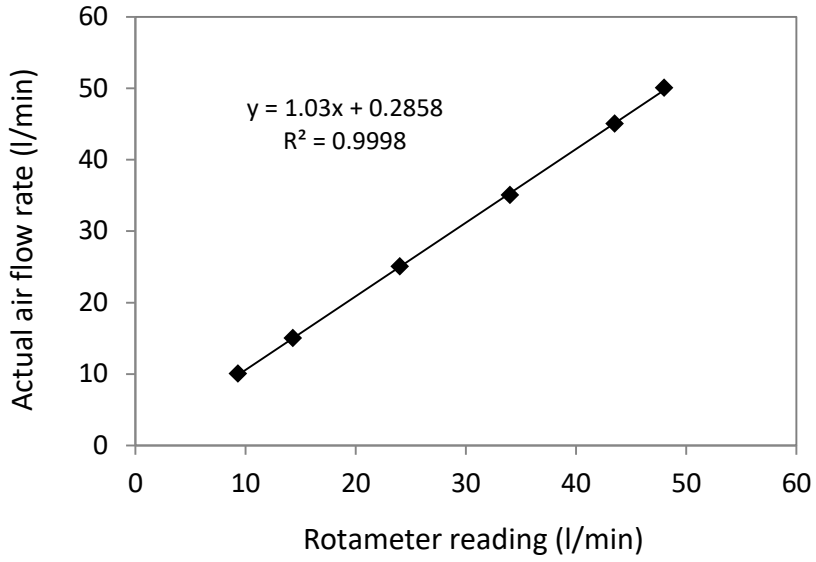

- *Rotameter 2 (CO_2 pulse detection sample):*

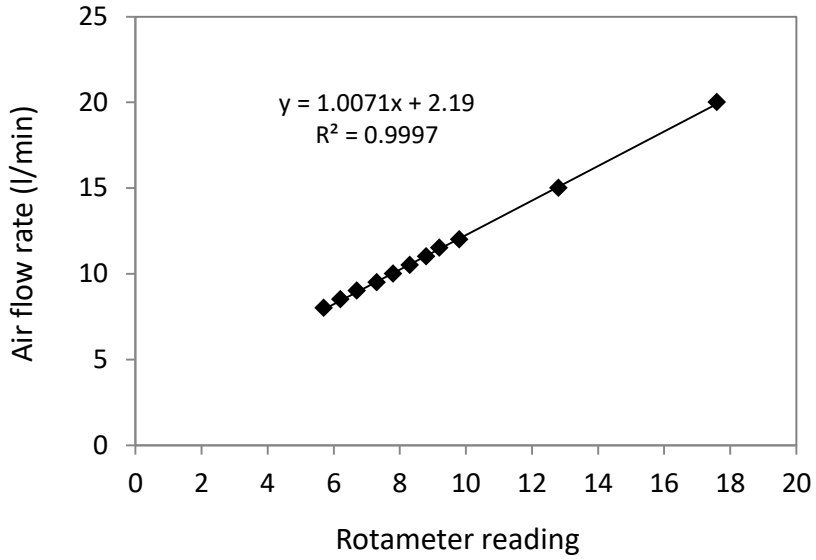

- *Orifice flow meter 1 (regenerator inlet):*

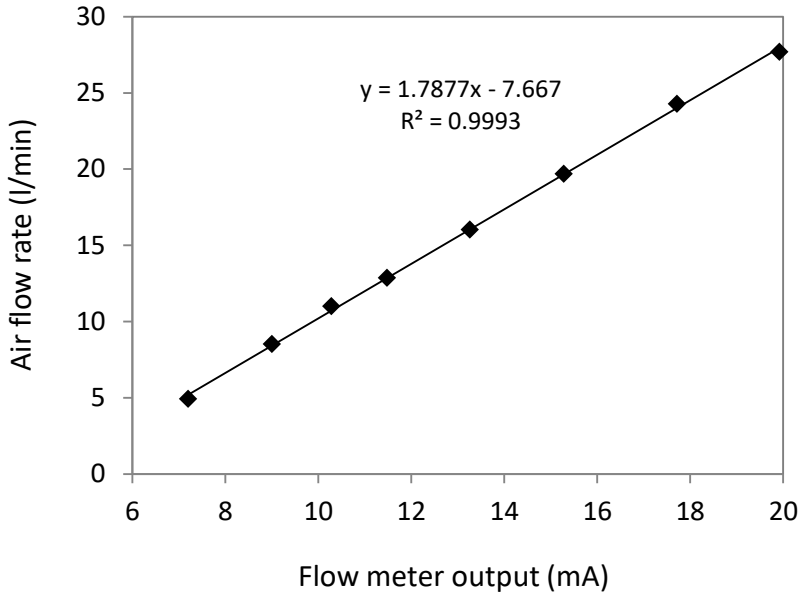

- *Orifice flow meter 2 (regenerator inlet):*

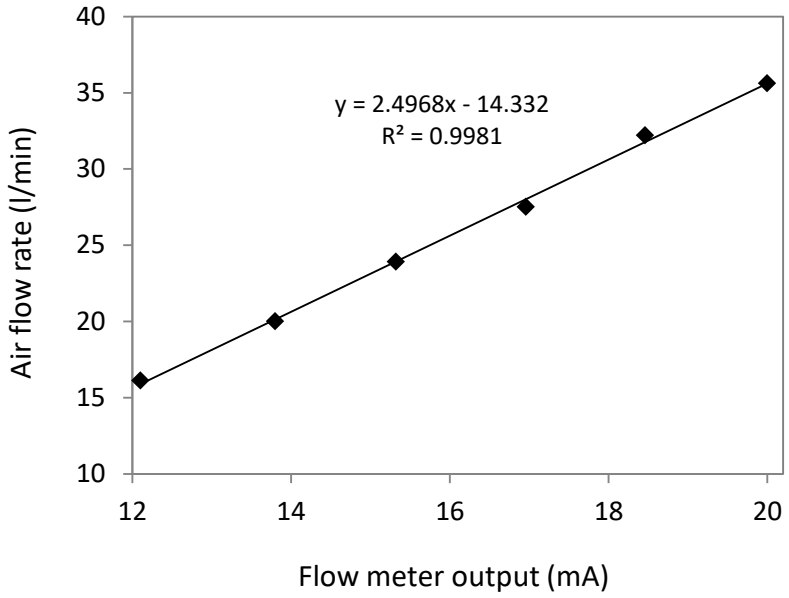

- *Orifice flow meter 3 (novel CFB riser inlet):*

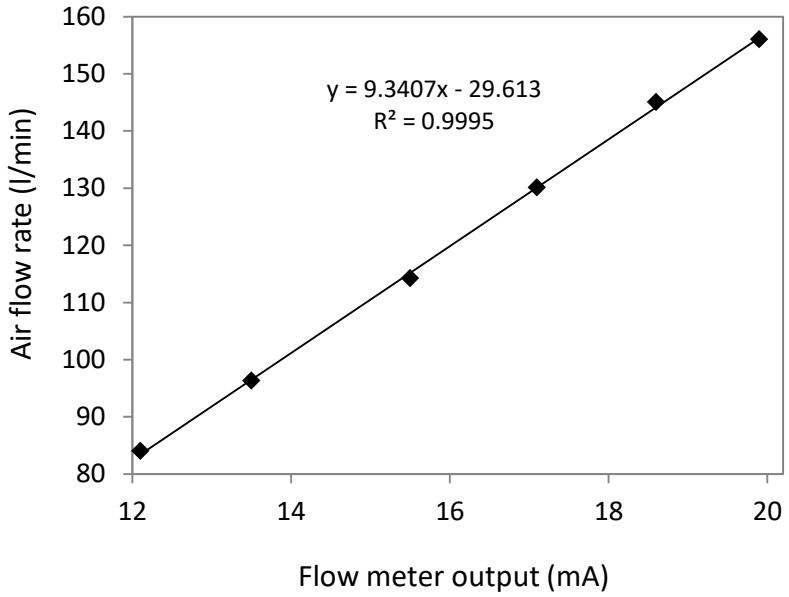

- *Orifice flow meter 4 (benchmark CFB riser inlet, novel CFB adsorber inlet):*